Doctoral Dissertation
Doctoral Program in Material Science and Technology (34th Cycle)

Advanced nanostructured optical glasses and glass-ceramics for photonic applications

Elisa Muzi

******

Supervisors
Prof. Davide Luca Janner
Prof. Matthieu Lancry

Doctoral Examination Committee:
Prof. Nadège Ollier, CEA-CNRS, École Polytechnique (IPP), (Paris, France)
Prof. Daniel Milanese, Department of Engineering and Architecture, University of Parma (Parma, Italy)

Politecnico di Torino
2022

This dissertation is presented in partial fulfillment of the requirements for Ph.D. degree in the Graduate School of Politecnico di Torino (ScuDo).

I hereby declare that the contents and organization of this dissertation constitute my own original work and does not compromise in any way the rights of third parties, including those relating to the security of personal data.

Elisa Muzi

26 May 2022

...to my parents and
to all the human beings
that lost their breath
for the Covid pandemic 2019

Acknowledgments

I would like to express my appreciation to Prof. Davide Janner for teaching me mental maps, to go beyond my limits, and to never doubt myself, except for evolving towards a higher quantum leap. I would like to express my appreciation to Prof. Matthieu Lancry for teaching me that everything is easy, if you try, you learn, but you truly have to believe in it. I would like to thank Diego Pugliese for his help in glass making and for our coffee breaks together. I would like to thank Maxime Cavillon for welcoming me and following me from the first day. I would like to express my gratitude to Bertrand Poumellec for teaching me how to take my time and how to tell a story without fear. I would like to thank Benjamin Sapali for his silent understanding and important initial training. I would like to express my gratitude to Duccio Gallichi Nottiani, a special colleague and especially a friend, a constant presence in all the most disparate scenarios of our lives from the first day we met, including songs, books, hopes, and sol-gel synthesis. I would like to thank Prof. Monica Ferraris and the Glance Group for hosting me at DISAT. Thanks to the ICCMO Chinese group, Yitao Wang, Juan Xe, Qiong Xie and Jiafeng Lu, for all our lunches together and sharing new points of view. I would like to thank Ruyue Que, a dear colleague and friend, a constant, discreet, clear, and beautiful presence. I would like to thank David Msika, a special French friend who understands things without having to explain them to him. I would like to thank all the people of Paris-Saclay University, especially those of ICCMO and of my hallway, for welcoming me and also saying goodbye with a smile. Thanks to Valérie for finding a laptop. Thanks to whom my laptop has been configured by and not only. Thanks to Maison Orion group for making the lockdown less heavy. Thanks to all the French people who taught me that French is my second language to express myself as I really am. Thanks to my parents, my Franciscan brothers and sisters, my extended Italian family, my friends, for support and endurance. Thank God, for making all this possible.

Abstract

Ultrafast laser-oriented crystallization of glass materials is an emerging and promising research field. Glass is an ideal functionalization enabler material, and it permits the study of light-driven crystallization induced by ultrashort pulses. Femtosecond (fs, 1 fs = 10-15 s) laser direct writing (FLDW) is a tool that enables nano-structuring and multi-functionalization for the fabrication of new active photonic devices in 3D. It takes advantage of efficient nonlinear absorption processes triggered by high light power densities (typ. 1-100 TW/cm^2).

This Ph.D. work principally investigates the effect of laser irradiation conditions, through the control of four tunable laser parameters (pulse energy, repetition rate, polarization, and scanning speed), on glass crystallization in 3D. The first part of this work relates on the synthesis of borate glasses by sol-gel technique, and silicate and borosilicate ones by the conventional melt-quenching one. Then, a second part is dedicated to femtosecond laser irradiation of the silicate and borosilicate samples to trigger, and control, localized and oriented crystallization of non-centrosymmetric nanocrystals of $LiNbO_3$. Patterns including dots and lines were written inside the glass samples, and laser-structural modification threshold energies were identified. A third part is related to the characterization of the laser-induced structures. Second harmonic generation (SHG), originating from $LiNbO_3$ nanocrystals, was investigated. The effect of laser polarization on the nanocrystal orientation was investigated through its angular dependency of SHG intensity. The study of nanocrystals orientation concerns the effect of SiO_2 substitution with B_2O_3 into the glass matrix. The nanocrystals orientation and laser track microstructure is further investigated through electron backscattering diffraction (EBSD).

Through laser writing, nanogratings, i.e., lamellar-like structures growing perpendicular to the laser polarization, were observed in both silicate and borosilicate glasses. These sub-wavelength structures induced a birefringent response taking its root from the local variation of refractive indices between glass and crystal phases. Additionally, it was found that B_2O_3-rich glasses promote fabrication of birefringent structures, precisely a larger and faster birefringent response (>150 nm at λ=550 nm) than B_2O_3-free glass as well as lower glass-making temperatures.

The effect of scanning speed on crystallization mechanisms is discussed through from the basis of Time Temperature Transformation (TTT) and Continuous Cooling Transformation (CCT) diagrams. For the ease to nucleate and grow crystals in B_2O_3-rich glasses (21% mol), the crystallization domain is wider relative to B_2O_3-free glasses glass. It is demonstrated that the progressive substitution of SiO_2 with B_2O_3 (from 0% to 21% mol) leads to a progressively fast crystallization of $LiNbO_3$ nanocrystals induced by fs-laser irradiation.

As a final note, a suitable choice of laser parameters is critical to control both size and orientation of photo-precipitated nonlinear nanocrystals. A direct consequence is an enhanced tunability in optical properties essential for photonic applications.

Contents

1. Introduction 1
    1.1 Motivation of the work 1
    1.2 Objectives 5
    1.3 Structure of the chapters 5
    1.4 Bibliography 6
2. Fabrication and characterization of lithium niobium silicate and borosilicate glasses 10
    2.1 Glass: definition chemistry, and phase separation 10
        2.1.1 Debate on glass definition 10
        2.1.2 Glass chemistry 14
        2.1.3 Phase separation: nucleation and growth 16
    2.2 Melt quenching technique 18
        2.2.1. Lithium niobium silicate glass fabrication 20
        2.2.2 Lithium niobium borosilicate glass fabrication 21
    2.3 Glass polishing 22
    2.4 Glass characterization 23
        2.4.1 Differential Scanning Calorimetry (DSC) 23
        2.4.2 Scanning Electron Microscopy (SEM) combined with Energy-Dispersive X-ray Spectrometry (EDS) 24
        2.4.3 Ultraviolet–visible spectroscopy (UV spectra) 25
        2.4.4 Thermal diffusivity measurements 26

2.5 $LiNbO_3$: crystallographic and optical properties 28
2.5.1 Crystallographic properties 29
2.5.2 Optical properties 31
2.6 Conclusions 34
2.7 Bibliography 35
3. Laser and optical materials properties 40
3.1 Laser: brief history and typology 40
3.1.1 Basics and brief history of laser typologies 40
3.1.2 Ultra-fast laser 45
3.1.3 Gaussian beam 46
3.1.4 Spherical aberration 49
3.1.5 Light scattering 50
3.2 Laser-matter interaction 51
3.2.1 Free electron formation 51
3.2.2 Relaxation of photo-excited electrons 54
3.2.3 Femtosecond laser-induced defects 56
3.3 Femtosecond Laser Direct Writing (FLDW) 57
3.3.1 Femtosecond laser for glass-ceramics fabrication: working principle and setup 57
3.3.2 Femtosecond laser-induced structural changes in glasses 58
3.3.3 Brief bibliographical overview on femtosecond laser-induced crystallization in glasses 62
3.4 Optical properties and non-linear effects 63
3.4.1 Linear and non-linear optics: introduction 63
3.4.2 Light polarization, refractive index, and birefringence 64
3.4.3 Physical quantities and non-linear optical phenomena: macroscopic theory [90] 67
3.5 Conclusions 71
3.6 Bibliography 72

4. Femtosecond Direct Laser Writing (FDLW): experimental section and results 83
4.1 Glass selection for Femtosecond Direct Laser Writing 84
4.2 Femtosecond Direct Laser Writing (FDLW) 84
4.2.1 Fs-laser writing of dots (static mode) 87
4.2.2 Fs-laser writing of lines (dynamic mode) 91
4.3 Polarized light microscopy 94
4.4 Second Harmonic Generation (SHG) measurements 99
4.5 Quantitative Phase Microscopy (QPM) 102
4.6 Microstructure analysis 106
4.6.1 Scanning Electron Microscopy (SEM) 106
4.6.2 Electron Back Scatter Diffraction (EBSD) 108
4.7 Conclusions 112
4.8 Bibliography 112
5. Crystallization mechanisms and kinetics upon laser-glass 117
5.1 Agreement between SHG response and EBSD maps in LNS and LNSB glass matrices 118
5.1.1 Three regimes and landscapes 118
5.1.2 Link between laser parameters and SHG measurements 123
5.2 Investigation on nanocrystals orientation and nanogratings through scanning speed variation 140
5.2.1 Requirements for nanocrystals precipitation 140
5.2.2 Nanogratings in LNS and LNSB 142
5.2.3 Influence of glass chemical structure and bonding on nano-gratings formation 146
5.3 TTT and CCT diagrams: crystallization dynamics description by femtosecond laser modification in case study of LNS glass 153
5.4 Laser-induced crystallization domain in LNS34 and LNS13B21 164
5.5 Boron as convenient addition in glass network 169

5.6 Conclusions 170
5.7 Bibliography 171
6. Sol-gel process for glass synthesis: a route towards the fabrication of Bi_2O_3 – B_2O_3 – Fe_2O_3 179
6.1 Introduction and general features 180
6.1.1 General overview of the sol-gel process 180
6.1.2 Sol-gel typical features 184
6.2 Overview on nanoparticles and bulk glasses fabricated by sol-gel process 188
6.3 Towards a new synthesis route of Bi_2O_3 – B_2O_3 – Fe_2O_3 190
6.3.1 Introduction 190
6.3.2 A brief overview of bismuth ferrite ($BiFeO_3$) and BBF system 192
6.3.3 Pechini method overview 194
6.3.4 The modified Pechini method for BBF synthesis 197
6.3.5 Towards successful composition: focus on three experiments 200
6.3.6 Activity outlook and future improvements 206
6.4 Conclusions 207
6.5 Bibliography 208
7. Conclusions and future outlooks 216
7.1 Main achievements 216
7.2 Future outlooks 219
7.3 Bibliography 221
Appendix 222
A - Classical Nucleation Theory (CNT) 222
B - Generic microscopic model of the origin of optical nonlinearity 226
C - Second harmonic generation 233
D - Trends of SHG intensity for all the four glass compositions: curves and polar representations 237
E - Quantitative Phase Microscopy (QPM) 245

Bibliography 248

List of Figures

Figure 1: Ph.D. work objectives and specific issues according to NANOMAX project 4

Figure 2: Structural classification of materials: when the stable phases present an excess of entropy, they can be transformed into non-crystalline solids that are always unstable or metastable phases [3] 12

Figure 3: Atomic structure of SiO_2 a) crystal (Quartz) and b) glass (so-called silica) [18] 14

Figure 4: a) Scheme of a glass-forming substance, specifically enthalpy versus temperature plot sowing four distinct states: liquid (L), supercooled liquid (SCL), glass (G) and crystal (C). T_m = melting temperature, T_g = glass transition temperature [13]; b) Change of enthalpy with the temperature for the different allotropic phase (cooling at a fixed rate, q ($t_{OBS} \sim 1/q$)) [adapted from http://www.certev.ufscar.br/documentos/arquivos/gupta-slide] 16

Figure 5: Schematic free energy diagram of the spinodal decomposition. (a) Spinodal decomposition is shown on the phase diagram displaying a miscibility gap. Note that the boundary separating the metastable and the unstable region is known as spinodal curve that can be obtained by performing a common tangent construction of the free-energy curve. (b) The free energy curve is plotted as a function of composition for the phase separation temperature T_2. In the spinodal region, the curvature of the free-energy curve is negative. Note that the binary mixture with initial temperature (T_1) is cooled quickly to a lower temperature (T_2). X_1 and X_2 are the equilibrium compositions that correspond to the free energy minima. The spinodes are marked as S_1 and S_2 in the diagram. In the spinodal region, the curvature of the free-energy plot is negative [23] 18

Figure 6: SiO_2 - $LiNbO_3$ - B_2O_3 ternary phase diagram 19

Figure 7: Scheme of glass making process starting from the chemical powders . 20

Figure 8: Example of LNS glass plate after the glass cooling (typ. 5cm size and few mm thick) 21

Figure 9: a) crucible after glass casting; three highlighted zones of glass in different view: transparent, rough, and white zones; b) glass on the heating plate; c) side view of the glass..... 22

Figure 10: Differential scanning calorimetry (DSC) scans for four glasses composition with an increasing amount of B_2O_3 in the batch compositions in mol% 24

Figure 11: a) Elemental composition analysis for four glass composition by SEM-EDS analysis; b) Exploration of Nb/Si ratio: ratio theoretical vs ratio experimental 25

Figure 12: Absorption spectra for LNS (precisely, LNS34), LNSB (precisely, LNS13B21) and SiO_2 (Suprasil) for sake of comparison..... 26

Figure 13: Thermal diffusivity curves extracted from measurements effectuated in ICCMO of a) LNS27B7, b) LNS20B14, c) LNS13B21. Black dots correspond to the run-up ramp and red ones to descent ramp..... 27

Figure 14: Temperature spatial distribution evolution T(r,t) after pulse deposition inside the glass, as time increases from t_1 to t_4. At decreasing of maximum temperature with time, the width of the distribution increases [31]..... 28

Figure 15: a) Phase-equilibrium diagram for $LiNbO_3$ [36] and b) scheme of the furnace for Czochralski growth at $LiNbO_3$ [37]..... 29

Figure 16: Positions of the lithium atoms (double cross-hatched circles) and the niobium atoms (single cross-hatched circles) with respect to the oxygen octahedra in the a) paraelectric phase and b) ferroelectric phase of lithium niobate, the horizontal line on the right side stands for the oxygen layers [38]; c) atomic structure of $LiNbO_3$ [40]..... 30

Figure 17: Trend of refractive indexes versus wavelength of congruently growth of $LiNbO_3$ [43]..... 32

Figure 18: Principal laser properties: a) coherence [2]; b) representation of linewidth by Full Width at Half Maximum (FWHM) in a plot of frequency in function of power [3] 41

Figure 19: The three electron-photon interaction processes in atoms occurring in the laser: absorption, spontaneous emission, and stimulated emission [2]..... 42

Figure 20: Representation of a) Equilibrium Boltzmann distribution and b) population inversion after pumping that constitutes the guiding principle in lasers [4] 42

Figure 21: a) Principal laser components (https://www.ulsinc.com/learn); b) Four-level laser system (https://it.wikipedia.org/wiki/population inversion)..... 43

Figure 22: Exponential relation between gain and intensity, highlighting the specific value in saturation mode [5] 44

Figure 23: Schematic diagram of laser basic working principle..... 44

Figure 24: Scheme of components of the first ruby laser..... 45

Figure 25: a) CPA Scheme [14]; b) our CPA configuration in which the chirp is illustrated with colours and the signal is treated by a fiber amplifier..... 46

Figure 26: Irradiation scheme of laser in the XY plane of a glass sample..... 47

Figure 27: Gaussian beam: a) change in wavefront radius with propagation distance [15], b) the definition of numerical aperture [16], and c) the embedded Gaussian [15] 49

Figure 28: Interface spherical aberration scheme due to the refractive index mismatch along laser propagation direction [18] 50

Figure 29: Schematic diagram of the photoionization of an electron in an atomic potential for different values of the Keldysh parameter (γ). In a solid, the electron is promoted from the valence band to the conduction band rather than ionized: a) multiphoton ionization, c) tunneling ionization, b) the above processes combined, and d) avalanche ionization: free carrier absorption followed by impact ionization [24]. 52

Figure 30: Different photoionization regimes with varying photon energy and laser intensity. The dashed grey line shows the case of $\gamma = 1.5$ for C_{60} ionization, which separates the multiphoton regime ($\gamma > 1.5$) from the tunneling regime ($\gamma << 1.5$) [26] 53

Figure 31: a) Schematic representation of the dynamics of fs laser interactions with dielectrics. The numbers from 1 to 5 correspond to the process as described within the text (after S. Guizard, LSI, CEA, Saclay France and [29]), b) timescale of the physical phenomena associated with the interaction of a fs laser pulse with transparent material [27]..... 54

Figure 32: Ultrafast picosecond and femtosecond fiber lasers | IPG Photonics... 57

Figure 33: fs laser fabrication in 3D: a) a laser damage line, b) the cross-section of a line written by moving the sample parallel to the incident laser beam, and c) the cross-section of a line written by moving the sample perpendicular to the incident laser beam [40]. 58

Figure 34: Scheme of a fs laser beam focused in bulk fused silica: a) fs laser focused below the sample surface resulting in high intensity in the focal volume, b) energy nonlinearly absorbed and free-electron plasma created by multiphoton/tunneling and avalanche photoionization, c) hot-electron plasma formed transfers energy to silica lattice on ~10 ps time scale resulting in one of three types of a permanent modification, and d) fs laser-induced various modifications in glass as a function of pulse energy: here it is possible to distinguish the three threshold regimes T1, T2, and T3 in correspondence of the phenomena generated [42]. 60

Figure 35: Pulse energy versus numerical aperture (NA) and pulse duration: diagram for a) small pulse duration (45 – 60 fs), b9 160 fs, c) 200 fs, and d) 250 fs (region II disappears) with SiO_2 [41]..... 62

Figure 36: a 400-nm thick non-linear mirror that reflects radiation at twice the input light frequency [82]..... 63

Figure 37: Light polarization scheme [88]..... 64

Figure 38: ordinary and extraordinary rays of light on a crystal [89]..... 65

Figure 39: k-vector magnitude surfaces for uniaxial crystals. The Poynting vector is normal to these surfaces. (a) Positive uniaxial crystal, walk-off is toward the z-axis (optic axis). (b) Negative uniaxial crystal, walk-off is away from the z-axis [90]. 66

Figure 40: Illustration of dispersion in the index of refraction. The two resonant features show regions anomalous dispersion; these regions are accompanied by high losses [91]..... 66

Figure 41: Schematic diagram of the energy and momentum conservation..... 69

Figure 42: Thermal poling used to introduce a second-order nonlinearity into the material (http://www.eie.gr/nhrf/institutes/tpci/researchteams/mspc/mspc-nanostructuredmat-en.html)..... 70

Figure 43: Schematic diagram of the femtosecond laser system used at ICCMO 85

Figure 44: a) laser writing scheme: the translation stage displacement is in the XY sample plane, while the laser beam propagation direction is along Z; b) top view of three different laser polarization configurations referenced to laser writing direction along the Y-axis: parallel (Y_y), at 45° (Y_{45}) and perpendicular (Y_x)..... 87

Figure 45: Static dots under white light for a) LNS34 and b) LNS27B7 88

Figure 46: Scheme of space-selective crystallization induced by tightly focused femtosecond laser pulses adapted from [5]..... 89

Figure 47: Heatmaps of incubation time for four glasses: a) LNS34; b) LNS27B7; c) LNS20B14 and d) LNS13B21 90

Figure 48: Evolution of incubation time in function of delivered laser power depending on glass composition [6] 91

Figure 49: Scheme of irradiation program for lines according to these following writing conditions: laser beam direction = Z, writing direction along Y, three different laser polarization configurations: Y_x, Y_{45} and Y_y, NA = 0.6, pulse duration = 250 fs, repetition rate = 200 kHz, pulse energy from 0.25 to 2 µJ, scanning speed= 1 µm/s for LNS34, LNS27B7, LNS20B14, and LNS13B21 glasses 92

Figure 50: Scheme of irradiation program for 5 mm lines at these specific irradiation conditions: laser beam direction = Z, writing direction along Y, two laser polarization configurations Y_x and Y_y, NA = 0.6, repetition rate = 200 kHz, pulse duration = 250 fs, two values of pulse energy 0.5 and 1 µJ and different scanning speed respectively from 1 µm/s to 200 µm/s for a) LNS34 and for b) LNS13B21 from 1 µm/s to 200 µm/s at 0.5 µJ and from 1 µm/s to 625 µm/s at pulse energy equal to 1 µJ 93

Figure 51: Optical microscope images of lines written by fs-laser in LNS34 and LNS13B21 glasses in Y_x polarization configuration, at various scanning speeds, two pulse energies: 0.5 and 1 µJ/pulse, and repetition rate fixed at 200 kHz..... 94

Figure 52: Dots, written according to polarizer direction, Y_y laser polarization configuration, pulse duration = 250 fs, irradiation time = 1s (after waiting incubation time), under polarized light at analyzer and polarizer crossed (P = polarizer, A = analyzer)..... 95

Figure 53: Lines under polarized light written according to analyzer direction (P = polarizer, A = analyzer), at repetition rate equal to 200 kHz and scanning speed equal to 1 µm/s 96

Figure 54: Optical microscope images of lines at different scanning speed (1, 75 and 350 µm/s) under different illumination condition for LNS13B21 glass at a pulse energy of 0.5 µJ; (P = polarizer, A = analyzer) [18]..... 97

Figure 55: Retardance in nm measured at 550 nm at the center of the irradiated lines as a function of scanning speed for LNS34 and LNS13B21, at two pulse energies (0.5 and 1 µJ/pulse), repetition rate fixed at 200 kHz and for a) Y_y and b) Y_x laser polarization configurations [18]. 98

Figure 56: a) Second Harmonic Generation (SHG) setup used for all the experiments of this Ph.D. work [19]; b) SHG detected under static irradiation at the end of the incubation time of a few seconds [6]..... 99

Figure 57: SHG spectrum obtained for LNS13B21 lines written at 1.25 μJ/pulse, at Y_x polarization configuration, at fixed repetition rate equal to 200 kHz and scanning speed equal to 1 μm/s. The reference position of the laser polarizer is 0°, which coincides with the position corresponding to 180°..... 100

Figure 58: normalized SHG intensity profiles for the four glass compositions as a function of probing polarization angle in the XY plane for 0.5 and 1.25 μJ/pulse a) at Y_x and b) Y_{45} polarization configuration; c) polar representation for LNS13B21 glass for 0.5 and 1.25 μJ/pulse with three polarization configuration Y_y, Y_{45} and Y_x [6]..... 101

Figure 59: QPM analysis process represented through the CCD camera mounted on the microscope: the three lines represent a phase image converted into a software representation after applying the MATLAB code to extract black background and white lines images..... 103

Figure 60: QPM images for LNS27B7 glass on lines at three polarization configurations Y_y, $Y_{45,}$ and Y_x at pulse energies of a) 0.25 μJ, b) 0.5 μJ, c) 0.75 μJ and d) 1 μJ..... 105

Figure 61: QPM analysis modulation in which the phase change in rad is highlighted by a plot where we can see three peaks in correspondence of each set of the three lines reported on the previous Figure 60..... 106

Figure 62: Presence of nanogratings detected by Scanning Electron Microscopy analysis for LNS13B21 line at pulse energy equal to 0.5 μJ, repetition rate fixed at 200 kHz, and scanning speed equal to 75 μm/s..... 107

Figure 63: Scanning electron micrographs of the laser track cross-section induced by fs-laser on LNS13B21 glass sample and for different scanning speeds. In yellow there is the area where crystallization within the laser track, associated with crystallization, is detected; in orange, the area where lamella-like nanogratings are observed. Fixed parameters are: λ = 1330 nm; f = 200 kHz; NA = 0.6; pulse duration = 250 fs; focal depth = 240 μm (in air) [18]..... 108

Figure 64: Electron Back Scatter Diffraction (EBSD) micrographs of the laser track cross-section for both LNS34 and LNS13B21 glass sample, for two pulse energies (0.75 and 1.25 μJ/pulse) and with laser polarization either parallel or perpendicular to the scanning direction [6]..... 109

Figure 65: Size distribution of single texture regions for LS34 and LNS13B21 for Yy configuration and two different pulse energies (0.75 and 1.25 μJ/pulse). Irradiations conditions: λ= 1030 nm, NA = 0.6, f = 200 kHz, focus depth = 240 μm in air, writing speed = 1 μm/s [6]. 110

Figure 66: Scanning electron microscope (SEM) micrographs and electron backscatter diffraction (EBSD) maps on the laser track cross-sections induced by fs-laser on LNS13B21 for different scanning speed. Fixed parameters are: pulse energy = 0.5 μJ; configuration = Y_y (laser polarization parallel to the scanning direction); λ = 1330 nm; f = 200 kHz; NA = 0.6; pulse duration = 250 fs; focal depth = 240 μm (in air) [18]. 111

Figure 67: a) number of single texture regions and their averaged diameter, assuming a spherical shape, as a function of scanning speeds; b) pole figures of the $LiNbO_3$ c axis (labeled 0001); extracted from data of laser cross sections at Y_y polarization reported in EBDS maps of Figure 4.20 [18]. The writing direction is in the center of pole figures; the laser propagation is at the top and the bottom of each pole figure. 111

Figure 68: LNS pulse energy-repetition rate landscape [12]. 119

Figure 69: Pulse energy - polarization direction landscape for LNS glasses closed to $30Li_2O – 30Nb_2O_5 – 40SiO_2$, highlighting the presence of three regimes. k is the laser propagation direction, e stands for the writing laser polarization direction, and S is the scanning direction. Other parameters: 1030 nm, 300 fs, NA = 0.6, 300 kHz, 5 μm/s, and focus depth 350 μm [3]. 119

Figure 70: High repetition rate fs laser-induced regimes in LNS glass according to pulse energy indicated in white in each SEM micrograph. For regime 2 and 3, the left image is a SEM micrograph, and the right one is the corresponding inverse pole figure (IPF) of the cross section of the irradiated line. The scanning direction is perpendicular to the paper plane. The color of IPF is obtained from on $LiNbO_3$ space group R3c, coding along scanning direction. These are configurations in which laser polarization is (a – d) parallel or (e) perpendicular to scanning direction. Laser polarization direction is marked by green e, while scanning direction id displayed by red S. k represents the laser come from the top. Other parameters for $33Li_2O – 33Nb_2O_5 – 34\ SiO_2$ are 1030 nm, 300 fs, 300 kHz, 5 μm/s, and focus depth 350 μm [3]. 120

Figure 71: Pulse energy-scanning speed landscape that shows domains of fs laser-induced crystallization in LNS glasses close to $30Li_2O – 30Nb_2O_5 – 40SiO_2$. Other

parameters are λ = 1030 nm, NA = 0.6, repetition rate = 200-300 kHz, parallel configuration [3]. 122

Figure 72: Pulse energy – repetition rate landscape in which domains of fs laser-induced crystallization in LNS glasses at varying scanning speed and focus depth indicating collecting results of Poumellec et al. [6] and the from Veenhuizen et al. [13]. Other parameters are λ = 1030 nm, NA = 0.6, pulse duration = 300 fs, parallel configuration. In this case, green marks indicate regime 2 of LSN glasses, and the red marks show regime 3 n LNS glasses [3]. 122

Figure 73: Pulse energy effect shown through three different values in curves trend of normalized second harmonic generation intensity of irradiated lines as function of probing laser polarization in the XY plane. Other parameters: writing speed 5 μm/s, writing direction is along 45° direction, laser polarization is parallel to Y [7]. 123

Figure 74: Writing speed effect shown through normalized second harmonic generation intensity of irradiated lines as function of probing laser polarization angle, varying pulse energy at a) 0.8 μJ and b) 1.4 μJ. Other parameters: writing direction is along 45°direction, laser polarization is parallel to Y [7]..... 124

Figure 75: Writing orientation effect through normalized second harmonic generation intensity of irradiated lines as function of probing laser polarization angle, at two different writing speed a) 1μm/s and b) 25 μm/s. Other parameters: pulse energy 1.4 μJ, laser polarization is parallel to Y [7]. 124

Figure 76: Variation of anisotropy magnitude-pulse energy trend as function of scanning speed. Other parameters: writing direction is along 45° direction, laser polarization is parallel to Y [7]. 125

Figure 77: EBSD characterization of $33Li_2O – 33Nb_2O_5 – 34SiO_2$: a) EBSD scan images of lines cross-sections irradiated at 2.0 – 0.6 μJ with polarization parallel to the laser beam direction that is coding the crystal orientation along x; b) EBSD images of lines cross-sections irradiated at 2.0 μJ with polarization perpendicular to laser beam direction coding crystal orientation along x; EBSD scan image coding the crystal orientation along the x-axis and along the y-axis at c) 1.0 μJ and d) 0.6 μJ, respectively. The polarization for writing is parallel to the laser motion direction. Other laser parameters: repetition rate = 300 kHz, scanning speed = 5 μm/s, pulse duration = 300 fs, wavelength = 1030 nm, and NA = 0.6 [15]..... 126

Figure 78: Normalized SHG intensity for four glass composition as a function of probing polarization angle in the XY plane for a) Y_x, b) Y_{45} and c) Y_y at the two

lowest pulse energies, 0.5 and 0.75 μJ/pulse. Femtosecond laser conditions used: λ = 1030 nm, NA = 0.6, RR = 200 kHz, focus depth = 240 μm in air, scanning speed = 1 μm/s [1]. 130

Figure 79: Comparison between four pulse energy values a) 0.5, b)1.5, c) 1.75 and d) 2 μJ at laser polarization configuration Y_x. Femtosecond laser conditions used: λ = 1030 nm, NA = 0.6, RR = 200 kHz, focus depth = 240 μm in air, scanning speed = 1 μm/s. 131

Figure 80: Comparison between four pulse energy values a) 0.5, b)1.5, c) 1.75 and d) 2 μJ at laser polarization configuration Y_{45}. Femtosecond laser conditions used: λ = 1030 nm, NA = 0.6, RR = 200 kHz, focus depth = 240 μm in air, scanning speed = 1 μm/s. 132

Figure 81: Comparison between four pulse energy values a) 0.5, b)1.5, c) 1.75 and d) 2 μJ at laser polarization configuration Y_y. Femtosecond laser conditions used: λ = 1030 nm, NA = 0.6, RR = 200 kHz, focus depth = 240 μm in air, scanning speed = 1 μm/s. 132

Figure 82: Normalized SHG intensity for all glass compositions according to a) Y_x at 1.25 μJ; b) Y_y at 1.25 μJ; c) Y_x at 2 μJ and d) Y_y at 2 μJ..... 133

Figure 83: Polar representations for LNS34 and LNS13S21 glasses at 1.25 and 2 μJ/pulse with three laser polarization configurations indicated by double headed arrows in coordinates of the reference system: //, 45°, and ⊥..... 134

Figure 84: Inverse Pole Figure (IPF) obtained through electron backscatter diffraction (EBSD): the color in the black background represents the crystalline part for LNS34 and LNS13B21 according Y_x and Y_y at 1.25 μJ/pulse. Other laser parameters are λ = 1030 nm; f = 200 kHz; NA = 0.6; pulse duration = 250fs; focal depth = 240 μm (in air); scanning speed = 1 μm/s..... 135

Figure 85: Inverse Pole Figure (obtained from EBDS analysis) for LNS34 at a) Y_y, and b) Y_x and for LNS13B21 sample at c) Y_y and d) Y_x, coding the crystal orientation according to the scheme reported in the figure through Axis 1 (A1 on the left), Axis 2 (A2 in the middle), and (A3 on the right) corresponding to beam direction, laser polarization, writing direction respectively, at 1.25 μJ and configurations parallel (three maps on the left) and perpendicular (three maps on the right) to laser polarization. Other laser parameters are λ = 1030 nm; f = 200 kHz; NA = 0.6; pulse duration = 250fs; focal depth = 240 μm (in air); scanning speed = 1 μm/s..... 137

Figure 86: Polar figures referred to LNS34 at 1.25 μJ for a) Y_y, b) Y_x and LNS13B21 at 1.25 μJ for c) Y_y, d) Y_x. where A1 is the beam direction (z axis), A3 is the writing direction (y axis for Y_x and Y_y configurations), polarization is along A2 (x axis) for Y_x and along A3 for Y_y configurations..... 138

Figure 87: Inverse Pole Figure (obtained from EBDS analysis) for a) LNS34, and b) LNS13B21 sample, coding the crystal orientation according to the scheme reported in the figure through Axis 1 (A1 on the left), Axis 2 (A2 in the middle), and (A3 on the right) corresponding approximately to beam direction, laser polarization, writing direction respectively, at 2 μJ and configurations parallel (three maps on the left) and perpendicular (three maps on the right) to laser polarization. Other laser parameters are λ = 1030 nm; f = 200 kHz; NA = 0.6; pulse duration = 250fs; focal depth = 240 μm (in air); scanning speed = 1 μm/s. 139

Figure 88: Polar figures referred to LNS34 at 2 μJ for a) Y_y, b) Y_x and LNS13B21 at 2 μJ for c) Y_y, d) Y_x. where A1 is the beam direction, A2 is the laser polarization, A3 is the writing direction..... 140

Figure 89: pulse energy-repetition rate landscape highlighting the three regimes of laser induced modifications for a) $32.5Li_2O$-$27.5Nb_2O_5$-$40SiO_2$ (mol%) [2], [3]; b) for $33Li_2O$-$33Nb_2O_5$-$34SiO_2$ (LNS34) (mol%). In addition, the trend of dots written in our experiment in static mode revealed the energy thresholds for LNS34 [2]. 142

Figure 90: Scanning electron micrographs of the laser track cross sections induced by fs-laser on LNS13B21 glass sample for different scanning speed. Lamella-like nano-gratings are observed and, for comparison at different scanning speed, the upper and lower zone limits are bounded by two orange lines [2]..... 143

Figure 91: Morphology of the fs laser track with laser polarization, along Y direction, is perpendicular to X direction of scanning: a) SEM micrograph on left side and the corresponding IPF coding along laser polarization direction on the right side for 1 μJ/pulse; b) this is a magnification of Figure 5.22a enclosed in the red rectangle; c) scheme of laser-induces structures, with forces and main parameters indicated: d_E is the nanostructures thickness, Λ_E is the distance between the dashes, Λ_Z is the distance between the nanostructure lines; scanning direction is along Z, also writing direction is indicated; morphology of the laser track varying the pulse energy: d) 0.8 and e) 1.4 μJ/pulse. Other fundamental parameters are: $32.5Li_2O$ – $27.5Nb_2O_5$ – $40SiO_2$ (mol%), 1030 nm, 500 kHz, 300 fs, 5 μm/s, NA = 0.6, focal depth 300 μm in air [4]..... 143

Figure 92: TEM micrographs (bright field mode of self-assembled nanostructure in LNS glass at various pulse energies (a – b) 0.7, (c – d) 1.3, and (e) 1.8 μJ/pulse. The laser propagation direction is perpendicular to the paper plane for (a – d); nanostructure along the laser propagation direction is illustrated in (e). K is the laser propagation direction. Writing laser polarization direction is indicated by the green double arrows. The micrographs are referred to $33Li_2O$ – $33Nb_2O_5$ – 34 SiO_2 (mol%), at 1030 nm, 300 fs, 300 kHz, 5 μm/s, and focus depth 350 μm [3]. 144

Figure 93: Field-Emission Gun Scanning Electron Microscope (FEG-SEM) secondary electron images of femtosecond laser track cross-section for the writing laser polarization (a, b) perpendicular to the scanning direction and (c, d) parallel to the scanning direction. Other laser parameters are: pulse energy = 0.5 μm/pulse; wavelength = 1030 nm; pulse duration = 300 fs; repetition rate = 500 kHz; NA = 0.6 [25]..... 145

Figure 94: Plasma density (2D FDTD (Finite-difference time-domain) around a single void at the coordinate origin for different stages of structure growth. a) Plasma growth in polarization direction; b) Saturation of growth and generation of a second structure; c) Periodic plasma structure formed by subsequent growth, considering that illumination is a continuous wavelength plane wave [46]..... 150

Figure 95: Carrier density generated by a plane wave normally incident on a half-space ($z > 0$) with many inhomogeneities. The growth structures direction is backwards against the propagation one: from the inhomogeneous/homogeneous border at $z = 0$ and the grating has a period of $\sim \lambda/2n = 275$ nm. In a) there is a panel with polarization and laser propagation indicated, while a cut through the grating planes at $z = -300$ nm is reported in panel b) [46]..... 150

Figure 96: Scheme of the laser beam geometry incoming on rough surface indicated as "selvedge": κ_i is the wave-vector component parallel to the surface; θ_{inc} is the angle of incidence **Z** indicates the positive direction; $l \ll \lambda$ is the selvedge thickness compared to laser wavelength [53]..... 152

Figure 97: TTT and CCT diagrams [57]..... 154

Figure 98: a) Scheme of spatial temperature distribution achieved by static laser as a function of distance from the laser focus beam. In the left side there is a representation of temperature variation at the focus center; the right side shows a position a bit away according to repetition rate. The area in blue shaded represents the approximated beam width. Yellowish and brownish ones correspond to the amplitude of the temperature variation at the steady state; b) Time evolution of the temperature relative to a fixed point according to the distance from the focus center

in scanning mode. The scanning beam, arbitrary limited, is enclosed in the red zone [3]. 155

Figure 99: Scheme of the nucleation and growth rates; b) TTT curve derived by time integration of the rates [3]..... 156

Figure 100: a) only the TTT and CCT curves; these curves with laser thermal treatment curve b) for places experiencing maximum average T larger than T_m and c) for places at maximum temperature smaller than T_m [3]..... 160

Figure 101: Time evolution of the temperature relative to a fixed point according to the distance from the focus center in scanning mode and SEM micrograph and EBSD map of the cross section of the laser track obtained at intermediate pulse energy in regime 2 for LNS glass [3] 160

Figure 102: Time evolution of the temperature for a fixed point according to the distance from the focus center in scanning mode, and SEM micrograph and EBSD map of the cross section of the laser track obtained at high pulse energy in regime 3 for LNS glass. The green dashed line in the SEM micrograph is the beam boundary, otherwise the red dashed one highlights the crystallized volume boundary [3]. 161

Figure 103: Interpretation of the morphology acquired by high pulse energy (regime 3 for LNS glass) in the plane perpendicular to laser propagation direction (XY plane). The blue circle reported inside the bouquet-like laser track cross-section shows the beam size inside which the temperature is almost homogeneous. The green curves represents the bouquet morphology illustrated in the map above [3]. 162

Figure 104: Time evolution of the temperature for a fixed point according to the distance from the focus center in scanning mode at very high pulse energy of 4 μJ and formed single texture interpretation [3]..... 163

Figure 105: Interpretation of the presence of non-crystallized area in the section of laser traces [3]..... 164

Figure 106: Morphology of laser tracks at pulse energy equal to 0.5 μJ according to polarization configuration Y_y: electron backscatter diffraction (EBSD) maps and scanning electron microscope (SEM) micrographs on the laser track cross-sections induced by fa-laser on LNS13B21 glass sample and for different scanning speeds. Other fixed parameters are: pulse energy = 0.5 μJ; configuration Y_y (laser polarization // to the scanning direction; $\lambda = 1030$ nm; f = 200 kHz; NA = 0.6; pulse duration = 250 fs; focal depth = 240 μm (in air). 165

Figure 107: Representation of crystallization domain for: a) LNS, b) LNSB glasses in TTT (time – temperature – transformation) diagram; T_m: melting temperature of $LiNbO_3$, T_p: crystallization peak temperature, T_g: glass transition temperature [2] 166

Figure 108: Scheme of the effect of the scanning speed on the crystallization for the two glasses a) LNS and b) LNSB [2] 167

Figure 109: Scheme explaining the effect of scanning speed on the heat-affected volume (HAV) width [2] 168

Figure 110: Scheme of the treatment curves crossing the nose of the crystallization domain: at increasing the scanning speed (v), also the energy power (E_p) must be increased to preserve the nanocrystal microstructure [2] 169

Figure 111: a) Ideal $LiNbO_3$ crystal structure with stoichiometric composition without point defects (Li_{Li}); b) nonideal $LiNbO_3$ crystal structure with Nb antisites (Nb_{Li}) [61] 170

Figure 112: Scheme of sol-gel steps highlighting the variability of different final products that can be achieved (adapted from [1]) 181

Figure 113: Comparison scheme between melt-quenching and sol-gel process for glass synthesis [16] 182

Figure 114: Sol-gel steps and respective scientific discipline involved [18] 183

Figure 115: Scheme of different steps highlighted by hydrolysis and condensation reactions [19] 184

Figure 116: The main reactions in the sol-gel process of an alkoxide $M(OR)_4$, (1) hydrolysis of an alkoxy group, (2) condensation of two-OH species, and (3) mixed condensation of a-OH group and an alkoxy group species [19] 185

Figure 117: A typical classification of gel typologies. The attention is focused on metal- and polymer complex [29] 186

Figure 118: Representation of a gel generated by acid (a) and basic catalysis (b) [30] 187

Figure 119: Overview of various products obtained by sol-gel synthesis in Polytechnic of Turin: a) pure silica nanoparticles (basic synthesis at room temperature inspired by Stöber method with tetramethyl orthosilicate (TEOS), H_2O, C_2H_5OH and NH_4OH); b) small nanoparticles and aggregates found after pure silica bulk glass synthesis based on TEOS and use of CH_3COOH as solvent and catalyst; c) final transparent silica bulk glass obtained by same synthesis process of b) after

thermal treatment at 600°C for 2h at 1°/min; d) fiber-shape silica glass doped with neodymium ($Nd(NO_3)_3 \cdot 6H_2O$, 0.5% mol) (molar ratio 1 : 4 : 4 = TEOS : CH_3COOH : H_2O) after calcination at 600°C for 2h; e) FESEM image of sample d) at 100X; e) fiber-shape silica glass doped with neodymium ($Nd(NO_3)_3 \cdot 6H_2O$, 1.5% mol) (molar ratio 1 : 4 : 4 = TEOS : CH_3COOH : H_2O) after calcination at 600°C for 2h; g) allumino-silicate bulk glasses at 90% SiO_2 – 10% Al_2O_3 and 50% SiO_2 – 50% Al_2O_3 respectively; h) neodymium doped silica bulk glass after aging at T_{room} for 24 days realized only with TEOS, CH_3COOH and $Nd(NO_3)_3 \cdot 6H_2O$ (2,3% wt)..... 190

Figure 120: Mechanism promoting the coexistence of magnetic and electric long-range order: the case of lone - pair in $BiFeO_3$. The two Bi^{3+} electrons shift away from the Bi^{3+} ion generating the ferroelectricity and towards FeO_6 octahedra, giving rise to a spontaneous polarization P along the [111+ direction. Lone - pair is represented by the red isosurface of electron localization function of $BiFeO_3$ [45] 191

Figure 121: Clear terminology and schemes referred to multiferroics [45]..... 192

Figure 122: Pechini-type in-situ polymerizable complex (IPC) method: illustration of the chemical reaction between a polybasic carboxylic acid chelate and ethylene glycol during the formation of a complex perovskite oxide [29]..... 196

Figure 123: Synthesis methods scheme analyzed in the review highlighting the Modified Pechini as the one chosen in this work [67]..... 197

Figure 124: Flowsheet showing the Modified Pechini method steps [68]..... 198

Figure 125: Glass-forming region for Bi_2O_3 - B_2O_3 - Fe_2O_3 system enclosed in yellow [81]: the final and successful composition is reported in light blue point 201

Figure 126: Solution of first attempt with a probe to maintain a constant temperature of 75°C during the process 202

Figure 127: Sample in a falcon vial a) before the addition of Fe and B component; b) after the introduction of all the precursors; c) in the beginning of its heating at 75°C; d) solution after a few hours of heating; e), f) suspension after heating not finished yet, some white precipitates are visible in the bottom of the vial; g) suspension at the end of the process is dark yellow not red; h) thin-film deposed on glass slide after synthesis to check its consistency..... 204

Figure 128: a) yellow and transparent solution after citric acid addition; b) solution at 70°C with starting change of color to red; c) solution at 75°C; d) last 10 ml of

solution at 80°C; e), f) red resin at the final stage; g) glass slide with solution after spin coating at 2000 rpm 204

Figure 129: Few red aggregates on the glass that probably indicate a surface crystallization 205

Figure 130: TG-DTA analyses of red polymeric resin..... 205

Figure 131: yellow and transparent solution after citric acid addition; b) solution at 38°C; c) solution at 66°C; d) solution at 70°C; e), f) solution at 76°C; g) solution at 78°C; h) red resin in the end of synthesis 206

Figure 132: a) mold; b) transfer of solution in the mold by Pasteur pipette; c) full molds; d) full dry mold; e) consistency of resin in the mold; part of resin was spread on two glass slides after spin coating at 2000 rpm, and this is the resin aspect f) before and g) after thermal treatment at 100°C for 7 hours..... 206

Figure 133: Modified Pechini method steps carried out, highlighted in red rectangle [68] 207

Figure A134: a) The free energy change associated with homogeneous nucleation of a sphere of radius r in which the $T < T_m$; b) variation of r^* critical with the under-cooling of the melt [2]..... 223

Figure A135: a) Scheme of free energy according to configurational parameter; b) a superimposition of the nucleation and growth [2] 225

Figure A136: a) material medium without electric field; b) material medium with electric field that induces an electrical dipole moment; c) electromagnetic wave representation [6]..... 226

Figure A137: Scheme of dielectric materials as bound oscillators [6]..... 226

Figure A138: Diagram of real and imaginary part of susceptibility [6] 228

Figure A139: Schematic representations of polarization and electric field in function of time at a) input frequency ω and b) at frequency 2ω, 3ω,….[6]..... 231

Figure A140: how potential curve (U) changes in non-centrosymmetric and centrosymmetric medium, the signal of the electric field and the curves of the respective polarization signals (Lorentz atomic model) [7] 232

Figure A141: Scheme of SHG phenomenon from two different points of view: a) non-linear optical medium diagram and b) virtual energy diagram..... 233

Figure A142: SHG scheme..... 233

Figure A143: Quantitative phase measurement of the written lines with a line spacing of 50 μm in pure silica: a) phase image and b) profile (line's cross section) 245

Figure A144: Schematic of quantitative phase microscopy setup..... 246

Figure A145: QPM measurement provides different information: a) three bright field images: one in-focus (I_0) and the other two very slightly positively/negatively (I_+/I.) defocused images were captured to calculate the quantitative phase image φ; b) Quantitative phase change information of the arrow in cross the waveguide structure; c) DIC image of the waveguide structure using the calculated phase information from a) [9]..... 247

List of Tables

Table 1: Properties of different states (a = crystal or grain diameter; d = hard sphere atomic diameter) [4]..... 12

Table 2: Glass labels and batch compositions..... 19

Table 3: Batch calculation for LSN precursors powder to obtain glass by melt quenching..... 21

Table 4: Batch calculation for LNS13B21 precursors powder to obtain glass 21

Table 5: Polishing steps list of glasses..... 23

Table 6: Crystallographic parameters of $LiNbO_3$..... 30

Table 7: Point group properties [83]..... 68

Table 8: Laser parameters used in all the experiments 85

Table 9: Laser parameters variable in different experiments..... 86

Nomenclature

LED: light-emitting diode

UV: ultraviolet-visible

FLDW: Femtosecond Laser Direct Writing

fs: femtosecond

3D: three dimensions

LNS: $Li_2O – Nb_2O_5 – SiO_2$

SHG: second harmonic generation

LNSB: $Li_2O – Nb_2O_5 – SiO_2 – Bi_2O_3$

QPM: quantitative phase microscopy

SEM: scanning electron microscopy

EBSD: electron backscatter diffraction

EDS: energy dispersive X-ray spectroscopy

CCT : continuous cooling trasnformation

TTT: time-temperature transformation

DSC: differential scanning calorimetry

NCS: non-crystalline solid

SRO: short-range order

SCL: supercooled liquid

T_g: glass transition temperature

T_f: fictive temperature

T_m: melting temperature

t_{OBS}: observation time

CNT: classical nucleation theory

LNS34: 33% LiO_2 – 33% Nb_2O_5 – 27% SiO_2 – 0% B_2O_3

LNS27B7: 33% LiO_2 – 33% Nb_2O_5 – 27% SiO_2 – 7% B_2O_3

LNS20B14: 33% LiO_2 – 33% Nb_2O_5 – 20% SiO_2 – 14% B_2O_3

LNS13B21: 33% LiO_2 – 33% Nb_2O_5 – 13% SiO_2 – 21% B_2O_3

RT: room temperature

LASER: light amplification by stimulation of radiation

FWHM: Full Width Half Maximum

CPA: chirped pulse amplification

CW: continuous wave

NA: numerical aperture

MPI: multiphoton ionization

VB: valence bond

CB: conduction bond

ps: picosecond

STE: self-trapped excitons

NBOHC: nonbridging oxygen hole center

POR: peroxy radical

STH: self-trapped holes

PL: photoluminescence

SiODC: silicon oxygen- deficient center

IR: infrared

T1: first threshold

T2: second threshold

T3: third threshold

KDP: Potassium Dihydrogen Phosphate crystal

BBO: barium borate

NLO: non-linear optical

EO: Electro-Optic effect

UST: ultrasonic surface treatment

RR: repetition rate

Ep: energy pulse

PFT: pulse front tilt

P: polarizer

A: analyzer

R: retardance

CCD: charge-coupled device

IPF: inverse pole figure

AOW: asymmetric orientational writing

DC: direct current

RGB: red-green-blue

HAV: heat-affected volume

FEG-SEM: Field-Emission Gun Scanning Electron Microscope

VNG: volume nanogratings

2D: two dimensions

FDTD: Finite-difference time-domain

T_p: peak crystallization temperature

T_x: crystallization onset temperature

BBF: $Bi_2O_3 – B_2O_3 – Fe_2O_3$

CVD: chemical vapor deposition

PVD: physical vapor deposition

IPC: in-situ polymerizable complex

PCS: polymer-complex solution

SCD: supercritical drying

DLS: dynamic light scattering

FESEM: Field emission scanning electron microscopy

XRD: X-ray Powder Diffraction

TEOS: tetramethyl orthosilicate

TG-DTA: Thermogravimetry-Differential Thermal Analysis

TEM: transmission electron microscopy

XPS: X-ray photoelectron spectroscopy

Chapter 1

Introduction

1.1 Motivation of the work

Optics and photonics are key enabling technologies for modern society, and our world leverages the latest advancements in these fields (e.g., LED lighting, optical telecommunications). Those two research fields are vibrant and closely connected by the ever-present challenge of selecting or formulating the optimal material for a target application. Light interaction with materials can be a key element to cope with this challenge. Indeed, when we expose a functional material, like glass, to continuous wave or nanosecond pulsed lasers, the irradiation induces substantial structural modifications by linear (one-photon) or at most weakly non-linear (two-photon) absorption. The irradiating energy activates point defects in the glass network, resulting in absorption in the material optical bandgap range. This corresponds to a relevant change of the absorption spectrum producing growth of some absorption bands and bleaching of others. Light is also responsible for other structural permanent volume variations through the transport of atoms or ions. This migration of electrons extracted from ionized atoms or/and ions is representative of the fundamental contribution of chemistry in the study of laser-matter interaction. The consequent glass chemical composition variation determines a change in photosensitivity to ultraviolet (UV) laser irradiation, and it depends also on material thermal history and on environmental conditions. Indeed, the photochemistry processes generate the physical properties in the material after laser irradiation.

Consequently, the production of new active optical and interesting photonic devices by multi-photon absorption for a variation of non-linear optical properties during the glass-ceramic transformation is achievable through the versatile Femtosecond (fs, 1 fs = 10^{-15} s) Laser Direct Writing (FLDW) [1]. The devices obtainable by FLDW are many: frequency converters, Bragg gratings, low-loss optical waveguides, computer memory, graded index lenses, birefringent optics, data storage, microfluidic system, and non-linear optics [2]–[7].

One of the key elements of FLDW that grant flexibility and broad applicability is that the lasers used for FLDW (typ. 200 fs) allow reaching a high peak power intensity (typ. TW/cm^2 scale) in a short time scale leading to an efficient non-linear multi-photon absorption [8], e.g., six photons at 800 nm or even eight photons at 1030 nm in SiO_2. This result is indeed an exciting and effective method to induce permanent modifications in three dimensions (3D) [9] with nano-scale spatial resolution in single-step processing [10], [11], including space charge migration [12], stress fields [13], and crystalline phase transformations [14]. In addition, it is possible to obtain the nano-structuring of material. Moreover, the improvement of properties, the increasing of performance and the opportunity of new physics could be promising elements towards a real glass multi-functionalization [15] by femtosecond laser irradiation.

Basically, by focusing a fs pulse inside a dielectric transparent material like glass mounted on a computer-controlled 3D motion stage, by controlling the fs-laser parameters [16] (specifically, in this Ph.D. work, pulse energy, repetition rate, polarization, scanning speed, etc. [17], [18]), various modifications can be achieved. By controlling those process parameters, it is possible to study the ultra-fast laser-matter interaction and its effect on material properties [18], deriving from non-linear photons absorption phenomena [19]. The control of the light action in a focal volume of glass allows to master crystallization and associated texturing/structuring, leading to optical functionalization at the micro-scale with a large degree of flexibility. This opens the door to a new discipline of laser materials science: the laser-oriented crystallization of glass materials.

The present work focuses on borate glasses fabricated by sol-gel technique and silicate and borosilicate ones realized by the melt quenching process. The silicate and borosilicate samples are then irradiated with femtosecond lasers to trigger and control localized and oriented crystallization of $LiNbO_3$ [7], [20]. Below are listed the key motivations of this thesis:

1) Fs-laser induced nanostructure in glass represents a significant route to design and fabricate architectures in optics [3]. In this research, starting

from silica-based glasses, the material systems have been extended to multicomponent glasses, including borosilicate glasses [17], [21].

2) Among the various fs-laser modifications, glass crystallization to produce $LiNbO_3$ will be examined. This crystal is a material that can be photo-precipitated in a wide range of glass compositions. Thus, it is suitable for many applications in many different fields because of its optical transparency [22], a wide range of chemical compositions, and favorable laser-induced crystallization [23], high Curie temperature [24], ferroelectricity, pyroelectricity, piezoelectricity, and large non-linear coefficients [25].
In $Li_2O – Nb_2O_5 – SiO_2$ (LNS) glass, used as reference material, fs-laser irradiation induced the migration of glass constituted cations, locally modified chemical composition, and allowed crystalline phase precipitation at the micrometer scale. A $LiNbO_3$ phase was acquired when crystallization occurred on sub-micron or nanometer scales, but not the silica-rich counterpart. Therefore, we wondered whether a phase separation actually occurs and if silica could be included in the $LiNbO_3$ structure, as $LiNbO_3$ exhibits a significant departure from stoichiometry when doped with transition metal elements. In addition, the modifications (e.g., whether there is an fs laser-induced nanostructure) in this glass system are fascinating to explore and explain. So far, there is a systematic report about mastering the second harmonic generation (SHG) in the LNS glass system, but we intend to introduce a new discussion about borosilicate glass matrices, the so-called LNSB ($Li_2O – Nb_2O_5 – SiO_2 – Bi_2O_3$). There is a problem due to off-stoichiometric composition, i.e., whenever lithium niobate is synthesized not from Li_2O and Nb_2O_5, but other oxides such as SiO_2 and B_2O_3 are also used. In [26], Komatsu proposes an interesting interpretation employed to discuss the origin of crystallization mechanisms in glasses. In particular, it is necessary to analyze the presence of two different types of nanodomains in glass (the weak and the strong ones), the stability and strength of chemical bonds, between former and former, former and modifier, modifier and modifier and bonds with intermediate oxides [26].

3) The crystal size has to be smaller than the wavelength to prevent excessive losses in transparent devices, considering the large refractive

index difference between polycrystalline (e.g., $LiNbO_3$ ~2.3) and glass matrix (e.g., SiO_2 ~1.45) [27]. Generally, the crystalline size should stay below $\lambda/10$ to maintain the transparency of composite materials. Yet, to maintain a non-linear optical crystal phase with high SHG property, the crystal size must be larger than ~100 nm [28].

4) The control of crystal orientation is necessary to obtain a coherent non-linear optical response [29]. For $LiNbO_3$, the SHG maximum value is reached when probing laser polarization is parallel to the polar axis [14]. This is valid for $LiNbO_3$ made by the LNS glass matrix. In this research, the exploration starts from LNS glass and moves to $LiO_2 – Nb_2O_5$ - $SiO_2 – B_2O_3$ (LNSB) glass matrix, studying the role of B_2O_3 addition, primarily focusing on scanning speed role [18].

This thesis work is part of the NANOMAX (advanced nanostructured materials and nano-crystals for photonic applications) project, based on collaboration between two academic institutions: Polytechnic of Turin (POLITO) in Italy and Université Paris-Saclay (UPSaclay) in Orsay, France, and funded by JOINT Projects of Compagnia di San Paolo. Figure 1 shows the objectives and specific issues of the Ph.D. work in the Nanomax project framework. In the following sections, an initial definition of the main research objectives will follow, and finally, the chapters' layout will be detailed.

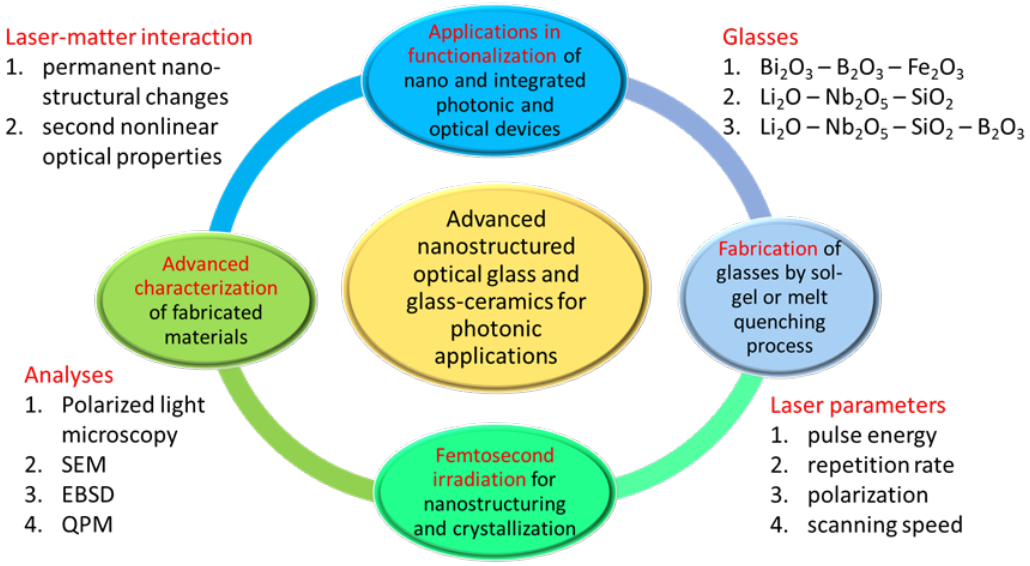

Figure 1: Ph.D. work objectives and specific issues according to NANOMAX project

1.2 Objectives

This research aims to contribute to the elaboration of non-linear optics in glass by fs-laser direct writing. We investigated the crystallization inside LNSB glasses induced by fs-laser irradiation, employing the results that emerged from [30] for LNS glasses, mastering the fs-laser modifications on material, such as crystallization, nanostructure, and the corresponding optical properties. In detail, the main objectives are:

1) From the LSN glass results, clarify how the regimes of fs-laser modifications vary with pulse energy and writing configurations (laser polarization orientation versus scanning direction) to give a clear picture of fs laser-LNSB glass interaction regimes.
2) Determine the chemical redistribution and the evolution of the glass microstructure according to the laser parameters and the increasing of B_2O_3-amount in the glass composition.
3) Control the size and orientation of fs laser-induced non-linear optical $LiNbO_3$ crystal [17].
4) Explore the optical properties as SHG and form birefringence due to the above architecture and find the relationship between fs laser-induced modifications and optical properties [17].
5) Investigate the mechanisms behind the fs laser-induced properties in LNSB glasses, proposing an interpretation of how nucleation and growth of crystals happen in LNSB glasses in comparison with LNS ones [18].

1.3 Structure of the chapters

The introductory chapter contains the motivation of the work, an exploration of the state of the art, and a short overview of all issues dealt with during this Ph.D. work.

Chapter 2 includes a general discussion on the glass to provide the reader an adequate background with respect to this thesis content, such as chemical properties, phase separation theory, before introducing the LNS and LNSB fabrication by melt-quenching technique. In conclusion, a brief overview of the properties of $LiNbO_3$ crystal is presented.

Chapter 3 is dedicated to background information on laser history and laser typologies, laser-matter interaction, with a specific section explaining the choice of

femtosecond laser. The end of this Chapter is dedicated to optical properties and non-linear effects.

Chapter 4 covers the experimental results obtained by Femtosecond Direct Laser Writing (FDLW) in glass in both static and dynamic modes. To study the crystallization mechanisms, a series of advanced characterizations are employed, including polarized light microscopy, second harmonic generation (SHG) measurements, quantitative phase microscopy (QPM), scanning electron microscopy (SEM), and electron backscatter diffraction (EBSD).

Chapter 5 is dedicated to the interpretation of Chapter 4 results. In particular, an investigation of crystallization kinetics and mechanisms through the effect of laser-material interaction on optical properties is described. The link between SHG detection and EBSD maps about LNSB, the nano-crystals orientation through SEM-EDS micrographs, and the nanograting formation as the origin of birefringence and refractive variation is employed to discuss what happens in LNS and LNSB through femtosecond laser irradiation. In addition, the last two sections will bring the discussion using continuous cooling transformation (CCT) and time-temperature transformation (TTT) diagrams, a valuable and straightforward method to explain and compare the domain of crystallization in the different glass compositions.

Chapter 6 is an overview of the sol-gel process, firstly describing the main characteristics and advantages of this "chemical" glass fabrication technique with respect to the solid-state melt-quenching one. A specific section is dedicated to the fabrication and characterization of $Bi_2O_3 – B_2O_3 – Fe_2O_3$ glasses.

Chapter 7 concludes this thesis work and highlights future perspectives in the extension of this work to other glass matrices. Finally, an Appendix is inserted to explain key theoretical concepts and advanced characterizations more extensively.

1.4 Bibliography

[1] R. Stoian *et al.*, "Investigation and control of ultrafast laser-induced isotropic and anisotropic nanoscale-modulated index patterns in bulk fused silica," *Opt. Mater. Express*, vol. 3, no. 10, p. 1755, Oct. 2013, doi: 10.1364/OME.3.001755.

[2] R. R. Gattass and E. Mazur, "Femtosecond laser micromachining in transparent materials," *Nature Photonics*, vol. 2, no. 4, Art. no. 4, Apr. 2008, doi: 10.1038/nphoton.2008.47.

[3] M. Beresna, M. Gecevičius, and P. G. Kazansky, "Ultrafast laser direct writing and nanostructuring in transparent materials," *Adv. Opt. Photon.*, vol. 6, no. 3, p. 293, Sep. 2014, doi: 10.1364/AOP.6.000293.

[4] D. Choudhury, J. R. Macdonald, and A. K. Kar, "Ultrafast laser inscription: perspectives on future integrated applications," *Laser & Photonics Reviews*, vol. 8, no. 6, pp. 827–846, Nov. 2014, doi: 10.1002/lpor.201300195.

[5] B. McMillen, B. Zhang, K. P. Chen, A. Benayas, and D. Jaque, "Ultrafast laser fabrication of low-loss waveguides in chalcogenide glass with 0.65 dB⁄cm loss," p. 3.

[6] Cartlidge Edwin, "A photonic upgrade for computer memory," *Optics and Photonics News*, pp. 24–31, Apr. 2016.

[7] C. Fan *et al.*, "Three-dimensional photoprecipitation of oriented LiNbO_3-like crystals in silica-based glass with femtosecond laser irradiation," *Opt. Lett.*, vol. 37, no. 14, p. 2955, Jul. 2012, doi: 10.1364/OL.37.002955.

[8] D. Tan, K. N. Sharafudeen, Y. Yue, and J. Qiu, "Femtosecond laser induced phenomena in transparent solid materials: Fundamentals and applications," *Progress in Materials Science*, vol. 76, pp. 154–228, Mar. 2016, doi: 10.1016/j.pmatsci.2015.09.002.

[9] R. Stoian, "Volume photoinscription of glasses: three-dimensional micro- and nanostructuring with ultrashort laser pulses," *Appl. Phys. A*, vol. 126, no. 6, p. 438, Jun. 2020, doi: 10.1007/s00339-020-03516-3.

[10] R. Taylor, C. Hnatovsky, and E. Simova, "Applications of femtosecond laser induced self-organized planar nanocracks inside fused silica glass," *Laser & Photon. Rev.*, vol. 2, no. 1–2, pp. 26–46, Apr. 2008, doi: 10.1002/lpor.200710031.

[11] M. Lancry, B. Poumellec, J. Canning, K. Cook, J.-C. Poulin, and F. Brisset, "Ultrafast nanoporous silica formation driven by femtosecond laser irradiation: In the heart of nanogratings," *Laser & Photonics Reviews*, vol. 7, no. 6, pp. 953–962, Nov. 2013, doi: 10.1002/lpor.201300043.

[12] T. T. Fernandez, J. Siegel, J. Hoyo, B. Sotillo, P. Fernandez, and J. Solis, "Controlling plasma distributions as driving forces for ion migration during fs laser writing," *J. Phys. D: Appl. Phys.*, vol. 48, no. 15, p. 155101, Apr. 2015, doi: 10.1088/0022-3727/48/15/155101.

[13] B. Poumellec, L. Sudrie, M. Franco, B. Prade, and A. Mysyrowicz, "Femtosecond laser irradiation stress induced in pure silica," *Opt. Express*, vol. 11, no. 9, p. 1070, May 2003, doi: 10.1364/OE.11.001070.

[14] A. Stone *et al.*, "Direct laser-writing of ferroelectric single-crystal waveguide architectures in glass for 3D integrated optics," *Sci Rep*, vol. 5, no. 1, p. 10391, Sep. 2015, doi: 10.1038/srep10391.

[15] J.-H. Song, S.-H. Min, S.-G. Kim, Y. Cho, and S.-H. Ahn, "Multi-functionalization Strategies Using Nanomaterials: A Review and Case Study in Sensing Applications," *Int. J. of Precis. Eng. and Manuf.-Green Tech.*, vol. 9, no. 1, pp. 323–347, Jan. 2022, doi: 10.1007/s40684-021-00356-1.

[16] F. Chen and J. R. V. de Aldana, "Optical waveguides in crystalline dielectric materials produced by femtosecond-laser micromachining: Optical waveguides in crystalline dielectric materials," *Laser & Photonics Reviews*, vol. 8, no. 2, pp. 251–275, Mar. 2014, doi: 10.1002/lpor.201300025.

[17] E. Muzi *et al.*, "Polarization-oriented $LiNbO_3$ nanocrystals by femtosecond laser irradiation in LiO_2 –Nb_2O_5 –SiO_2 –B_2O_3 glasses," *Opt. Mater. Express*, vol. 11, no. 4, p. 1313, Apr. 2021, doi: 10.1364/OME.417461.

[18] E. Muzi *et al.*, "Towards a Rationalization of Ultrafast Laser-Induced Crystallization in Lithium Niobium Borosilicate Glasses: The Key Role of the Scanning Speed," *Crystals*, vol. 11, no. 3, p. 290, Mar. 2021, doi: 10.3390/cryst11030290.

[19] J. Cao, M. Lancry, F. Brisset, L. Mazerolles, R. Saint-Martin, and B. Poumellec, "Femtosecond Laser-Induced Crystallization in Glasses: Growth Dynamics for Orientable Nanostructure and Nanocrystallization," *Crystal Growth & Design*, vol. 19, no. 4, pp. 2189–2205, Apr. 2019, doi: 10.1021/acs.cgd.8b01802.

[20] X. He *et al.*, "Size-controlled oriented crystallization in SiO_2-based glasses by femtosecond laser irradiation," *J. Opt. Soc. Am. B*, vol. 31, no. 2, p. 376, Feb. 2014, doi: 10.1364/JOSAB.31.000376.

[21] S. Richter *et al.*, "Laser induced nanogratings beyond fused silica - periodic nanostructures in borosilicate glasses and ULE™," *Opt. Mater. Express*, vol. 3, no. 8, p. 1161, Aug. 2013, doi: 10.1364/OME.3.001161.

[22] H. Vigouroux *et al.*, "Crystallization and Second Harmonic Generation of Lithium Niobium Silicate Glass Ceramics," *Journal of the American Ceramic Society*, vol. 94, no. 7, pp. 2080–2086, 2011, doi: https://doi.org/10.1111/j.1551-2916.2011.04416.x.

[23] Y. Yonesaki, K. Miura, R. Araki, K. Fujita, and K. Hirao, “Space-selective precipitation of non-linear optical crystals inside silicate glasses using near-infrared femtosecond laser,” *Journal of Non-Crystalline Solids*, vol. 351, no. 10–11, pp. 885–892, Apr. 2005, doi: 10.1016/j.jnoncrysol.2005.01.076.

[24] R. S. Weis and T. K. Gaylord, “Lithium niobate: Summary of physical properties and crystal structure,” *Appl. Phys. A*, vol. 37, no. 4, pp. 191–203, Aug. 1985, doi: 10.1007/BF00614817.

[25] M. M. Choy and R. L. Byer, “Accurate second-order susceptibility measurements of visible and infrared nonlinear crystals,” *Phys. Rev. B*, vol. 14, no. 4, pp. 1693–1706, Aug. 1976, doi: 10.1103/PhysRevB.14.1693.

[26] T. Komatsu, “Design and control of crystallization in oxide glasses,” *Journal of Non-Crystalline Solids*, vol. 428, pp. 156–175, Nov. 2015, doi: 10.1016/j.jnoncrysol.2015.08.017.

[27] G. H. Beall and D. A. Duke, “Transparent glass-ceramics,” p. 13.

[28] H. Jain, “Transparent Ferroelectric Glass-Ceramics,” *Ferroelectrics*, vol. 306, no. 1, pp. 111–127, Jan. 2004, doi: 10.1080/00150190490458446.

[29] H. Vigouroux *et al.*, “Synthesis and Multiscale Evaluation of $LiNbO_3$ -Containing Silicate Glass-Ceramics with Efficient Isotropic SHG Response,” *Adv. Funct. Mater.*, vol. 22, no. 19, pp. 3985–3993, Oct. 2012, doi: 10.1002/adfm.201200651.

[30] J. Cao, L. Mazerolles, M. Lancry, and B. Poumellec, “Creation and orientation of nano-crystals by femtosecond laser light for controlling optical non-linear response in silica-based glasses,” Université Paris-Saclay, France, 2017. [Online]. Available: Jing Cao. Creation and orientation of nano-crystals by femtosecond laser light for controlling optical non-linear response in silica-based glasses. Material chemistry. Université Paris-Saclay, 2017. English. ⟨NNT : 2017SACLS055⟩. ⟨tel-01988887⟩

Chapter 2

Fabrication and characterization of lithium niobium silicate and borosilicate glasses

This chapter is about materials, the starting glasses that will be irradiated to transform them into crystals, precisely $LiNbO_3$. The first section describes what glass is, entering deeply in glass chemistry and phase separation. The second section shows the melt-quenching technique applied to fabrication of lithium niobium silicate and borosilicate glasses. The third and fourth sections deal with the polishing and characterization, specifically: Differential Scanning Calorimetry (DSC), Scanning Electron Microscopy (SEM) combined with Energy-Dispersive X-ray Spectrometry (EDS), Ultraviolet- Visible Spectroscopy (UV) and thermal diffusivity. In conclusion, two paragraphs are dedicated to $LiNbO_3$, respectively its crystallographic and optical properties.

2.1 Glass: definition chemistry, and phase separation

2.1.1 Debate on glass definition

The modern debate about the definition of glass began in 1932 with Zachariasen. Glass can be defined as a supercooled liquid from the point of view of physical chemistry or a solid from the theory of elasticity. If we know nothing about the

atomic arrangement, it is not enough the definition as a liquid supercooled or a solid [1]. Experimental evidence has demonstrated that glass strength may overtake the corresponding crystalline one. Then, it means that there must be a glass network with different characteristics compared to those of the crystalline one. From the results of the X-ray diffraction experiments, the glass network is non-periodic and not symmetrical. The isotropy is a natural consequence of the absence of symmetry in the glass network, and the atoms are all structurally different from each other. In this case, migration is possible for detached atoms [1]. In 1973, Doremus announced the following definition: "A material formed by cooling from the normal liquid state which has shown no discontinuous change in properties at any temperature but has become more or less rigid through a progressive increase in its viscosity" [2]. Besides, Roy, in his classification of non-crystalline solids, argued "In the literature, all non-crystalline solids are often referred to as "glass"" [3]. To highlight that this definition was too simplistic, Cooper and Gupta stated that this can cause confusion if a quantitative definition of glass, independent of the history of its treatments, is not given [4]. It is difficult to find a tool to recognize a non-crystalline material; otherwise, structural differences can be used to explore its origin (the parent materials) and its behavior [3]. Non-crystalline materials are always unstable or metastable phases, as represented in the following Figure 2. This structural classification depends on the parent materials and the process used to synthesize non-crystalline materials. In case of an excess of free energy, the material has been frozen or quenched by a sudden change of a thermodynamic intensive variable: temperature in glasses and vapor deposited non-crystalline solids, pressure, or chemical potential in gel [3].

Besides, glass can be defined as an isotropic solid if some parameters were specified: the normalized correlation range and the structural relaxation time. χ is the normalized correlation range equal to $\chi \equiv \frac{R-d}{d}$ where R is the correlation range used to distinguish between polycrystalline and non-crystalline states, and d is the hard sphere diameter. For glass or a normal liquid $\chi \cong 1$, and, in general, χ assumes a particular value equal to a/d where a is the grain size, for single crystals and polycrystalline aggregates, i.e., in case of anisotropic materials [4].

The other characteristic parameter is the structural relaxation time τ (s), allowing a distinction between liquids and glasses. For glass as isotropic material, $\tau >> 10^3$ s [4].

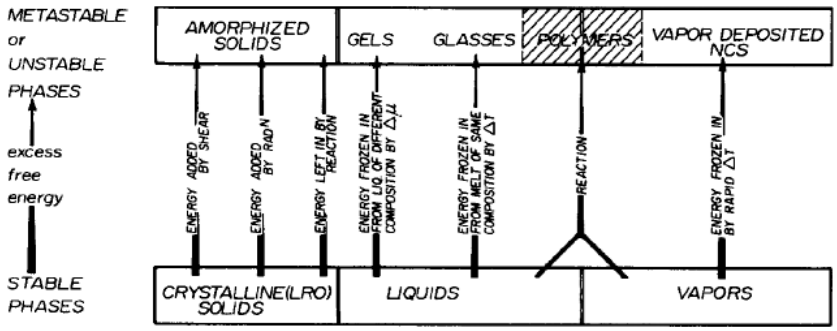

Figure 2: Structural classification of materials: when the stable phases present an excess of entropy, they can be transformed into non-crystalline solids that are always unstable or metastable phases [3]

The properties for the most important different states are reported in Table 1.

Table 1: Properties of different states (a = crystal or grain diameter; d = hard sphere atomic diameter) [4]

State of aggregation	Normalization correlation range, χ	Structural relaxation time, τ(s)	Isotropy
Crystal	≈a/d	$\gg 10^3$	−
Polycrystal	≈a/d	$\gg 10^3$	+, −
Glass	≈1	$\gg 10^3$	+
Normal liquid	≈1	$\ll 10^3$	+
Dilute gas	→0	$\ll 10^3$	+

A few years after, Wong and Angell, in 1976, introduced the concept of crystallinity: "Glass is an X-ray amorphous material that exhibits the glass transition. This being defined as that phenomenon in which a solid amorphous phase exhibits with changing temperature (heating) a more or less sudden change in its derivative thermodynamic properties such as heat capacity and expansion coefficient, from crystal-like to liquid like values." [5].
Mari suggested in the same year this glass definition: "Amorphous solids that are obtained by fast cooling a molten mass averting its crystallization" [6].
A first turn comes when it begins to distinguish between glass and solid amorphous. For Zarzycki, in 1982, the glass was "a non-crystalline solid that presents the phenomenon of glass transition" [7] and Gupta, in 1996, deepened this distinction by inserting two main rules derived from Zachariasen's conditions for glass formation [1]: a system is a good non-crystalline solid (NCS) former if *(i)* the short-

range order (SRO) of the crystal is indistinguishable from the SRO of NCS and if *(ii)* it is topologically disordered. Among all the materials that satisfy these two rules, i.e., all the NCS, only the ones that satisfy a third rule can be properly called *glasses*: *(iii)* a glass must show the same SRO at the solid-state and after melting. If this latter condition is not satisfied, it will be only an amorphous solid [8].

In the 21st century, the first interesting definition was from Shelby in 2005: "An amorphous solid completely lacking in long-range order, periodic atomic structure, and exhibiting a region of glass transformation behavior," or "Any material, inorganic, organic or metallic, formed by any technique, which exhibits glass transformation behavior" [9].

In 2010, Varshneya proposed a new definition: "Glass is a solid having a non-crystalline structure, which continuously converts to a liquid upon heating" [10], and this was reported in [11].

After three years, Gutzow and Schmelzer introduced a new concept: "Glasses are thermodynamically non-equilibrium kinetically stabilized amorphous solids, in which the molecular disorder and the thermodynamic properties correspond to the state of the respective undercooled melt as a generic temperature T* are frozen-in" [12].

The crucial breakthrough in the debate occurred in 2017 when Zanotto and Mauro provided two definitions: "Glass is a nonequilibrium, non-crystalline state of matter that appears solid on a short time scale but continuously relaxes towards the liquid state" and another more technical "Glass is a nonequilibrium, non-crystalline condensed state of matter that exhibits a glass transition. The structure of glasses is similar to that of their parent supercooled liquid (SCL), and they spontaneously relax towards the SCL state. Their ultimate fate, in the limit of infinite time, is to crystallize" [13]. The latter definition sparked a discussion in which Popov proposed *metastability* [14] while Zanotto and Mauro stood by the fact that glass was an *unstable material* [15].

The last definition was from Rajaramakrishna and Kaewkhao in 2019: "Glass is an amorphous solid which exhibits glass transition temperature by arresting the kinetics below supercooled liquid region when bypassed crystallization" [16]. This was not accepted since it neglects the concept of the unstable nature of glass matter. Then the definition of Zanotto and Mauro is now adopted and included in the third edition of the book of Fundamentals of Inorganic Glasses by Varshneya and Mauro [17]. The statements of Zanotto and Mauro were revealed the most detailed, complete, and comprehensible and they explained that even though glass can be

considered as a solid and immutable material, it is a liquid if it was checked on a long, almost infinite, timescale.

2.1.2 Glass chemistry

After this introduction, we can bring out the following definition of "glass" as a ceramic material generated from a structural freezing process of a supercooled liquid that solidifies in an amorphous way, without long-range periodicity but a short-range order, as shown in Figure 3. It is also an isotropic material with a mixed chemical bond composed of electropositive ionic and electronegative covalent structures. The fundamental condition of glass formation is to create long chains or large networks.

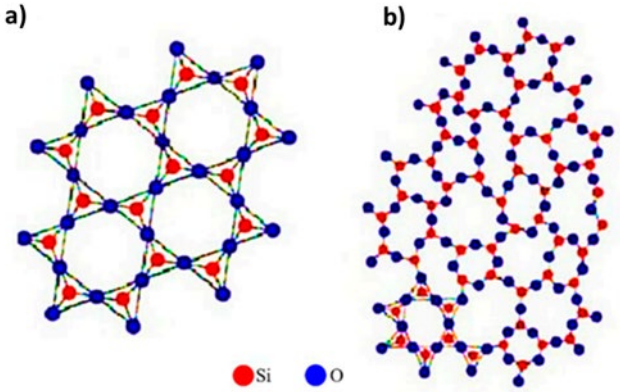

Figure 3: Atomic structure of SiO_2 a) crystal (Quartz) and b) glass (so-called silica) [18]

The Zachariasen-Warren network theory presents the conventional glass formation according to these five basic principles [19]:

1. A compound tends to form a glass if it easily forms polyhedral groups as the smallest building units.
2. Polyhedra should not share more than one corner.
3. Anions should not bind more than two central atoms of a polyhedron. Thus, in simple glasses anions form bridges between two polyhedra.
4. The number of corners of polyhedral must be less than 6.
5. At least three corners of a polyhedron must connect with the neighbor polyhedra.

For unconventional glass melts, it could be possible to use Sun's theory; its peculiarity is the connection of glass formation process to the ability or inability of

molecular bonds to rearrange in the liquid state during crystallization. Sun indicated precisely four requirements [20]:

1) the very high bond strength of atoms in the chains or networks.
2) minimal formation of a small ring of these strongly bonded atoms.
3) at least a continuous chain has to be formed configuratively and structurally with the relative numbers of various atoms in the chains or networks.
4) the coordination numbers of the glass forming atoms should be as small as possible to keep the bond strong.

For glass formation, it is possible to distinguish the anions like O^{2-}, S^{2-} and F^{-}. The cations establish the role of the compound in glass formation according to their dimensions and coordination numbers, i.e., the number of neighbors surrounding each atom. The glassmaking components bonds connect the atoms together for the three-dimensional network formation, in which it is interesting to distinguish three classes of oxides:

1) The *formers* which represent the glass network backbone may form glass with ordinary laboratory techniques (B_2O_3, SiO_2, GeO_2, P_2O_5, As_2O_5, Sb_2O_5, V_2O_5, ZrO_2, P_2O_3, Sb_2O_3, Bi_2O_3). Their cations have a coordination number generally equal to 3 or 4.
2) The *modifiers* that do not produce a glass under ordinary conditions change the glass properties and weaken its structure (Na_2O, Li_2O, K_2O, CaO, SrO). In this case, the coordination number are equal 6.
3) The *intermediates*, which are in a middle position between formers and modifiers: they could be included in one of two classes depending on the specific case of the glassmaking process (Nb_2O_5, Al_2O_3, BeO, ZnO, CdO, PbO, TiO_2), and then, they could reinforce or loosen the glass network, depending on the particular case [3].

Once the glass network has been formed, it is no longer possible to distinguish the oxides and only the bonds *M - O* remain and based on the bond energy of the oxides, it is possible to classify between 80 kcal characterizing the network formers, 60 kcal typical of modifiers and an energy between 60 and 80 kcal that allows to detect the intermediate oxides [20].

Glass formation, unlike a crystalline material, occurs by state transition from liquid to solid in a continuous way through a progressive viscosity increase during cooling to achieve a completely rigid structure. Moreover, no latent solidification heat flow occurs during the continuous state transition, as there is no net passage from disorder to order as it occurs in crystals. A simple but not simplistic and fair

definition of glass could be summarized into a rigid solid with volumetric thermal expansion like a crystal, but with a microstructure like a liquid. In addition, glass presents a time-dependent behavior called glass transition state. We can note that the glass transition temperature (T_g) depends on a cooling rate that does not allow the time required for crystallization. It is the temperature in which mechanic behavior change drastically from elastic to viscous, and specific volume variation rate for the thermal component is equal to the structural one.

For example, silica glass has the orthosilicate tetrahedra as repetitive unit $(SiO_4)^{4-}$. However, it is challenging to predict the tetrahedra arrangement accurately, and then silica network polymerization is influenced considerably by his thermal history, i.e., the thermal treatments previously occurred which have determined its structural evolution. Since the glassy state is not an equilibrium state, the usually employed thermodynamic variables to define his state are not enough, then we need a configurational parameter, the so-called fictive temperature (T_f). A glass is at its fictive temperature, (that may be different from his actual temperature T), if its configuration corresponds to that in equilibrium at this temperature. Then, if the glass was brought abruptly from its actual temperature to the fictive one, its structure should not change since it corresponds to the equilibrium one, as represented in the following Figure 4.

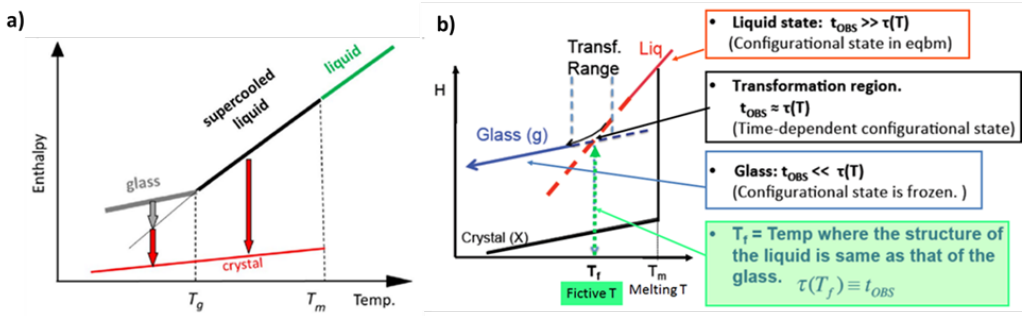

Figure 4: a) Scheme of a glass-forming substance, specifically enthalpy versus temperature plot sowing four distinct states: liquid (L), supercooled liquid (SCL), glass (G) and crystal (C). T_m = melting temperature, T_g = glass transition temperature [13]; b) Change of enthalpy with the temperature for the different allotropic phase (cooling at a fixed rate, q ($t_{OBS} \sim 1/q$)) [adapted from http://www.certev.ufscar.br/documentos/arquivos/gupta-slide]

2.1.3 Phase separation: nucleation and growth

The phase separation process between a liquid and a solid in a glass consists of nucleation and growth of crystals, i.e., crystallization. Generally, this occurs through the classical nucleation theory (CNT), a simple theoretical model proposed by Gibbs.

When nucleation takes place in the liquid phase or glass because of the thermal fluctuation of the chemical composition, no interface is generated, and it is not possible to distinguish the parent phase from the one produced; this is called homogeneous. For details about CNT, refer to the section of Appendix A.
Even though this theory has been employed to describe the crystallization process of glasses. However, this method presents a large discrepancy between the calculated and experimental results, due to the real practice of solidification of glassy alloys often involves heterogeneous nucleation [21]. This kind of nucleation happens at some preferred sites that are much greater than others. If we compare to the homogeneous nucleation, there is an effect mainly because of the diminished thermodynamic barrier, towards a decrease of the contribution of the effective surface energy to the work of critical cluster formation [22].
For glasses, a heterogeneous nucleation can also occur in extraneous particles and in correspondence of a second phase evenly distributed in the glass and formed with a mechanism called spinodal decomposition. This phase separation does not occur by nucleation and growth. We consider a non-ideal two-component endothermic solution, free energy vs composition curve may show two minima and between them a spinode in a certain range of temperature. Solution composition inside the spinode is unstable since it tends to separate in two different phases in correspondence of the minima, lowing the system total free energy. The miscibility gap diminishes progressively at increasing temperature until disappears beyond a temperature where only a phase coexists. The spinodal decomposition occurs when a solution is stable at a certain temperature, while cooling enters the immiscibility gap. If this gap is over the liquid temperature, the separation occurs in macroscopic scale e in this case, the glass will be opalescent or layered. If the miscibility gap is under liquid temperature, second phase generation will happen on a microscopic scale for the low diffusion rate. The glass will be homogeneous and transparent, being the biphasic structure detectable only at high magnifications of the electron microscope.
In Figure 5, the segregation into solution occurs initially through small local composition fluctuations, after the two phases become more distinct and revealed by chemical attack. Moreover, the phases seem often interconnected in a tridimensional continuity of the particles from which they were generated.

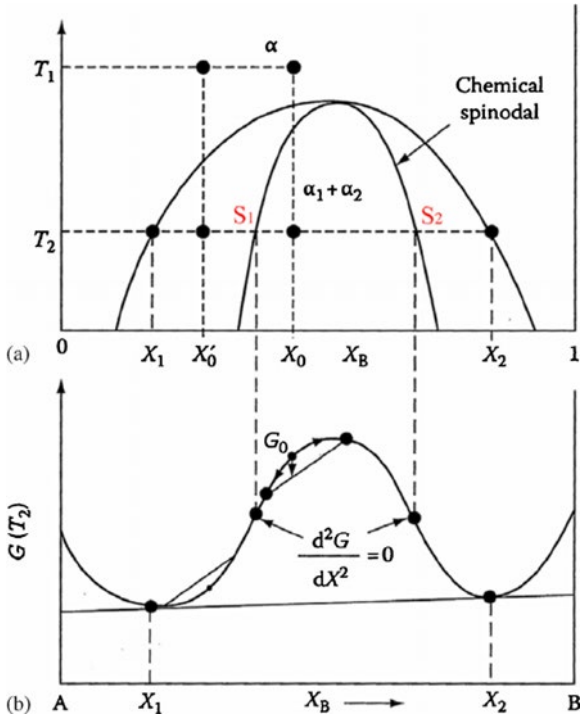

Figure 5: Schematic free energy diagram of the spinodal decomposition. (a) Spinodal decomposition is shown on the phase diagram displaying a miscibility gap. Note that the boundary separating the metastable and the unstable region is known as spinodal curve that can be obtained by performing a common tangent construction of the free-energy curve. (b) The free energy curve is plotted as a function of composition for the phase separation temperature T_2. In the spinodal region, the curvature of the free-energy curve is negative. Note that the binary mixture with initial temperature (T_1) is cooled quickly to a lower temperature (T_2). X_1 and X_2 are the equilibrium compositions that correspond to the free energy minima. The spinodes are marked as S_1 and S_2 in the diagram. In the spinodal region, the curvature of the free-energy plot is negative [23].

2.2 Melt quenching technique

This To prepare a glass by melt quenching, the chemical components as starting batch materials were weighted according to the suitable composition (%mol) and mixed homogeneously to a fine powder in a pestle and mortar, then transferred to a specific crucible and heated until the melting point. After the melt is cast and quickly poured on a brass or stainless block kept at 300°C, and then pressed with another brass or stainless block to get glass. This last step of the melt quenching process can be considered properly also an annealing and the glass samples subjected to this treatment have been proved stable during the characterizations over the year, as it is possible to verify in the next fourth chapter dedicated to

experimental results. Once the glass is obtained, cutting and mirror polishing are carried out for the required shape and size [16].

As regards the glasses synthesized in this thesis work, a dedicated and specific process is chosen illustrated hereafter. Below, in Figure 6, it is shown the ternary phase diagram for SiO_2 – $LiNbO_3$ – B_2O_3 where the four glasses composition, employed in the experiences, are placed, and reported in an extended way in the following Table 2:

Table 2: Glass labels and batch compositions

Label	Glass batch composition (molar percentage)
LNS34	33% LiO_2 – 33% Nb_2O_5 – 27% SiO_2 – 0% B_2O_3
LNS27B7	33% LiO_2 – 33% Nb_2O_5 – 27% SiO_2 – 7% B_2O_3
LNS20B14	33% LiO_2 – 33% Nb_2O_5 – 20% SiO_2 – 14% B_2O_3
LNS13B21	33% LiO_2 – 33% Nb_2O_5 – 13% SiO_2 – 21% B_2O_3

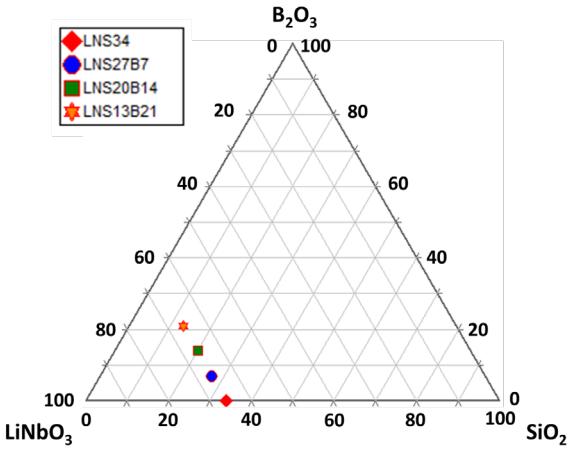

Figure 6: SiO_2 - $LiNbO_3$ - B_2O_3 ternary phase diagram

The melt quenching technique with which the four glasses were made is listed in seven steps described extensively afterwards and reported in the following Figure 7:

1. Powder mix with acetone for three times
2. Heat treatment at 200°C for two hours
3. Room temperature rise at 5°C/min up to 1000°C
4. Temperature maintenance at 1000 °C for 1h
5. Raise from 1000°C to melting temperature to 5°C/min
6. Melting temperature maintenance for 2 hours
7. Quenching between two metal plates preheated around 350°C

Figure 7: Scheme of glass making process starting from the chemical powders

Once the precursors have been weighed and put in the mortar, acetone has been added twice or more as needed to allow a suitable homogenization of the powder. Continuous mixing with a pestle is done from top to bottom, and it is fundamental not to make a circular movement not to attach everything to the mortar walls. When it is obtained a dry powder, acetone is added again. It must be mixed with the pestle until it is again a dry powder, then it will be ready. The powder is put into the platinum crucible and baked at 200°C for two hours to evaporate all the acetone. The next day, when the oven is cold, the crucible is introduced, and a ramp from room temperature is set. The crucible is introduced into a furnace, and the melting program is started with a two-step process (first-step of ramp in n°3 and 4 and second step in n°5 and 6 of the abovementioned list). The first ramp to 1000°C is made for decarbonization of the precursor Li_2CO_3 to form Li_2O, eliminating CO_2. The second ramp, from 1000°C to melting temperature, is carried out to obtain a homogeneous fusion of the mixture, even though it is important not to go beyond the established holding time of two hours, to avoid the volatilization of Li_2O and B_2O_3.

Subsequently, to release stress, the molten mixture is quenched between two metal plates preheated at around 350°C, forming the final glass product. The collected glass samples can thus be polished.

2.2.1. Lithium niobium silicate glass fabrication

To obtain 30 g of glass, the calculations for 33%Li_2O – 33%Nb_2O_5 – 34%SiO_2 (labeled LNS34, %mol) composition and powder mix with acetone for three times are reported in Table 3 and Figure 8:

Table 3: Batch calculation for LSN precursors powder to obtain glass by melt quenching

Final compound	Mole %	Precursors	Initial mole%	Initial wt%	Th.mass (g)	Exp.mass (g)
Nb_2O_5	33	Nb_2O_5	33	66.1874	19.8562	19.8566
Li_2O	33	Li_2CO_3	33	18.3990	5.5197	5.5209
SiO_2	34	SiO_2	34	15.4134	4.6240	4.6251

The following melting program for LNS34 deals with four steps:

1. RT rise at 5°C/min up to 1000°C
2. At 1000 °C for 1h.
3. Raise from 1000°C to 1400°C to 10°C/min
4. At 1400°C for 1 hour.

Figure 8: Example of LNS glass plate after the glass cooling (typ. 5cm size and few mm thick)

2.2.2 Lithium niobium borosilicate glass fabrication

The previous procedure is applied to $33Li_2O - 33Nb_2O_5 - 13\%SiO_2 - 21\%B_2O_3$ (labeled LNS13B21) glass, starting from a batch calculation of 30 g in Table 4 below:

Table 4: Batch calculation for LNS13B21 precursors powder to obtain glass

Final compound	Mole %	Precursors	Initial mole%	Initial wt%	Th.mass (g)	Exp.mass (g)
Nb_2O_5	33	Nb_2O_5	27.27	60.13	18.0389	18.0360
Li_2O	33	Li_2CO_3	27.27	16.72	5.0145	5.0140
SiO_2	13	SiO_2	10.74	5.35	1.6062	1.6070
B_2O_3	21	H_3BO_3	34.71	17.80	5.3404	5.3407

The following melting program for LNS13B21 deals with four steps:

1. RT rise at 5°C/min up to 1000°C
2. At 1000 °C for 1h.

3. Raise from 1000°C to 1350°C to 10°C/min
4. At 1350°C for 1 hour.

We note that the presence of B_2O_3 can promote the glass crystallization that is visible both on the crucible and on the glass produced through the white traces of following Figure 9 a), b) and c):

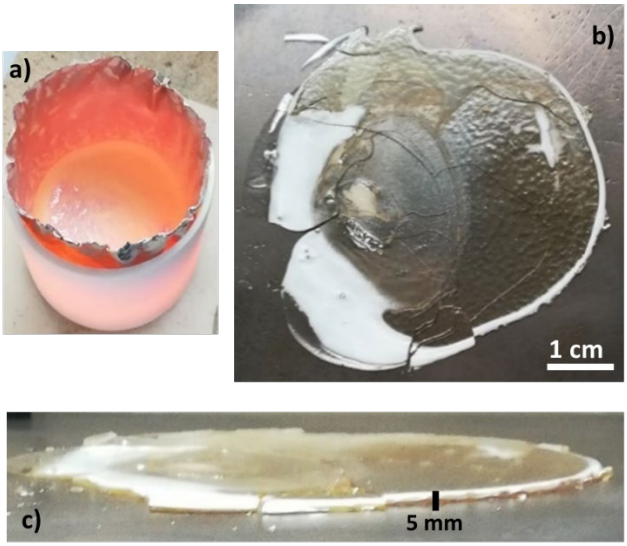

Figure 9: a) crucible after glass casting; three highlighted zones of glass in different view: transparent, rough, and white zones; b) glass on the heating plate; c) side view of the glass

In this case, a transparent sample is chosen, even with a rough surface. The sample has a smaller thickness than the LNS matrix sample. The same methodology is used for the synthesis of LNS27B7 and LNS20B14 glasses (composition given in Table 2).

2.3 Glass polishing

The pieces of raw glasses are polished double side by a polishing machine by SiC abrasive paper discs (purchased from PRESI) with decreasing grain size: P240, P600, P1200, P2500. After this step, the finishing polishing is done by another polishing machine (ESCIL, ESC 300 GTL) using different diamond lapping films. Finally, the last finishing step is done with colloidal silica (30nm grain size). The polishing paper and time are dependent on the sample hardness. Below in Table 5, we reported the polishing sequence generally employed, even though some steps could be skipped or kept a few minutes longer. Polished surfaces present more strength than non-polished ones.

Table 5: Polishing steps list of glasses

Polishing material	Time (min)
abrasive paper P240	8
abrasive paper P600	8
abrasive paper P1200	8
abrasive paper P2500	10
diamond disc 15 µm	10
diamond disc 9 µm	10
diamond disc 6 µm	10
diamond disc 3 µm	15
diamond disc 1 µm	15
colloidal silica 0.03 µm	20

2.4 Glass characterization

2.4.1 Differential Scanning Calorimetry (DSC)

The Differential Scanning Calorimetry is a thermal analysis that measures the heat absorbed or liberated during different transitions in the glass due to temperature treatment, and precisely *Differential* indicates a measurement of a sample relative to the reference, *Scanning* is referred to temperature ramp that in our case is equal to 10°C/min, and *Calorimetry* defines a heat measure. For a detailed explanation of the operating principle and for in-depth analysis of the DSC use for an exhaustive understanding of glasses, refer to the following complete reference [24].

Figure 10 provides the DSC scans of the four different glass compositions (in mol%) $33Li_2O – 33Nb_2O_5 – (34\text{-}x)\ SiO_2 – xB_2O_3$, with x = 0, 7, 14, and 21. In this case, the black curve corresponds to LNS and glass transition temperature (T_g), maximum crystallization peak tempering with (T_p), and onset crystallization temperature (T_x) were also indicated. It is not easy to distinguish the T_g for LNS and LNSB glass; consequently, the values were taken from Sciglass. For LNS, $T_g \approx 579$°C; otherwise, for LNS13B21 the value of $T_g \approx 520$°C. For both glasses, $T_m = 1257$°C corresponds to the melting temperature of $LiNbO_3$. By the observation, the progressive addition of B_2O_3 leads to shift down the crystallization peak to lower temperatures by about 150°C between LNS and LNSB with 21% mol% B_2O_3.

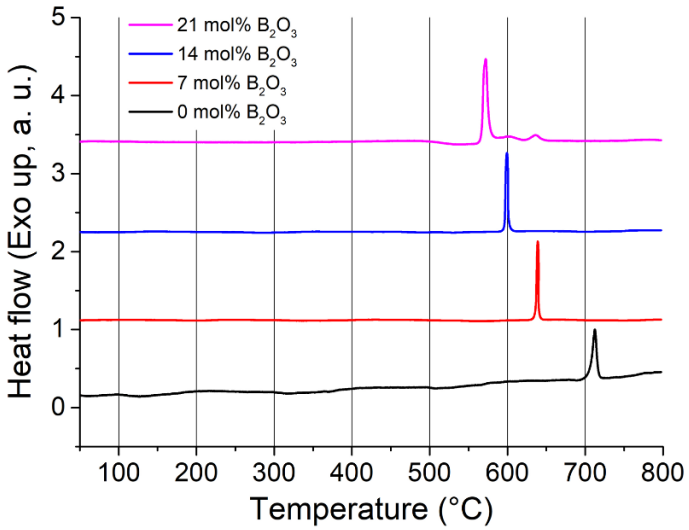

Figure 10: Differential scanning calorimetry (DSC) scans for four glasses composition with an increasing amount of B_2O_3 in the batch compositions in mol%

2.4.2 Scanning Electron Microscopy (SEM) combined with Energy-Dispersive X-ray Spectrometry (EDS)

The Scanning Electron Microscopy micrograph is employed to explore the laser tracks cross- section and to highlight the formation of nanogratings in borosilicate glass matrices.

Firstly, it is fundamental to focus the attention on elemental composition and Nb/Si ratio by SEM analysis that allows a higher resolution of the fs-laser-induced modifications in borosilicate glasses, reported in the following Figure 11a and b.

The self-organized nanostructures present an oriented phase separation already visible in LNS34 matrix explored in ref. [8]. They were discovered by SEM analysis in two passages illustrated in Section 4.6.1. For more detailed theory about its working principle, see [25].

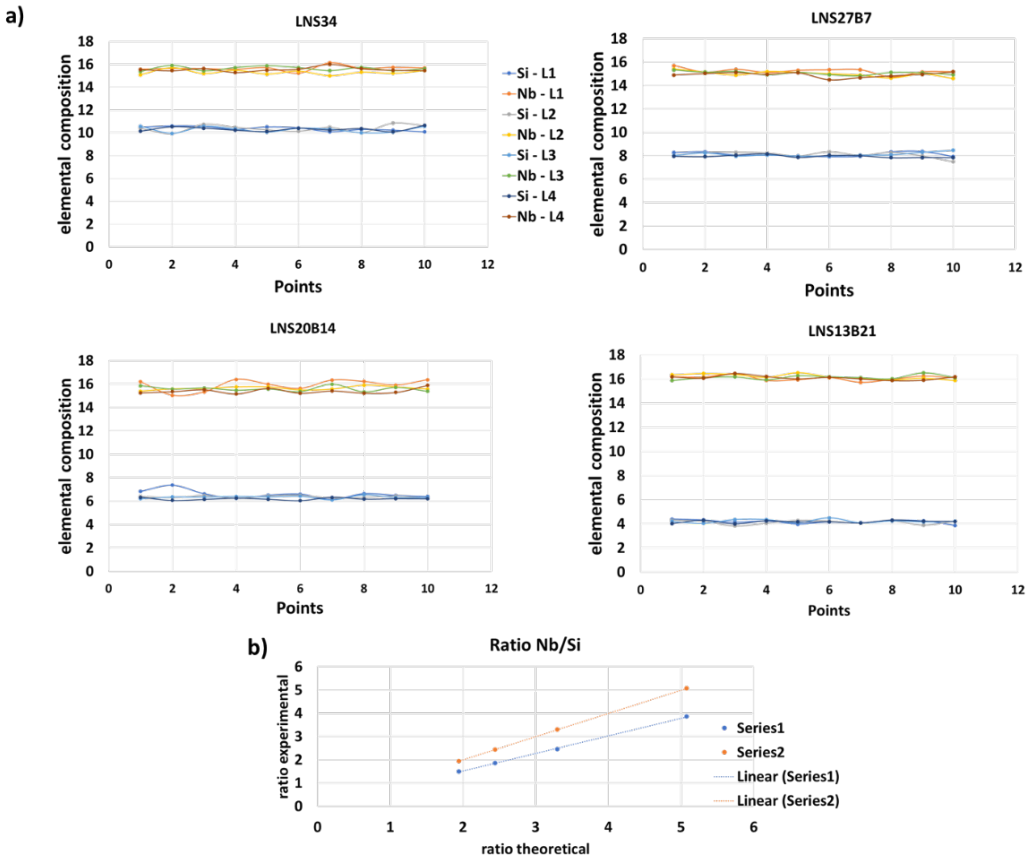

Figure 11: a) Elemental composition analysis for four glass composition by SEM-EDS analysis; b) Exploration of Nb/Si ratio: ratio theoretical vs ratio experimental

2.4.3 Ultraviolet–visible spectroscopy (UV spectra)

The absorption spectra [26], [27] of the fabricated glasses (LNS34 and LNS13B21) were measured. As it can be seen in Figure 12, there is no absorption band in the LNS and LNSB glasses. These absorption spectra were recorded by a Cary5000 spectrophotometer. The cut-off wavelength is shown to be around 350 nm for both glasses, whereas SiO_2 glass is more transparent down to the deep UV.

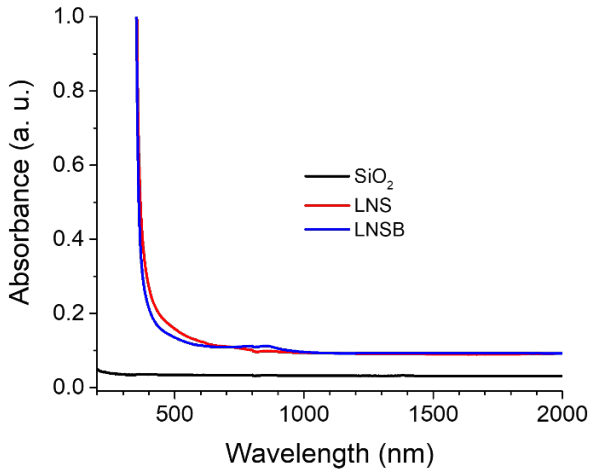

Figure 12: Absorption spectra for LNS (precisely, LNS34), LNSB (precisely, LNS13B21) and SiO_2 (Suprasil) for sake of comparison

2.4.4 Thermal diffusivity measurements

Thermal diffusivity indicates the heat transfer rate through a medium, precisely from the hotter side to the colder one. This property is connected to chemical species movement and represents the balance between heat that passes through a material and heat stored in it per unit volume. It is possible to study the interaction between materials by thermal diffusivity measurements. Thermal diffusivity measures the change in temperature produced in the unit volume of the material by the amount of heat that flows in unit time through a unit area of a layer of unit thickness with a unit temperature difference between its faces [27] – [29]. In this case, thermal diffusivity was measured between room temperature and 800°C, and the values were reported in the following Figure 13. The measurements were done in isotherm, and at each temperature a stabilization time was imposed. The ramp rate was set as 5°C/min. Each time a few points during cooling in a stationary state for each sample, during temperature increments. On the curves, black points indicate run-up ramp and red points descent ramp. We note there is an irreversible evolution of the sample around 600°C, under measurement conditions. This temperature corresponds to the crystallization peak of these glasses. This is why, in correspondence with this value of temperature, it is recorded a remarkable discordance regarding the trend of the curve for each of the three compositions examined.

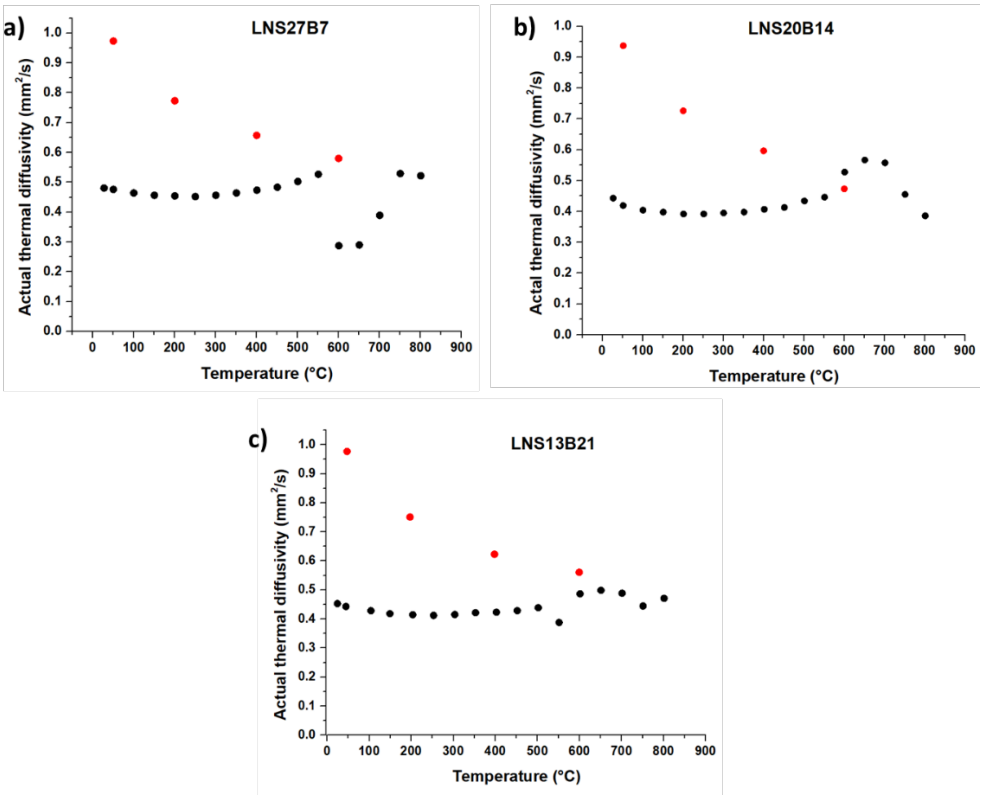

Figure 13: Thermal diffusivity curves extracted from measurements effectuated in ICCMO of a) LNS27B7, b) LNS20B14, c) LNS13B21. Black dots correspond to the run-up ramp and red ones to descent ramp

In our multidisciplinary discussion about laser-matter interaction, we have to take into account that thermal diffusivity affects the shape of the curve T (r, t), i.e., the scheme of the temperature spatial distribution evolution after pulse deposition inside the glass while time is evolving, reported in Figure 14, extracted from Figure 1c of Ref. [31]. Then, thermal diffusivity is linked to heat diffusion speed within the glass equal to $\sim \frac{4D_T}{w_0}$ where D_T is the thermal diffusivity and w_0 is the beam waist. The corresponding temporal magnitude affected by thermal diffusivity is diffusion time τ_D equal to $\frac{w_0^2}{4D_T}$, where $w_0 \sim 1$ µm. In our experimental conditions, heat diffusion speed corresponds to a few 10 m/s actually greater than scanning speed (< 1mm/s) [31]. The values found for LNS27B7, LNS20B14 and LNS13B21 reported on Figure 14 can be compared with D_T for LNS34 equal to $9 \cdot 10^{-7}$ m^2/s found in the literature [31], [33]. If we substitute the values of D_T and w_0, we obtain a $\tau_D \approx 0.28$ µs. This reveals a weak temporal overlapping between laser pulses, and

we enter into the so-called “single pulse regime.” From the comparison between thermal diffusivity values for silicate and borosilicate glasses, we noted a slight difference that it can be made explicit considering the definition of thermal diffusivity as $D_T = \kappa / [\rho C_p]$, where κ is the thermal conductivity, ρ is the density and C_p the heat capacity. Substituting the values found by Sciglass software, we found a difference of 6% in ρC_p between LNS34 and LNS13B21. Then, these profiles of spatial temperature distribution for both glasses just above are very comparable [31].

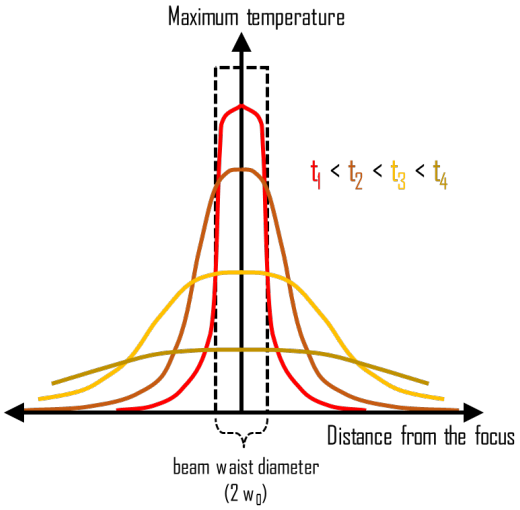

Figure 14: Temperature spatial distribution evolution T(r,t) after pulse deposition inside the glass, as time increases from t_1 to t_4. At decreasing of maximum temperature with time, the width of the distribution increases [31].

2.5 $LiNbO_3$: crystallographic and optical properties

Lithium niobate ($LiNbO_3$) is an artificial, dielectric, and multifunctional material of the 3m crystallographic group, firstly recognized as ferroelectric in 1949 by Matthias et al. [34]. It is naturally birefringent, and its properties such as pyroelectricity, piezoelectricity, nonlinearity, acousto-optic and electro-optic effects make it one of the targets and key materials for photonic, optical, and electronic applications, holographic data processing, and telecommunication technologies [35]. In particular, this Ph.D. thesis realized the 3D photo-precipitation of $LiNbO_3$ by femtosecond laser-induced crystallization.

Below, there are two sections on lithium niobate oxide's crystallographic and optical properties. It is important to consider that the optical properties basis is always orthogonal, whereas the crystallographic one is not. There are nevertheless a few rules for the coincidence of some axes.

2.5.1 Crystallographic properties

To study the formation of $LiNbO_3$, one fundamental point is to refer to the phase-equilibrium diagram of Li_2O – Nb_2O_5 reported in Figure 15a. This phase is found over a large range of solid solutions from ~ 45 mol% Li_2O at 1200°C, i.e., Li-poor compositions to the one towards the stoichiometric one [36]. When the ratio of Li / (Li + Nb) is 0.50, $LiNbO_3$ is stoichiometric; if the same ratio is equal to 0.485, we can define $LiNbO_3$ congruent and the proper solid phase directly appears from the liquid during the cooling process. For example, the Czochralski growth process illustrated in Figure 15b started by the precursors (Li_2CO_3 and Nb_2O_5) melted after the complete decomposition of Li_2CO_3. After the crystal seed addition, the crystal growth is initiated by the pulling process. As soon as the single crystal was formed, it was taken out. The formation of the crystal proceeds along the orientation of the c-axis. In this process, there are inevitable disadvantages like cracks, coloration creation, and segregation of constituent ions.

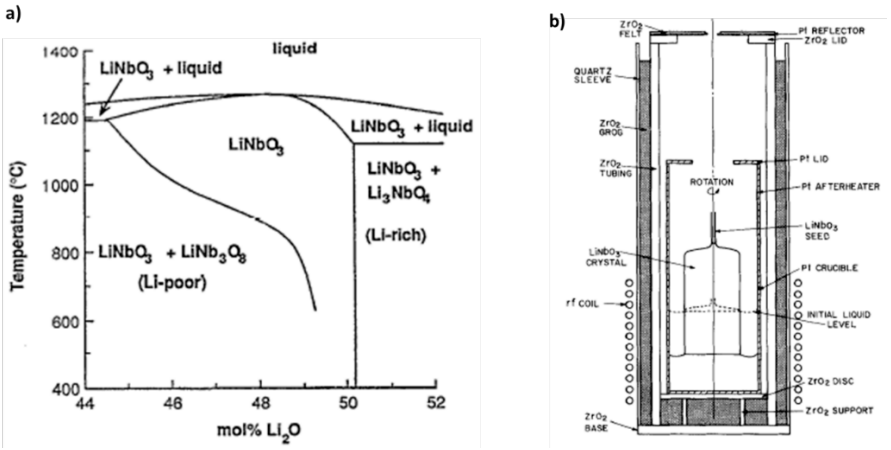

Figure 15: a) Phase-equilibrium diagram for $LiNbO_3$ [36] and b) scheme of the furnace for Czochralski growth at $LiNbO_3$ [37]

$LiNbO_3$ structure, reported in Figure 16a, is not centrosymmetric. The Curie temperature T_c (beyond which a material loses its ferromagnetism and becomes paramagnetic) of $LiNbO_3$ is very high and corresponds to ~1210°C [38], and this value depends on the crystal composition [36]. The distortion of the niobium-oxygen octahedron contributes to $LiNbO_3$ formation. Chains of the distorted oxygen octahedra with the common faces settled along with the polar axis c. When $LiNbO_3$ is in the paraelectric phase, the temperature satisfies this condition $T_c < T$

< T_m, as shown in Figure 16b. In this case, Nb^{5+} ions are in the center of the oxygen octahedron, otherwise the Li^+ ions are placed within the oxygen planes. Below T_c, $LiNbO_3$ is in the ferroelectric phase; the structure is composed by hexagonal close-packed oxide ions approximately where two-thirds of the octahedral sites are cations Li^+ and Nb^{5+} followed by a vacancy, and this sequence is repeated every third layer [39]. The condition of ferroelectricity is fulfilled when empty octahedra accept Nb^{5+} and Li^+ ions displaced from their octahedral centers in opposite directions along the c-axis. A spontaneous polarization, in the direction along the c axis, from -c face to +c face, is generated from ferroelectric $LiNbO_3$. This ferroelectric phase, reported in Figure 16c, has a conventional hexagonal unit cell with point group 3m, space group R3c with hexagonal axes (a_1 a_2 a_3 c). The c axis coincides with the polar axis (or optical axis). This +c face is the face positive when the crystal is cooled from the melt. The crystallographic parameters of $LiNbO_3$ crystal are reported in the following Table 6.

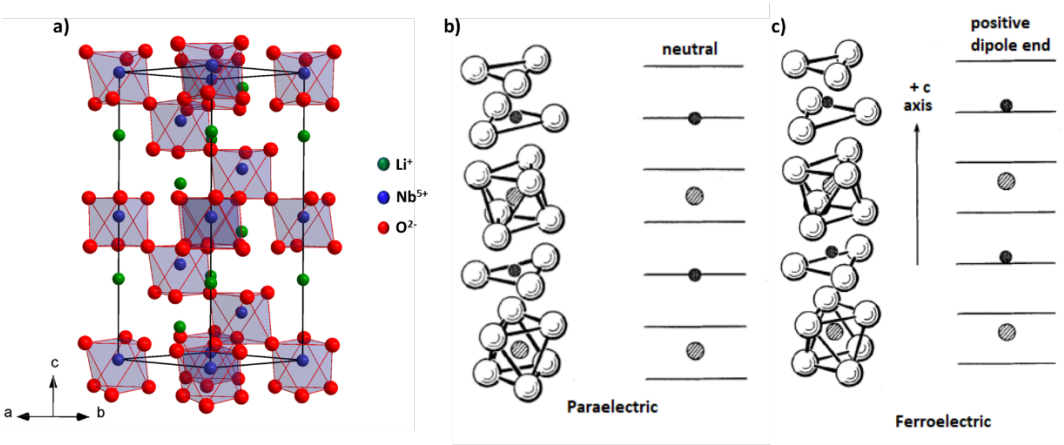

Figure 16: Positions of the lithium atoms (double cross-hatched circles) and the niobium atoms (single cross-hatched circles) with respect to the oxygen octahedra in the a) paraelectric phase and b) ferroelectric phase of lithium niobate, the horizontal line on the right side stands for the oxygen layers [38]; c) atomic structure of $LiNbO_3$ [40]

In addition, $LiNbO_3$ owns a very flexible host structure toward dopants and the formation of extensive solid solution areas. Remarkably, the physical properties of $LiNbO_3$ depend on the defects in the structure and can be improved by doping with some cations (e.g., Co^{2+} and Ni^{2+}). In the principal doping mechanism, the total number of cations remains constant [39].

Table 6: Crystallographic parameters of $LiNbO_3$

Items	Value
Crystal Symmetry	Trigonal

Point Group	3m
Space group	R3c (no. 161)
Lattice Constants (hexagonal)	a = 5.148 Å c = 13.863 Å

2.5.2 Optical properties

2.5.2.1 Absorption

There is a broad transparency range for $LiNbO_3$ between 420 and 5200 nm. $LiNbO_3$ is optically homogeneous (~ 5 x 10^{-5} /cm), with a damage threshold of 250 MW/cm^2 (1064 nm, 10 ns) [41]. $LiNbO_3$ composition (most of all, when some variation may occur due to doping or in solid solution) affects the position of the fundamental absorption edge [19]. This may be used to characterize the composition and homogeneity of $LiNbO_3$ [42]. The wavelength with a certain absorption coefficient (i.e., 15 or 20 cm^{-1}) defined the band edge position [42].

2.5.2.2 Refractive index

The direction of the electric field causes the electrical excitation for optically anisotropic material. In a linear, homogeneous, anisotropic dielectric, **D** is related to **E** in this way:

$$\mathbf{D} = \varepsilon\mathbf{E} \qquad (1)$$

Where ε is the permittivity of a material, expressed as second-order tensor (3 x 3 matrix)

$$\varepsilon_0 \begin{bmatrix} \varepsilon_{11} & \varepsilon_{12} & \varepsilon_{13} \\ \varepsilon_{21} & \varepsilon_{22} & \varepsilon_{23} \\ \varepsilon_{31} & \varepsilon_{32} & \varepsilon_{33} \end{bmatrix} \qquad (2)$$

Where ε_0 is the vacuum permittivity. The conservation of electromagnetic field energy ($\varepsilon_{ij} = \varepsilon_{ji}$) and the properties of crystal (symmetries) make the number of independent elements reduced.
Indeed, the dielectric matrix, i.e., the permittivity tensor, could be written in the following way when the crystal is oriented with the principal axes along the axes of a coordinate system:

$$\varepsilon_0 \begin{bmatrix} \varepsilon_{11} & 0 & 0 \\ 0 & \varepsilon_{22} & 0 \\ 0 & 0 & \varepsilon_{33} \end{bmatrix} \qquad (3)$$

D and **E** will have the same direction when **E** coincides with the direction of the principal axis of the dielectric constants. The relationship between the principal refractive index n_{kk} (k = 1,2,3) with ε_{kk} is equal to $n_{kk} = \sqrt{\varepsilon_{kk}}$. Now it is possible to write the dielectric matrix by refractive indexes. $LiNbO_3$ is a uniaxial crystal, then $\varepsilon_{11} = \varepsilon_{22} = n_o^2 \neq \varepsilon_{33} = n_e^2$, where n_o and n_e are respectively ordinary and extraordinary indexes, and the z-axis of the uniaxial crystal denoted the optic axis (in the direction of the optic axis). Then, the refractive index tensor of $LiNbO_3$ can be written as:

$$\begin{bmatrix} n_o & 0 & 0 \\ 0 & n_o & 0 \\ 0 & 0 & n_e \end{bmatrix} \qquad (4)$$

In the case of $LiNbO_3$, n_o is larger than n_e in the transparent range, as shown in Figure 17.

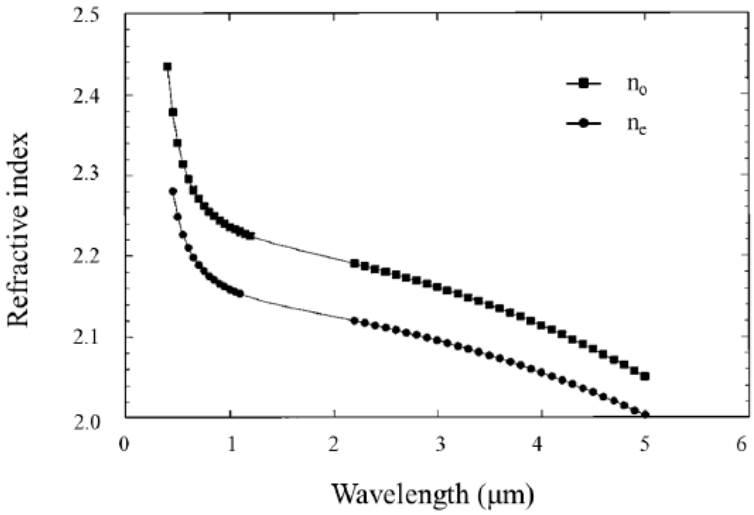

Figure 17: Trend of refractive indexes versus wavelength of congruently growth of $LiNbO_3$ [43]

The three-oscillator Sellmeier fitting the data appears in the solid curves at temperature measured of 21°C, in Figure 17. This equation is used to describe the dispersion of refractive index:

$$n^2(\lambda) = 1 + \sum_j \frac{A_j \lambda^2}{\lambda^2 - B_j} \qquad (5)$$

where A_j is the adsorption resonance of strength at a wavelength $\sqrt{B_j}$. For $LiNbO_3$ the Sellmeier equation valid for n_o and n_e is given by [43]:

$$n_o^2(\lambda) = 1 + \frac{2.6734\lambda^2}{\lambda^2 - 0.01764} + \frac{1.2290\lambda^2}{\lambda^2 - 0.05914} + \frac{12.614\lambda^2}{\lambda^2 - 474.6} \qquad (6)$$

$$n_e^2(\lambda) = 1 + \frac{2.9804\lambda^2}{\lambda^2 - 0.02047} + \frac{0.5981\lambda^2}{\lambda^2 - 0.0666} + \frac{8.9543\lambda^2}{\lambda^2 - 416.08} \quad (7)$$

where λ is the wavelength in μm.
For $LiNbO_3$, the refractive index is also a function of temperature and chemical composition [44]. There is also a relationship between electric susceptibility and refractive index of crystal described in [45]. The induced polarization characterized by the electric dipole susceptibility is equal to:

$$\mathbf{P_j^{(1)}}(\omega) = \varepsilon_0 \boldsymbol{\chi}_{\mathbf{jk}}^{(1)}(\omega)\mathbf{E_k}(\omega) \quad (8)$$

Where ε_0 is the permittivity of free space; $\boldsymbol{\chi}_{jk}^{(1)}$ is linear susceptibility tensor, a second rank tensor, a complex quality; and $\mathbf{E}_k(\omega)$ is the incident laser electric field. There is also a relationship in the eigen frame to the real part of the susceptibility between the dielectric constant $\varepsilon(\omega)$ and refractive $n(\omega)$:

$$n_{jk}^2(\omega) = \varepsilon_{jk}(\omega)/\varepsilon_0 = 1 + \boldsymbol{\chi}_{\mathbf{jk}}^{\prime(\mathbf{1})}(\omega) \quad (9)$$

Two independent elements characterize the electric susceptibility of $LiNbO_3$: one is along the polar axis, χ_{zz} and the other one is perpendicular to it χ_{xx} ($\chi_{xx} = \chi_{yy}$). It is possible to deduce the dielectric susceptibility from the refractive index for $LiNbO_3$. It has negative uniaxial birefringence with n_o (ordinary refractive index, electric field polarization normal to c axis) greater than n_e (extraordinary refractive index, electric field polarization parallel to c axis); indeed, the fast optical axis is along, whereas the slow optical axis perpendicular to the c axis. At the wavelength of 1030 nm, $n_o = 2.234$ and $n_e = 2.157$, i.e., the index normal to polar axis (i.e., χ_{xx}) is larger than one parallel to polar axis (i.e., χ_{zz}).

2.5.2.3 Nonlinear optical properties

The nonlinear coefficient of $LiNbO_3$ is: $d_{33} = 34.4$ pm/V, $d_{22} = 3.07$ pm/V, and $d_{31} = d_{15} = 5.95$ pm/V ref. [24]. The orientation of the polar axis of $LiNbO_3$ determines the second-order nonlinear optical properties (as discussed in Chapter 3). The relevant coefficient for a probe polarization along the polar axis of $LiNbO_3$ is the largest (d_{33}), compared to the coefficient for a probe polarization perpendicular to the polar axis (d_{22}). The description of the SHG in a crystal is summarized in ref. [47] for details. For a monochromatic input wave with frequency ω, the induced polarization at the harmonic frequency 2ω is written as:

$$\mathbf{P}_{2\omega}=\frac{\varepsilon_0}{2}\boldsymbol{\chi}^{(2)}_{2\omega}\mathbf{E}^{\mathbf{P}}_{\omega}\mathbf{E}^{\mathbf{P}}_{\omega} \quad (10)$$

Where ε_0 is the permittivity of free space, $\boldsymbol{\chi}^{(2)}_{2\omega}$ is the second-order nonlinear susceptibility tensor, and $\mathbf{E}^{\mathrm{P}}_{\omega}$ is the probing laser electric field.

Then, if we consider the expression of $\chi^{(2)}_{ijk}$ components, $\boldsymbol{\chi}^{(2)}_{2\omega}$ is a third-order rank tensor with 27 coefficients. When SHG analysis is made, another tensor is introduced:

$$d^{(2)}_{ijk}=\frac{1}{2}\chi^{(2)}_{ijk} \quad (11)$$

Now, $d^{(2)}_{ijk}$ is written in a contracted form, a 3 x 6 matrix, $d^{(2)}_{il}$. If $j=k$, $l=j$, otherwise, $l=-(j+k)$.

Then, for $LiNbO_3$, d_{il} is given by:

$$d_{il}=\begin{bmatrix} 0 & 0 & 0 & 0 & d_{31} & -d_{22} \\ -d_{22} & d_{22} & 0 & d_{31} & 0 & 0 \\ d_{31} & d_{31} & d_{33} & 0 & 0 & 0 \end{bmatrix} \quad (12)$$

2.6 Conclusions

This chapter introduces the materials investigated in this thesis, along with their most important properties. The next chapter is dedicated to laser direct writing. First, we focus on the glass since it is used as the base material and move to $LiNbO_3$ since it is the crystal phase induced from a glass phase in this work. The glass is generally described, including an interesting debate on its definition, its chemistry and phase separation. From this section, the melt-quenching technique, selected as the synthesis process, is described, along with the chosen glass compositions (lithium niobium silicate or borosilicate glass) and associated characteristics. A brief description of the post glass synthesis polishing process is also provided. The remainder of the chapter is devoted to the characterization of the glass samples. The aim of the aforementioned steps is to prepare the glass samples for subsequent femtosecond laser irradiation. Additionally, a DSC analysis is performed to find how the characteristic temperatures of synthesized glasses – i.e., glass transition temperature (T_g), maximum crystallization peak (T_p), and onset crystallization (T_x) temperatures - are affected by the increase of B_2O_3 in glass chemical composition.

Values of glass transition temperature found through Sciglass software are used as reference for our analysis, especially, $T_g \approx 579°C$ for LNS34, and $T_g \approx 520°C$ for LNS13B21. SEM-EDS analysis carried out on laser tracks cross-section highlights elemental compositions and Nb/Si ratio, and nanogratings formation in borosilicate glass matrices. Moreover, the UV absorption spectra are provided to set the use of the femtosecond laser based on the optical transparency window of the material. Finally, thermal diffusivity measurements intend to show how the heat diffusion speed is a fundamental parameter to understand the temperature spatial distribution evolution, after laser pulse deposition inside the glass. To have an overview on the optical and crystallographic properties of the product that we propose to obtain and maintain a common thread with the next chapters, the last section of this chapter dedicated to crystalline $LiNbO_3$.

2.7 Bibliography

[1] W. H. Zachariasen, "THE ATOMIC ARRANGEMENT IN GLASS," *J. Am. Chem. Soc.*, vol. 54, no. 10, pp. 3841–3851, Oct. 1932, doi: 10.1021/ja01349a006.

[2] "9780471891741: Glass Science, 2nd Edition - AbeBooks - Doremus, Robert H.: 0471891746." https://www.abebooks.com/9780471891741/Glass-Science-2nd-Edition-Doremus-0471891746/plp (accessed Aug. 24, 2021).

[3] R. Roy, "CLASSIFICATION OF NON-CRYSTALLINE SOLIDS," *Journal of Non-Crystalline Solids*, vol. 3, pp. 33–40, 1970.

[4] A. R. Cooper and P. K. Gufta, "An Operational Definition of the Glassy State," *J American Ceramic Society*, vol. 58, no. 7–8, pp. 350–351, Jul. 1975, doi: 10.1111/j.1151-2916.1975.tb11507.x.

[5] "Glass structure by spectroscopy: By J. Wong and C. A. Angell. Pp. 864 + xv. Marcel Dekker, New York and Basel. 1976. SFrs 145 - [PDF Document]," *vdocuments.mx*. https://vdocuments.mx/glass-structure-by-spectroscopy-by-j-wong-and-c-a-angell-pp-864-xv.html (accessed Oct. 13, 2021).

[6] E. A. Mari, *Los vidrios: propiedades, tecnologías de fabricación y aplicaciones*, 1ª ed. Buenos Aires: Alsina, 1982.

[7] J. Zarzycki, *Les verres et l'état vitreux*. Dunod, 1997.

[8] P. K. Gupta, "Non-crystalline solids: glasses and amorphous solids," *Journal of Non-Crystalline Solids*, vol. 195, no. 1–2, pp. 158–164, Feb. 1996, doi: 10.1016/0022-3093(95)00502-1.

[9] J. E. Shelby, *Introduction to Glass Science and Technology*. Royal Society of Chemistry, 2005.

[10] A. Varshneya and J. Mauro, "Comment on misconceived ASTM definition of 'Glass' by A. C. wright," *Glass Technology - European Journal of Glass Science and Technology Part A*, vol. 51, Feb. 2010.

[11] A. K. Varshneya, *Fundamentals of inorganic glasses.* Boston, London: Academic, 1994.

[12] I. Gutzow and J. Schmelzer, "The Vitreous State: Thermodynamics, Structure, Rheology, and Crystallization," *undefined*, 2013, Accessed: Aug. 25, 2021. [Online]. Available: https://www.semanticscholar.org/paper/The-Vitreous-State%3A-Thermodynamics%2C-Structure%2C-and-Gutzow-Schmelzer/35805f6f8a1516a0b9fcc3006be8780755634fea

[13] E. D. Zanotto and J. C. Mauro, "The glassy state of matter: Its definition and ultimate fate," *Journal of Non-Crystalline Solids*, vol. 471, pp. 490–495, Sep. 2017, doi: 10.1016/j.jnoncrysol.2017.05.019.

[14] A. I. Popov, "What is glass?," *Journal of Non-Crystalline Solids*, vol. 502, pp. 249–250, Dec. 2018, doi: 10.1016/j.jnoncrysol.2018.01.039.

[15] E. D. Zanotto and J. C. Mauro, "Response to comment on 'The glassy state of matter: Its definition and ultimate fate,'" *Journal of Non-Crystalline Solids*, vol. 502, pp. 251–252, Dec. 2018, doi: 10.1016/j.jnoncrysol.2018.01.040.

[16] R. Rajaramakrishna and J. Kaewkhao, "Glass material and their advanced applications," *KSS*, Jul. 2019, doi: 10.18502/kss.v3i18.4769.

[17] A. K. Varshneya and J. C. Mauro, *Fundamentals of Inorganic Glasses.* Elsevier, 2019.

[18] Muhammadfibonacci, "Crystal structure (crystalline,polycrystalline and amorphous)," *Muhammadfibonacci*, Sep. 18, 2011.

http://muhammadfibonacci.blogspot.com/2011/09/crystal-structure-crystallinepolycrysta.html (accessed Aug. 25, 2021).

[19] W. Vogel, *Glass Chemistry*, 2nd ed. Berlin Heidelberg: Springer-Verlag, 1994. doi: 10.1007/978-3-642-78723-2.

[20] K.-H. Sun, "FUNDAMENTAL CONDITION OF GLASS FORMATION," *J American Ceramic Society*, vol. 30, no. 9, pp. 277–281, Sep. 1947, doi: 10.1111/j.1151-2916.1947.tb19654.x.

[21] S. B. Lee and N. J. Kim, "Kinetics of crystallization in continuously cooled BMG," *Materials Science and Engineering: A*, vol. 404, no. 1–2, pp. 153–158, Sep. 2005, doi: 10.1016/j.msea.2005.05.038.

[22] V. M. Fokin, E. D. Zanotto, N. S. Yuritsyn, and J. W. P. Schmelzer, "Homogeneous crystal nucleation in silicate glasses: A 40 years perspective," *Journal of Non-Crystalline Solids*, vol. 352, no. 26–27, pp. 2681–2714, Aug. 2006, doi: 10.1016/j.jnoncrysol.2006.02.074.

[23] S. Sarkar, S. Banerjee, S. Roy, R. Ghosh, P. P. Ray, and B. Bagchi, "Composition dependent non-ideality in aqueous binary mixtures as a signature of avoided spinodal decomposition," *J Chem Sci*, vol. 127, no. 1, pp. 49–59, Jan. 2015, doi: 10.1007/s12039-014-0749-y.

[24] Q. Zheng *et al.*, "Understanding Glass through Differential Scanning Calorimetry," *Chem. Rev.*, vol. 119, no. 13, pp. 7848–7939, Jul. 2019, doi: 10.1021/acs.chemrev.8b00510.

[25] N. Erdman, D. C. Bell, and R. Reichelt, "Scanning Electron Microscopy," in *Springer Handbook of Microscopy*, P. W. Hawkes and J. C. H. Spence, Eds. Cham: Springer International Publishing, 2019, pp. 229–318. doi: 10.1007/978-3-030-00069-1_5.

[26] "59801397_020660.pdf." Accessed: Jul. 12, 2021. [Online]. Available: https://www.agilent.com/cs/library/primers/Public/59801397_020660.pdf

[27] "High-Performance UV-Vis, Cary 5000 UV-Vis-NIR spectrophotometer | Agilent." https://www.agilent.com/en/product/molecular-spectroscopy/uv-vis-uv-vis-nir-spectroscopy/uv-vis-uv-vis-nir-systems/cary-5000-uv-vis-nir (accessed Jul. 12, 2021).

[28] A. n Salazar, "On thermal diffusivity," *Eur. J. Phys.*, vol. 24, no. 4, pp. 351–358, Jul. 2003, doi: 10.1088/0143-0807/24/4/353.

[29] R. A. Morgan, K. I. Kang, C. C. Hsu, C. L. Koliopoulos, and N. Peyghambarian, "Measurement of the thermal diffusivity of nonlinear anisotropic crystals using optical interferometry," *Appl. Opt.*, vol. 26, no. 24, p. 5266, Dec. 1987, doi: 10.1364/AO.26.005266.

[30] A. G. Whittington, "Heat and Mass Transfer in Glassy and Molten Silicates," in *Measurements, Mechanisms, and Models of Heat Transport*, Elsevier, 2019, pp. 327–357. doi: 10.1016/B978-0-12-809981-0.00010-3.

[31] E. Muzi *et al.*, "Towards a Rationalization of Ultrafast Laser-Induced Crystallization in Lithium Niobium Borosilicate Glasses: The Key Role of the Scanning Speed," *Crystals*, vol. 11, no. 3, p. 290, Mar. 2021, doi: 10.3390/cryst11030290.

[32] J. Cao, L. Mazerolles, M. Lancry, and B. Poumellec, "Creation and orientation of nano-crystals by femtosecond laser light for controlling optical non-linear response in silica-based glasses," Université Paris-Saclay, France, 2017. [Online]. Available: Jing Cao. Creation and orientation of nano-crystals by femtosecond laser light for controlling optical non-linear response in silica-based glasses. Material chemistry. Université Paris-Saclay, 2017. English. ﷺNNT : 2017SACLS055ﷺ. ﷺtel-01988887ﷺ

[33] N. P. Bansal and R. H. Doremus, Eds., "Handbook of Glass Properties," in *Handbook of Glass Properties*, San Diego: Academic Press, 1986, pp. 671–677. doi: 10.1016/B978-0-08-052376-7.50027-8.

[34] B. T. Matthias and J. P. Remeika, "Ferroelectricity in the Ilmenite Structure," *Phys. Rev.*, vol. 76, no. 12, pp. 1886–1887, Dec. 1949, doi: 10.1103/PhysRev.76.1886.2.

[35] M. Manzo, F. Laurell, V. Pasiskevicius, and K. Gallo, "Lithium Niobate: The Silicon of Photonics!," in *Nano-Optics for Enhancing Light-Matter Interactions on a Molecular Scale*, B. Di Bartolo and J. Collins, Eds. Dordrecht: Springer Netherlands, 2013, pp. 421–422. doi: 10.1007/978-94-007-5313-6_42.

[36] P. F. Bordui, R. G. Norwood, D. H. Jundt, and M. M. Fejer, "Preparation and characterization of off-congruent lithium niobate crystals," *Journal of Applied Physics*, vol. 71, no. 2, pp. 875–879, Jan. 1992, doi: 10.1063/1.351308.

[37] M. Eriksrud, G. Nakken, and A. P. Grande, “SOLID-SOLUTION RANGE OF L1NbO3,” p. 3.

[38] R. S. Weis and T. K. Gaylord, “Lithium niobate: Summary of physical properties and crystal structure,” *Appl. Phys. A*, vol. 37, no. 4, pp. 191–203, Aug. 1985, doi: 10.1007/BF00614817.

[39] M. Paul, M. Tabuchi, and A. R. West, “Defect Structure of Ni,Co-Doped $LiNbO_3$ and $LiTaO_3$,” *Chem. Mater.*, vol. 9, no. 12, pp. 3206–3214, Dec. 1997, doi: 10.1021/cm970511t.

[40] “Lithiumniobat,” *Wikipedia*. May 22, 2021. Accessed: Jul. 16, 2021. [Online]. Available: https://de.wikipedia.org/w/index.php?title=Lithiumniobat&oldid=212242857

[41] “LiNbO3 Crystal Properties,Nonlinear Optical Crystal - China Bluebean.” https://de.bbotech.com/product.php?cid=135 (accessed Jul. 17, 2021).

[42] F. Physik and U. Osnabrtick, “Optical methods to characterise the composition and homogeneity of lithium niobate single crystals,” p. 8.

[43] D. E. Zelmon, D. L. Small, and D. Jundt, “Infrared corrected Sellmeier coefficients for congruently grown lithium niobate and 5 mol% magnesium oxide –doped lithium niobate,” *J. Opt. Soc. Am. B*, vol. 14, no. 12, p. 3319, Dec. 1997, doi: 10.1364/JOSAB.14.003319.

[44] U. Schlarb and K. Betzler, “Refractive indices of lithium niobate as a function of temperature, wavelength, and composition: A generalized fit,” *Phys. Rev. B*, vol. 48, no. 21, pp. 15613–15620, Dec. 1993, doi: 10.1103/PhysRevB.48.15613.

[45] D. E. Clark, W. B. White, and A. J. Machiels, “CRC handbook of laser science and technology,” Jan. 1986, Accessed: Jul. 22, 2021. [Online]. Available: https://www.osti.gov/biblio/5485389-crc-handbook-laser-science-technology

[46] F. Träger, Ed., *Springer Handbook of Lasers and Optics*, 2nd ed. Berlin Heidelberg: Springer-Verlag, 2012. doi: 10.1007/978-3-642-19409-2.

[47] M. J. Weber, *CRC Handbook of Laser Science and Technology: Optical Materials/Part I: Nonlinear Optical Properties/Radiation Damage (CRC handbook of laser science and technology)*. Crc Pr I Llc, 1986.

Chapter 3

Laser and optical materials properties

This chapter provides a general understanding of the interaction of ultrashort laser pulses (i.e., femtosecond pulses) with the glass materials. After a brief history of laser typologies, the second section will explain laser-matter interaction before introducing the key optical properties associated with laser processing in the glass. The third section will focus on the choice of near-IR femtosecond laser and its advantages relative to other lasers. Optical properties and second-order non-linear effects will be described in the last section. Second Harmonic Generation (SHG) will be a specific focus as it is the most relevant non-linear property studied in this Ph.D. work.

3.1 Laser: brief history and typology

3.1.1 Basics and brief history of laser typologies

This In nature, all things promote their lowest energy state. The laser does not work in this way. This particularity will be explained in this section and used to define its working principle. Laser (*light amplification by stimulated emission of radiation*) was pronounced for the first time by G. Gould in 1957 [1]. In the beginning, it was only a "solution looking for a problem," but after, it turned out to be promising for the development of civilization in the optical field. Three main

properties characterize it: laser beam linewidth, coherence, and laser power, visible in the following Figure 18:

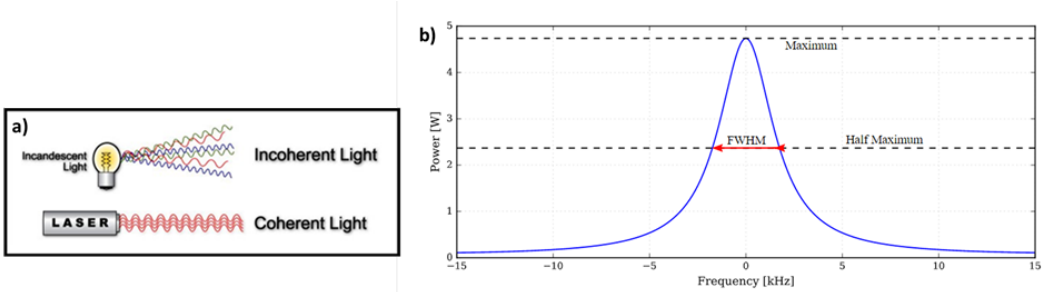

Figure 18: Principal laser properties: a) coherence [2]; b) representation of linewidth by Full Width at Half Maximum (FWHM) in a plot of frequency in function of power [3]

A laser is characterized by a high monochromaticity, a possibility of beam collimation by a small spot size, and a wide tuning wavelength range. Another peculiar parameter is the fluence corresponding to the laser pulse energy (J) divided by the effective focal spot area (cm^2). The line width of a laser is the width of its optical spectrum and is typically defined as the Full Width ay Half Maximum (FWHM). It could be defined as the width of the power spectral density of the emitted field in terms of frequency, wavelength, or wavenumber.

These unique properties allow its use in a variety of applications as photonics, optics, electronics, medical surgery, telecommunication, and display screens. If the elements implicated in the word *Laser* are analyzed distinctively, it could be easy to understand its working principle. “La” (light amplification) is to define which process is it, “se” (stimulated emission) indicates how this process is done, and “r” (radiation) explains what is used for this process [2]. More precisely, three electron-photon interaction processes can occur inside the laser: absorption, spontaneous emission, and stimulated emission, as reported in Figure 19.

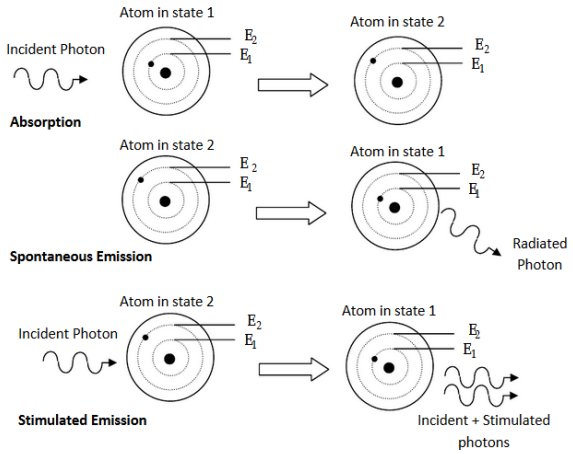

Figure 19: The three electron-photon interaction processes in atoms occurring in the laser: absorption, spontaneous emission, and stimulated emission [2]

The laser works through a population inversion. The term "inversion," that is present in the guiding principle in making lasers indicates a condition not verified in normal conditions (equilibrium Boltzmann distribution, in Figure 20a) when the population in the lower energy state is higher than the excited states one. In the population inversion, the number of excited atoms is higher than the one of atoms in the ground state, as shown in Figure 20b.

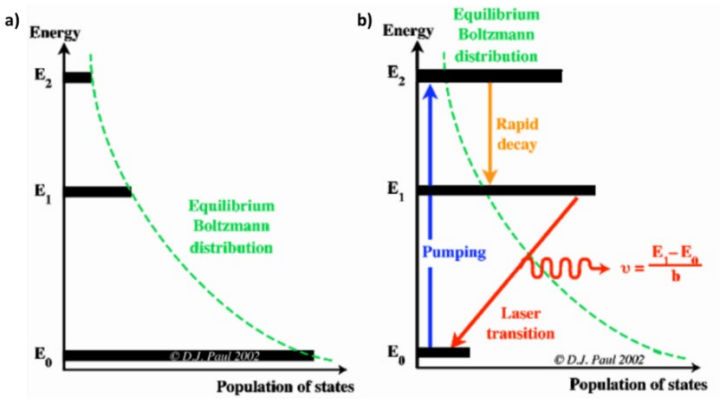

Figure 20: Representation of a) Equilibrium Boltzmann distribution and b) population inversion after pumping that constitutes the guiding principle in lasers [4]

This allows amplifying the light by optical pumping. When an electromagnetic wave enters an inverted medium, one of the incoming photons is amplified, producing two coherent photons. They have the same energy, same direction of propagation, and same polarization state. The associated wave shows the same phase of the incoming photon. This process is called stimulated emission. It was

introduced by Albert Einstein in 1917 [5]. Light Amplification is reached when photons are subject to multiple passes through the laser active medium, and then population inversion is established. It is regulated by the following equation (13):

$$\frac{dI(z)}{dz} = \sigma_{21} \Delta N I(z) \qquad (13)$$

where the intensity variation dI along z is influenced by σ_{21}, the stimulated emission cross-section of the transition, valid in conditions of population inversion expressed by $\Delta N = (N_2 - N_1)$. The essential components of a laser system, indicated in Figure 21a, are:

1. *Gain medium*: active laser medium produced by stimulated emission. There was a system of three or four-level laser (Figure 21b) to generate a population inversion
2. *Pumping source*: a continuous external energy supply that allows population inversion to be achieved, such as flash tube/laser diode (optical pumping), chemical reaction, or electric current.
3. *Optical resonator*: an optical cavity in which light circulates created by two parallel mirrors: one *total reflector* (see in Figure 21a component 3) and the other *partial reflector* (see in Figure 21a component 4, output coupler).

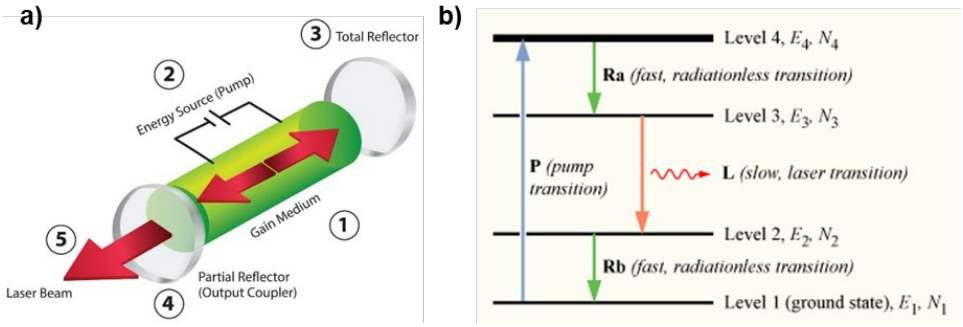

Figure 21: a) Principal laser components (https://www.ulsinc.com/learn); b) Four-level laser system (https://it.wikipedia.org/wiki/population inversion)

Typically, electrons pumping is the starting point. Then, the laser goes to an excited state. This process continues for a short time, precisely a few hundred nanoseconds, and it is sufficient to achieve a gain higher than a threshold value quickly. Then, photons are trapped in the resonant cavity and exponentially increase in these conditions. The number of photons does not grow indefinitely. The same thing is also valid for the stimulated emission rate because population inversion decreases

as photons power supply and the gain have the same extent. There will be a moment when the gain will be equal to the lasing threshold value. Then, it is said that the gain saturates the threshold value, and this proves that lasing process is self-limiting, as illustrated by Figure 22. Saturation is a phenomenon that readily occurs in ultra-short pulses: it is necessary to know how to treat it or delay its appearance.

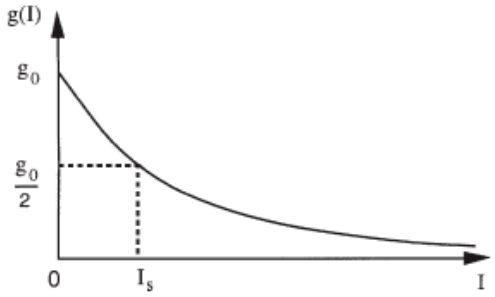

Figure 22: Exponential relation between gain and intensity, highlighting the specific value in saturation mode [5]

Therefore, a laser is an amplifier, a resonant optical cavity, and an oscillator. It is a way to confine the radiation. The complete lasing process is described clearly in the following Figure 23 [6]:

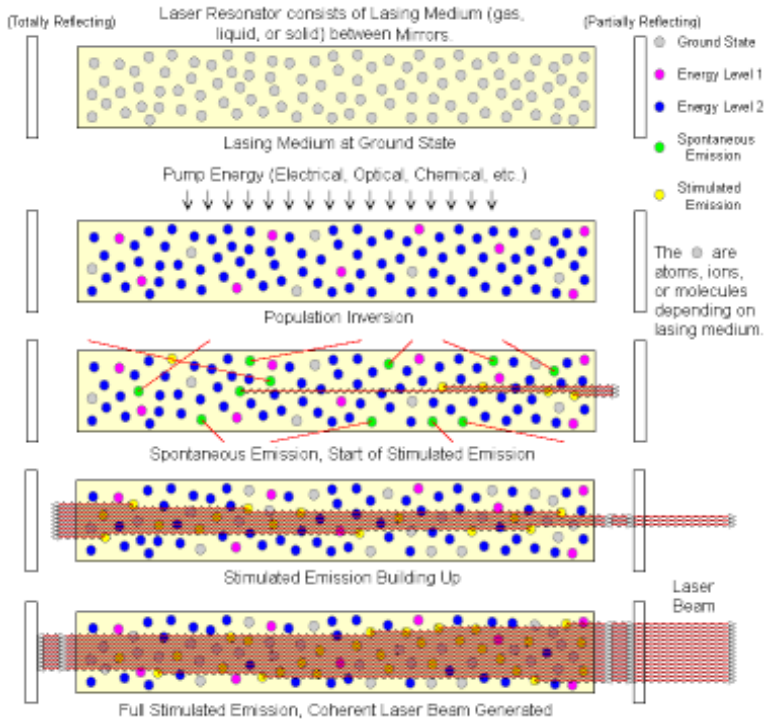

Figure 23: Schematic diagram of laser basic working principle (https://sites.google.com/site/puenggphysics/home/unit-i/basic-of-laser-action)

In 1960, T. H. Maiman fabricated the first laser using a ruby crystal pumped by a xenon flash lamp, reported in Figure 24 [7].

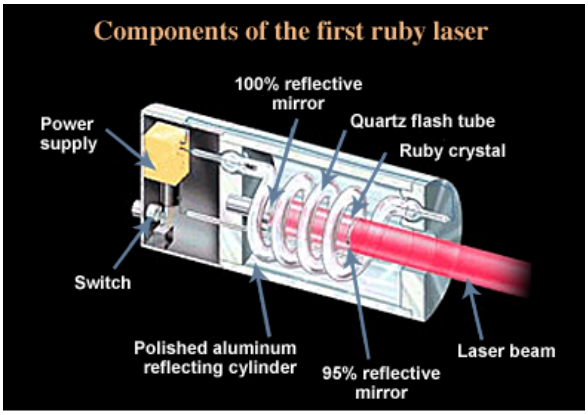

Figure 24: Scheme of components of the first ruby laser
(Theodore Maiman Invents the First Working Laser: History of Information)

However, the beam quality and the reproducibility of the laser were not performative. Since then, various new types of lasers have been invented, and laser performance was improved. So far, high laser energy has been achieved in a long pulse laser system. Decreasing the laser pulse duration results in a large laser peak power. In addition, by reducing the laser wavelength, higher energy photons can be produced (e.g., X-ray laser). In particular, the ultra-short pulses open a new way of laser material processing (e.g., in 3D and with a lateral spatial resolution below the diffraction limit).

3.1.2 Ultra-fast laser

This The attention towards optical pulses in the picosecond range (ps, 1 ps = 10^{-12} s) and femtosecond led to the dedicated use of ultra-fast lasers. Nowadays, new frontiers are opened in the field of ultra-fast laser-atom interaction, with pulse duration as short as 10^{-18} s, called attosecond (at). Attosecond physics is the one of electrons in motion at atomic and molecular length scales [8]. The physics of this very short pulse is based on non-linear and nonperturbative laser-atom interaction [9].

Mode locking is a way to obtain these short laser pulses on the order of picoseconds (10^{-12} s) or femtoseconds (10^{-15} s) [10]. Ultra-short pulse duration, high pulse repetition rate, broad spectrum, and high peak intensity are the typical main characteristics of ultrafast lasers. Amplification of ns pulse or longer one can be achieved without damaging the laser amplifier, but if the intensity is higher than non-linear effects (e.g., self-focusing). Chirped pulse amplification (CPA) is a technique, as illustrated in Figure 25a, to amplify ultra-fast high-power lasers to high energy levels (> 10^{20} W/cm^2) [11], [12]. Lowering the peak power during amplification is the task of CPA by temporally stretching the pulses (i.e., laser pulse duration varies from about 100 fs to several ns). Another advantage of the CPA technique is the miniaturization of the laser system in a compact high-power one. The laser setup for the generation of a CPA is reported in the following Figure 25b. In our case, mode locking was done with a SESAM mirror as oscillator [13].

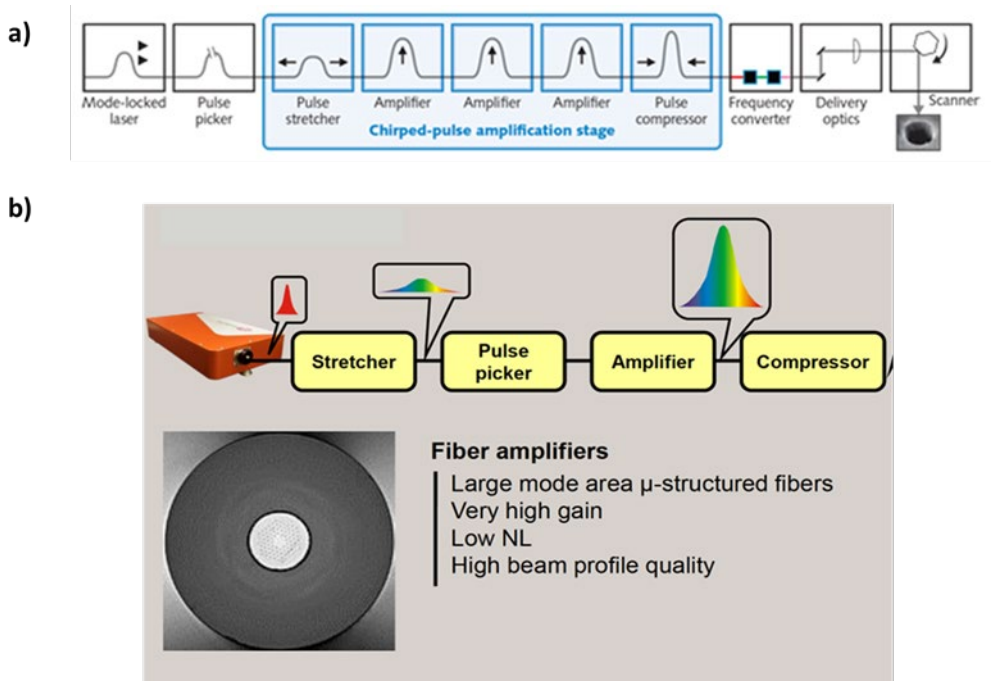

Figure 25: a) CPA Scheme [14]; b) our CPA configuration in which the chirp is illustrated with colours and the signal is treated by a fiber amplifier.

3.1.3 Gaussian beam

Before describing pulsed lasers, it is preliminary to explore how a continuous wave (CW) Gaussian beam propagates along z-direction (z = 0 taken as the focal point of the focused laser) according to the scheme shown in Figure 26.

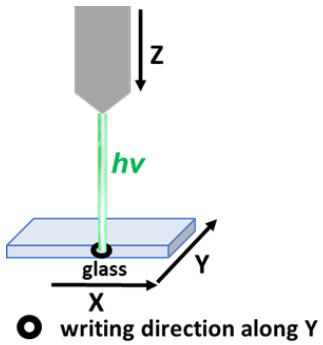

Figure 26: Irradiation scheme of laser in the XY plane of a glass sample

The concept of embedded Gaussian is useful as a construct to assist with both laboratory measurements and theoretical modeling. The fundamental Gaussian beam (exactly order TEM_{00} mode) is given by [14]:

$$E(r,z) = E_{00}\frac{\omega_0}{\omega(z)}\cdot exp\left[\frac{-r^2}{\omega^2(z)}\right]\cdot exp\left[-i\,\frac{kr^2}{2r(z)}\right]\cdot\{-i[kz - \Phi(z)]\} \quad (14)$$

$$\varphi(z) = arctan\,(z/z_R) \quad (15)$$

$$R(z) = z\left[1 + \sqrt{1 + (z_R/z)^2}\right] \quad (16)$$

$$\omega(z)=\omega_0\sqrt{1 + (z/z_R)^2} \quad (17)$$

$$z_R = \pi\omega_0^2/\lambda \quad (18)$$

$$\theta = \lambda/\pi\omega_0 \quad (19)$$

$$I(r,z) = \frac{\varepsilon_0 cn}{2}\cdot E(r,z)\cdot E(r,z)^* = I_{00}\left(\frac{\omega_0}{\omega(z)}\right)^2 exp\left(\frac{-2r^2}{\omega^2(z)}\right) \quad (20)$$

$$I_{00} = \frac{\varepsilon_0 cn}{2}E_{00}^2 \quad (21)$$

where the beam has circular symmetry, r is the radial distance from the beam center axis, z is the axial distance from the "*beam waist*", E_{00} is the amplitude of the electric field at the origin, $\omega_0 = \omega(0)$ is the "*beam waist*" at the focus, i.e., the radial size at the narrowest point, $\omega(z)$ is the radium of the beam at distance z from the waist, $R(z)$ is the radius of curvature, k is the wavenumber, $\varphi(z)$ is the Gouy phase shift, z_R is Rayleigh length, λ is the laser wavelength, and θ is the beam spreading angle, or divergence (with units or radians).

In Figure 27 [15], the spot size is $\sqrt{2}\omega_0$, at z_R, the *1/e* position of electric field and the center intensity are reduced to half the maximum value. z_R is a variable to show how far the beam is collimated. When z is far from the beam waist, the relationship between $\omega(z)$ and z becomes linear:

$$\omega(z) \approx \omega_0 \left(\frac{z}{z_R}\right) \tag{22}$$

When $\omega \rightarrow \omega_0$, $R \rightarrow \infty$, and $\theta \rightarrow 0$ is the case of a perfectly collimated beam with no diffraction effect; when $\theta \rightarrow constant$ and $\omega \rightarrow \theta_z$, $R \rightarrow z$, is a geometrical beam spreading from a point source. The Rayleigh range has the relationship with the numerical aperture (NA) like:

$$z_R = \frac{\omega_0}{NA} \tag{23}$$

$$\omega_0 = \frac{\lambda}{\pi NA} \tag{24}$$

$$NA = n \cdot sin\alpha \tag{25}$$

and it is a parameter to measure the ability to collect light. Then, the focusing lens or the microscope objective can influence the beam focal spot size, shape, and energy redistributions.

Figure 27c shows that the actual beam waist (ω_{OR}) is M times larger than the Gaussian beam (ω_0), and the real beam divergence (θ_R) is M larger than the one of the Gaussian one (θ). They have the same radius of curvature and Rayleigh length. The beam waist radius and the far-field divergence are constant as the beam propagates through an optical system. The ratio of the beam parameter production of the real beam one to a Gaussian beam one is given by:

$$M^2 = \frac{\omega_0 \theta_R}{\omega_0 \theta} = \frac{\pi \omega_{OR} \theta_R}{\lambda} \tag{26}$$

Here M^2 (or beam quality factor) is dimensionless and can be used to define the degree of variation from an ideal Gaussian beam, $M^2 = 1$, and for real beam, $M^2 > 1$. M^2 increases with the increasing output power. For a high-power laser system, the by-product of lasing in solid-state media (i.e., heat) has a significant effect on laser performance. The wave-front distortion occurs due to the thermal lensing effect. In fact, due to the focusing mode of laser beam, together with non-linear effects (i.e., self-focusing), the precise measuring of spot size and energy density inside the glass is difficult or even impossible. For the laser of this work, M^2 is less than 1.2. The laser is working in TEM_{00} mode and generating an appropriate Gaussian beam.

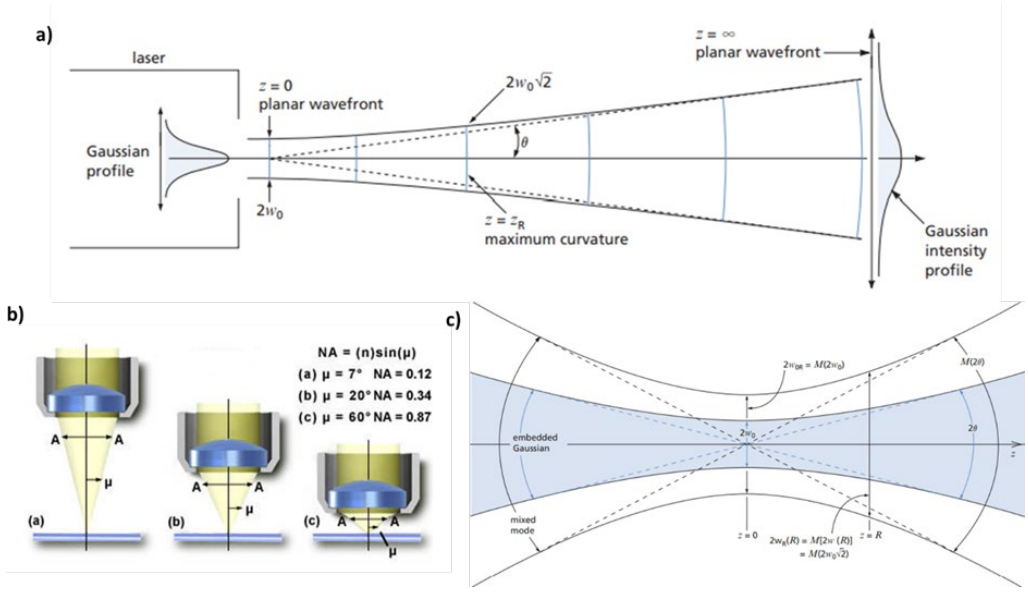

Figure 27: Gaussian beam: a) change in wavefront radius with propagation distance [15], b) the definition of numerical aperture [16], and c) the embedded Gaussian [15]

3.1.4 Spherical aberration

Parallel light rays focused on a single point can obtain a perfect beam, but the spherical surface of a lens can induce spherical aberration. In short, the light rays pass through the central part of the focus further than those passing through the lens's edges, leading to many focal points along the propagation direction. Further, the rays from the lens center are, the larger the error is. In this thesis, an aspheric lens is used to minimize spherical aberration.

However, spherical aberration may also be caused by a refractive index mismatch, e.g., at the air-silica interface [17]. Figure 28 represents the central region of light focused shallower than the adjacent one. This interface spherical aberration elongates the focal spot along the laser propagation direction. The focal displacement (δ) is equal to:

$$\delta = |OF_0|\left(\sqrt{\frac{n^2-NA^2}{1-NA^2}} - n\right) \tag{27}$$

$$NA = n_0 \sin\theta \tag{28}$$

where F_0 is the geometrical focus in air, F_1 is the focus point under paraxial approximation for the ray 1, (F_2 is the same for the ray 2), F_3 is the focus of the

marginal rays (i.e., ray 3), *O* is the crossing point of the light axis and the interface, *n* is the sample refractive index, and n_0 is imaging medium refractive index between the objective front lens and the sample, which is equal to $sin\theta$ here (θ is in degree). The focusing depth in this sample is defined as $d = nlOF_0l$.

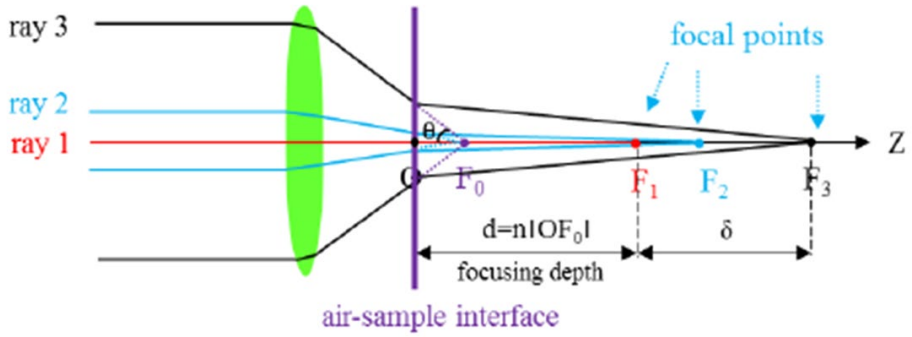

Figure 28: Interface spherical aberration scheme due to the refractive index mismatch along laser propagation direction [18]

Spherical aberration affects the light intensity distribution along the laser propagation direction. At high laser power, an extensive plasma channel along the laser incident direction can be observed, and the length of this channel increases with the focused depth [18]. The electric field distribution in material for the paraxial distribution is given in [19], [20]. Spherical aberration influences the threshold pulse energy for fs laser-induced modification as a function of the focusing depth [17].

3.1.5 Light scattering

Scattering is a phenomenon in which a wave of a specific wavelength λ when it encounters and interacts with the matter, it undergoes a deviation from its straight direction. Scattering is of two typologies: the elastic one in which the wave energy is preserved before and after the interaction, and the inelastic one where the wave energy is changed. Both Mie and Rayleigh are elastic scattering. Elastic Mie scattering occurs when the size of the particle radius is close to or larger than λ, and most of the incident light scatters in the forward direction. Rayleigh scattering is for particles much smaller than λ (i.e., $< \lambda/10$). The scattered light in the forward and backward directions is the same. The direction perpendicular to the incident light has the lowest degree angle.

In particular, for glass-ceramic materials, the amount of scattered light depends on the refractive index difference of the two phases (i.e., $\Delta n = n_2 - n_1$) and the size and

distribution of crystals in the glass [21]. Regarding the materials used in the experiments of this thesis work, the refractive index difference is an important parameter to consider if we intend to precipitate nanocrystals in a glass. Then, for $LiNbO_3$ embedded in amorphous phases (i.e., SiO_2), there is a refractive index difference between glass and crystal, respectively ~ 2.3 and ~ 1.45. The size of crystals has to be much smaller than λ, to maintain the low scattering loss and to obtain transparent devices, precisely the crystalline size below $\lambda/10$ to maintain the transparency of composite materials.

3.2 Laser-matter interaction

Non-linear effects characterize ultrafast laser-matter interaction. The short pulse duration and high peak power sufficient to induce direct bond breaking are some of the interesting and valuable fs-laser typical properties, the excitation is an adiabatic process, and many dielectric media are transparent to the laser wavelength in 400 – 2000 nm spectral window [22]. In this section, the non-linear absorption, as multiphoton and tunneling ionization, others several non-linear optical effects, and the micro-machining in transparent materials are presented before introducing the direct femtosecond laser writing in the next section.

3.2.1 Free electron formation

Transparent materials in the visible to the near-infrared window have a wide-bandgap (E_g), that is the energy to reach the delocalized states because the incident photon energy is smaller than material bandgap energy indicated in symbols as follows, $h\nu_0 < E_g$. Fused silica has E_g = 9 eV, where 1 eV = 1.60 10^{-19} J. A laser beam with wavelength equal to 1030 nm (i.e., $h\nu_0$ = 1.2 eV < 9 eV) cannot be absorbed in the linear interaction regime [23]. At high-intensity laser radiation, it is possible to promote electrons to higher energy states by non-linear absorption, through the two following different approaches, reported in Figure 29:

1) Multiphoton ionization (MPI) occurs mainly at short wavelength and low electric field, precisely when $mh\nu > E_g$, where m is the number of absorption photons (Figure 29a). At least eight photons, for example, at λ of 1030 nm, are needed to promote an electron from the valence band (VB) to conduction band (CB) in fused silica. The density of electrons (ρ_e) in the CB depends strongly on the laser intensity (I) and is given by:

$$\left(\frac{d\rho_e}{dt}\right)_{MPI} = \delta_m I^m \qquad (29)$$

t is the time, and δ_m is the multiphoton absorption coefficient for m-photon absorption [24].

1) Tunneling ionization occurs mainly at long wavelength and strong electric field (Figure 29c): the material's band gap is distorted due to the application of an intense laser electric field. The potential barrier between the CB and VB is reduced. Then, electrons can escape from their bound states by direct band transitions. Unlike MPI, ionization in strong fields occurs very quickly: the electron escapes at a time much shorter than the laser period [25]. The transition between the above two different ionization regimes is described by the Keldysh parameter γ equals to:

$$\gamma = \frac{\omega}{\omega_t} = \frac{\omega}{e}\sqrt{\frac{mcn\varepsilon_0 E_g}{I}} \qquad (30)$$

ω is the laser frequency, ω_t is the frequency of electron tunneling through a potential barrier, m is the electron mass, and n is the refractive index of the material [24].

The discriminating value of the Keldysh parameter is ~1.5 (see Figure 29b), and it indicates the combination of two processes. When $\gamma >> 1.5$, MPI dominates; for $\gamma << 1.5$, tunneling prevails [24]. The MPI is dominating for fused silica (Eg = 9 eV). The E_g of $LiNbO_3$ is 3.7 eV: compared with fused silica, the tunneling effect increases.

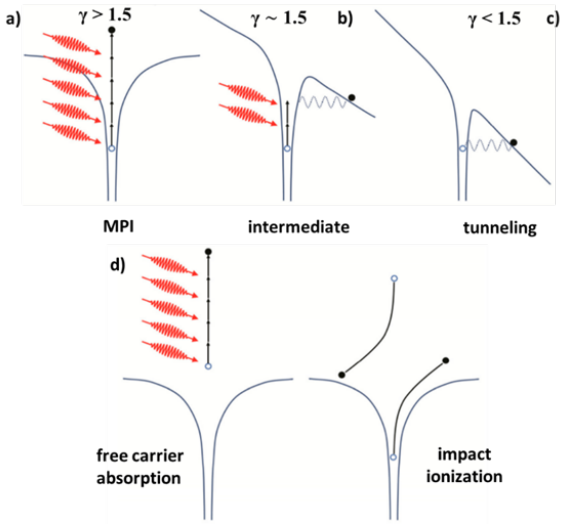

Figure 29: Schematic diagram of the photoionization of an electron in an atomic potential for different values of the Keldysh parameter (γ). In a solid, the electron is promoted from

the valence band to the conduction band rather than ionized: a) multiphoton ionization, c) tunneling ionization, b) the above processes combined, and d) avalanche ionization: free carrier absorption followed by impact ionization [24].

Different photoionization regimes according to photo energy and laser intensity are illustrated in Figure 30 [26].

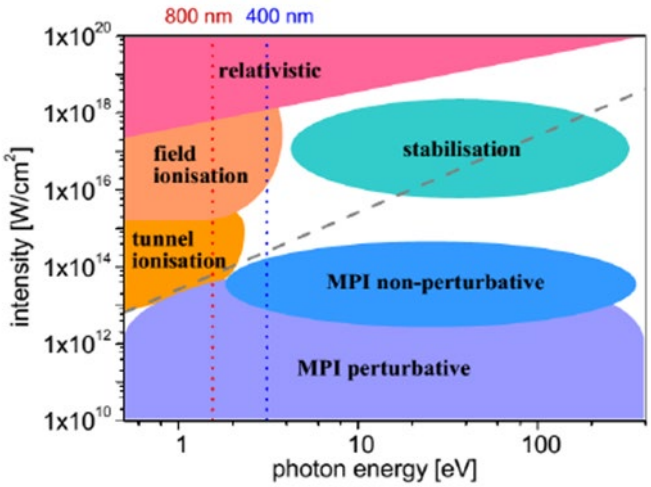

Figure 30: Different photoionization regimes with varying photon energy and laser intensity. The dashed grey line shows the case of $\gamma = 1.5$ for C_{60} ionization, which separates the multiphoton regime ($\gamma > 1.5$) from the tunneling regime ($\gamma << 1.5$) [26]

In addition to direct excitations of electrons by laser electric field, avalanche ionization affects the energy deposition process from light to material. Seeded excited electrons have been promoted to the CB by MPI or tunneling ionization, or the intrinsic defects can be easily ionized by a process like thermal excitation [24]. These electrons can absorb photons linearly. Their energy increases until a value larger than the CB (i.e., free-carrier absorption). This electron with enough energy ($2E_g$) can ionize electrons in the VB (i.e., impact ionization), leading to two electrons at the minimum of the CB. This process, linearly dependent on laser intensity (I), happens only if the laser electric field is present. The density of electrons in the CB due to this process grows according to the following relation:

$$\left(\frac{d\rho_e}{dt}\right)_{avalanche} = \alpha I \rho_e \qquad (31)$$

where α is the avalanche ionization coefficient. According to MPI, the material E_g affects the energy required to span the bang gap. However, the optical breakdown threshold is nearly not dependent on the E_g and the threshold intensity, increasing

by only about a factor 2 [27]. This is mainly related to the avalanche photon-ionization, which is linearly dependent on the laser intensity. Non-linear absorption may affect the absorption of ultrashort pulses by the glass [28]. The absorption increases with an increase of pulse energy, which can be explained by a photoionization rate increase with the increase of laser intensity. A higher repetition rate is vital for enhancing the absorption of sub-ps pulses.

3.2.2 Relaxation of photo-excited electrons

Interpreting the mechanism of the fs laser-induced modifications in dielectrics is still an open question. The excited electron-ion plasma is produced at the focal volume by fs-laser during excitation, and the subsequent dissipation of the energy into the lattice leads to various modifications as refractive index variations. The material continues to undergo changes in µs, although the light absorption occurs at fs timescale [27]. Figure 31a represents the process of the interaction between fs laser and dielectrics, while Figure 31b shows the timescale of the relevant physical phenomena associated with fs laser interaction with transparent materials.

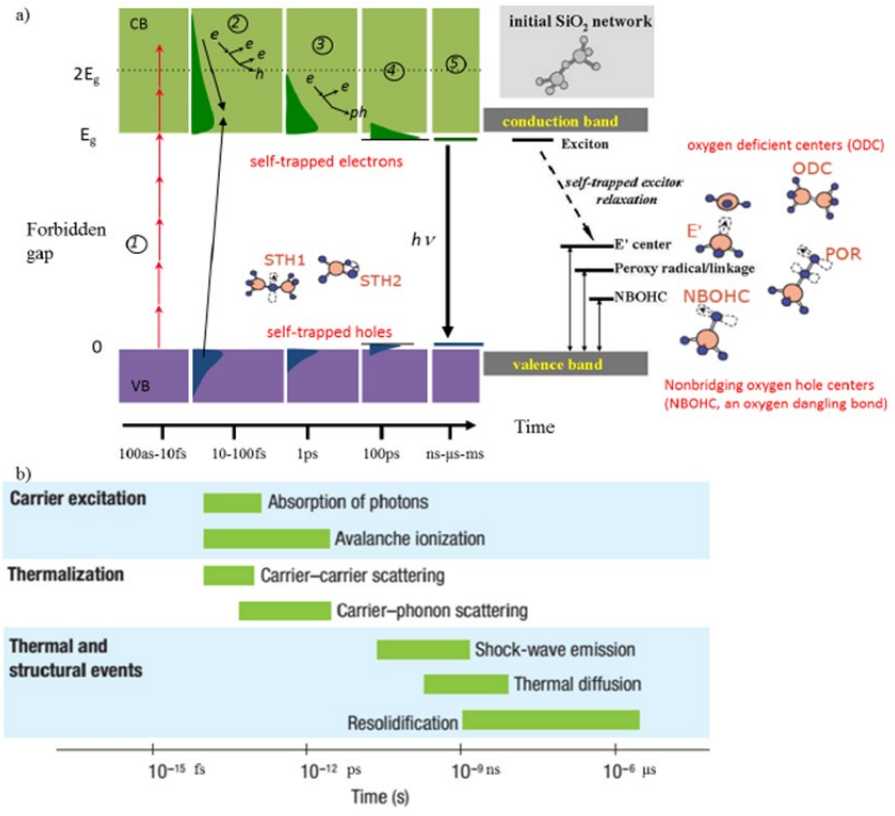

Figure 31: a) Schematic representation of the dynamics of fs laser interactions with dielectrics. The numbers from 1 to 5 correspond to the process as described within the text

(after S. Guizard, LSI, CEA, Saclay France and [29]), b) timescale of the physical phenomena associated with the interaction of a fs laser pulse with transparent material [27]

The following main phenomena can be noted from the scheme reported in Figure 31.

1) Laser absorption produces free-electron plasma in the CB and holes in the VB.
2) The formed plasma is then heated by laser electromagnetic field through free carrier absorption, or the electron density grows through avalanche ionization until the plasma frequency in according to this following relation to reach the light frequency:

$$\sqrt{\frac{\rho_e e^2}{4\pi^2 \varepsilon_0 m}}$$

The energy distributed by the excited electrons to other electrons (i.e., carrier-carrier scattering) within a timescale of 10-100 ps results in the energy redistribution between the excited carriers. The fs-laser irradiation creates electron-hole pairs.

3) The electron plasma relaxes by coupling with the lattice (lattice heating). The ultra-short laser pulses can transfer from the laser-excited electrons to the lattice after the laser pulse is completed [28]. Around tens of ps is the timescale for the electron energy transfers to the lattice. In that case, the laser pulse duration (τ) has an important effect on the material modifications. When τ is simultaneous, the laser energy can be deposited to the lattice during irradiation (i.e., carrier-photon scattering). The excited phonons can transfer the energy to the non-irradiated part by thermal diffusion. If the temperature in the affected area is high enough, permanent damages occur.

   Typically, the damage threshold observed for the surface of the material (e.g., fused silica) is proportional to $\tau^{0.5}$ when $\tau > 10\ ps$, indicating the transfer of electron kinetic energy to the lattice and diffuse during the laser pulse. In addition, short pulse ($\tau < 10\ ps$) damage can be confined into a small zone (i.e., at the peak of the Gaussian beam), where the laser intensity is sufficient to produce MPI. Because there is insufficient time for lattice coupling, less collateral damage occurs, and the damaged region is much smaller with ultrashort pulses than with long pulses [30].
4) Exciton is a bound state of an electron and an electron-hole, attracted by the electrostatic Coulomb force. It is an electrically neutral quasi-particle

existing in semiconductors. Self-trapped excitons (STEs) can be formed within a few ps. In glasses or in crystals, excitons interact with phonons, the lattice vibrations. A photon with energy near E_g can be absorbed, creating a loosely bound Wannier-Mott exciton in the network [31]. Self-trapping results in dressing excitons with a dense cloud of virtual phonons which strongly suppresses the ability of excitons to move across the lattice [32]. This means a local deformation of the crystal lattice around the exciton. It should be of an atomic scale, of about an eV below the CB.

5) Then STEs annihilate and energy relaxation as light or to the lattice again or produce point defects and structural modifications. The exciton could either recombine or drop to a slightly lower energy state, named STE, or combine non-radiatively back into the ground state by a phonon-assisted process. This STE occurs in the network structure as a point defect pair [33]. Excited electrons and holes relax into STE by electron-phonon coupling at the time scale of 100 fs. Decay of STE can be achieved by radiative recombination with photon emission with a lifetime of ns at room temperature or a non-radiative way by coupling with lattice phonons or transforming into point defects [34].

The time for heat diffusion is 1 μs, at a certain high repetition rate (ca. > 100 kHz), the thermal accumulation occurs. In that case, the pulse energy of the fs laser could be deposited at the focal point inside transparent materials, causing a thermal accumulation effect, and the heat-affected zones were minimized. In comparison with typical 3D material processing techniques (e.g., photolithography), fs laser micro-machining is a rapid, flexible, and clean fabrication, without using toxic photo resist comparing with photolithography. By this means, high precision sub-micrometer resolution spatial controlled modifications in 3D in bulk material are realized.

3.2.3 Femtosecond laser-induced defects

Silica has SiO_4 tetrahedron as its structural unit, in which the Si atom is bonded to four O atoms with an O – Si – O angle of 109.5°. The formation of the defects starts from the relaxation of self-trapped excitons, E' center (oxygen vacancies with a trapped hole or 3-fold-coordinated silicon), and nonbridging oxygen hole center (NBOHC, a dangling oxygen bond). By adding an interstitial O atom to NBOHC, peroxy radical (POR) can be created, as shown in Figure 31. E'-center, POR, and NBOHC are three fundamental centers that can be detected by electron spin resonance. Self-trapped holes (STH)1 would be a small polaron consisting of a hole trapped at a normal bridging oxygen, and the STH2 might be an Anderson localized state where a hole is trapped on two normal oxygens [35].

Laser irradiation can create defects (i.e., oxygen vacancy defect), leading to the sample's photoluminescence (PL). Intrinsic defect PL was firstly observed in an annealed and neutron-irradiated amorphous a-SiO_2 [36]. Since then, many investigations have been reported to determine the origins and structure of defects in different types of silica [37]. Gee et al. [38] demonstrated that PL centers are unique bonding configurations that mainly depend on the material chemistry rather than the degree of long-range order.
It is worth noting that oriented silicon oxygen-deficient center, SiODC(II) defects, have been created in silica by IR fs-laser irradiation, especially within Type II regime [39]. The IR photon energy is below the E_g of the material, but the induced defects are like those observed for UV irradiation. This indicates that the multi-photonic nature of the mechanism leads to the creation of defects by IR fs laser. In addition, these laser-induced defects can decrease the damage threshold of silica [32] by creating defect levels in the gap. Those are easier to ionize changing incubation period for collective transformation.

3.3 Femtosecond Laser Direct Writing (FLDW)

After a brief history focused on a femtosecond laser, this part aims to motivate the choice of this typology of laser for my experiments.

3.3.1 Femtosecond laser for glass-ceramics fabrication: working principle and setup

In Figure 32, there is a representation of the advantages and disadvantages of picosecond and femtosecond lasers.

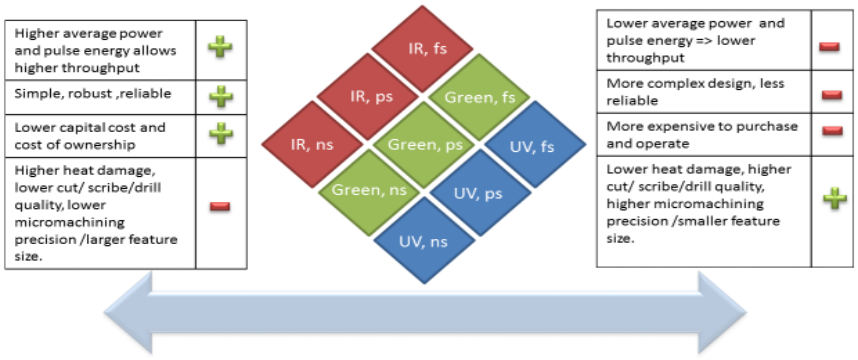

Figure 32: Ultrafast picosecond and femtosecond fiber lasers | IPG Photonics

The first example of 3D glass modification with fs-laser dates back to 1996. Davis et al. [40] presented the fabrication of waveguides inside silica, Ge-doped silica, borate, soda-lime silicate, and fluorozirconate bulk glasses by tightly focused fs laser (810 nm, 120 fs, 200 kHz). This is the starting point of fs laser micromachining in optics [27].

The 3D fabrication setup is shown in Figure 33 below. The laser beam was focused by a microscope objective and injected into the glass, fixed in an XYZ stage, translated at a certain speed, either perpendicular or parallel to the incident laser beam, thus fabricating writing lines inside the glass. Focusing the laser beam on the near glass surface, glass modifications, most likely due to thermal shock, occur at high laser powers related to damage thresholds [40]. The modification in glass is related to the damage threshold at certain irradiation conditions. Focusing on the interior of the glass, no cracking was detected in any of the glasses regardless of laser power (average power of the laser between 40 and 800 mW at the glass location).

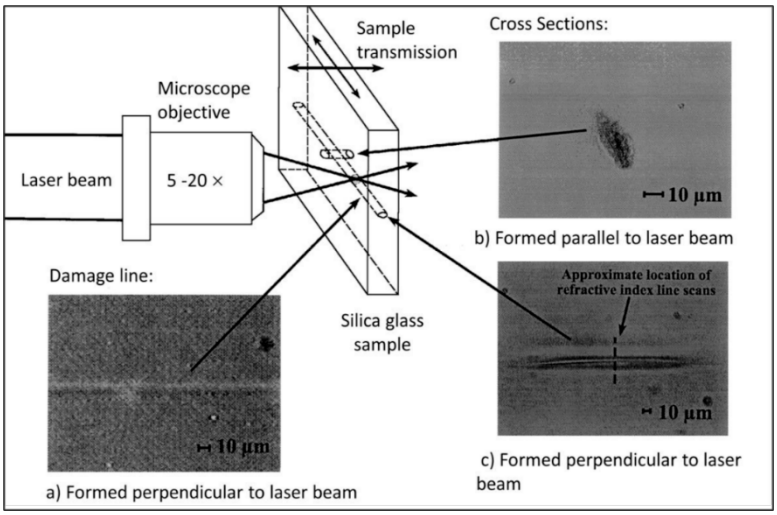

Figure 33: fs laser fabrication in 3D: a) a laser damage line, b) the cross-section of a line written by moving the sample parallel to the incident laser beam, and c) the cross-section of a line written by moving the sample perpendicular to the incident laser beam [40].

3.3.2 Femtosecond laser-induced structural changes in glasses

By studying the following seven laser parameters and how they are interlinked, taking into account also laser wavelength and the focal depth on the sample, it is possible to discover and demonstrate how crystallization, induced by femtosecond laser irradiation, changes glass nanostructure and optical properties [41]:

1. *pulse energy*
2. *the numerical aperture of the objective and focusing depth*
3. *duration of the pulse*
4. *pulse repetition rate*
5. *laser wavelength*
6. *scanning speed (and thus the cumulated number of pulses)*
7. *writing configuration (i.e., polarization orientation with respect to the scanning direction)*

At high pulse energy, multiphoton absorption is the primary cause of energy transfer to the glass. Interband transitions in transparent materials correspond to a linear absorption in the wavelength of the focusing laser beam. All the laser parameters affect the shape of interaction volume. The light intensity distribution in this volume changes, influencing the energy threshold. Precisely, multiphoton ionization (MPI) occurs as an electron-hole pair formation. The non-zero free electron density increases the kinetic energy of electron plasma. Increasing beam energy, optical and physical processes, focusing strength, and numerical aperture (NA) are interconnected by balancing the non-linear increase of the refractive index and the defocusing effect of electron plasma.

When relaxation of photo-excited electrons takes place, glass modifications occur, showing the following possible effects on the materials reported in Figure 34. Firstly, electron-phonon coupling, as an interaction between light and glass networks, represents self-trapped excitons (STE). Then, electrons annihilate radiatively in the lifetime of nanoseconds at room temperature. They could transform into point defects called in silica case SiE' and NBOHC (bond breaking) and after into a silicon oxygen-deficient center quoted as SiODC (II). Therefore, the electron energy transmitted to the lattice by the non-radiative coupling of electrons generates an increase in the lattice's nonequilibrium temperature. Suppose this increase in temperature is longer than the glass relaxation time. In that case, glass modification will occur, and it could be possible to create permanent densification or volume expansion accompanied by the formation of a stress field.

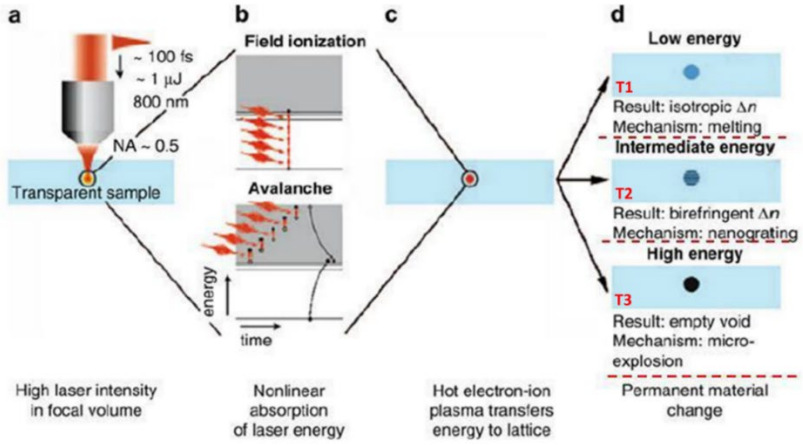

Figure 34: Scheme of a fs laser beam focused in bulk fused silica: a) fs laser focused below the sample surface resulting in high intensity in the focal volume, b) energy nonlinearly absorbed and free-electron plasma created by multiphoton/tunneling and avalanche photoionization, c) hot-electron plasma formed transfers energy to silica lattice on ~10 ps time scale resulting in one of three types of a permanent modification, and d) fs laser-induced various modifications in glass as a function of pulse energy: here it is possible to distinguish the three threshold regimes T1, T2, and T3 in correspondence of the phenomena generated [42].

No crystals usually formed at a low repetition rate, as shown in Figure 34. Depending on the pulse energy delivered to the sample, four regimes with three thresholds can be defined in fused silica with the increase of pulse energy [43]. To analyze these regimes deeply, Figure 35 is reported when increasing the pulse duration [41].

- **T1** is the first threshold related to isotropic refractive index change generation without apparent structure damage. The contrast of the refractive index change can be either positive or negative depending on the materials, for silica glass also can be positive or negative [25]. The refractive index change can reach the maximum at 6 x 10^{-3} in fused silica, which is larger than the one induced by UV ns laser [39]. This modification can be annealed by heating the sample within 600-800°C [44]. The energy operating window for T1 is narrow, which increases in size at the shortest pulse duration [45]. This modification can be used to fabricate low-loss optical waveguides [38]. Poumellec et al. proposed that this modification can be explained by a fictive temperature (T_f) increase [34], [41]. Glass modifications are due to the relaxation of STE. The temperature increases during a time long enough to change the average disorder (i.e., a change of T_f) [46] and thus specific volume changes (densification or expansion). The non-radiative relaxation of excited electrons by coupling with the lattice corresponds to an increase of nonequilibrium temperature (several

thousand degrees in the illuminated zone) just limited by thermal conduction [34].

- **T2** is the second threshold related to the generation of form birefringence. The fs laser-induced birefringence can be explained by both stress [47] and form birefringence due to self-organized periodic nanostructures formation (i.e., nanogratings), oriented perpendicular to laser polarization direction [48]. This modification has applications such as polarization converters, microfluidic, and nanofluidic channels [49]. Typically there is an anisotropic index variation; its magnitude can reach as large as 10^{-2} [50]. Lancry et al. [51] showed that the index contrast is because the nanoplanes are nanoporous, produced by a glass decomposition leading to the generation of molecular oxygen. In addition, these nanostructures show extraordinary thermal stability [52].
- **T3** is the third threshold related to the formation of the voids (disruptive modification). A void surrounded by a high refractive index crust occurs at high pulse energy. This phenomenon is due to the Coulomb repulsion between the ions, generating pressures higher than the material's Young's modulus. A shockwave results in a less dense or hollow core in the focal volume. This modification has potential applications in 3D optical storage [53] and photonic crystal [54].

The domains of these fs laser-induced thresholds in glasses are dependent on laser parameters. As shown in Figure 35, all four regions occur at low pulse duration (45 - 60 fs). T1 threshold decreases with the increase of NA. At 160 fs, T3 moves down and becomes dependent on NA at strong focusing. At 200 fs, T3 moves a little bit lower. At this pulse duration, T1 is coincident with T2 at strong focusing. At 250 fs, T3 is downshifting, and there is no observation of the isotropic index zone [41]. However, at a high repetition rate, due to the heat accumulation, causing glass local melting, nanostructures can be erased. This can affect the properties of the fs laser-modified glass.

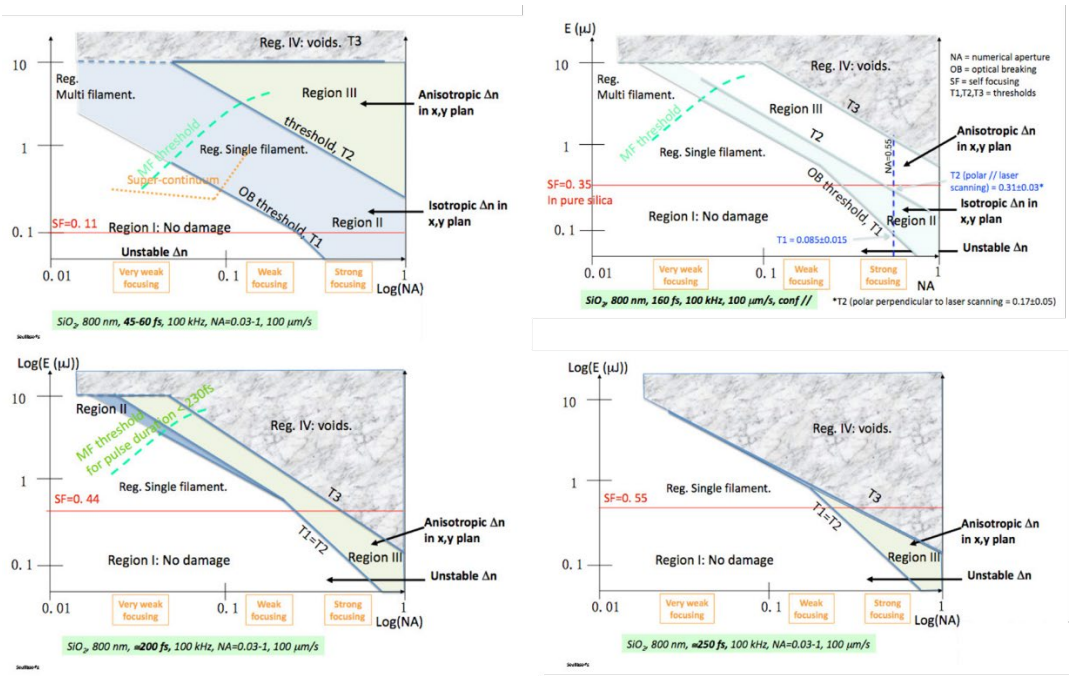

Figure 35: Pulse energy versus numerical aperture (NA) and pulse duration: diagram for a) small pulse duration (45 – 60 fs), b9 160 fs, c) 200 fs, and d) 250 fs (region II disappears) with SiO_2 [41]

3.3.3 Brief bibliographical overview on femtosecond laser-induced crystallization in glasses

In this work, laser-induced crystallization in glasses will be explored to highlight its potential applications in photonics. Then, before starting the investigation on experimental section and results interpretation, it is worth to report a brief and specific bibliographical section relative to this topic.

Different typologies of laser, as continuous wave (CW) [54], long laser pulses (i.e., ns laser [55]), and ultra-short laser pulses (i.e., fs laser [56], [57]) have been proven to be powerful tools to induce crystallization in glass by Komatsu et al. [58], [59], [60] Hirao et al. [61], Miura et al. [62], Honma et al. [63], Qiu et al. [64], [65], Jain et al. [66], Sigaev et al. [67], Poumellec et al. [68]. Especially, CW laser used for $(100\text{-}x)LiBO_2\text{-}xNb_2O_5$ ($5 \leq x \leq 20$) glasses is reported in [69], as a useful reference to comparison with the results obtained by carrying out the process with the femtosecond laser to produce $LiNbO_3$. Now, we intend to mention the most relevant references about femtosecond lasers by Qiu et al. [70]–[73], Stone et al. [74], [75], Poumellec et al. [76]–[78], Yonesaki et al.[79], Komatsu et al. [80], Jain et al. [81].

3.4 Optical properties and non-linear effects

The invention of lasers, capable of generating nearly monochromatic light beams of very high light intensity, allowed the observation of new physical effects that depend closely on the intensity of light and are described in the field of non-linear optics theory. Optical properties of materials depend nonlinearly on the intensity of the beam and on its characteristics, and this is the origin of the term "non-linear optics." For instance, when an infrared light beam is sent into a 400-nanometer-thick non-linear mirror that reflects radiation at twice the input light frequency, light coming out of the material is green. This is due to non-linear optics phenomena that cause the color change of the light beam, as represented in Figure 36 [82].

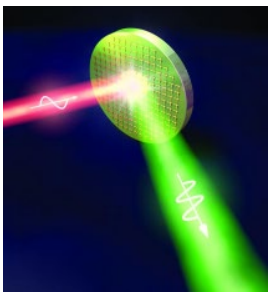

Figure 36: a 400-nm thick non-linear mirror that reflects radiation at twice the input light frequency [82]

3.4.1 Linear and non-linear optics: introduction

Linear optics is fundamental to determining the performance and characteristics of non-linear optical systems. Focusing, material dispersion, and birefringence are only a few examples of optical properties that strongly influence non-linear behavior. For linear optics, individual inputs such as different laser beams are analyzed independently. It is important to remember that when coherent beams of light are superposed, it seems that the beams affect each other, resulting in interesting interference patterns. In linear optical systems, there is no exchange between independent optical inputs. Instead, in non-linear optical systems, there are energy exchanges between the inputs. The vehicle of this exchange is the polarization of the optical medium. Polarization has a central role from the standpoint of energy transfer. Much work in non-linear optics is dedicated to determining the polarization [83].

The research area has been devoted naturally to non-centrosymmetric crystals ($LiNbO_3$, KDP, BBO, etc.). The investigation of non-linear optical (NLO) properties is closely linked to the discovery of Lasers by Theodore Harold Maiman in 1960. In 1961, Franken evidenced for the first time on a quartz crystal the second harmonic generation [84]. That opened to the exploration of various applications based on the concept of frequency conversion, starting from the interaction of monochromatic light sources and high fluence laser interaction with the material.
An optical field introduces the polarization that becomes the key to understanding linear and non-linear optical properties [83]. A field-dependent susceptibility introduces the non-linear polarization. An anharmonic oscillator model explains this connection. The regime of conventional non-linear optics with electrons bound to atoms is replaced by one of relativistic non-linear optics with free electrons in relativistic plasmas [85]. The non-linear effects discovery starts from investigating laser peak power from 10^6 W/cm^2 (or MW/cm^2) to 10^9 W/cm^2 (or GW/cm^2). Because in this power range, the applied laser electric field (typically 10^5 - 10^8 V/m) is comparable to E_a. The susceptibility of material is dependent on the laser electric field. In that case, the refraction index of the material is not constant but dependent on the laser intensity [86]. Therefore, the material's response to the laser field is nonlinearly dependent on laser intensity.

3.4.2 Light polarization, refractive index, and birefringence

Birefringence is the optical property of a material having a refractive index that depends on the polarization and propagation direction of light [87]. Figure 37 shows how a linear polarizer polarizes unpolarized light.

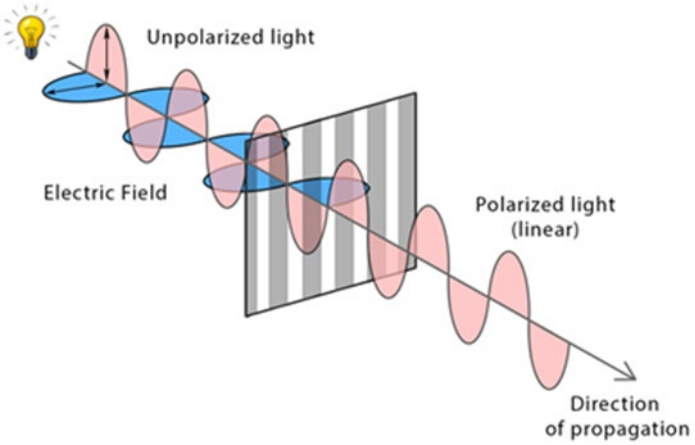

Figure 37: Light polarization scheme [88]

Retardance is the integrated effect of birefringence, acting along the path of the light into the optical sample, and the quantitative relation is expressed by R = B x L where B is the birefringence and L is the thickness of the birefringent object. When the light path comes across an optical material, there is birefringence if the beam is divided into two rays with two polarization components, which travel at different velocities. The birefringence measurement corresponds to the difference of refractive indices of the components within the material. This effect, measured in radians, represents a phase difference by which the two orthogonal components of the linearly polarized light will exit the sample. These two orthogonal components are parallel to two orthogonal axes associated with the optical material, the so-called “fast axis” and “slow axis”. The axis along which light moves the fastest is called the fast axis. Conversely, the slow axis corresponds to the axis along which the refractive index is the highest.

Glass is an optically isotropic transparent material. Crystals fall into two classifications: isotropic and anisotropic, depending on their optical behavior and whether their axes are equivalent. They change depending on the material. It is well known that for any direction of light propagation in a crystal, there are two orthogonal linearly polarized eigenpolarizations. They describe the polarization state. Indeed, we need to determine the directions of e- and o-polarizations and the e- and o-indices associated to the different polarizations comparing with the optical crystal axes, the ordinary and the extraordinary ones, as shown in Figure 38.

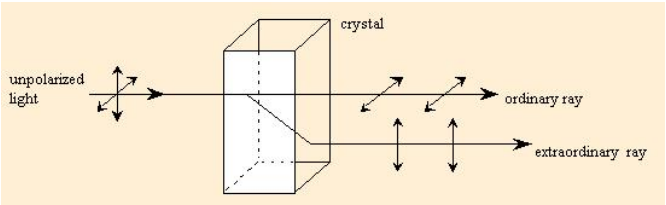

Figure 38: ordinary and extraordinary rays of light on a crystal [89]

If the optical axes are equivalent and similarly interact with light, they characterize isotropic crystals, regardless of their orientation regarding incident light waves. A constant angle at which the light into the crystal is refracted and a single velocity without being polarized by interaction with electronic components of the crystalline lattice are typical in an anisotropic medium. There are no birefringence effects in this case. Otherwise, anisotropy presents a non-uniform spatial distribution of properties, which results in different values in each direction invested by the path of the light.

One typology of anisotropic crystal is defined as uniaxial. When light enters a non-equivalent axis, it is refracted into two rays, each polarized with their vibration directions oriented at right angles to one another and traveling at different velocities. This is a birefringence phenomenon exhibited to a greater or lesser degree in all anisotropic crystals [87]. Poynting vector and its walk-off for negative uniaxial crystal, such as $LiNO_3$, are shown in the following Figure 39.

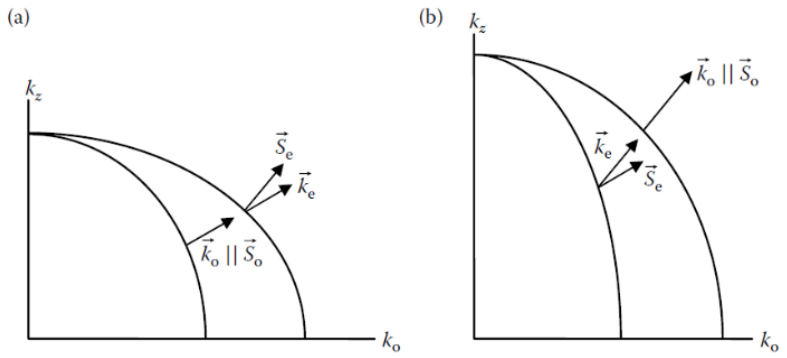

Figure 39: k-vector magnitude surfaces for uniaxial crystals. The Poynting vector is normal to these surfaces. (a) Positive uniaxial crystal, walk-off is toward the z-axis (optic axis). (b) Negative uniaxial crystal, walk-off is away from the z-axis [90].

The refractive index is calculated by the orientation of the material and the polarization state of the electric field. The refractive index is also a function of wavelength. In this case, it is better to discuss the refractive index dispersion, n(ω): the refractive index decreases as the wavelength increases. There are zones in which it is possible to see an anomalous dispersion with high loss, as it is visible in the following Figure 40 [91]:

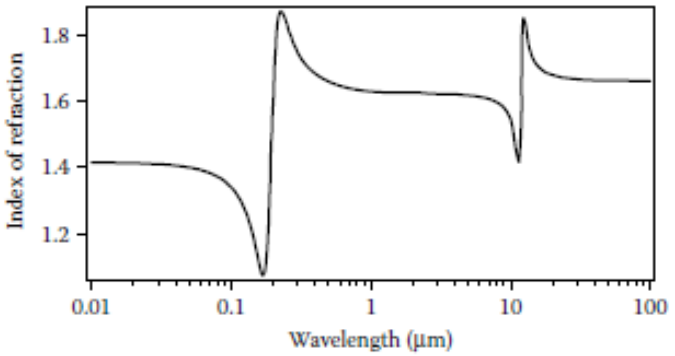

Figure 40: Illustration of dispersion in the index of refraction. The two resonant features show regions anomalous dispersion; these regions are accompanied by high losses [91].

Interestingly, the qualitative aspects of the index dispersion curve are derived using a simple mechanical oscillator model that treats the electrons in the material as independent masses attached to springs [91]. This interpretation will also be used for explaining the SHG theory microscopically.

3.4.3 Physical quantities and non-linear optical phenomena: macroscopic theory [90]

In summary, optics studies the interrelation between light and matter. Laser irradiation enables the interaction between incident optical waves and the propagating medium. For the discussion about the generic microscopic model of the origin of optical nonlinearity, see the section B reported in Appendix. Macroscopically, the effect of a wave on the material is described by polarization $\vec{P}$ induced in the material itself by the electric field associated with it. The polarization induced cannot be expressed by this following simplified form (32) for intense electric fields:

$$\vec{P} = f(\vec{E}) \qquad (32)$$

When the electric field $(\vec{E})$ of lightwave shows high intensity, the material manifests its response through a macroscopic polarization $\vec{P}$ with non-linear components. The intensity is proportional to the square of the electric field. When intensity increases, optical parameters of the material change with incoming light intensity. This dependency defines the passage from linear to non-linear optics. The different regimes are hidden in the Taylor polynomial expansion of the macroscopic polarization as reported in equation (33), and it is interesting to analyze pulsed optics effects.

$$\vec{P} = \varepsilon_0\{\chi^{(1)}\vec{E} \cdot + \chi^{(2)} \cdot \vec{E}\vec{E} + \chi^{(3)} \cdot \vec{E}\vec{E}\vec{E} \ldots\} \qquad (33)$$

ε_0 is vacuum dielectric permittivity and χ dielectric susceptibility. The first term $\chi^{(1)}$ is linear to refractive index n_0 of the medium. When light intensity increases, non-linear terms $\chi^{(2)}$ comes into play, taking into account non-linear optics effects like Second Harmonic Generation (SHG). This summarizes the SHG macroscopic theory based on the tensor of non-linear susceptibility. $\chi^{(3)}$ describes third-order effects such as third-harmonic generation, four-wave mixing, and the intensity

dependence of the refractive index. Typical values of $\chi^{(2)}$ for dielectric crystals, semiconductors, and organic materials are in the range from 10^{-24} to 10^{-21} m/V, and typical values of $\chi^{(3)}$ for glasses, crystals, semiconductor, semiconductor-doped glasses, and organic materials are 10^{-34} to 10^{-29} $(m/V)^2$ [92].
Suppose the point group symmetry of any material is known, precisely the point group properties reported in Table 7. In that case, this leads to important restrictions on the possible form of the non-linear coefficients $\chi^{(2)}$ and $\chi^{(3)}$.

Table 7: Point group properties [83]

Crystal System	Unit Cell Properties	Point Groups	Centrosymmetric
Triclinic	$\alpha \neq \beta \neq \gamma \neq 90°$ $a \neq b \neq c$	1	$\bar{1}$
Monoclinic	$\alpha = \gamma = 90°$ $a \neq b \neq c$	2, *m*	2/*m*
Orthorhombic	$\alpha = \beta = \gamma = 90°$ $a \neq b \neq c$	222, *mm*2	*mmm*
Tetragonal	$\alpha = \beta = \gamma = 90°$ $a = b \neq c$	4, $\bar{4}$, 422, 4*mm*, $\bar{4}$2*m*	4/*m*, $\frac{4}{m}mm$
Trigonal (rhombohedral)	$\alpha \neq \beta \neq \gamma \neq 90°$ $a = b = c$	3, 32, 3*m*	$\bar{3}$, $\bar{3}m$
Hexagonal	$\alpha = \beta = 90° \gamma = 120°$ $a \neq c$	6, 6/*m*, 622, 6*mm*, –62*m*	$\bar{6}$, $\frac{6}{m}mm$
Cubic	$\alpha = \beta = \gamma = 90°$ $a = b = c$	23, 432, $\bar{4}$3*m*	$m\bar{3}$, $m\bar{3}m$

In another general way, it can be written that when wave mixing interacts with the material subjected to laser irradiation, the second-order non-linear susceptibility term $\chi^{(2)}$ (associated to $-\omega_3; \omega_1, \omega_2$) is a tensor of rank 3, $\omega_3 = \omega_1 \pm \omega_2$ is the resulting frequency of the wave mixing of the incident frequencies ω_1 e ω_2. In the term below $\chi^{(2)}_{ijk}$ there are 27 components. *ijk* are indices related to the vector's polarization state associated with the polarization or the electric field in the chosen (*x, y, z*) Cartesian coordinates. A combination of two-excitation electric fields at different frequencies and different polarizations is included in this non-linear term. Highlighting the components also referred to the electric field, it is possible to write in a simplified manner the second-order non-linear polarization as in the equation (34):

$$P_i(\omega_3) = \varepsilon_0 \chi^{(2)}_{ijk} (-\omega_3; \omega_1, \omega_2) E_j(\omega_1) E_i(\omega_2) \quad (34)$$

The medium response defined by the frequency ω_3 is different from those associated with the excitation light waves, but still verifies the two fundamental rules: the energy conservation ($E = h\omega/2\pi$, h is the Plank's constant) and the

momentum conservation ($p = hk/2\pi$, k is the wave vector), as represented in Figure 41:

$$\omega_3 = \omega_1 + \omega_2 \qquad \mathbf{k}_3 = \mathbf{k}_1 + \mathbf{k}_2$$

Figure 41: Schematic diagram of the energy and momentum conservation

Two are the main out of resonance phenomena when states 1 or 2 in the example do not represent the material's real electronic or vibrational state: Second Harmonic Generation (SHG) and Electro-Optic effect (EO). The first one represents the material response at twice the frequency of the fundamental wave obtained by combining two identical electric fields associated with light waves of the same frequency and polarization. The second one exhibits the refractive index modification, combining static or modulated electric field with the light wave associated electric field and an associated birefringence directly proportional to the electric field. The materials that exhibit the second harmonic generation become targets for the fabrication of electro-optic devices such as optical modulators or tunable light sources based on wave mixing materials.

Glasses are centrosymmetric. Then they do not show naturally the second order nonlinearity. The main two techniques to break the centrosymmetry are thermal poling and the fabrication of glass-ceramics. Thermal poling consists of the application of an electric field during thermal treatment. The second-order nonlinearity is localized on a thin film of few microns at the anode side of the polarized glass, as illustrated in Figure 42:

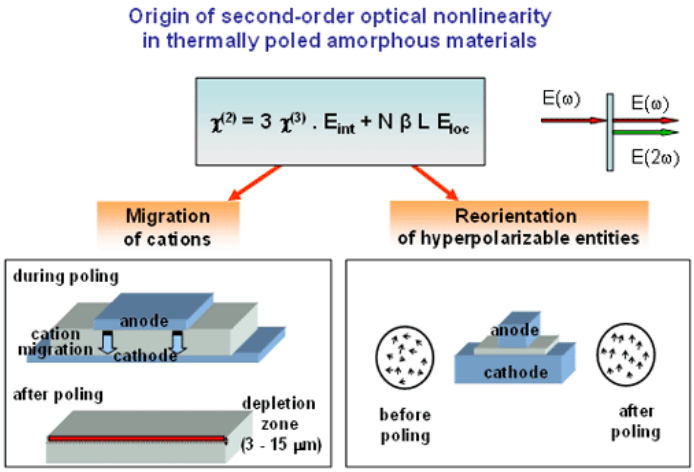

Figure 42: Thermal poling used to introduce a second-order nonlinearity into the material (http://www.eie.gr/nhrf/institutes/tpci/researchteams/mspc/mspc-nanostructuredmat-en.html)

On the other hand, the fabrication of glass-ceramics is based on crystalline phase precipitation within the glass matrix, principally ferroelectric crystals. The characteristic of ferroelectricity allows having an intrinsic polarization deriving from an electric dipole not compensated inside the crystalline structure [93]. The first time in which it is demonstrated the effect of ferroelectricity by precipitating non-centrosymmetric crystals in glass matrix was in 1991 by Komatsu's team [94]. However, it is difficult to control the transparency of the material for obtaining polycrystalline formation for the following conditions:

- The particle shall be far below the wavelength to maintain the scattering loss to a Rayleigh type of low intensity.
- The refractive index difference between the crystalline particles and the matrix shall be the lowest possible.

Glass-ceramic transparency is achieved only if at least one of these criteria is valid inside the material [95]. For glass-ceramic to be used in second-order nonlinearity optics, the particle size must be in the order of 100 nm to present ferroelectric properties [93]. The control of particle size in the order of nanometers becomes crucial not to have an optical signal loss. An example of a typical value to ensure transparency is a crystalline size below $\lambda/10$ [93]. The optimum size of the crystallites corresponds to a trade-off between the global transparency and the SHG response, which is dependent on the volume portion of the crystalline matter and the number of crystallites [96], [97].

A preferred orientation shown by glass-ceramics aligned microstructures allows taking advantage of specific physical properties of crystals directly dependent on

their microstructure[98]. The glass-ceramic devitrification without any external constraint shows that the crystals in bulk usually tend to be randomly oriented, and it is not easy to explore macroscopically anisotropic properties [98], [99]. Non-linear optical crystals have crystallographic anisotropies. The most attractive goal is the crystallization orientation in the desired direction inside the glass matrices. A preferred orientation in the microstructure permits taking advantage of specific physical properties of the crystals. When a glass-ceramic devitrified without any external constraint, the crystals in bulk usually tend to be randomly oriented, and macroscopic anisotropic properties can hardly be exploited. Different methods have induced Oriented crystallization, such as conventional thermal gradient, ultrasonic surface treatment (UST), mechanical hot extrusion, crystallization under electric or magnetic field, and femtosecond laser irradiation [100]. A tropistic field that constrains other directions is an interesting way to induce crystals orientation in glasses.

3.5 Conclusions

The present chapter introduces the most important tool of this work, the laser, ranging from its history, its essential components, and an overview of different typologies. The invention of laser has been a revolution; it has yield to the development of new fields in photonics, optics, and electronics, previously unconceivable. Moreover, it was possible to develop new frontiers in the ultra-fast pulses domain, by mode locking. We employed this technique in our experiments through femtosecond laser irradiation. Short overviews of the Gaussian beam, spherical aberration, and light scattering are preliminary to the treatment of laser-matter interaction. Then, the study of non-linear optical effects allows to introduce how femtosecond laser pulses act on the material and to explain the choice of this tool between the other typologies. Despite the countless advantages in the use of femtosecond lasers the mechanisms that induce structural modifications in dielectric materials are still not fully understood. In this work, seven laser parameters – i.e., pulse energy, numerical aperture and focusing depth, duration of the pulse, pulse repetition rate, laser wavelength, scanning speed, and writing configuration- are varied to investigate how they affect the laser-induced nanostructuring (e.g., crystallization) and optical properties. Four regimes with three thresholds (isotropic refractive index change, generation of form birefringence, and formation of voids) are characterized, and compared to the most

ubiquitous glass material: silica (SiO_2). Glasses centrosymmetry could be broken by the fabrication of glass-ceramic with the photo-precipitation of non-linear crystals. Their non-linear response can be characterized by second harmonic generation (SHG). We therefore focused our attention on this non-linear property used as a mean to confirm the formation and orientation of non-centrosymmetric crystals in glass.

3.6 Bibliography

[1] J. Hecht, "Short history of laser development," *Opt. Eng*, vol. 49, no. 9, p. 091002, Sep. 2010, doi: 10.1117/1.3483597.

[2] N. J. S, "Laser 101 – pt. 1: The Basics." https://www.norwegiancreations.com/2018/04/laser-101-pt-1-the-basics/ (accessed May 06, 2021).

[3] "04_Linewidth | Learn Laser Interferometry with Finesse." http://www.gwoptics.org/learn/02_Plane_waves/01_Fabry_Perot_cavity/04_Linewidth.php (accessed May 19, 2021).

[4] "University of Glasgow :: Electronics and Electrical Engineering :: Prof. Douglas J. Paul." http://userweb.eng.gla.ac.uk/douglas.paul/QCL/popinversion.html (accessed May 21, 2021).

[5] C. Hirlimann, "Laser Basics," in *Femtosecond Laser Pulses: Principles and Experiments*, C. Rullière, Ed. New York, NY: Springer, 2005, pp. 1–23. doi: 10.1007/0-387-26674-7_1.

[6] "Optical Resonator and Laser Action - Engineering Physics Class." https://sites.google.com/site/puenggphysics/home/unit-i/basic-of-laser-action (accessed May 06, 2021).

[7] "Theodore Maiman Invents the First Working Laser : History of Information." https://historyofinformation.com/detail.php?id=3338 (accessed May 06, 2021).

[8] P. Agostini and L. F. DiMauro, "The physics of attosecond light pulses," *Rep. Prog. Phys.*, vol. 67, no. 6, pp. 813–855, May 2004, doi: 10.1088/0034-4885/67/6/R01.

[9] M. Hentschel *et al.*, "Attosecond metrology," *Nature*, vol. 414, no. 6863, Art. no. 6863, Nov. 2001, doi: 10.1038/35107000.

[10] U. Keller, "Recent developments in compact ultrafast lasers," *Nature*, vol. 424, no. 6950, Art. no. 6950, Aug. 2003, doi: 10.1038/nature01938.

[11] D. Strickland and G. Mourou, "Compression of amplified chirped optical pulses," *Optics Communications*, vol. 56, no. 3, pp. 219–221, Dec. 1985, doi: 10.1016/0030-4018(85)90120-8.

[12] M. Pessot, P. Maine, and G. Mourou, "1000 times expansion/compression of optical pulses for chirped pulse amplification," *Optics Communications*, vol. 62, no. 6, pp. 419–421, Jun. 1987, doi: 10.1016/0030-4018(87)90011-3.

[13] "Zhang and Zhao - Semiconductor Saturable Absorber Mirror.pdf." Accessed: May 17, 2022. [Online]. Available: http://www.phys.unm.edu/msbahae/physics555/termpapers05/Zhang-Zhao-SESAM.pdf

[14] "Ultrafast Lasers: Chromatic-dispersion tuning enables efficient manufacturing of CPA femtosecond lasers," *Laser Focus World*, Feb. 01, 2019. https://www.laserfocusworld.com/lasers-sources/article/16556342/ultrafast-lasers-chromaticdispersion-tuning-enables-efficient-manufacturing-of-cpa-femtosecond-lasers (accessed Jul. 17, 2021).

[15] "B. D. Guenther - Modern Optics-Wiley (1990)," *Scribd*. https://www.scribd.com/document/399514200/B-D-Guenther-Modern-Optics-Wiley-1990 (accessed May 06, 2021).

[16] "Gaussian-Beam-Optics.pdf." Accessed: May 06, 2021. [Online]. Available: http://experimentationlab.berkeley.edu/sites/default/files/MOT/Gaussian-Beam-Optics.pdf

[17] "Anatomy of a Microscope - Numerical Aperture and Resolution | Olympus LS." https://www.olympus-lifescience.com/en/microscope-resource/primer/anatomy/numaperture/ (accessed May 06, 2021).

[18] C. Hnatovsky, R. S. Taylor, E. Simova, V. R. Bhardwaj, D. M. Rayner, and P. B. Corkum, "High-resolution study of photoinduced modification in fused silica produced by a tightly focused femtosecond laser beam in the presence of aberrations," *Journal of Applied Physics*, vol. 98, no. 1, p. 013517, Jul. 2005, doi: 10.1063/1.1944223.

[19] Q. Sun, H. Jiang, Y. Liu, Y. Zhou, H. Yang, and Q. Gong, "Effect of spherical aberration on the propagation of a tightly focused femtosecond laser pulse inside fused silica," *J. Opt. A: Pure Appl. Opt.*, vol. 7, no. 11, pp. 655–659, Oct. 2005, doi: 10.1088/1464-4258/7/11/006.

[20] M. Gu, D. Day, O. Nakamura, and S. Kawata, "Three-dimensional coherent transfer function for reflection confocal microscopy in the presence of refractive-index mismatch," *J. Opt. Soc. Am. A, JOSAA*, vol. 18, no. 8, pp. 2002–2008, Aug. 2001, doi: 10.1364/JOSAA.18.002002.

[21] A. Marcinkevičius, V. Mizeikis, S. Juodkazis, S. Matsuo, and H. Misawa, "Effect of refractive index-mismatch on laser microfabrication in silica glass," *Applied Physics A: Materials Science & Processing*, vol. 76, no. 2, pp. 257–260, Feb. 2003, doi: 10.1007/s00339-002-1447-z.

[22] S. Hendy, "Light scattering in transparent glass ceramics," *Appl. Phys. Lett.*, vol. 81, no. 7, pp. 1171–1173, Aug. 2002, doi: 10.1063/1.1499989.

[23] H.-B. Sun and S. Kawata, "Two-Photon Photopolymerization and 3D Lithographic Microfabrication," in *NMR • 3D Analysis • Photopolymerization*, N. Fatkullin, T. Ikehara, H. Jinnai, S. Kawata, R. Kimmich, T. Nishi, Y. Nishikawa, and H.-B. Sun, Eds. Berlin, Heidelberg: Springer, 2004, pp. 169–273. doi: 10.1007/b94405.

[24] "Diagram technique for nonequilibrium processes.pdf."

[25] C. B. Schaffer, A. Brodeur, and E. Mazur, "Laser-induced breakdown and damage in bulk transparent materials induced by tightly focused femtosecond laser pulses," *Meas. Sci. Technol.*, vol. 12, no. 11, pp. 1784–1794, Nov. 2001, doi: 10.1088/0957-0233/12/11/305.

[26] B. J. Buerke, "Accurate measurement of tunneling ionization rates of atoms in a high-intensity laser field," 2000. Accessed: May 07, 2021. [Online]. Available: http://adsabs.harvard.edu/abs/2000PhDT.....74B

[27] I. Shchatsinin, “Free clusters and free molecules in strong, shaped laser fields,” 2009, doi: 10.17169/refubium-12418.

[28] R. R. Gattass and E. Mazur, “Femtosecond laser micromachining in transparent materials,” *Nature Photonics*, vol. 2, no. 4, Art. no. 4, Apr. 2008, doi: 10.1038/nphoton.2008.47.

[29] I. Miyamoto, “Local Melting of Glass Material and Its Application to Direct Fusion Welding by Ps-laser Pulses,” *JLMN*, vol. 2, no. 1, pp. 7–14, Mar. 2007, doi: 10.2961/jlmn.2007.01.0002.

[30] S. S. Mao *et al.*, “Dynamics of femtosecond laser interactions with dielectrics,” *Appl Phys A*, vol. 79, no. 7, pp. 1695–1709, Nov. 2004, doi: 10.1007/s00339-004-2684-0.

[31] B. C. Stuart, M. D. Feit, A. M. Rubenchik, B. W. Shore, and M. D. Perry, “Laser-Induced Damage in Dielectrics with Nanosecond to Subpicosecond Pulses,” *Phys. Rev. Lett.*, vol. 74, no. 12, pp. 2248–2251, Mar. 1995, doi: 10.1103/PhysRevLett.74.2248.

[32] G. H. Wannier, “The Structure of Electronic Excitation Levels in Insulating Crystals,” *Phys. Rev.*, vol. 52, no. 3, pp. 191–197, Aug. 1937, doi: 10.1103/PhysRev.52.191.

[33] M. Ueta, H. Kanzaki, K. Kobayashi, Y. Toyozawa, and E. Hanamura, “The Exciton and Excitonic Molecule in Cuprous Halides,” in *Excitonic Processes in Solids*, M. Ueta, H. Kanzaki, K. Kobayashi, Y. Toyozawa, and E. Hanamura, Eds. Berlin, Heidelberg: Springer, 1986, pp. 116–202. doi: 10.1007/978-3-642-82602-3_3.

[34] J. D. Musgraves, K. Richardson, and H. Jain, “Laser-induced structural modification, its mechanisms, and applications in glassy optical materials,” *Optical Materials Express*, vol. 1, pp. 921–935, Sep. 2011, doi: 10.1364/OME.1.000921.

[35] M. Lancry, B. Poumellec, A. Chahid-Erraji, M. Beresna, and P. Kazansky, “Dependence of the femtosecond laser refractive index change thresholds on the chemical composition of doped-silica glasses,” *Optical Materials Express*, vol. 1, pp. 711–723, Aug. 2011, doi: 10.1364/OME.1.000711.

[36] A. Igarashi, T. Komori, T. Tamaki, H. Arimoto, T. Fukuda, and W. Watanabe, "Phase measurement of structural modifications created by femtosecond laser pulses in glass with phase-shifting digital holographic microscopy," *OE*, vol. 56, no. 11, p. 111702, Mar. 2017, doi: 10.1117/1.OE.56.11.111702.

[37] M. Watanabe, S. Juodkazis, H.-B. Sun, S. Matsuo, and H. Misawa, "Luminescence and defect formation by visible and near-infrared irradiation of vitreous silica," *Phys. Rev. B*, vol. 60, no. 14, pp. 9959–9964, Oct. 1999, doi: 10.1103/PhysRevB.60.9959.

[38] C. M. Gee and M. Kastner, "Intrinsic-defect photoluminescence in amorphous and crystalline SiO2," *Journal of Non-Crystalline Solids*, vol. 35–36, pp. 927–932, Jan. 1980, doi: 10.1016/0022-3093(80)90319-1.

[39] M. Lancry, B. Poumellec, R. Desmarchelier, and B. Bourguignon, "Oriented Creation of Anisotropic Defects by IR Femtosecond Laser Scanning in Silica," *Optical Materials Express*, vol. 2, pp. 1809–1821, Dec. 2012, doi: 10.1364/OME.2.001809.

[40] K. M. Davis, K. Miura, N. Sugimoto, and K. Hirao, "Writing waveguides in glass with a femtosecond laser," *Opt Lett*, vol. 21, no. 21, pp. 1729–1731, Nov. 1996, doi: 10.1364/ol.21.001729.

[41] B. Poumellec, M. Lancry, A. Chahid-Erraji, and P. G. Kazansky, "Modification thresholds in femtosecond laser processing of pure silica: review of dependencies on laser parameters [Invited]," *Opt. Mater. Express, OME*, vol. 1, no. 4, pp. 766–782, Aug. 2011, doi: 10.1364/OME.1.000766.

[42] R. Osellame, G. Cerullo, and R. Ramponi, Eds., *Femtosecond Laser Micromachining: Photonic and Microfluidic Devices in Transparent Materials*. Berlin Heidelberg: Springer-Verlag, 2012. doi: 10.1007/978-3-642-23366-1.

[43] L. Sudrie, M. Franco, B. Prade, and A. Mysyrowicz, "Study of damage in fused silica induced by ultra-short IR laser pulses," *Optics Communications*, vol. 191, no. 3–6, pp. 333–339, May 2001, doi: 10.1016/S0030-4018(01)01152-X.

[44] A. Couairon, L. Sudrie, M. Franco, B. Prade, and A. Mysyrowicz, "Filamentation and damage in fused silica induced by tightly focused femtosecond laser pulses," *Phys. Rev. B*, vol. 71, no. 12, p. 125435, Mar. 2005, doi: 10.1103/PhysRevB.71.125435.

[45] C. Hnatovsky *et al.*, "Pulse duration dependence of femtosecond-laser-fabricated nanogratings in fused silica," *Appl. Phys. Lett.*, vol. 87, no. 1, p. 014104, Jul. 2005, doi: 10.1063/1.1991991.

[46] V. R. Bhardwaj, P. B. Corkum, D. M. Rayner, C. Hnatovsky, E. Simova, and R. S. Taylor, "Stress in femtosecond-laser-written waveguides in fused silica," *Opt. Lett.*, vol. 29, no. 12, p. 1312, Jun. 2004, doi: 10.1364/OL.29.001312.

[47] J. D. Mills, P. G. Kazansky, E. Bricchi, and J. J. Baumberg, "Embedded anisotropic microreflectors by femtosecond-laser nanomachining," *Appl. Phys. Lett.*, vol. 81, no. 2, pp. 196–198, Jun. 2002, doi: 10.1063/1.1492004.

[48] R. Taylor, C. Hnatovsky, and E. Simova, "Applications of femtosecond laser induced self-organized planar nanocracks inside fused silica glass," *Laser & Photon. Rev.*, vol. 2, no. 1–2, pp. 26–46, Apr. 2008, doi: 10.1002/lpor.200710031.

[49] E. Bricchi, B. G. Klappauf, and P. G. Kazansky, "Form birefringence and negative index change created by femtosecond direct writing in transparent materials," *Opt. Lett.*, vol. 29, no. 1, p. 119, Jan. 2004, doi: 10.1364/OL.29.000119.

[50] M. Lancry, B. Poumellec, K. Cook, and J. Canning, "Nanogratings and molecular oxygen formation during femtosecond laser irradiation in silica," in *Proceedings of the International Quantum Electronics Conference and Conference on Lasers and Electro-Optics Pacific Rim 2011 (2011), paper C229*, Aug. 2011, p. C229. Accessed: May 10, 2021. [Online]. Available: https://www.osapublishing.org/abstract.cfm?uri=CLEOPR-2011-C229

[51] E. Bricchi and P. G. Kazansky, "Extraordinary stability of anisotropic femtosecond direct-written structures embedded in silica glass," *Appl. Phys. Lett.*, vol. 88, no. 11, p. 111119, Mar. 2006, doi: 10.1063/1.2185587.

[52] E. N. Glezer *et al.*, "Three-dimensional optical storage inside transparent materials," *Opt. Lett.*, vol. 21, no. 24, p. 2023, Dec. 1996, doi: 10.1364/OL.21.002023.

[53] H.-B. Sun *et al.*, "Arbitrary-lattice photonic crystals created by multiphoton microfabrication," *Opt. Lett.*, vol. 26, no. 6, p. 325, Mar. 2001, doi: 10.1364/OL.26.000325.

[54] R. Sato, Y. Benino, T. Fujiwara, and T. Komatsu, "YAG laser-induced crystalline dot patterning in samarium tellurite glasses," *Journal of Non-Crystalline Solids*, vol. 289, no. 1–3, pp. 228–232, Aug. 2001, doi: 10.1016/S0022-3093(01)00736-0.

[55] D. M. Shevyakina *et al.*, "Local Crystallization of Lithium-Niobium-Silicate Glass by Copper-Vapor Laser Beam," *Glass Ceram*, vol. 72, no. 5–6, pp. 194–198, Sep. 2015, doi: 10.1007/s10717-015-9754-y.

[56] Y. Teng, J. Zhou, K. Sharafudeen, S. Zhou, K. Miura, and J. Qiu, "Space-selective crystallization of glass induced by femtosecond laser irradiation," *Journal of Non-Crystalline Solids*, vol. 383, pp. 91–96, Jan. 2014, doi: 10.1016/j.jnoncrysol.2013.04.015.

[57] K. Miura, J. Qiu, T. Mitsuyu, and K. Hirao, "Space-selective growth of frequency-conversion crystals in glasses with ultrashort infrared laser pulses," *Opt. Lett., OL*, vol. 25, no. 6, pp. 408–410, Mar. 2000, doi: 10.1364/OL.25.000408.

[58] T. Komatsu, "Design and control of crystallization in oxide glasses," *Journal of Non-Crystalline Solids*, vol. 428, pp. 156–175, Nov. 2015, doi: 10.1016/j.jnoncrysol.2015.08.017.

[59] T. Komatsu, K. Koshiba, and T. Honma, "Preferential growth orientation of laser-patterned LiNbO3 crystals in lithium niobium silicate glass," *Journal of Solid State Chemistry*, vol. 184, no. 2, pp. 411–418, Feb. 2011, doi: 10.1016/j.jssc.2010.12.016.

[60] T. Komatsu *et al.*, "Patterning of Non-Linear Optical Crystals in Glass by Laser-Induced Crystallization," *J American Ceramic Society*, vol. 90, no. 3, pp. 699–705, Mar. 2007, doi: 10.1111/j.1551-2916.2006.01441.x.

[61] A. Stone *et al.*, "Direct laser-writing of ferroelectric single-crystal waveguide architectures in glass for 3D integrated optics," *Sci Rep*, vol. 5, no. 1, p. 10391, Sep. 2015, doi: 10.1038/srep10391.

[62] Y. Shimotsuma, S. Mori, Y. Nakanishii, E. Kim, M. Sakakura, and K. Miura, "Self-assembled glass/crystal periodic nanostructure in $$\hbox {Al}_2\hbox {O}_3\text {-}\hbox {Dy}_2\hbox {O}_3$$Al2O3-Dy2O3 binary glass," *Appl. Phys. A*, vol. 124, no. 1, p. 82, Jan. 2018, doi: 10.1007/s00339-017-1507-z.

[63] T. Honma, Y. Benino, T. Fujiwara, T. Komatsu, and R. Sato, "Technique for writing of nonlinear optical single-crystal lines in glass," *Appl. Phys. Lett.*, vol. 83, no. 14, pp. 2796–2798, Oct. 2003, doi: 10.1063/1.1615833.

[64] X. Liu, J. Zhou, S. Zhou, Y. Yue, and J. Qiu, "Transparent glass-ceramics functionalized by dispersed crystals," *Progress in Materials Science*, vol. 97, pp. 38–96, Aug. 2018, doi: 10.1016/j.pmatsci.2018.02.006.

[65] B. Zhu, Y. Dai, H. Ma, S. Zhang, G. Lin, and J. Qiu, "Femtosecond laser induced space-selective precipitation of nonlinear optical crystals in rare-earth-doped glasses," *Opt. Express*, vol. 15, no. 10, p. 6069, 2007, doi: 10.1364/OE.15.006069.

[66] D. Savytskii, B. Knorr, V. Dierolf, and H. Jain, "Demonstration of single crystal growth via solid-solid transformation of a glass," *Sci Rep*, vol. 6, no. 1, p. 23324, Sep. 2016, doi: 10.1038/srep23324.

[67] S. Lotarev, S. Fedotov, A. Lipatiev, M. Presnyakov, P. Kazansky, and V. Sigaev, "Light-driven nanoperiodical modulation of alkaline cation distribution inside sodium silicate glass," *Journal of Non-Crystalline Solids*, vol. 479, pp. 49–54, Jan. 2018, doi: 10.1016/j.jnoncrysol.2017.10.008.

[68] J. Cao, B. Poumellec, F. Brisset, and M. Lancry, "Pulse energy dependence of refractive index change in lithium niobium silicate glass during femtosecond laser direct writing," *Opt. Express*, vol. 26, no. 6, p. 7460, Mar. 2018, doi: 10.1364/OE.26.007460.

[69] B. H. Venkataraman *et al.*, "Optical diffraction of second-harmonic signals in the LiBO2-Nb2O5 glasses induced by self-organized LiNbO3 crystallites," *Appl. Phys. Lett.*, vol. 87, no. 9, p. 091113, Aug. 2005, doi: 10.1063/1.2037198.

[70] X. Du *et al.*, "Space-selective precipitation of ZnO crystals in glass by using high repetition rate femtosecond laser irradiation," *Opt. Express*, vol. 22, no. 15, p. 17908, Jul. 2014, doi: 10.1364/OE.22.017908.

[71] Y. Dai *et al.*, "Direct writing three-dimensional Ba2TiSi2O8 crystalline pattern in glass with ultrashort pulse laser," *Appl. Phys. Lett.*, vol. 90, no. 18, p. 181109, Apr. 2007, doi: 10.1063/1.2734919.

[72] B. Zhu *et al.*, "Greatly enhanced effect of silver on femtosecond laser-induced precipitation of nonlinear optical crystals in glasses," *Opt. Lett.*, vol. 34, no. 11, p. 1666, Jun. 2009, doi: 10.1364/OL.34.001666.

[73] Y. Dai, B. Zhu, J. Qiu, H. Ma, B. Lu, and B. Yu, "Space-selective precipitation of functional crystals in glass by using a high repetition rate femtosecond laser," *Chemical Physics Letters*, vol. 443, no. 4–6, pp. 253–257, Aug. 2007, doi: 10.1016/j.cplett.2007.06.076.

[74] A. Stone *et al.*, "Formation of ferroelectric single-crystal architectures in LaBGeO5 glass by femtosecond vs. continuous-wave lasers," *Journal of Non-Crystalline Solids*, vol. 356, no. 52–54, pp. 3059–3065, Dec. 2010, doi: 10.1016/j.jnoncrysol.2010.03.048.

[75] A. Stone *et al.*, "Directionally controlled 3D ferroelectric single crystal growth in LaBGeO_5 glass by femtosecond laser irradiation," *Opt. Express*, vol. 17, no. 25, p. 23284, Dec. 2009, doi: 10.1364/OE.17.023284.

[76] X. He, B. Poumellec, Q. Liu, F. Brisset, and M. Lancry, "One-step photoinscription of asymmetrically oriented fresnoite-type crystals in glass by ultrafast laser," *Opt. Lett.*, vol. 39, no. 18, p. 5423, Sep. 2014, doi: 10.1364/OL.39.005423.

[77] M. Lancry, B. Poumellec, J. Canning, K. Cook, J.-C. Poulin, and F. Brisset, "Ultrafast nanoporous silica formation driven by femtosecond laser irradiation: In the heart of nanogratings," *Laser & Photonics Reviews*, vol. 7, no. 6, pp. 953–962, Nov. 2013, doi: 10.1002/lpor.201300043.

[78] J. Cao, L. Mazerolles, M. Lancry, D. Solas, F. Brisset, and B. Poumellec, "Form birefringence induced in multicomponent glass by femtosecond laser direct writing," *Opt. Lett.*, vol. 41, no. 12, p. 2739, Jun. 2016, doi: 10.1364/OL.41.002739.

[79] Y. Yonesaki, K. Miura, R. Araki, K. Fujita, and K. Hirao, "Space-selective precipitation of non-linear optical crystals inside silicate glasses using near-infrared femtosecond laser," *Journal of Non-Crystalline Solids*, vol. 351, no. 10–11, pp. 885–892, Apr. 2005, doi: 10.1016/j.jnoncrysol.2005.01.076.

[80] K. Ogawa, T. Honma, and T. Komatsu, "Birefringence imaging and orientation of laser patterned β-BaB2O4 crystals with bending and curved shapes

in glass," *Journal of Solid State Chemistry*, vol. 207, pp. 6–12, Nov. 2013, doi: 10.1016/j.jssc.2013.08.021.

[81] K. Veenhuizen, S. McAnany, D. Nolan, B. Aitken, V. Dierolf, and H. Jain, "Fabrication of graded index single crystal in glass," *Sci Rep*, vol. 7, no. 1, p. 44327, Jun. 2017, doi: 10.1038/srep44327.

[82] J. Lee *et al.*, "Giant nonlinear response from plasmonic metasurfaces coupled to intersubband transitions," *Nature*, vol. 511, no. 7507, pp. 65–69, Jul. 2014, doi: 10.1038/nature13455.

[83] *Fundamentals of Nonlinear Optics*. CRC Press, 2017. doi: 10.1201/9781315116433.

[84] P. A. Franken, A. E. Hill, C. W. Peters, and G. Weinreich, "Generation of Optical Harmonics," p. 3, 1961.

[85] D. Umstadter, "Relativistic laser–plasma interactions," p. 15.

[86] "Encyclopedia of Nonlinear Science," *Routledge & CRC Press*. https://www.routledge.com/Encyclopedia-of-Nonlinear-Science/Scott/p/book/9781138012141 (accessed May 10, 2021).

[87] "Birefringence," *Wikipedia*. May 06, 2021. Accessed: May 10, 2021. [Online]. Available: https://en.wikipedia.org/w/index.php?title=Birefringence&oldid=1021778314

[88] "Polarization of Light: Definition, Diagram, and Applications," *Science Facts*, Apr. 16, 2020. https://www.sciencefacts.net/polarization-of-light.html (accessed May 10, 2021).

[89] "Stanford: Advanced Optical Ceramics Laboratory." http://web.stanford.edu/group/scintillators/ceramicprocessing.html (accessed May 14, 2021).

[90] R. W. Boyd, *Nonlinear optics*, 3rd ed. Amsterdam ; Boston: Academic Press, 2008.

[91] C. Hirlimann, "Laser Basics," in *Femtosecond Laser Pulses: Principles and Experiments*, C. Rullière, Ed. New York, NY: Springer, 2005, p. 36. doi: 10.1007/0-387-26674-7_1.

[92] F. Träger, Ed., *Springer Handbook of Lasers and Optics*, 2nd ed. Berlin Heidelberg: Springer-Verlag, 2012. doi: 10.1007/978-3-642-19409-2.

[93] H. Jain, "Transparent Ferroelectric Glass-Ceramics," *Ferroelectrics*, vol. 306, no. 1, pp. 111–127, Jan. 2004, doi: 10.1080/00150190490458446.

[94] T. Komatsu, H. Tawarayama, H. Mohri, and K. Matusita, "Properties and crystallization behaviors of TeO2□LiNbO3 glasses," *Journal of Non-Crystalline Solids*, vol. 135, no. 2–3, pp. 105–113, Nov. 1991, doi: 10.1016/0022-3093(91)90410-8.

[95] G. H. Beall and D. A. Duke, "Transparent glass-ceramics," p. 13.

[96] E. L. Falcão-Filho *et al.*, "Third-order optical nonlinearity of a transparent glass ceramic containing sodium niobate nanocrystals," *Phys. Rev. B*, vol. 69, no. 13, p. 134204, Apr. 2004, doi: 10.1103/PhysRevB.69.134204.

[97] J.-K. Lee *et al.*, "Magnetic anisotropy study of ion-beam synthesized cobalt nanocrystals," *Appl. Phys. Lett.*, vol. 89, no. 18, p. 182502, Oct. 2006, doi: 10.1063/1.2364176.

[98] D. I. H. Atkinson and P. W. McMILLAN, "Glass-ceramics with random and oriented microstructures," *Journal of Materials Science*, vol. 12, pp. 443–450, 1977.

[99] C. Rüssel, "Oriented crystallization of glass. A review," *Journal of Non-Crystalline Solids*, vol. 219, pp. 212–218, 1997.

[100] H. Zeng, B. Poumellec, C. Fan, G. Chen, A. Erraji-Chahid, and M. Lancry, "Preparation of Glass-Ceramics with Oriented Nonlinear Crystals: A Review," in *Advanced in Materials Science Research*, Nova Science, 2012, pp. 89–134

Chapter 4

Femtosecond Direct Laser Writing (FDLW): experimental section and results

In this chapter, we investigate the formation of $LiNbO_3$ nonlinear optical crystals induced by Femtosecond Direct Laser Writing (FDLW) in several glass matrices, starting with the "reference" lithium niobium silicate (LNS) glass, with a progressive substitution of SiO_2 with B_2O_3. This chapter comprises six sections. The first Section discusses the glass composition selected for irradiation. The second Section includes laser setup and irradiation conditions to specify how irradiation of dots (static mode) and lines (dynamic mode) were performed. The third Section deals with polarized light microscopy techniques to detect and characterize birefringent structures induced by laser irradiation. The fourth Section is dedicated to second harmonic generation (SHG) detection to characterize the polarization-dependent orientation of $LiNbO_3$ crystals inside the glass. The fifth Section includes quantitative phase microscopy (QPM) measurements to investigate the refractive index variation induced during laser writing. Finally, the last Section presents the characterization of the formed nanostructures using the electron backscattering diffraction (EBSD) technique.

4.1 Glass selection for Femtosecond Direct Laser Writing

The objective of this thesis work is to induce and control 3D modifications of optical properties in glasses. The photo-precipitation of crystals by ultrashort laser pulses enables one to manipulate the processed material's size, shape, and orientation (s). The glass selection is based on the possibility to control the variation of optical properties induced by fs-laser irradiation and the variation of volume fraction (i.e., number and size) of the crystals (sometimes called the *active phase*) dispersed inside the glass matrix. Some requisites for maintaining optical transparency are the small size of the crystals to minimize light scattering (size typically < 1/10 of the wavelength) and a slight crystal/glass refractive index difference. Non-centrosymmetric crystals generate second-order nonlinear effects such as second harmonic generation.

In this work, we first irradiated LNS glass as our glass reference (specifically LNS34, see Chapter 2). We thus investigate the fs-laser response in other glasses presenting a progressive increase of B_2O_3 concentration, which is known to lower the crystallization temperature and increase the crystallization rate. Below, all the results about experiments and characterizations of the laser transformations inside the glass(es) are presented, and an extensive comprehensive interpretation of the driving mechanisms at play is presented in Chapter 5.

4.2 Femtosecond Direct Laser Writing (FDLW)

A commercial Yb-doped fiber amplifier fs laser (Satsuma, Amplitude Systèmes Ltd.) emitting at 1030 nm at room temperature with 100 kHz to MHz repetition rate is used in this Ph.D. work experiments. The fs-laser irradiation was performed on LNS34 glass, as taken as a reference, and then on the other glasses, namely LNS27B7, LNS20B14, and LNS13B21. Please note that the glass labels and specific compositions can be found in Chapter 2.

An aspheric lens with a numerical aperture (NA) equal to 0.6 focused the laser beam inside the glasses at 240 µm below the sample top surface (in air). According to Figure 4.1 schematically representing the laser setup, the laser propagation was defined along the +Z direction. Irradiated dots and lines were drawn continuously in the plane perpendicular to the laser beam propagation direction, i.e., the XY plane.

One of the most critical laser parameters is light polarization. It is set linear and can be controlled by rotating a half-wave plate along the light path highlighted with the red dashed rectangle. Control of pulse energy is made by combining a half-wave

plate and a polarizing beam splitter cube represented within the green dashed rectangle in Figure 43. Another relevant parameter is the laser power that was measured and calibrated prior to any experiment.

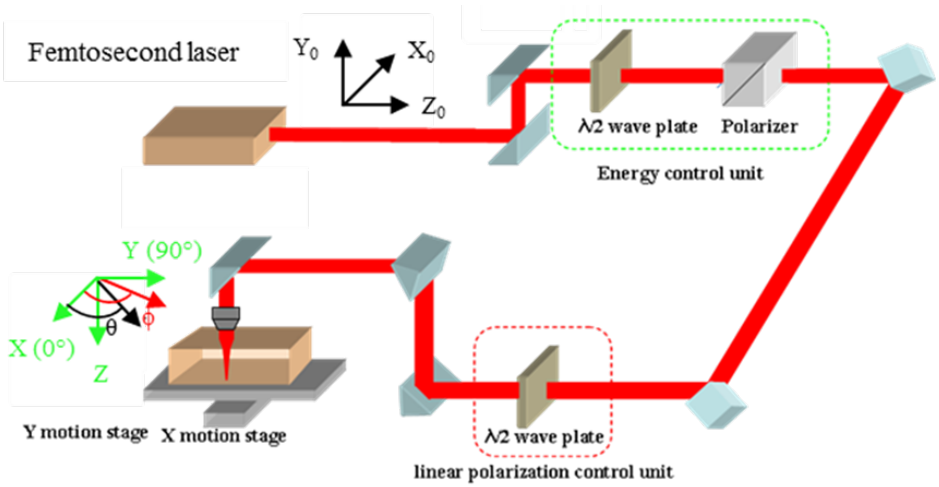

Figure 43: Schematic diagram of the femtosecond laser system used at ICCMO

This scheme shows the black right-handed cartesian coordinate system coming from the laser. In detail, X_0 corresponds to the horizontal direction in which the right side is declared positive; Y_0 is the vertical direction with upside defined positive; $+Z_0$ represents laser propagation direction. The odd number of mirrors on the optical table causes the variation of the coordinate system from right-handed to left-handed. The reference of writing configuration is based on the green left-handed cartesian coordinate system. The preprogrammed pattern was written in the XY plane by moving the sample stages. Writing laser polarization angle indicated by φ and scanning direction identified with θ are referred to +X direction in the XY plane. Then, the writing configuration is defined as (θ, φ) [1]. Table 8 shows all the laser parameters employed in our experiments.

Table 8: Laser parameters used in all the experiments

parameter	value
wavelength	1030 nm
pulse duration	250 fs

repetition rate (RR)	100 – 510 kHz
pulse energy (E)	0.25 – 2.5 µJ/pulse
numerical aperture (NA)	0.6
focal depth	240 µm in air (300 µm from sample surface)
writing speed	from 1 to 625 µm/s
laser polarization (referred to writing direction)	parallel (Y_y) at 45° (Y_{45}) perpendicular (Y_x)
scanning direction	along Y

Some parameters are fixed depending on the experiments (described below), and others vary during laser writing. Table 9 represents three series of experiments, highlighting how each parameter presented is changed. The variations of laser parameters enable the investigation of the different crystallization kinetics for the four glass compositions (LNS34, LNS27B7, LNS20B14, and LNS13B21).

Table 9: Laser parameters variable in different experiments

typology of experiment	pulse energy (µJ/pulse)	repetition rate (kHz)	polarization	scanning speed (m/s)
dots	0.25 – 2.5	100, 200, 340, 510	Y_y	/
lines	0.25 – 2	200	Y_y, Y_{45}, Y_x	1
lines	0.5, 1	200	Y_y, Y_x	1 – 625

Then, to investigate the crystallization as a function of glass composition, and subsequently glass nano-structuring and optical properties variations, fs-laser writing is performed through two sequential ways:

- **Static irradiation**, corresponding to the first line of Table 9. In this experiment, dots are written inside the samples, and the time taken by the material to generate green light under irradiation (characteristic of SHG) is monitored. This time is called the incubation time and is of the order of seconds. The observed green light is indicative of glass crystallization and the formation of non-

centrosymmetric crystals (therein $LiNbO_3$). These experiments are performed for varying pulse energy and frequency (pulse repetition rate) values.

- **Dynamic irradiation**, corresponding to lines 2 and 3 of Table 9. Lines were written subsequently to static irradiation for the duration of the incubation time previously determined. The experiment was repeated for different laser irradiation conditions, including a varying scanning speed, and using different pulse energies and three laser polarization configurations. These irradiation configurations are reported in the following Figure 44, together with the green left-handed cartesian coordinate system according to Figure 43.

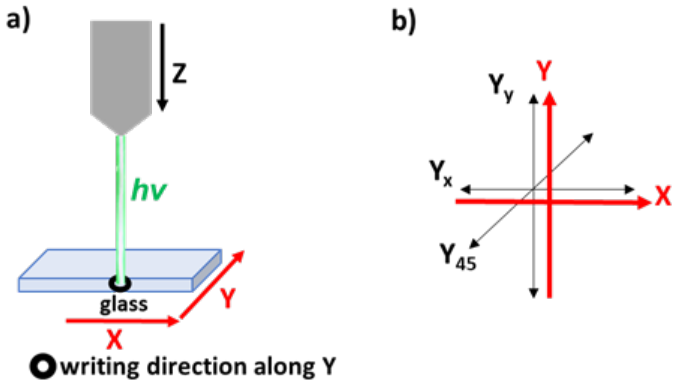

Figure 44: a) laser writing scheme: the translation stage displacement is in the XY sample plane, while the laser beam propagation direction is along Z; b) top view of three different laser polarization configurations referenced to laser writing direction along the Y-axis: parallel (Y_y), at 45° (Y_{45}) and perpendicular (Y_x)

4.2.1 Fs-laser writing of dots (static mode)

After sample alignment on the XY plane of the translation stage, the first experiment consisted in writing dots in a static way, i.e., a writing speed being equal to zero. The only two parameters changed are pulse energy and repetition rate. Below are optical microscope pictures (see Figure 45a and b) for two of the four glasses employed (LNS34 and LNS27B7) under white light illumination (transmission mode). We noted that dot size becomes larger as both pulse energy and repetition rate increase.

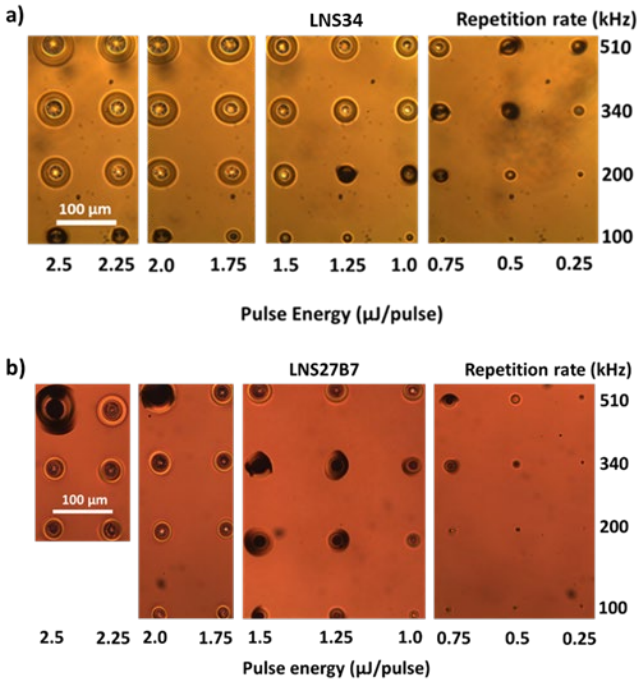

Figure 45: Static dots under white light for a) LNS34 and b) LNS27B7

The irradiation in static mode allows to study the static crystallization threshold by recording the time for detecting SHG around the focal point of the laser beam. This is a fundamental parameter defined according to pulse energy and repetition rate. Green light (at (515 nm) constitutes a criterion of the nonlinear optical $LiNbO_3$ crystals precipitation inside glass, which corresponds to the double frequency of the incident fs laser with 1030 nm central wavelength [2]. We observed that the incubation time was drastically reduced by addition of B_2O_3 and increasing repetition rate to induced crystalline onset. This identifies the existence of incubation state as indicative of chemical diffusion by cumulative effect. For static mode, incubation time corresponds to irradiation time because it is calculated exactly until when we can detect green light from the sample, then after the seconds necessary we waited only 1s more.

One can assume, from Figure 46, that three zones are highlighted from the center: the first is the one closer to laser beam (enclosed in red); the second, where elemental migration starts (enclosed in yellow), shows a melted zone and the third corresponds to the nucleation area (enclosed in white).

The melted zone exists only when the energy or the repetition rate is large enough, otherwise we are in the case of solid-solid transformation which has been extensively described in Ref. [3] and [4].

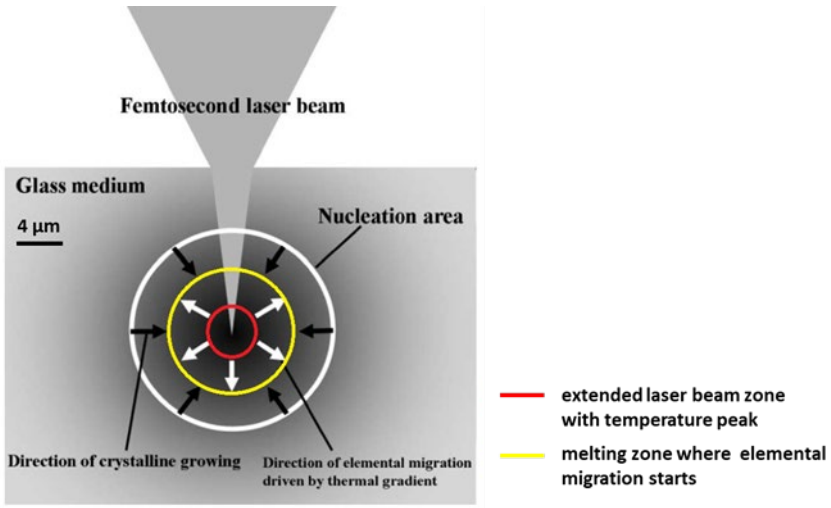

Figure 46: Scheme of space-selective crystallization induced by tightly focused femtosecond laser pulses adapted from [5]

This scheme of space-selective crystallization is taken up by Ref. [5] for $32.5Li_2O - 27.5Nb_2O_5 - 40SiO_2$ that is also adapted to our LNS and LNSB glass matrices. Then, a thermal gradient is induced, partly inside the irradiated volume. Accordingly, it causes radial migration and eventually a chemical gradient (depends on the Soret coefficients). Thermal gradient is visible through the graduation of color inside the irradiated glass medium: darker (lighter) color concides with the higher (lower) temperature region. The influent area (~ 20 µm in diameter) is greater than the laser beam waist (~ 2 µm in diameter). Nucleation happens at a certain distance from the focusing point because of the thermal and chemical gradients. Inner region where nucleation takes place has higher temperature than outside one, so that nanocrystal growth occurs toward the inside one [5].
Incubation time is measured for each glass sample in the pulse energy-repetition rate landscape, and the results are reported on heatmap type graphs in Figure 47.

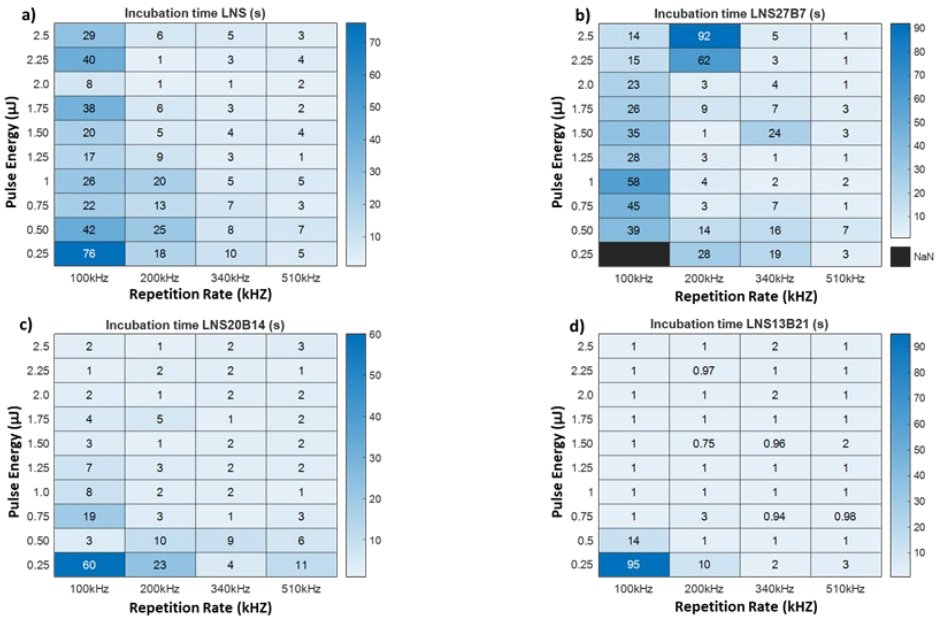

Figure 47: Heatmaps of incubation time for four glasses: a) LNS34; b) LNS27B7; c) LNS20B14 and d) LNS13B21

The comparison between the incubation times for the four different glass compositions, as a function of delivered average laser power (i.e., Power = Pulse energy (E) × Repetition Rate (RR)), is represented in Figure 48. As the amount of boron oxide increased, the incubation time correspondingly decreased. For dots characterization under polarized light, see next section 4.3.

In this case, we represent a plot of incubation time in function of delivered laser power.

Then, the heat accumulation is controlled by the pulse frequency and affects the temperature, but if pulse energy does not affect the heat accumulation, it acts on the temperature. It can be noted that if steady state is quickly reached (in a few hundred pulses), then this steady state is rather defined by the average power deposited, and therefore the temperature defining incubation time is also determined by the supplied power. If we consider the average temperature over a period and the number of periods, the average temperature depends on the average delivered power according to this following E_p x RR, and the number of periods is equivalent to time. This is the reason why we plotted incubation time vs delivered laser power in the following Figure 48.

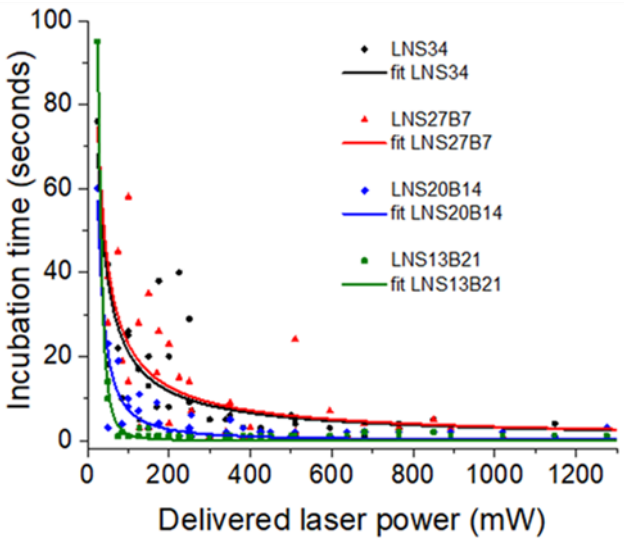

Figure 48: Evolution of incubation time in function of delivered laser power depending on glass composition [6]

This step of static writing is preliminary to write lines. In fact, if lines are scanned directly skipping the static step, green light during fs laser fabrication could not be continued or not be possible to achieved. We have to distinguish between conditions in regime 2 and regime 3.
Regime 2 shows local crystallization only where is the light without influence of a neighboring unirradiated volume. Then the presence of nanocrystals may be recognized by SHG light in illuminated volume. In case of regime 3, all is completely different: the center dots melts whereas crystallization begins out of the beam. The large intensity in the beam and light scattering allow to detect easily SHG from scattered IR light [7].

4.2.2 Fs-laser writing of lines (dynamic mode)

Two different series of experiments were performed, varying pulse energy, laser polarization, and writing speed. We intend to investigate the variation of crystallization kinetics and the impact of the scanning speed on the photoinduced transformations as a function of the glass composition.

1) In this set of experiments for the four glass compositions, two parameters are varied: pulse energy, laser polarization. The irradiation scheme for the first experiment performed on the four glasses is reported in Figure 49:

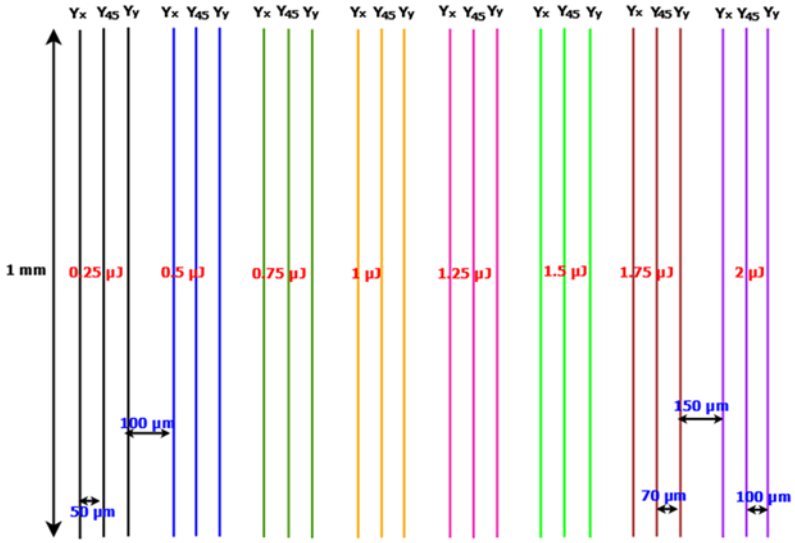

Figure 49: Scheme of irradiation program for lines according to these following writing conditions: laser beam direction = Z, writing direction along Y, three different laser polarization configurations: Y_x, Y_{45} and Y_y, NA = 0.6, pulse duration = 250 fs, repetition rate = 200 kHz, pulse energy from 0.25 to 2 µJ, scanning speed= 1 µm/s for LNS34, LNS27B7, LNS20B14, and LNS13B21 glasses

2) In the second series of experiments, we also varied the scanning speed, and we studied what happens to the crystallization kinetics of LNS34 and LNS13B21. The drawing of the irradiation program for LNS34 and LSN13B21glasses is reported in the following Figure 50a and b.

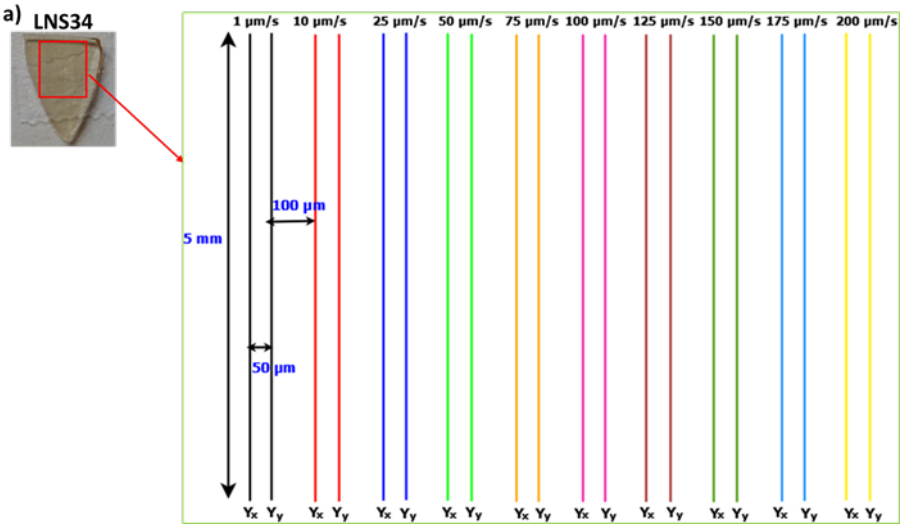

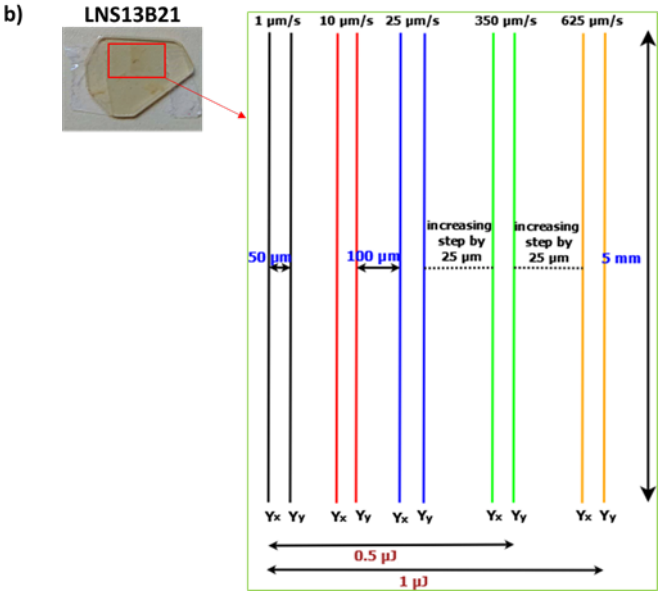

Figure 50: Scheme of irradiation program for 5 mm lines at these specific irradiation conditions: laser beam direction = Z, writing direction along Y, two laser polarization configurations Y_x and Y_y, NA = 0.6, repetition rate = 200 kHz, pulse duration = 250 fs, two values of pulse energy 0.5 and 1 µJ and different scanning speed respectively from 1 µm/s to 200 µm/s for a) LNS34 and for b) LNS13B21 from 1 µm/s to 200 µm/s at 0.5 µJ and from 1 µm/s to 625 µm/s at pulse energy equal to 1 µJ

The lines were analyzed under an optical microscope in transmission mode and using white light. Under these conditions, we intend to check the index change, absorption, or scattering by the contrast between lines and background. LNS34 shows lines black until 25 µm/s at 0.5 µJ/pulse and until 100 µm/s at 1 µJ/pulse; after they become transparent as a sign of no crystallization. The effective line crystallization was confirmed by EBDS analysis, which will be discussed in the specific section 4.6.2. It must be pointed out that as the B_2O_3 content is progressively increased, the crystalline lines could be drawn at higher writing speed, as shown in Figure 51. Comparing LNS34 and LNS13B21, lines show a discontinuous track that creates within irregularity in each line, but crystallization in LNS13B21 is maintained, until 225 µm/s at 0.5 µJ/pulse and until 600 µm/s at 1 µJ/pulse. Moreover, it is possible to detect a brown color for lines with intermediate

scanning speed (75 – 225 µm/s at 0.5 µJ/pulse and 350 – 600 µm/s at 1 µJ/pulse) in the case of LNS13B21 glass.

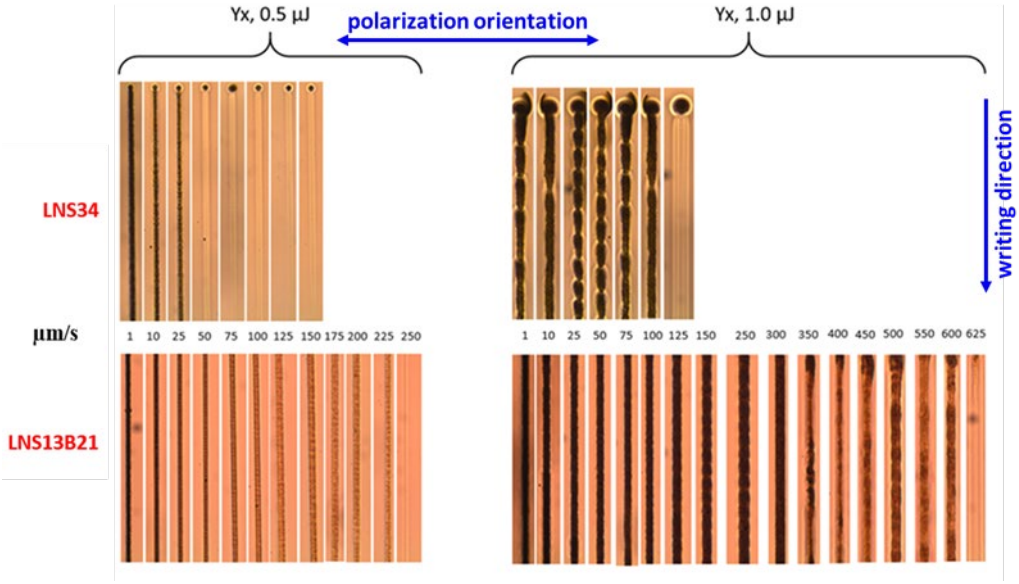

Figure 51: Optical microscope images of lines written by fs-laser in LNS34 and LNS13B21glasses in Y_x polarization configuration, at various scanning speeds, two pulse energies: 0.5 and 1 µJ/pulse, and repetition rate fixed at 200 kHz

4.3 Polarized light microscopy

The irradiated dots and lines of all experiments have been investigated using an OLYMPUS BX60 microscope apparatus by polarized light microscopy. The conventional microscope is equipped with an analyzer placed before the sample and a polarizer placed after the sample, which is in crossed positions with respect to each other. Information on the polarized light configuration, the working principle of a polarized light microscope, and all its accessories can be found in Refs. [8], [9], and [10].

The polarized light microscopy allows determining the presence of birefringence in irradiated dots and lines, crossing the analyzer (A) and polarizer (P) in transmission mode.

Figure 52 is an image of LNS27B7 glass dots written on the sample turned of 45° on the microscope plate, i.e., X and Y axes rotated of 45° from analyzer and polarizer crossed. The dot is an object of cylindrical symmetry. Then, if we turn a picture with dots, we should have the same image. But if there is a pulse front tilt (PFT) effect, this is no longer valid. Thus, it is known from the literature that

repetition rate plays a role in the effects of thermal accumulation, leading to a steady rise in temperature in the focal region [11]. In static mode, as the repetition rate increases, a black zone appears around the focus laser beam at lower pulse energies. This black zone was already visible under white light. Under polarized light, it becomes even more evident, and, it expands at increasing pulse energy [12]–[16]. The white light is due to neutral axes of dots not aligned with analyzer and polarizer.

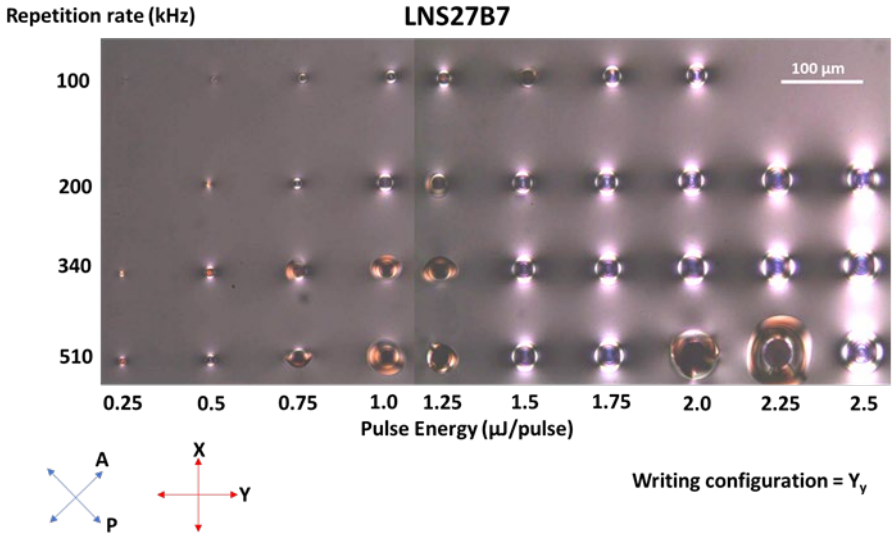

Figure 52: Dots, written according to polarizer direction, Y_y laser polarization configuration, pulse duration = 250 fs, irradiation time = 1s (after waiting incubation time), under polarized light at analyzer and polarizer crossed (P = polarizer, A = analyzer)

Figure 53 shows lines inscribed in the LNS20B14 sample at different pulse energies and three polarization configurations. A First Order (Full Wave) Retardation Plate (550 nm, Olympus U-TP530) was employed to detect the slow and fast axis of the written lines by the method reported in [17] and inserted at the angle of 45° with respect to the microscope polarizer and analyzer, as shown in Figure 53. Birefringence is identified if lines were oriented with the neutral axis in a diagonal position with respect to the microscope polarizer and analyzer.
The totally dark zone corresponds to a non-irradiated, and therefore, glassy area.
When polarization configuration was changed, the intensity of the irradiated lines reached a minimum at Y_x or Y_y, but maximum at Y_{45}, i.e., when laser polarization configuration is oriented to a diagonal position to the analyzer.

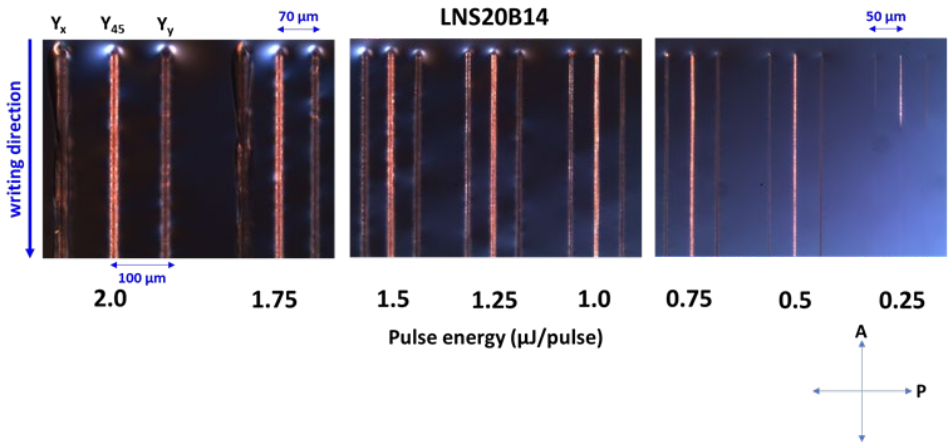

Figure 53: Lines under polarized light written according to analyzer direction (P = polarizer, A = analyzer), at repetition rate equal to 200 kHz and scanning speed equal to 1 µm/s

Focusing the attention on LNS13B21 glass according to the second series of experiments, Figure 53 represents lines in three regimes of scanning speed under different microscope analysis conditions: low at 1 µm/s, medium at 75 µm/s and high regime at 350 µm/s. At low speed, lines appear black, and no light passes through them. When speed is equal to 75 µm/s, lines become brown, and the light can pass through them. At high speed, lines are transparent, and no crystallization is detectable, then light passes entirely through them. We represent in Figure 54 different illumination conditions: under white light, under polarized light at polarizer and analyzer crossed and finally with a full λ waveplate inserted with its orientation perpendicular to the laser scanning direction.

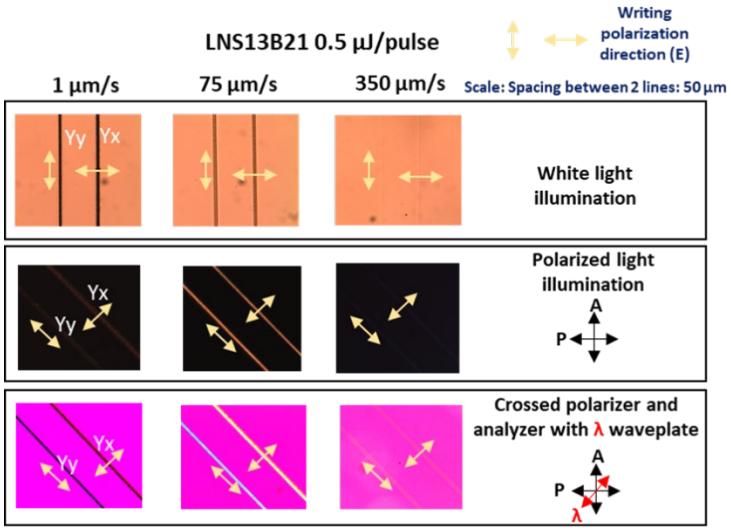

Figure 54: Optical microscope images of lines at different scanning speed (1, 75 and 350 µm/s) under different illumination condition for LNS13B21 glass at a pulse energy of 0.5 µJ; (P = polarizer, A = analyzer) [18].

Under polarized light conditions, the background shows up black due to glass isotropy. The lines appear dark when placed parallel either to the polarizer (P) or the analyzer (A). Otherwise, when the lines were rotated at any other angle than parallel to P or A, light passes through them, with a maximum at an angle of 45° with respect to both A and P axes (with a precision of $\pm$ 5°). This peculiarity reaches the maximum for the medium speed regime (75 µm/s), demonstrating that the orientation of the neutral axes is parallel and perpendicular to the line scanning direction.

After the insertion of a full retardation waveplate and the neutral axes at 45° from A and P, the background is isotropic, appearing magenta, and it is possible to distinguish the slow axis and the fast axis. If a line appears blue, the slow axis of the irradiated line at that place is parallel to the slow axis of the full-wave retardation plate. If it is yellow, the slow axis at that place is perpendicular to the slow axis of the full-wave retardation plate. This phenomenon is more evident at the medium regime of scanning speed than low and high ones. Then, the slow axis of the inscribed line is found perpendicular to the writing laser polarization, and this feature is related to the formation of quasi-periodic lamellas with two different refractive indices.

Finally, we measured retardance (R) quantitatively at the center of each irradiated line as reported in Figures 55a and b.

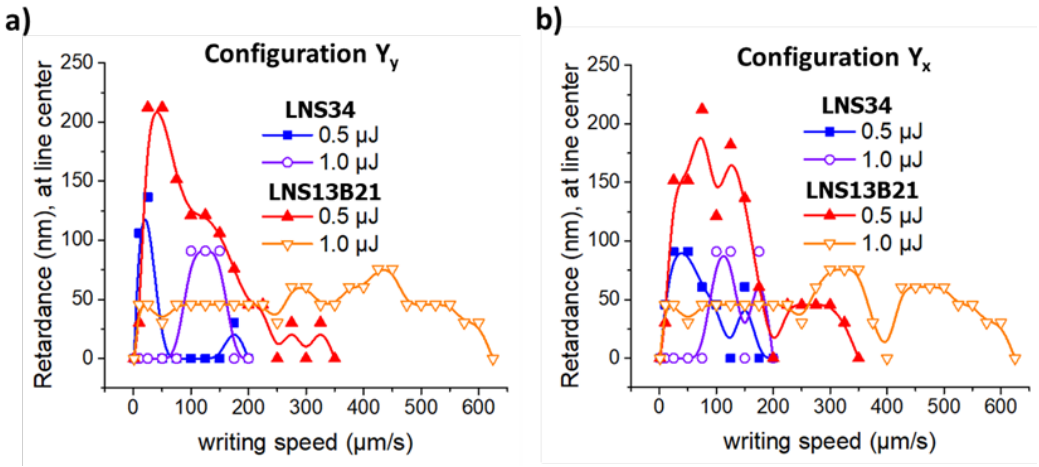

Figure 55: Retardance in nm measured at 550 nm at the center of the irradiated lines as a function of scanning speed for LNS34 and LNS13B21, at two pulse energies (0.5 and 1 µJ/pulse), repetition rate fixed at 200 kHz and for a) Y_y and b) Y_x laser polarization configurations [18].

Different trends were found in the two glasses LNS34 and LNS13B21. In the case of LNS34, the retardance emerges from the formation of a sub-wavelength and lamellar-like structure with periodic alternation of $LiNbO_3$-rich regions (crystallized) with $LiNbO_3$-poor (vitreous) ones, leading to form birefringence, and as the consequent effect the retardance [1]. When scanning speed is equal to 1 µm/s, retardance measured is null, and this result is the same for the two energies pulse and two glasses analyzed. The situation changes for LNS13B21: as the scanning speed is progressively increased, the retardance also raises until it reaches a maximum. Going from 1 to 0.5 µJ/pulse, the retardance enhances, precisely by a factor equal to 4 (until to 200 nm). According to results in Figure 51, for LNS13B21, at 0.5 µJ/pulse retardance disappears beyond 350 µm/s, whereas for 1 µJ/pulse it is evident until 600 µm/s. For LNS34, the maximum does not exceed 100 nm. In this case, if retardance increases just from a few µm/s until 50 µm/s at 0.5 µJ/pulse, it starts to raise latter for 1 µJ/pulse, but both show a step decay at 200 µm/s. By referring to the three-speed regimes described above, the low-speed regime shows a birefringent response, but the white light is scattered as it passes through the cross-section due to the presence of large crystallites along the laser

track. In conclusion, no writing polarization effect is detected on the retardance amplitude, and the maximum response for LNS13B21 is about twice larger compared to LNS34.

4.4 Second Harmonic Generation (SHG) measurements

The SHG intensity was detected in transmission mode with the fundamental laser beam of 1030 nm, propagating perpendicularly to the sample XY plane at pulse energy = 0.1 μJ/pulse. According to the setup reported in Figure 56a, the transmitted SHG light of 515 nm, i.e., λ/2 with λ = 1030 nm, was recorded after passing an IR low pass filter mounted before a spectrometer collector. The spot size (diameter) of the probing beam was approximately 30 μm, well overlapping each laser track during SHG measurements. The repetition rate during the measurement was set at 100 kHz. Figure 56b shows the SHG detected under the static condition of laser irradiation at the end of incubation time of a few seconds.
For a more detailed definition and theoretical treatment of Second Harmonic Generation (SHG), see the section C of Appendix.

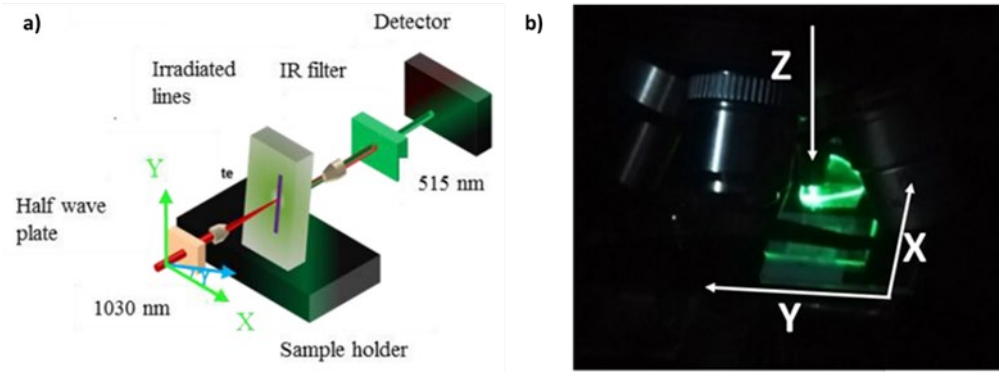

Figure 56: a) Second Harmonic Generation (SHG) setup used for all the experiments of this Ph.D. work [19]; b) SHG detected under static irradiation at the end of the incubation time of a few seconds [6]

SHG intensity was measured for all the four investigated glasses according to the laser irradiation condition reported in Figure 49. For each irradiated line, we detected the SHG intensity in the XY plane according to the azimuthal angle (θ) of the probe beam polarization until 180° starting from the polarizer reference position at 0°, i.e., along X. The probe beam propagation direction was set perpendicular to the XY plane, and its electric field direction was parallel to this plane.

The curves intensities obtained were normalized from the SHG spectrum values, according to the following expression:

$$I_{norm} = \frac{I(\theta)}{MAX\ (I(\theta))} \qquad (32)$$

where MAX (I (θ)) is the maximum calculated on all the intensities values as a function of probing angle I(θ). A SHG spectrum for the pulse energy equal to 1.25 μJ and for the Y_x configuration in LNS13B21 is reported in Figure 57, as an example.

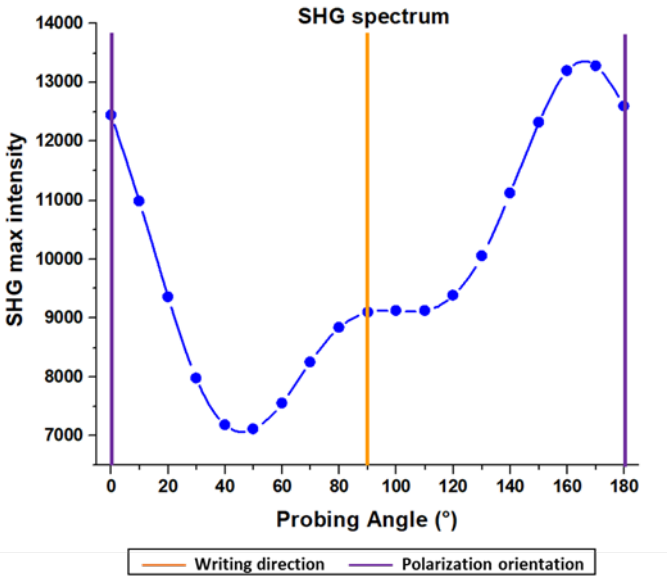

Figure 57: SHG spectrum obtained for LNS13B21 lines written at 1.25 μJ/pulse, at Y_x polarization configuration, at fixed repetition rate equal to 200 kHz and scanning speed equal to 1 μm/s. The reference position of the laser polarizer is 0°, which coincides with the position corresponding to 180°.

Normalized SHG intensity profiles for the four glass compositions as a function of probing polarization angle in the XY plane were reported in Figure 58. Other trends for all four compositions can be found in the section D of Appendix.

The effect of the writing laser polarization orientation on the crystals was investigated by the angular dependency of the SHG intensity. Figures 58a and b show SHG curves at two pulse energies (0.5 and 1.25 μJ for two polarization configurations, Y_x and Y_{45}). The choice of these two values of pulse energies was made because of important changes well visible in SHG curves for the four glasses.

At 0.5 µJ, a strong SHG modulation is evident with respect to an azimuth-θ of 90° for all four glasses. When pulse energy reaches 1.25 µJ, a second maximum on the curves in the direction of the polarization is found, and the trend of the curves begins to present complex responses different for each glass composition.

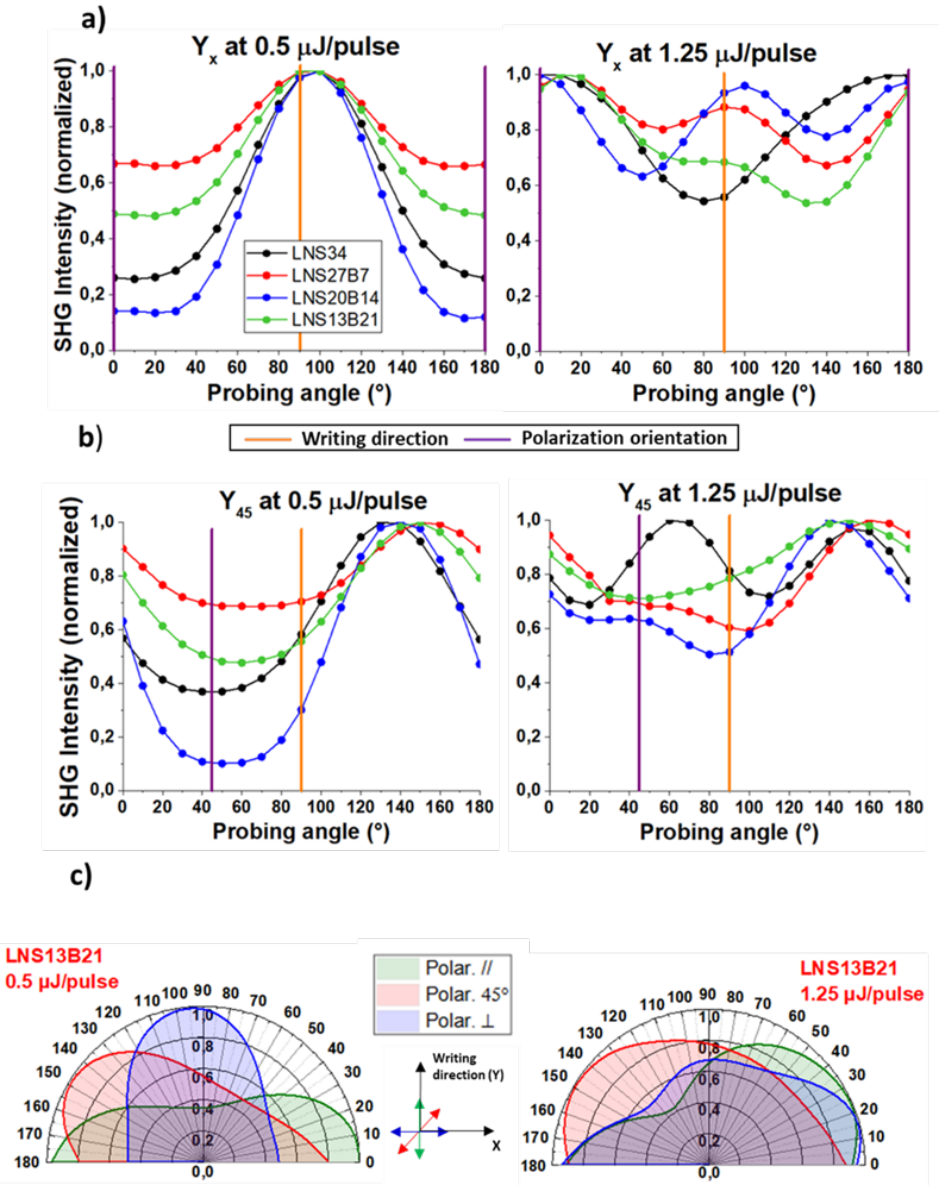

Figure 58: normalized SHG intensity profiles for the four glass compositions as a function of probing polarization angle in the XY plane for 0.5 and 1.25 µJ/pulse a) at Y_x and b) Y_{45} polarization configuration; c) polar representation for LNS13B21 glass for 0.5 and 1.25 µJ/pulse with three polarization configuration Y_y, Y_{45} and Y_x [6].

This is according to results reported in [20]. If we explore the pulse energy effect, it is noted that at low pulse energy (in our case, it corresponds to 0.5 μJ), a well - defined cosine-like curve with a period of 180° is obtained, and a SHG_{min} intensity is found at a probing angle close to writing laser polarization direction, precisely at 90°. When we increase the pulse energy to 1.25 μJ, the cosine-like curve is modified, and a second minimum occurs, revealing a second texture of the crystals with the polar axis oriented closer to parallel to the writing laser polarization.
Specifically, in our case, at 0.5 μJ/pulse, the normalized SHG intensity (I/I_{max}) shows a sinusoidal trend with strong contrast ($I_{max} – I_{min} / (I_{max} + I_{min}$) up to 0.9 for LNS20B14. The maximum with respect to the direction perpendicular to the laser polarization is at 90° and 135° for Y_x and Y_{45} configurations, respectively. Otherwise, the SHG_{min} intensity is found in the correspondence of a probing angle perpendicular to the angle value of SHG_{max}.
Increasing the pulse energy progressively from 0.5 to 1.25 μJ/pulse, the SHG presents a complex response because of the presence of another crystalline texture oriented in a different direction. The low energy texture, i.e., the population leading to SHG_{max} for θ perpendicular to writing polarization, is still emerging at 1.25 μJ. In addition, a second population of $LiNbO_3$ crystals with a preferential orientation appears in the SHG response, visible in Figure 58c. This phenomenon is very clear with the configuration $Y_{45,}$ for which there is no maximum in the direction of writing.
A slight departure of the minima and the maxima of the SHG modulation from the probing angle equal to 90° is observed due to an asymmetric orientational writing effect as previously observed at low speeds (i.e., 1 μm/s) in LNS34 glass [20]. These results are strictly linked to EBSD maps reported in section 4.6.2.

4.5 Quantitative Phase Microscopy (QPM)

Quantitative Phase Microscopy (QPM) is a non-interferometric solution used to analyze the refractive index profile of the focal region after femtosecond laser permanent modifications. For more details about QPM, see the section E of the Appendix.
A CCD camera mounted on an optical microscope in transmission mode captures the sample images according to the conditions provided in Figure 59.
QPM directly measures the phase shift and, analyzing light propagation on the sample; the refractive index variation can be calculated according to the following formula:

$$\Delta n = \Delta\varphi \frac{\lambda}{2\pi L} \qquad (33)$$

where $\Delta\varphi$ is the phase shift (in radians) of the non-polarized light at λ=550 nm and L the thickness of the sample along the light propagation direction [21].

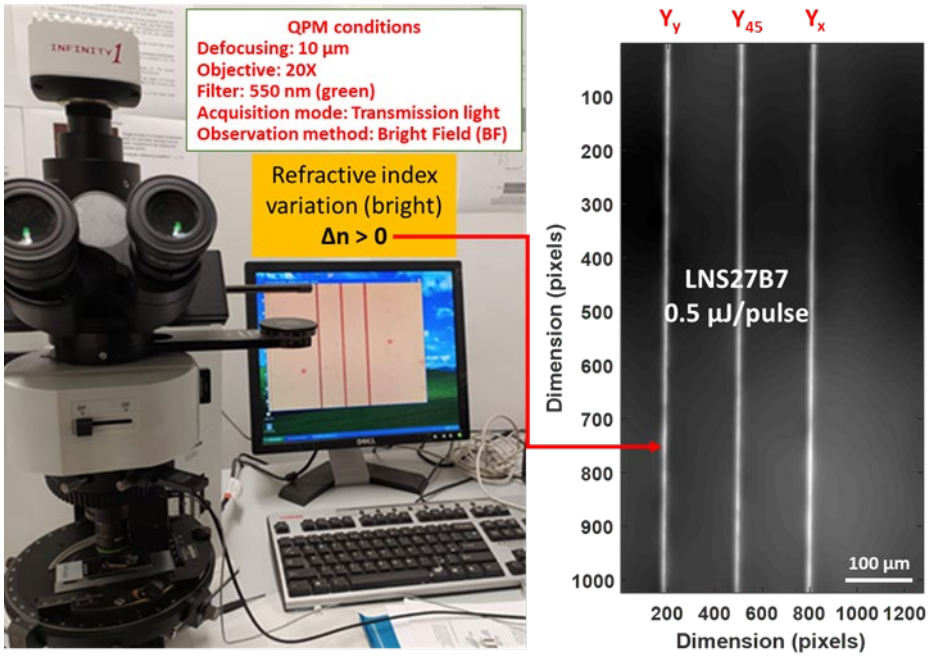

Figure 59: QPM analysis process represented through the CCD camera mounted on the microscope: the three lines represent a phase image converted into a software representation after applying the MATLAB code to extract black background and white lines images.

If Δn is positive, it means that the refractive index increases, and this phenomenon confirms the presence of crystallization. To determine the variation in the refractive index, the procedure carried out for LNS34 reported on Ref. [22] is used, starting from the valid assumption for which $\overline{n_{cryst}} > n_{glass}$ and results included in Ref. [23]. For glass, the refractive index is constant and equal to 1.462 at 515 nm [24]. Now, we intend to explore what to insert in $\overline{n_{cryst}}$. We consider the configuration shown in Figure 44. From EBSD measurements and SEM micrographs, we deduced the self-organized periodic nanostructure, that induced a form birefringence, the so-called nanogratings in which two different phases were discovered, a glassy phase that presents a single refractive index, and a crystalline one identified by $LiNbO_3$

where the typical anisotropy is quantified by two different and directional refractive indices ($n_{2,XX}$ and $n_{2,YY}$).

The refractive index in the YX plane (Y scanning direction) is derived from the relative permittivity ($\overline{\overline{n_c^2}} = \overline{\overline{\varepsilon_{r,c}}}$).

For $LiNbO_3$, the relative permittivity matrix in the crystal reference is expressed by:

$$\overline{\overline{\varepsilon_{r,c}}} = \begin{bmatrix} \varepsilon_o & 0 & 0 \\ 0 & \varepsilon_o & 0 \\ 0 & 0 & \varepsilon_e \end{bmatrix} \quad (34)$$

where ε_o is the relative permittivity perpendicular to the polar axis, and ε_e is the one along the polar axis. From this, and the previous expression, we can calculate n_o (ordinary refractive index) and n_e (extraordinary refractive index). The refractive indices in 2D are computed from these following equations.

$$n_{XX}^2 = \frac{n_1^2 n_{2,XX}^2}{f n_{2,XX}^2 + (1-f) n_1^2} \quad (35)$$

$$n_{YY}^2 = f n_1^2 + (1-f) n_{2,YY}^2 \quad (36)$$

where n_1 corresponds to refractive index of glass, and n_2 is relative to crystals. In this case we consider two different indices indicative of typical crystalline anisotropy ($n_{2,XX}$ and $n_{2,YY}$) and with

$$f = \frac{d_1}{d_1 + d_2} \quad (37)$$

where d_1 is glassy part thickness and d_2 is the crystalline part thickness (μm).

$$n_{2,XX}^2 = \varepsilon_{r,sample,XX}^{texture} \quad (38)$$

$$n_{2,YY}^2 = \varepsilon_{r,sample,YY}^{texture} \quad (39)$$

$$\overline{\overline{\varepsilon_{r,sample}^{texture}}} = \frac{\sum_i S_i \overline{\overline{B_i}}\, \overline{\overline{\varepsilon_{r,c}}}\, \overline{\overline{B_i^{-1}}}}{\sum_i S_i} \quad (40)$$

where i is relative to the grain, S_i is the number of measurement points in the grain, $\overline{\overline{\varepsilon_{r,c}}}$ is the relative dielectric constant tensor for one crystal in crystal reference, and $\overline{\overline{B_i}}$

is the matrix for changing the reference from the crystal indexed i to the sample reference. The B_i matrices and S_i weights are derived from the EBSD measurements [22]. Then, we found $\overline{n_{cryst}}$, as a 2D average value for the form birefringence of nanogratings between n_{XX} and n_{YY}.

Consequently, once demonstrated the presence of crystallization due to the variation in refractive index Δn, we can compare the three lines trends with different pulse energies. Figure 60 shows how the trend of the three lines represented in the previous Figure 59 trend changes, at increasing pulse energy from 0.25 to 1 µJ for LNS27B7 glass.

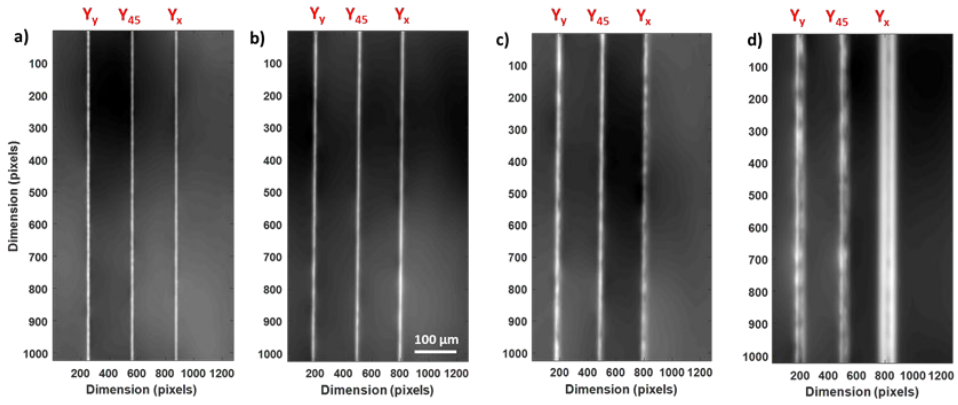

Figure 60: QPM images for LNS27B7 glass on lines at three polarization configurations Y_y, Y_{45}, and Y_x at pulse energies of a) 0.25 µJ, b) 0.5 µJ, c) 0.75 µJ and d) 1 µJ.

It is possible to note that at 1 µJ, the image starts to reveal some irregularities that correspond to the splitting of two of three peaks reported in the following Figure 61d. This is the critical value of pulse energy where the width of the lines begins to become larger than the general trend until 0.75 µJ.

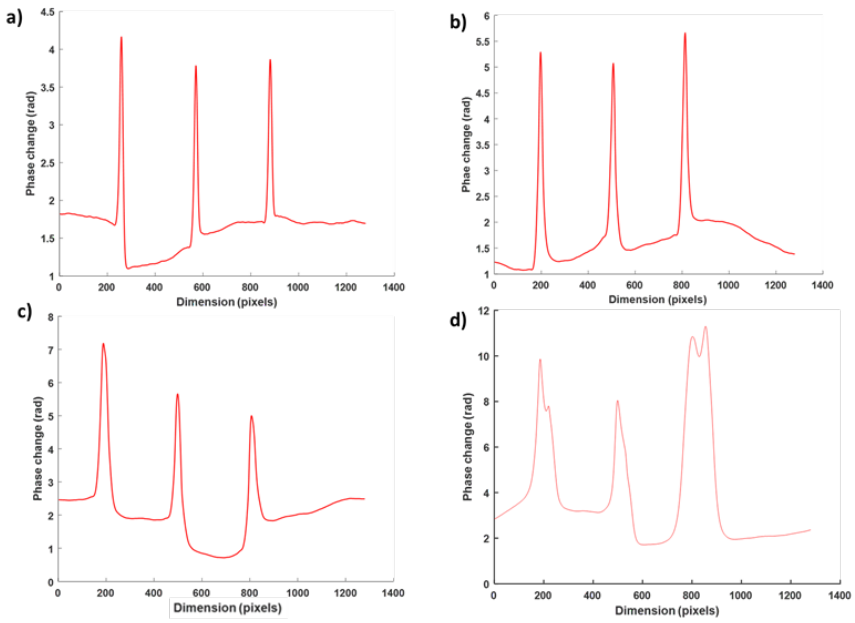

Figure 61: QPM analysis modulation in which the phase change in rad is highlighted by a plot where we can see three peaks in correspondence of each set of the three lines reported on the previous Figure 60.

4.6 Microstructure analysis

4.6.1 Scanning Electron Microscopy (SEM)

Scanning electron microscopy (SEM) was employed to observe the nanostructures on the laser-modified area. For more details about SEM, refer to [25].
SEM micrographs of LNS13B21 laser track cross-section for two polarization configurations Y_x and Y_y at 75 μm/s were reported in Figure 62. SEM analysis is done for exploring nanostructure but, in our case, exhibits the formation of nanogratings. Laser irradiation produces in the material these self-organized nanogratings, specifically where there is an oriented phase separation, composed of a crystalline and a glassy phase. This structure is visible when zooming in this yellow rectangle area. Nanogratings are a lamellar-like structure that grows in the direction perpendicular to the laser polarization. This nanostructure induced birefringence because of the refractive index difference between the two phases (lithium niobate-rich regions, crystalline with lithium niobate-poor vitreous ones).

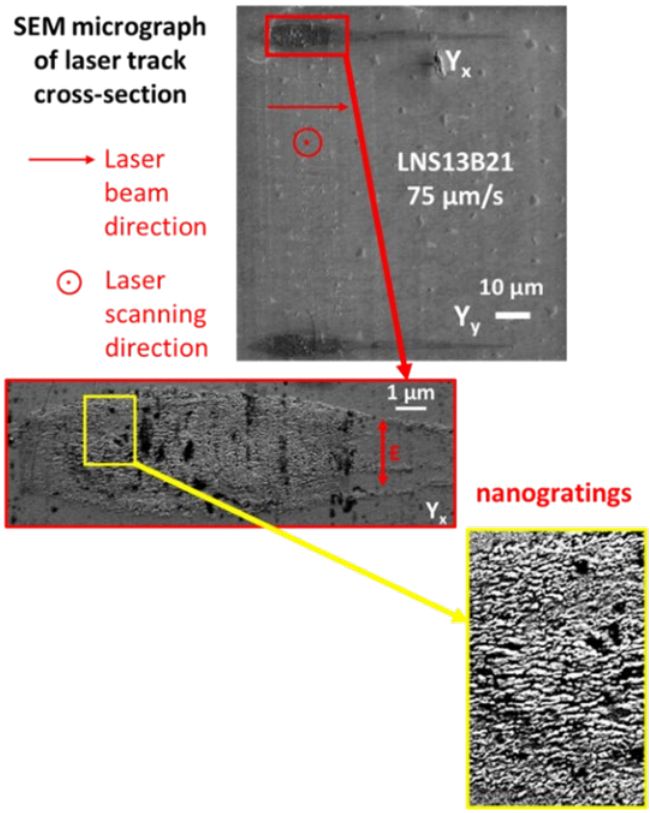

Figure 62: Presence of nanogratings detected by Scanning Electron Microscopy analysis for LNS13B21 line at pulse energy equal to 0.5 µJ, repetition rate fixed at 200 kHz, and scanning speed equal to 75 µm/s.

Considering the same sample at different scanning speeds, we noted that different aspects of nanogratings and various zones are identified and reported in Figure 63. Firstly, the observed crystallized volume diminishes at increasing scanning speed, as highlighted in yellow. In addition, the length, and not so much the width, of the region where lamella-like structuring is observed, in orange, also progressively decreases as scanning speed increases.

At 1 µm/s, there is a complete overlap between the crystallized and lamellas regions; otherwise, it is much reduced at higher speeds until 150 µm/s. This is very similar to observations reported in [19]. At low pulse energy of 0.5 µJ/pulse, the lamella area also coincides with the crystallized one. Otherwise, at higher pulse energy, the lamella area becomes smaller with respect to the crystallized one, i.e., the overlap is reduced. Then, lamellas forming nanogratings result from direct interaction with the laser light, whereas crystallization is not.

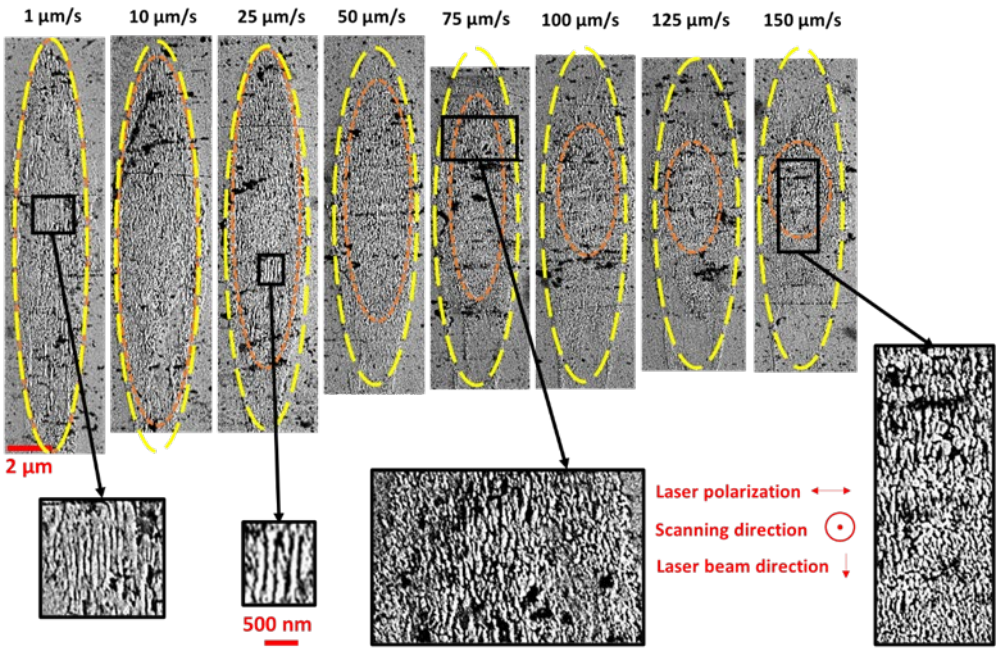

Figure 63: Scanning electron micrographs of the laser track cross-section induced by fs-laser on LNS13B21 glass sample and for different scanning speeds. In yellow there is the area where crystallization within the laser track, associated with crystallization, is detected; in orange, the area where lamella-like nanogratings are observed. Fixed parameters are: λ = 1330 nm; f = 200 kHz; NA = 0.6; pulse duration = 250 fs; focal depth = 240 µm (in air) [18].

4.6.2 Electron Back Scatter Diffraction (EBSD)

Electron Back Scatter Diffraction (EBSD) allows to validate the presence of lithium niobate crystals and study their morphology, nanostructure, and orientation inside the laser tracks cross-sections. According to the following Figure 64, black parts indicate the amorphous zones; otherwise, when colors are present, they correspond to crystals with an assigned space group and orientation. The reference indication is the crystal axis perpendicular to the laser polarization, corresponding to the maximum of the SHG intensity for all four glass compositions. The inverse pole figure (IPF) color code is based on the $LiNbO_3$ space group, with coding along the laser polarization direction. For a more detailed explanation of the EBSD working principle, refer to [26]–[30].

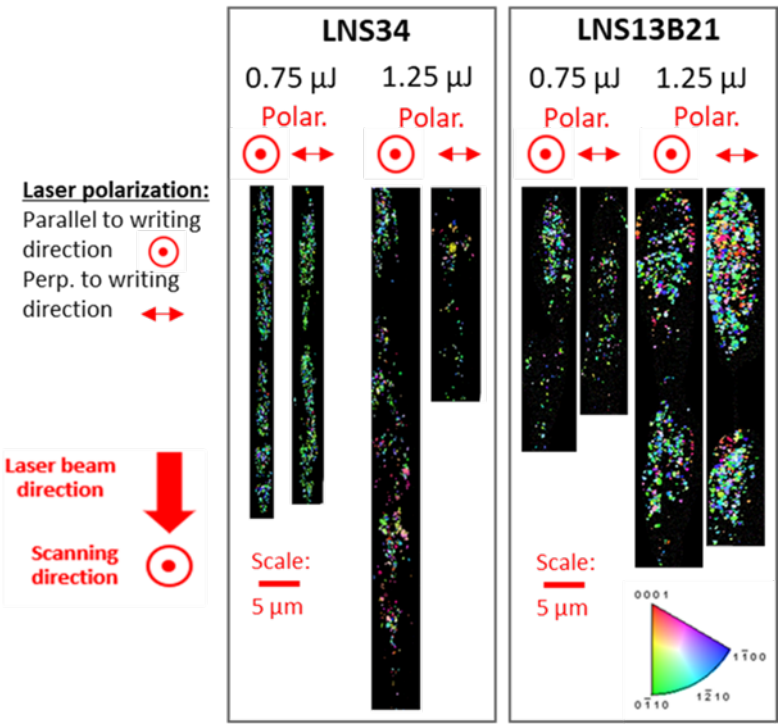

Figure 64: Electron Back Scatter Diffraction (EBSD) micrographs of the laser track cross-section for both LNS34 and LNS13B21 glass sample, for two pulse energies (0.75 and 1.25 µJ/pulse) and with laser polarization either parallel or perpendicular to the scanning direction [6]

Firstly, we observed that there was the precipitation of $LiNbO_3$ nanocrystals. Secondly, the inverse pole figure (IPF) color code shows the crystal c axis (along 0001 direction) found to be oriented perpendicular to the laser polarization, corresponding to the absence of red color on the EBSD map.
This is valid at the lowest pulse energy (i.e., 0.75 µJ/pulse). At higher energies, i.e., 1.25 µJ/pulse, crystal c axis orientation varies and is only partially oriented along the polarization direction. Then, we demonstrated the agreement between SHG response and EBSD results: in fact, at low pulse energies, the crystals are well oriented with c axis perpendicular to writing laser polarization and coincide with a maximum SHG contrast with a nearly single texturation. When pulse energy became higher, a part of the nanocrystals population exhibited c axis orientation along the polarization leading to a more spatially distributed SHG response.
Regarding the distribution of the crystals, we reported the size of single texture regions (in nm) as a function of the number of crystalline domains in Figure 65, for

LNS34 and LNS13B21 at Y_y polarization configuration, for 0.75 and 1.25 μJ/pulse. We noted the tendency to form larger regions with the same textures at the highest pulse energy compared to the lowest energy conditions.

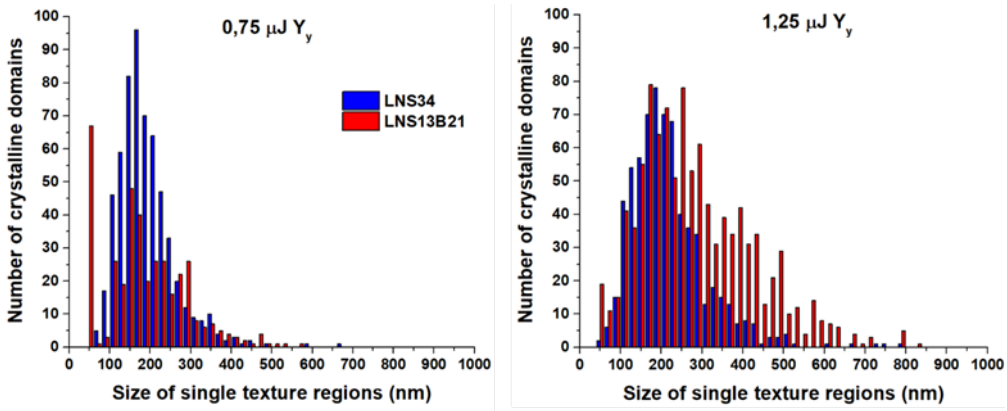

Figure 65: Size distribution of single texture regions for LS34 and LNS13B21 for Yy configuration and two different pulse energies (0.75 and 1.25 μJ/pulse). Irradiations conditions: λ= 1030 nm, NA = 0.6, f= 200 kHz, focus depth = 240 μm in air, writing speed = 1 μm/s [6].

If we consider the series of experiments at variable scanning speeds, we could represent the situation with other pictures that express the influence of speed on crystallization kinetics. In the following Figure 66, we compared SEM micrographs and EBSD maps for three different scanning speeds of LNS13B21 laser tracks cross-sections at Y_y configuration: there is a concentration of nanocrystals at laser track center in the head as the speed increases; at low speed, there are larger regions of similar crystalline orientation that correspond to similar color in the inverse pole figure (IPF). Here, it is already visible the presence of larger crystalline domains with the same orientation in the low-speed regime relative to the high-speed one, but in Figure 66, this phenomenon is highlighted quantitatively.

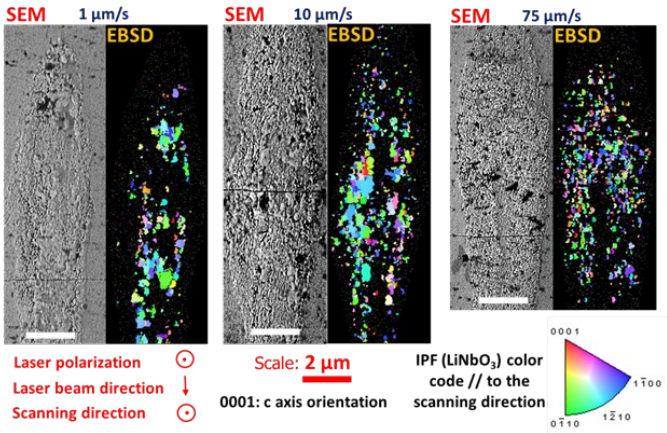

Figure 66: Scanning electron microscope (SEM) micrographs and electron backscatter diffraction (EBSD) maps on the laser track cross-sections induced by fs-laser on LNS13B21 for different scanning speed. Fixed parameters are: pulse energy = 0.5 µJ; configuration = Y_y (laser polarization parallel to the scanning direction); λ = 1330 nm; f = 200 kHz; NA = 0.6; pulse duration = 250 fs; focal depth = 240 µm (in air) [18].

In addition, also to have the complete information on the size distribution, Figure 67a shows the average size of the regions of the same orientation (single texture) as a function of scanning speed (in magenta) and the number of single texture regions per laser track (in blue). Figure 67b allows us to confirm the presence of a dominant texture: the pole figures of the $LiNbO_3$ c axis reveal that c axis is perpendicular to the laser polarization for all laser tracks. Indeed, as the scanning speed increases, the preferential orientation of c axis becomes less evident.

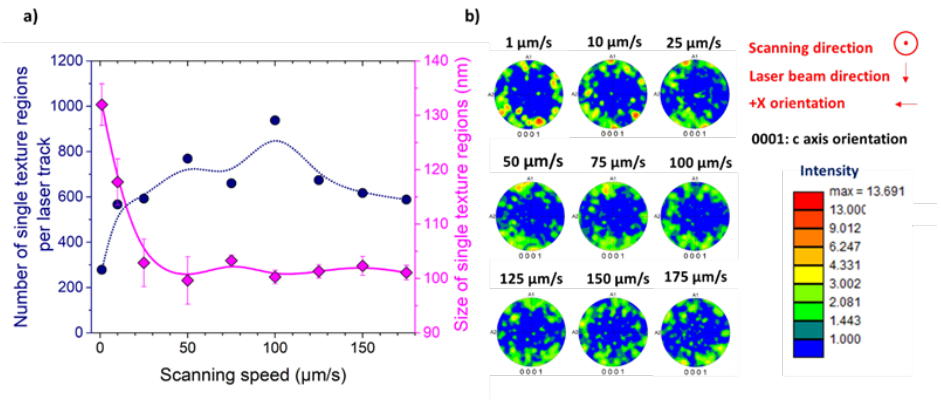

Figure 67: a) number of single texture regions and their averaged diameter, assuming a spherical shape, as a function of scanning speeds; b) pole figures of the $LiNbO_3$ c axis

(labeled 0001); extracted from data of laser cross sections at Y_y polarization reported in EBDS maps of Figure 4.20 [18]. The writing direction is in the center of pole figures; the laser propagation is at the top and the bottom of each pole figure.

4.7 Conclusions

This chapter begins by highlighting the relevance of a suitable glass matrix selection of specific optical transparency to minimize light scattering. To properly study the 3D modifications of optical properties in glass, the process of samples investigation first focuses on the irradiation of the LNS reference glass. Then, the LNSB matrices, including LNS13B21 presenting has the highest amount of B_2O_3, also are investigated. A detailed description of laser employed and its parameters, focusing on the pulse energy, repetition rate, light polarization, and scanning speed are used to describe both the static and dynamic modes utilized during the experiments. A suitable choice of laser parameters is fundamental because the glass chemical composition may affect them. Firstly, laser-induced dots are used to define a threshold energy value and an incubation time. Secondly, writing lines allow to consider the effect of scanning speed. Dots and lines are analyzed by polarized optical microscopy to provide retardance measurements induced by form birefringence and to identify slow and fast optical axes of the fabricated structures. Moreover, by retardance measurements, the maximum response for LNS13B21 was found to be about twice the value of the LNS glass. The SHG intensity is examined according to angular dependency by linear polarization, highlighting the orientation of nanocrystals c axis perpendicular to the polarization orientation. QPM was employed to study the variations of refractive indices of the written lines. Moreover, SEM analysis demonstrated the presence of lamellar nanogratings that grow in direction perpendicular to the laser polarization, clearly highlighting the role of laser polarization on the nanoscale phase separation. To identify the parameters a, b, c, and space group of $LiNbO_3$ through morphology, nanostructure, and orientation, EBDS analysis was carried out, demonstrating an agreement with SHG results.

4.8 Bibliography

[1] J. Cao, L. Mazerolles, M. Lancry, and B. Poumellec, “Creation and orientation of nano-crystals by femtosecond laser light for controlling optical non-linear response in silica-based glasses,” Université Paris-Saclay, France, 2017. [Online]. Available: Jing Cao. Creation and orientation of nano-crystals by

femtosecond laser light for controlling optical non-linear response in silica-based glasses. Material chemistry. Université Paris-Saclay, 2017. English. ⁄NNT : 2017SACLS055⁄. ⁄tel-01988887⁄

[2] J. Cao *et al.*, "Nanoscale Phase Separation in Lithium Niobium Silicate Glass by Femtosecond Laser Irradiation," *J. Am. Ceram. Soc.*, vol. 100, no. 1, pp. 115–124, Jan. 2017, doi: 10.1111/jace.14570.

[3] H. Jain, D. Savytskii, and V. Dierolf, "Single Crystal Growth via Solid → Solid Transformation of Glass," *Trans Indian Inst Met*, vol. 72, no. 8, pp. 1971–1979, Aug. 2019, doi: 10.1007/s12666-019-01737-6.

[4] D. Savytskii, B. Knorr, V. Dierolf, and H. Jain, "Demonstration of single crystal growth via solid-solid transformation of a glass," *Sci Rep*, vol. 6, no. 1, p. 23324, Sep. 2016, doi: 10.1038/srep23324.

[5] Y. Yonesaki, K. Miura, R. Araki, K. Fujita, and K. Hirao, "Space-selective precipitation of non-linear optical crystals inside silicate glasses using near-infrared femtosecond laser," *Journal of Non-Crystalline Solids*, vol. 351, no. 10–11, pp. 885–892, Apr. 2005, doi: 10.1016/j.jnoncrysol.2005.01.076.

[6] E. Muzi *et al.*, "Polarization-oriented $LiNbO_3$ nanocrystals by femtosecond laser irradiation in LiO_2–Nb_2O_5–SiO_2–B_2O_3 glasses," *Opt. Mater. Express*, vol. 11, no. 4, p. 1313, Apr. 2021, doi: 10.1364/OME.417461.

[7] J. Cao, M. Lancry, F. Brisset, L. Mazerolles, R. Saint-Martin, and B. Poumellec, "Femtosecond laser-induced crystallization in glasses: growth dynamics for orientable nanostructure and nano crystallization," p. 11.

[8] "Polarized Light Microscopy - Microscope Configuration | Olympus LS." https://www.olympus-lifescience.com/en/microscope-resource/primer/techniques/polarized/configuration/ (accessed Jul. 29, 2021).

[9] "Principles of Birefringence," *Nikon's MicroscopyU*. https://www.microscopyu.com/techniques/polarized-light/principles-of-birefringence (accessed Jul. 29, 2021).

[10] "Polarized Light Microscopy - The de Sénarmont Compensator | Olympus LS." https://www.olympus-lifescience.com/en/microscope-resource/primer/techniques/polarized/desenarmontcompensator/ (accessed Feb. 02, 2022).

[11] B. Poumellec, M. Lancry, A. Chahid-Erraji, and P. G. Kazansky, "Modification thresholds in femtosecond laser processing of pure silica: review of dependencies on laser parameters [Invited]," *Opt. Mater. Express, OME*, vol. 1, no. 4, pp. 766–782, Aug. 2011, doi: 10.1364/OME.1.000766.

[12] X. He *et al.*, "Size-controlled oriented crystallization in SiO_2-based glasses by femtosecond laser irradiation," *J. Opt. Soc. Am. B*, vol. 31, no. 2, p. 376, Feb. 2014, doi: 10.1364/JOSAB.31.000376.

[13] M. Beresna, M. Gecevičius, and P. G. Kazansky, "Ultrafast laser direct writing and nanostructuring in transparent materials," *Adv. Opt. Photon.*, vol. 6, no. 3, p. 293, Sep. 2014, doi: 10.1364/AOP.6.000293.

[14] M. Sakakura, M. Shimizu, Y. Shimotsuma, K. Miura, and K. Hirao, "Temperature distribution and modification mechanism inside glass with heat accumulation during 250kHz irradiation of femtosecond laser pulses," *Appl. Phys. Lett.*, vol. 93, no. 23, p. 231112, Dec. 2008, doi: 10.1063/1.3046101.

[15] H. Yao *et al.*, "Photosensitivity of barium germano-gallate glasses under femtosecond laser direct writing for Mid-IR applications," *Ceramics International*, p. S027288422102736X, Aug. 2021, doi: 10.1016/j.ceramint.2021.08.333.

[16] S. M. Eaton *et al.*, "Heat accumulation effects in femtosecond laser-written waveguides with variable repetition rate," *Opt. Express*, vol. 13, no. 12, p. 4708, 2005, doi: 10.1364/OPEX.13.004708.

[17] "Polarized Light Microscopy - The First Order (Full Wave) Retardation Plate | Olympus LS." https://www.olympus-lifescience.com/en/microscope-resource/primer/techniques/polarized/firstorderplate/ (accessed Jul. 29, 2021).

[18] E. Muzi *et al.*, "Towards a Rationalization of Ultrafast Laser-Induced Crystallization in Lithium Niobium Borosilicate Glasses: The Key Role of the Scanning Speed," *Crystals*, vol. 11, no. 3, p. 290, Mar. 2021, doi: 10.3390/cryst11030290.

[19] "Femtosecond Laser-Induced Crystallization in Glasses: Growth Dynamics for Orientable Nanostructure and Nanocrystallization | Crystal Growth & Design." https://pubs.acs.org/doi/10.1021/acs.cgd.8b01802 (accessed Jan. 14, 2021).

[20] J. Cao, B. Poumellec, F. Brisset, A.-L. Helbert, and M. Lancry, "Angular Dependence of the Second Harmonic Generation Induced by Femtosecond Laser Irradiation in Silica-Based Glasses: Variation with Writing Speed and Pulse Energy," *WJNSE*, vol. 05, no. 03, pp. 96–106, 2015, doi: 10.4236/wjnse.2015.53012.

[21] M. Lancry, B. Poumellec, A. Chahid-Erraji, M. Beresna, and P. Kazansky, "Dependence of the femtosecond laser refractive index change thresholds on the chemical composition of doped-silica glasses," *Optical Materials Express*, vol. 1, pp. 711–723, Aug. 2011, doi: 10.1364/OME.1.000711.

[22] J. Cao, L. Mazerolles, M. Lancry, D. Solas, F. Brisset, and B. Poumellec, "Form birefringence induced in multicomponent glass by femtosecond laser direct writing," *Opt. Lett.*, vol. 41, no. 12, p. 2739, Jun. 2016, doi: 10.1364/OL.41.002739.

[23] E. Bricchi, B. G. Klappauf, and P. G. Kazansky, "Form birefringence and negative index change created by femtosecond direct writing in transparent materials," *Opt. Lett.*, vol. 29, no. 1, p. 119, Jan. 2004, doi: 10.1364/OL.29.000119.

[24] I. H. Malitson, "Interspecimen Comparison of the Refractive Index of Fused Silica," *Journal of the Optical Society of America*, vol. 55, no. 10, pp. 1205–1209, Oct. 1965.

[25] N. Erdman, D. C. Bell, and R. Reichelt, "Scanning Electron Microscopy," in *Springer Handbook of Microscopy*, P. W. Hawkes and J. C. H. Spence, Eds. Cham: Springer International Publishing, 2019, pp. 229–318. doi: 10.1007/978-3-030-00069-1_5.

[26] "Géosciences Montpellier - How EBSD measurements work." http://www.gm.univ-montp2.fr/spip.php?article104 (accessed Aug. 19, 2021).

[27] V. Randle and O. Engler, *Introduction to Texture Analysis: Macrotexture, Microtexture and Orientation Mapping*. CRC Press, 2000.

[28] L. N. Brewer and J. R. Michael, "Risks of 'Cleaning' Electron Backscatter Diffraction Data," *Micros. Today*, vol. 18, no. 2, pp. 10–15, Mar. 2010, doi: 10.1017/S1551929510000040.

[29] S. I. Wright and M. M. Nowell, "EBSD Image Quality Mapping," *Microsc. Microanal.*, vol. 12, no. 01, pp. 72–84, Feb. 2006, doi: 10.1017/S1431927606060090.

[30] R. Petrov, L. Kestens, A. Wasilkowska, and Y. Houbaert, "Microstructure and texture of a lightly deformed TRIP-assisted steel characterized by means of the EBSD technique," *Materials Science and Engineering: A*, vol. 447, no. 1–2, pp. 285–297, Feb. 2007, doi: 10.1016/j.msea.2006.10.023.

Chapter 5

Crystallization mechanisms and kinetics upon laser-glass

This chapter aims to provide an interpretation of the results from the previous chapter: what happens inside the glass material during nanocrystals formation. The below discussion is based on the two published articles emerged from this Ph.D. work, below cited as the main explanatory bibliography [1] (especially for section 5.1), [2] (especially for section 5.3, as well as [3]), and on the content of Jing Cao's thesis [4], as regards the results obtained for the LNS glass matrix.

This chapter describes how laser induced crystallization evolves as a function of glass composition (four compositions taken). First, we focus our attention on B_2O_3 addition in the glass network, considering the effect on nanocrystal orientation influenced by different laser polarization configurations after the first publication in *Optical Materials Express* [1]. Then, describing in depth what happened under a scanning regime and considering only two compositions, the reference one (LNS34) and the one with the greatest amount of B_2O_3 (LNS13B21). The continuous cooling transformation (CCT) and time temperature transformation (TTT) diagrams were employed to interpret crystallization mechanisms following the discussion published in a second article in *MDPI Crystals*[2].

Structurally, chapter 5 is composed of five sections. The first one includes a discussion about nanocrystals nucleation and growth, focusing the attention on their orientation and exploring the interconnection between the nanostructure of the material, the optical properties, and the laser parameters. Secondly, the link between SHG response and EBSD maps provides information on how nanogratings

formation is connected to birefringence and refractive index variation, employing specific characterization results.
Furthermore, after a general introduction to explain how general TTT and CCT diagrams were modified by fs laser irradiation in the third section, the analysis of the crystallization domain between the two glass compositions, LNS34 and LNS13B21, is the subject of the fourth section. Finally, the advantageous addition of boron is the final topic included in the last section, to motivate all the explications provided until now.

5.1 Agreement between SHG response and EBSD maps in LNS and LNSB glass matrices

As theoretically described in chapter 3, femtosecond laser irradiation induces permanent transformations in glasses, including crystallization, specifically with respect to morphology, crystal texture and nanostructure. We intend to explore, in this section, what happens in lithium niobium borosilicate glasses (LNS27B7, LNS20B14 and LNS13B21) compared with the B_2O_3-free silicate one (LNS34), of which has been extensively studied by this research group [4] – [11]. Then, we will deeply discuss the mechanism of crystals orientation generated as a function of the laser polarization variation.
Following this, the ultra-fast laser-matter interaction analysis, according to variation of pulse energy, repetition rate, writing configuration and scanning speed raises a fundamental question. Which parameters have to be chosen optimally to obtain non-linear optical properties related to glass crystallization and consequentially adopted in applications of optics and photonics?

5.1.1 Three regimes and landscapes

We present here an overview showing how closely the four laser parameters are connected (pulse energy, repetition rate, laser polarization, and scanning speed) in the case of the reference composition LNS and then as the three compositions LNSB allowed the evolution of the results with the addition of B_2O_3 in the glass network. A general approach is to study parameter landscapes, starting with pulse energy – repetition rate landscape to show the connection between the laser parameters and the crystallization kinetics and mechanism, as reported in Figure 68 [12].

The deposited power (a), as a result of the pulse energy (E_p) multiplied by the repetition rate (RR) ($E_p \times RR = a$), affects the crystal growth.

Three regimes can be identified clearly to highlight threshold values of thermal power and consequently the interconnection between laser parameters variation and phenomena induced in glass depending on composition. We can describe three regimes considering Figure 68 and 69.

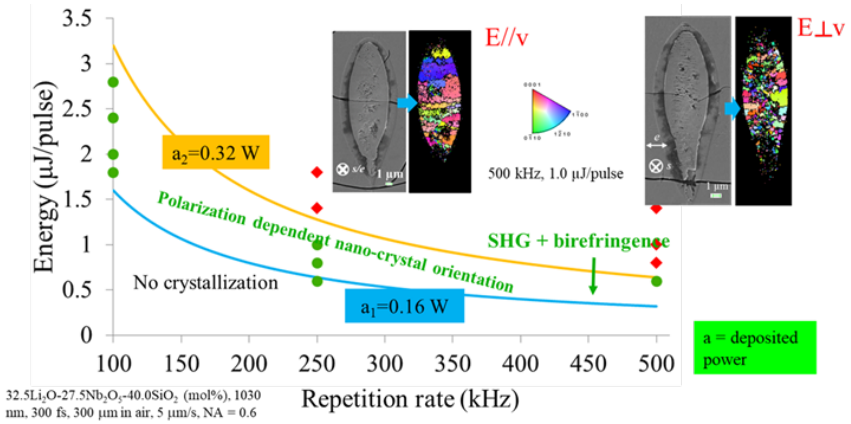

Figure 68: LNS pulse energy-repetition rate landscape [12]

This following figure shows the effective presence of a writing orientation effects [5]. Orientation means the movement along a specific direction [5]. The orientation direction depends on writing laser polarization: two configurations of laser polarization particularly studied, as reported in Figure 69 [3].

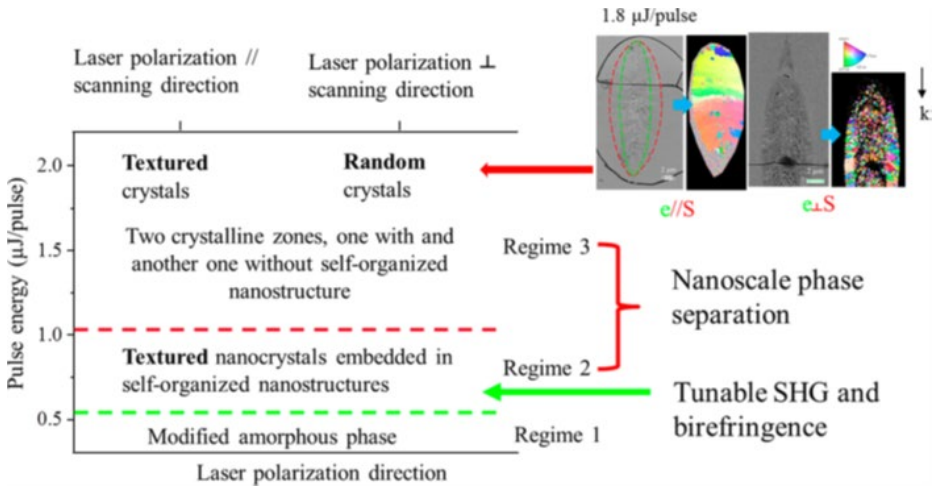

Figure 69: Pulse energy - polarization direction landscape for LNS glasses closed to $30Li_2O - 30Nb_2O_5 - 40SiO_2$, highlighting the presence of three regimes. k is the laser propagation direction, e stands for the writing laser polarization direction, and S is the scanning

direction. Other parameters: 1030 nm, 300 fs, NA = 0.6, 300 kHz, 5 µm/s, and focus depth 350 µm [3].

In the regime 1 (i.e., at low pulse energy, < 0.5 µJ/pulse), no crystallization occurs but it is possible to note modifications in amorphous structure revealed through an isotropic negative refractive index variation. The threshold value of thermal power is indicated on the diagram as a_1 and equal to 0.16 W.

Secondly, there is regime 2 (0.5 – 0.9 µJ/pulse, 300 kHz) in which nanocrystals growth direction is dependent on the laser polarization variation, and it is possible to tweak the orientation of nanocrystals by using light properties. The nanocrystals are embedded in self-organized nanostructures (nanogratings, which will be discussed in the following section), and they induce optical properties as tunable SHG and form birefringence. The nanoscale phase separation at the origin of nano-gratings starts to be detectable in regime 2 and continues to be present also in regime 3. Finally, regime 3 (1.0 – 2.2 µJ/pulse, 300 kHz) includes two different crystalline zones: one with nano-gratings and microcrystals oriented according to scanning direction parallel to laser polarization; the other one without nano-gratings and with nanocrystals randomly localized when scanning direction is perpendicular to laser polarization [5].

Moreover, summarizing through SEM micrographs and corresponding inverse pole figure (IPF) of the cross section of irradiated line, Figure 70 shows the possible crystals configurations and related regimes.

The right (framed) image encloses the cross section of the crystals orientations disordered referred to direction perpendicular to laser polarization reported in Figure 70.

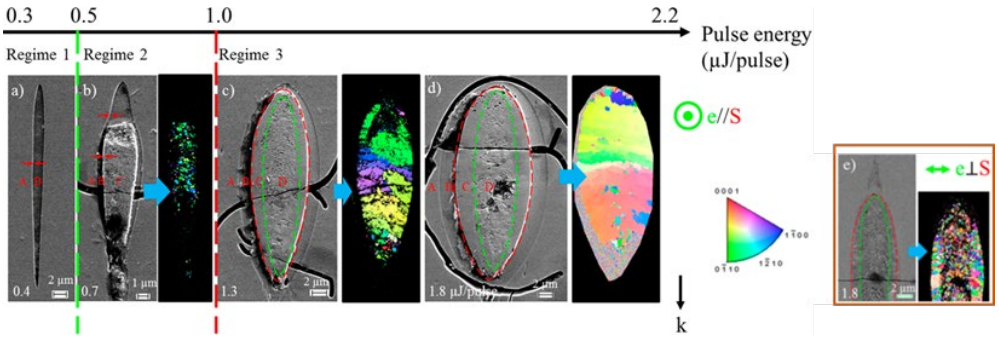

Figure 70: High repetition rate fs laser-induced regimes in LNS glass according to pulse energy indicated in white in each SEM micrograph. For regime 2 and 3, the left image is a SEM micrograph, and the right one is the corresponding inverse pole figure (IPF) of the cross section of the irradiated line. The scanning direction is perpendicular to the paper plane. The color of IPF is obtained from on $LiNbO_3$ space group R3c, coding along scanning direction. These are configurations in which laser polarization is (a – d) parallel or (e) perpendicular to scanning direction. Laser polarization direction is marked by green

e, while scanning direction id displayed by red S. k represents the laser come from the top. Other parameters for $33Li_2O - 33Nb_2O_5 - 34\ SiO_2$ are 1030 nm, 300 fs, 300 kHz, 5 μm/s, and focus depth 350 μm [3].

Moreover, we integrate the discussion by considering the scanning speed whose interconnection with pulse energy is well highlighted in the diagram of Figure 71 [3]. The pink line acts to separate regime 2 with nanocrystal orientation tunability and regime 3 with large grains and even single grain with polar axis aligned with scanning direction. In conditions of high energy and low speed, there is only a texture oriented and polarization-independent with the writing laser polarization direction *e* parallel to scanning speed *v*.

This is a scheme comparing different results obtained in Refs. [6], [7], [10], [13]. The significant role of writing laser polarization in the crystallization process was pointed out by describing in detail what occurs in regime 2 and 3.

The polar axis of crystals is not oriented along laser polarization in regime 2. The final crystallization morphology is controlled by writing configuration (the relative orientation of the laser scanning and laser polarization) in the case of regime 3. This is an effect of high pulse energy. In case of polarization parallel to scanning direction, we obtained large grains including amorphous phase since no chemical migration is detected at the grains scale.

Different results were highlighted by Veenhuizen *et al*, as only a single grain is acquired with polar axis parallel to the scanning direction at about 4.2 μJ/pulse at same scanning speed used in experiments reported in Ref. [3].

A nanoscale phase separation is revealed in regime 2 and 3. The issue of nano-gratings will be discussed in the next section 5.2.

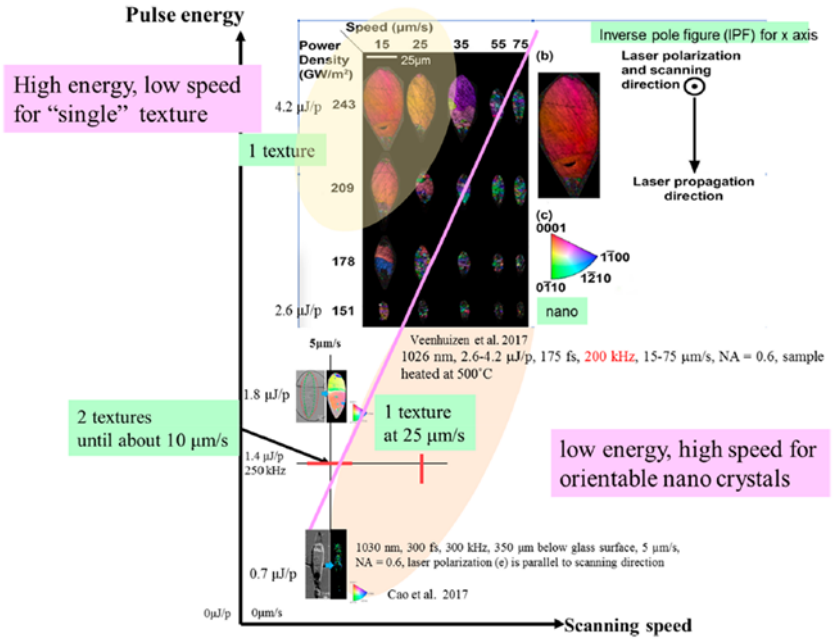

Figure 71: Pulse energy-scanning speed landscape that shows domains of fs laser-induced crystallization in LNS glasses close to $30Li_2O - 30Nb_2O_5 - 40SiO_2$. Other parameters are $\lambda = 1030$ nm, NA = 0.6, repetition rate = 200-300 kHz, parallel configuration [3].

To compare the results of different authors obtained in regime 2 and 3, according also to Figure 68, we may show the difference between experiments in Figure 72.

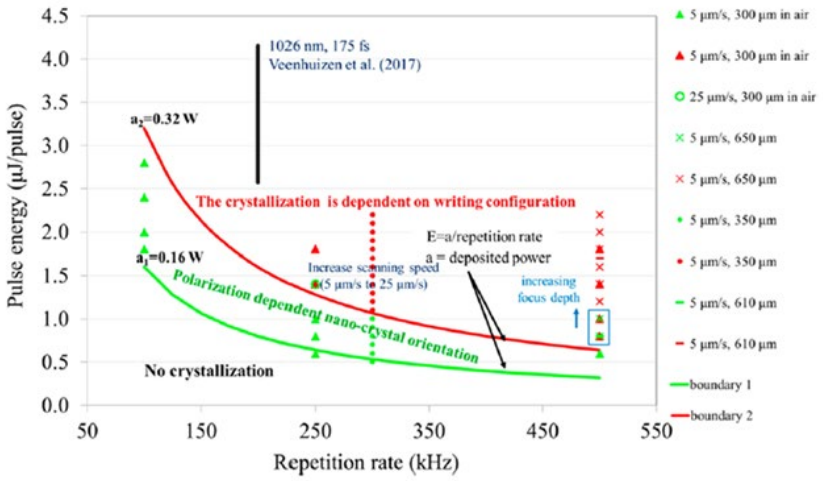

Figure 72: Pulse energy – repetition rate landscape in which domains of fs laser-induced crystallization in LNS glasses at varying scanning speed and focus depth indicating collecting results of Poumellec et al. [6] and the from Veenhuizen et al. [13]. Other parameters are $\lambda = 1030$ nm, NA = 0.6, pulse duration = 300 fs, parallel configuration. In this case, green marks indicate regime 2 of LSN glasses, and the red marks show regime 3 n LNS glasses [3].

5.1.2 Link between laser parameters and SHG measurements

Now, we intend to interconnect laser parameters with SHG measurements to explain the effect of single parameter on this optical property. Towards a comparison between LNS34 and the compositions with B_2O_3, after SHG detection, for a LNS glass matrix, specifically $32.5Li_2O - 27.5Nb_2O_5 - 40SiO_2$ (mol%), we start by reporting the results highlighting the pulse energy effect represented in the following Figure 73 [7].

In the case of LNS, at low pulse energy, the red curve at 0.8 µJ above presents a well-defined cosine-like trend with period of 180°. An angle of 90° close to writing laser polarization direction exhibits the minimum SHG intensity. When pulse energy is increased to 1.4 µJ, the green curve shows a second maximum at the place of the minimum on the simple cosine-like curve. This phenomenon becomes clear at pulse energy equal to 1.8 µJ, and it is made visible on the blue curve below.

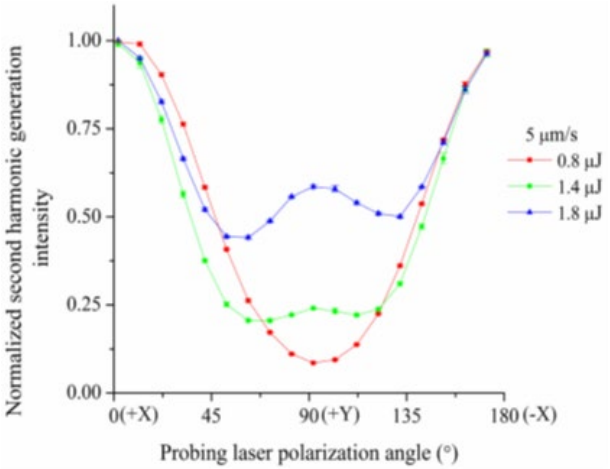

Figure 73: Pulse energy effect shown through three different values in curves trend of normalized second harmonic generation intensity of irradiated lines as function of probing laser polarization in the XY plane. Other parameters: writing speed 5 µm/s, writing direction is along 45° direction, laser polarization is parallel to Y [7].

There is also a dependence of the SHG on the writing speed, by keeping constant the pulse energy at 0.8 µJ or 1.4 µJ. This writing speed effect is visible as well-defined cosine-like curves trend in Figure 74a, highlighting the shift of the minimum value of SHG from 102° to 91°, really close to the writing polarization angle equal to 90°. For high pulse energy reported in Figure 74b, the SHG curve

varied from simple cosine-like curve, the blue curve, to the modified ones, the green and the red curve, by decreasing of the writing speed from 25 to 1 μm/s [7].

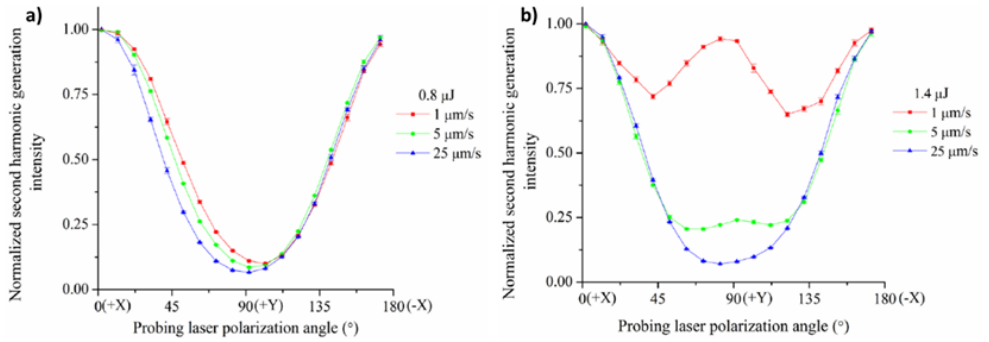

Figure 74: Writing speed effect shown through normalized second harmonic generation intensity of irradiated lines as function of probing laser polarization angle, varying pulse energy at a) 0.8 μJ and b) 1.4 μJ. Other parameters: writing direction is along 45° direction, laser polarization is parallel to Y [7].

The representation of the writing orientation effect is obtained starting from two different orientations typical of glass as center-symmetric material: the orientation at the forward direction of 45° and the one at the backward direction of 225°. In both directions, it is possible to reveal the presence of two different textures: one with *c* as the polar axis of nanocrystals (<0001>) perpendicular to the writing laser polarization, specifically X direction and one with the polar axis close to Y direction [7]. At low writing speed shown in Figure 75a, there is a conspicuous difference between two curves at different orientations. This effect, known as Asymmetric Orientational Writing (AOW) [11] is drastically reduced in correspondence of 25 μm/s, as shown in Figure 75b.

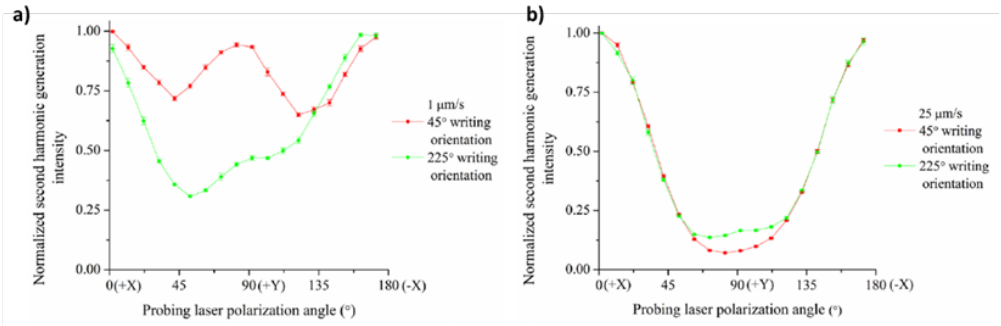

Figure 75: Writing orientation effect through normalized second harmonic generation intensity of irradiated lines as function of probing laser polarization angle, at two different writing speed a) 1μm/s and b) 25 μm/s. Other parameters: pulse energy 1.4 μJ, laser polarization is parallel to Y [7].

Another fundamental parameter is the angular contrast, which is characterized through the anisotropy magnitude expressed by the following equation:

$$anisotropy\ magnitude = (SHG_{max} - SHG_{min}) / (SHG_{max} + SHG_{min}) \quad (41)$$

For the LNS matrix, the variation of anisotropy magnitude as a function of scanning speed was explored, as reported in Figure 76.

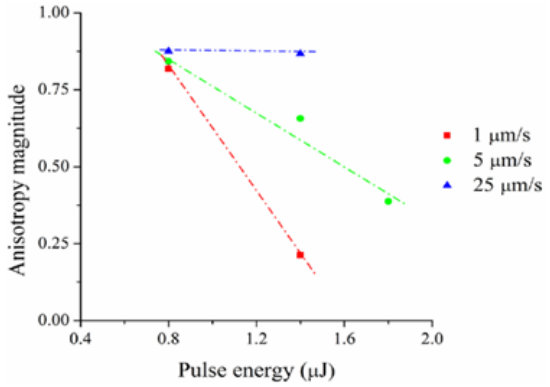

Figure 76: Variation of anisotropy magnitude-pulse energy trend as function of scanning speed. Other parameters: writing direction is along 45° direction, laser polarization is parallel to Y [7].

At 1 μm/s, the anisotropy magnitude is strongly depending on pulse energy; at 5 μm/s this trend is less pronounced with the increase of pulse energy, and it becomes not dependent on pulse energy at 25 μm/s.

These trends were extrapolated from the study of the SHG angular response of a single crystal. It is fundamental to refer to the $LiNbO_3$ theory about the second-order non-linear tensor for the symmetry R3c typical of this crystal. For its axial symmetry, the second-order non-linear susceptibility tensor ($\chi^{(2)}$) has the largest SHG coefficient ($d_{33} = 34.4$ pm/V) in the <0001> crystal direction, exactly along the polar axis. The others are $d_{31} = 5.95$ pm/V and $d_{22} = 3.07$ pm/V [14].

To quantify the relationship between the normalized SHG values and the variation of the angular probe at the generation of the two populations, the following expression has been employed:

$$I_{SHG}^{norm} = [\alpha + \beta f(\theta - \theta_1)] / [\alpha + \beta (a + b)] \quad (42)$$

where θ_1 is an angle shift from +X direction; α and β are the weights of the two populations. The number of the populations increases at increasing of pulse energy,

in case of a value equal to 1.8 μJ, three populations were obtained: one randomly oriented and two textured [7].

The data obtained with the SHG measurements are then validated with the EBSD analysis. Thanks to such microscopic analysis, it is possible to get interesting information about the formation of oriented non-linear crystals and textures. Comparing these two measurements, we must note that SHG averages the effect in the modified sample region, while the EBSD maps have a much finer resolution through laser track cross-sections surfaces.

Considering the LNS, as our reference exactly with the composition equal to $33Li_2O - 33Nb_2O_5 - 34SiO_2$, in comparison with LNSB matrices, EBSD maps show a large portion of disoriented $LiNbO_3$ crystals were randomly distributed, as reported in Figure 77 [15].

The presence of the green light confirms that the crystals acquired second-order non-linear optical properties and its nonuniform distribution indicates a non-homogeneous crystallization.

The femtosecond laser irradiation allows to obtain crystals not randomly oriented but reveals the presence of one or two or more textures. There is something that activates the formation of these textures, i.e., some forces are responsible for crystal orientation during their generation. The polar axis perpendicular to the writing laser polarization direction is one of the preferential orientation [7], [15], the one at low energy.

The thermal force leads to crystal orientation and is generated by a large thermal gradient in correspondence with focused irradiation at higher pulse energy.

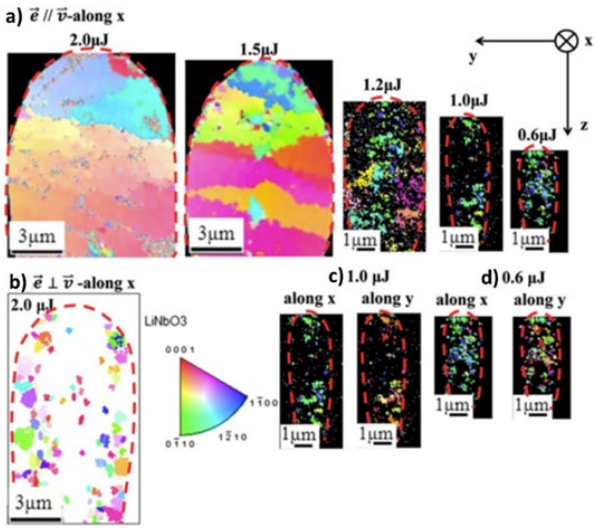

Figure 77: EBSD characterization of $33Li_2O - 33Nb_2O_5 - 34SiO_2$: a) EBSD scan images of lines cross-sections irradiated at 2.0 – 0.6 μJ with polarization parallel to the laser beam

direction that is coding the crystal orientation along x; b) EBSD images of lines cross-sections irradiated at 2.0 µJ with polarization perpendicular to laser beam direction coding crystal orientation along x; EBSD scan image coding the crystal orientation along the x-axis and along the y-axis at c) 1.0 µJ and d) 0.6 µJ, respectively. The polarization for writing is parallel to the laser motion direction. Other laser parameters: repetition rate = 300 kHz, scanning speed = 5 µm/s, pulse duration = 300 fs, wavelength = 1030 nm, and NA = 0.6 [15].

During nucleation, the dipole of nanocrystals is stimulated by a torque. As these nuclei can be assimilated to the final crystals, we observed that the ferroelectric $LiNbO_3$ might show a spontaneous dipole, it also exhibits an induced dipole with an anisotropic susceptibility so that the dipole is not always parallel to the applied electric field $\boldsymbol{E_\omega}$. We represented a non-oscillating torque $\widetilde{\Gamma_{DC}}$ generated within nanocrystal by this following expression:

$$\widetilde{\Gamma_{DC}} = DCpart\,(\boldsymbol{P_\omega} \wedge \boldsymbol{E_\omega}) \tag{43}$$

$$\boldsymbol{P_\omega} = \varepsilon_0\, \bar{\bar{\chi}}\, \boldsymbol{E_\omega} \tag{44}$$

$\bar{\bar{\chi}}$ is anisotropic with $\boldsymbol{P_\omega}$ the induced dipole, $\bar{\bar{\chi}}$ the first order susceptibility tensor, ε_0 the vacuum dielectric constant. The relative permittivity $\bar{\bar{\varepsilon_r}}$ of a media is related to its electric susceptibility, $\bar{\bar{\varepsilon_r}} = \bar{\bar{I}} + \bar{\bar{\chi}}$ where $\bar{\bar{I}}$ is the identity matrix.
The torque allows to have the dipole $\boldsymbol{P_\omega}$ aligned on the electromagnetic field, and this corresponds to be along the largest value of the susceptibility. These values change with non-stoichiometric compositions of $LiNbO_3$. There is an expression that connect refractive index with permittivity. Then, considering a crystal reference based on its principal axes, the permittivity tensor could be given by:

$$\varepsilon = \varepsilon_0 \begin{bmatrix} \varepsilon_{11} & 0 & 0 \\ 0 & \varepsilon_{22} & 0 \\ 0 & 0 & \varepsilon_{33} \end{bmatrix} \tag{45}$$

The principal refractive indices n_{kk} (k = 1, 2, 3) could be calculated by $\varepsilon_{kk} = n_{kk}^2$. In particular, for its symmetry, $LiNbO_3$ is a uniaxial crystal with $\varepsilon_{11} = \varepsilon_{22} = n_o^2 \neq \varepsilon_{33} = n_e^2$ where n_o and n_e are the ordinary and the extraordinary refractive indexes respectively. For $LiNbO_3$, n_o is greater than n_e. This corresponds to $\varepsilon_{\perp\, polar\, axis} > \varepsilon_{\parallel\, polar\, axis}$ [7].

The largest value is thus perpendicular to the nanocrystals' polar axis, which explains the existence of the texture with polar axis of nanocrystals perpendicular to the laser polarization.

When another texture appears in the SHG angular response with the polar axis aligned with the laser polarization, its origin is more complex to explain. Two possible explanations can be given: the second texture is not at the same location in the laser track of the previous one and the electromagnetic force has non-linear origin, or the force has different nature and this last is principal, i.e., thermal one but not dependent of the laser polarization.

In fact, it is most likely a question that could involve up to three forces: one is linear and of the first order, the second one originates from the displacement of growth front that appears when there is a melting at the center of the laser track, and the last one driven by the pulse front tilt (PFT) or by other nonlinear effects to be explored. This third shows a sensitivity towards the direction of displacement and the crystals configuration nature; hence, the effect on the texture in regime 3 could be described through this last force. Generally, this discussion is related to the femtosecond laser interaction with dielectrics [16]. Summarily, multiphoton ionization or tunneling ionization generating a quasi-free electron plasma in the conduction band causes the laser light absorption. The plasma just formed can be heated by the residue of laser pulse through free carrier of one or several photon absorptions and/or expands through avalanche ionization. The existence of an Asymmetric Orientational Writing (AOW) with the femtosecond laser can be explained by the action of the ponderomotive force action, i.e., the force generated by light on the electron that intensifies the plasma density on the side of the beam [11]. Then, the subsequent trapping indicates the space charge in the materials, producing a DC field and a consequent stress field that is exercised between two laser pulses as a typical memory effect [11].

Consequently, the spontaneous dipole of the nanocrystals that may have a parallel direction to polar axis generates a second torque. The direction of the induced DC electric field leads the direction of the polar axis [11]. It relies on the orientation of the pulse front tilt (PFT), (i.e., the phenomenon for which the arrival time of a pulse varies across the beam profile), of the writing laser polarization direction and of the direction of writing. The PFT was already present in fs laser dots writing where no polarization variation is expected. Then, this consolidates the importance of polarization role, evident in laser lines writing.

Also, the stress field affects the kinetics, and it depends on the orientation of writing. Lastly, the combination of a stress field differently oriented compared to PFT vector may induce a variety of crystallization, represented by the evident

intensity of the second texture, i.e., the one aligned with the laser polarization [7], [11].

5.1.2.1 The case of LNSB glass matrices

This explanation can be referred to and adapted to the case of the four compositions examined in this thesis work.
Firstly, the discovery of a more uniform orientation of the polar axis at 0.5 μJ, not detectable at higher pulse energy, occurs not only for LNS matrix but also for LNSB, as shown in the following Figure 78a, b, and c at the three laser polarization configurations Y_x, Y_{45} and Y_y. We observed a SHG complex response already at 0.75 μJ after SHG measurements for all four glass compositions: the results are in agreement with the LNS matrix treatment reported in Ref. [7] and [15].With reference to the trend shown in Figure 73, for a quantitative and explanatory comparison with the values referred to LNS (0.8, 1.4 and 1.8 μJ), these four pulse energy values (0.5, 1.5, 1.75 and 2 μJ) for the four our glass compositions were chosen, at three different configurations of laser polarization Y_x, Y_{45}, Y_y. Figure 78 represents the pulse energy and laser polarization effects at the same time, highlighted the difference in trend for the four glass compositions, also adding the angular contrast completely diverse for each sample.
If we consider the right picture corresponding to trends at 0.5 μJ/pulse, it is clearly noted that, the left image at 0.75 μJ/pulse shows curves drastically different from the right trend most of all in the case of LNS34 and LNS13B21, in both shape and angular contrast, with a pulse energy variation of only 0.25 μJ/pulse.
Continuing the investigation of these trends, we intend to verify whether this assessment will be confirmed even at higher impulse energies at a specific laser polarization configuration.

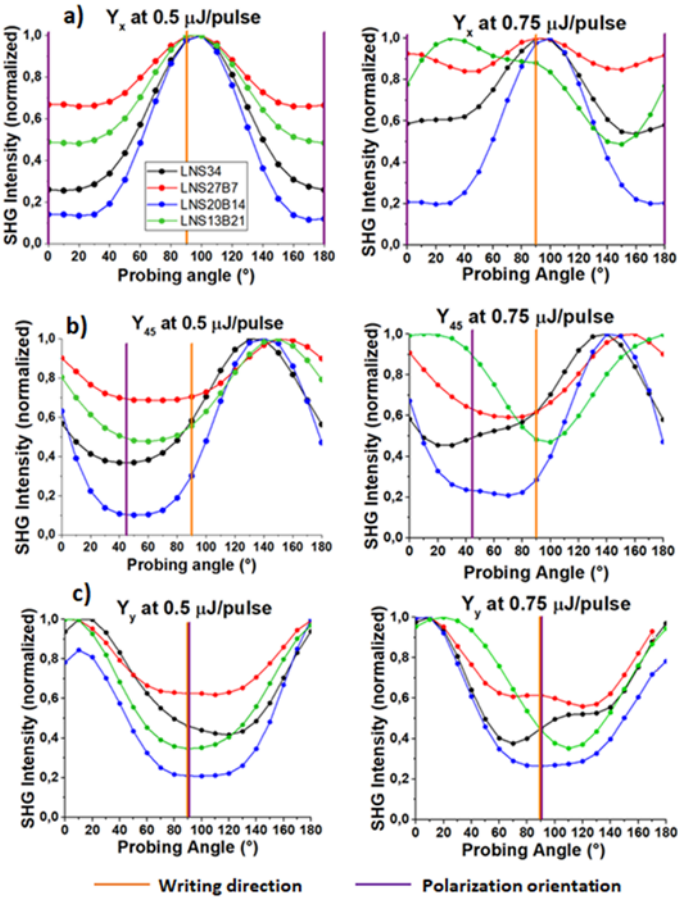

Figure 78: Normalized SHG intensity for four glass composition as a function of probing polarization angle in the XY plane for a) Y_x, b) Y_{45} and c) Y_y at the two lowest pulse energies, 0.5 and 0.75 µJ/pulse. Femtosecond laser conditions used: λ = 1030 nm, NA = 0.6, RR = 200 kHz, focus depth = 240 µm in air, scanning speed = 1 µm/s [1].

To have an overview and compare clearly the results at the three polarizations configurations, SHG trends are reported in a set of curves respectively for Y_x, Y_{45} and Y_y in Figures 79, 80 and 81.

This is a comparison between the most "stable" SHG curves at 0.5 µJ/pulse and the trends at the three highest pulse energy values 1.5, 1.75, and 2 µJ/pulse employed in our experiments.

The three images reveal how the compositions with B_2O_3 in the network have a clearly different trend compared to LNS one, at the three highest values of pulse energies. The sinusoidal behavior shown at 0.5 µJ/pulse became a variable trend, difficult to classify in a unique way, for all the four compositions.

Contrary to previous work on the LNS, no other SHG measurement experiments have been carried out varying the scanning rate and must confine our analysis on these trends. However, they already emphasized how the B_2O_3 addition had

unpredictable effects on the shape of the curves and on the formation or not of two crystals textures, that will be verified in more depth through the following EBSD analysis.

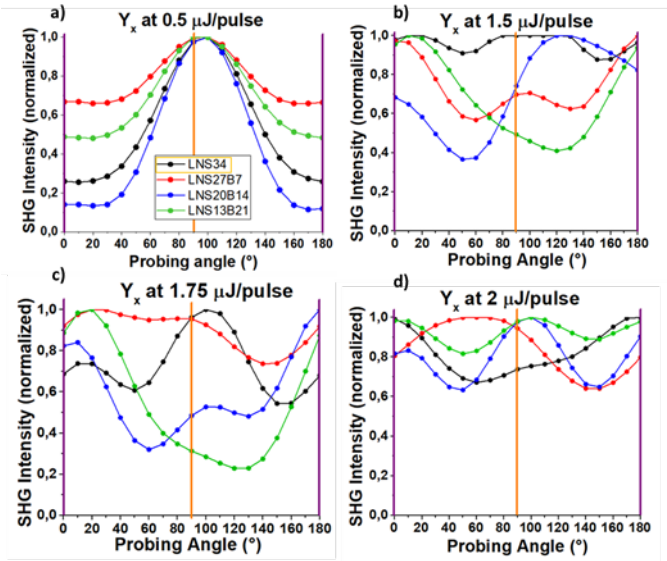

Figure 79: Comparison between four pulse energy values a) 0.5, b)1.5, c) 1.75 and d) 2 µJ at laser polarization configuration Y_x. Femtosecond laser conditions used: λ = 1030 nm, NA = 0.6, RR = 200 kHz, focus depth = 240 µm in air, scanning speed = 1 µm/s.

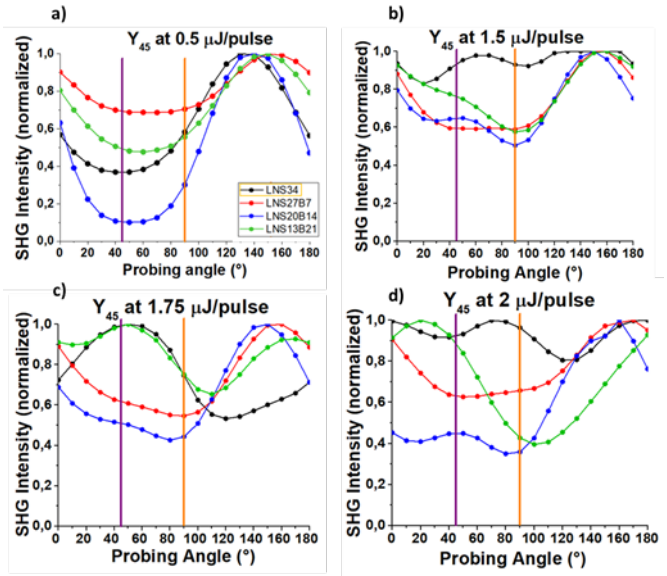

Figure 80: Comparison between four pulse energy values a) 0.5, b)1.5, c) 1.75 and d) 2 µJ at laser polarization configuration Y_{45}. Femtosecond laser conditions used: λ = 1030 nm, NA = 0.6, RR = 200 kHz, focus depth = 240 µm in air, scanning speed = 1 µm/s.

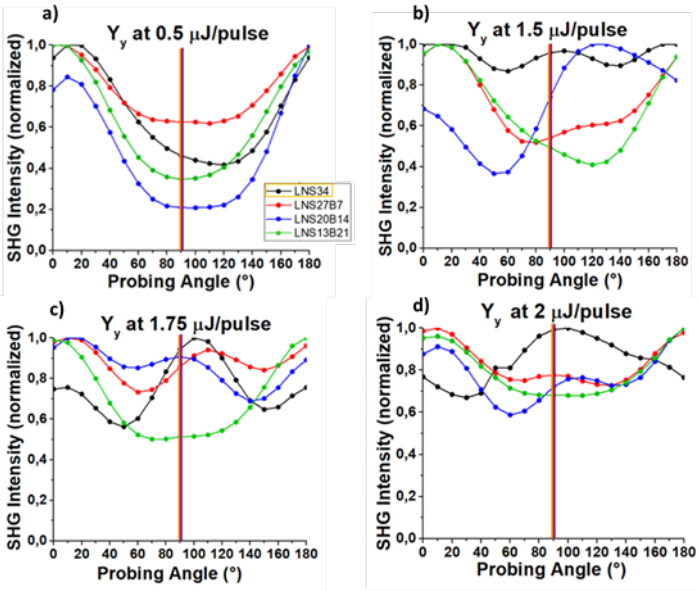

Figure 81: Comparison between four pulse energy values a) 0.5, b)1.5, c) 1.75 and d) 2 µJ at laser polarization configuration Y_y. Femtosecond laser conditions used: λ = 1030 nm, NA = 0.6, RR = 200 kHz, focus depth = 240 µm in air, scanning speed = 1 µm/s.

To have a complete picture, it is necessary to add to these SHG measurements, the relative EBSD maps in which through inverse pole figures (IPF) the two textures were properly represented, when identified.

In fact, crystals have micro or nano size, and they are not all oriented. For this reason, EBSD analysis is the best way to find the parameters and the symmetry group. For chemical composition investigation, the TEM analysis is very adequate. A combination of TEM and EBSD provides an overview of data needed to identify $LiNbO_3$.

In particular, for LNS, we have more data than LNSB glass matrix ones. EBSD indicates the space group and the parameters a, b, and c that clearly prove that we are working with $LiNbO_3$. Moreover, TEM analysis provides that Si remains inside the glassy zone, whereas the crystallization zone contains only Li, Nb and O elements. In addition, if we add to overall analysis the information from energy losses, the stoichiometry found appears to be really that of $LiNbO_3$.

For LNSB glass matrix, the information framework is different, simply because it is necessary to carry out further analyses; in fact, for now, EBSD provides the space group and parameters a, b, and c that indicate $LiNbO_3$.

Then, using the IPF maps to make micro-texture characterization of each sample considered, we consider the distribution of polar axis *c* in LNS34 and LNS13B21 samples. We intend to analyze if the two identified textures were located at the same place in the laser tracks.

Firstly, Figure 82 shows the SHG response at 1.25 and 2 µJ/pulse, focusing the attention on the reference sample LNS34 and on the one with the highest amount of B_2O_3, LNS13B21. A correspondence between increasing pulse energy and the presence of multiple directions in crystals orientation is confirmed and validated at the same time. Even though it is clearly still evident the population that reaches SHG extremes, the curve relative to LNS13S21 for Y_x shows a behavior with two minima (at 60° and at 130° for 1.25 and at 50° and 150° for 2 µJ/pulse) that are indicative of the presence of another population. This cannot be noted for configuration Y_y.

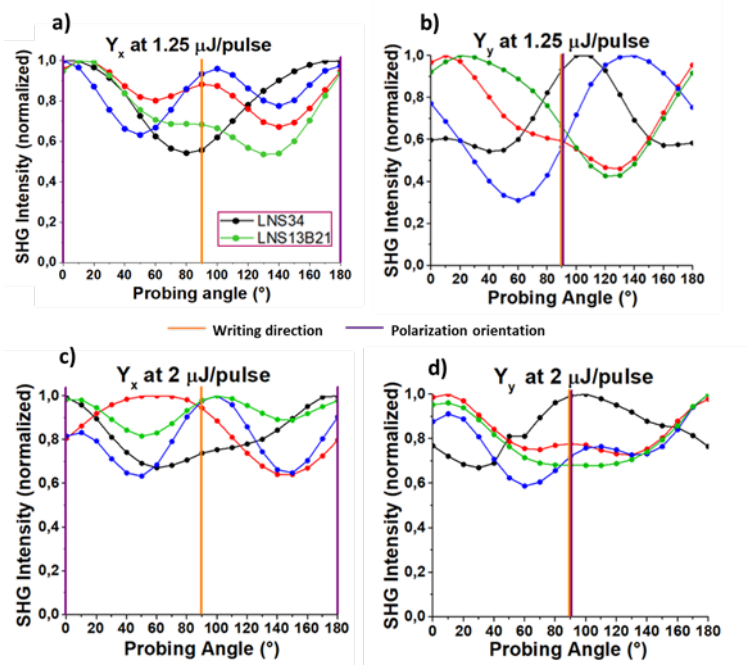

Figure 82: Normalized SHG intensity for all glass compositions according to a) Y_x at 1.25 µJ; b) Y_y at 1.25 µJ; c) Y_x at 2 µJ and d) Y_y at 2 µJ

We intend to find a link between the Figure 82 above and the results on textures revealed in the next Figures 83 and 84-87 where the polar representation and the EBSD analysis will be reported, respectively, at 1.25 and 2 µJ/pulse.

Secondly, another way to visualize the laser polarization orientations with respect to writing direction is through the polar diagrams shown in Figure 84. We chose to insert also the two found trends at 0.5 µJ/pulse, to highlight specifically how the "directionality" of SHG intensity at low pulse energy is drastically reduced, in comparison with the ones at 1.25 and 2 µJ/pulse. This is the evidence of laser polarization effect. The correspondence between LNS34 and LNS13S21 for 0.5 µJ/pulse at Y_x is unequivocal. At 1.25 µJ/pulse, the trend for the two compositions is completely different, otherwise we could find a partial correlation since it is indicative of the same direction just shifted from 90° in both glasses but at diverse configuration, Y_x and Y_y for LNS13S21 and LNS34 respectively.

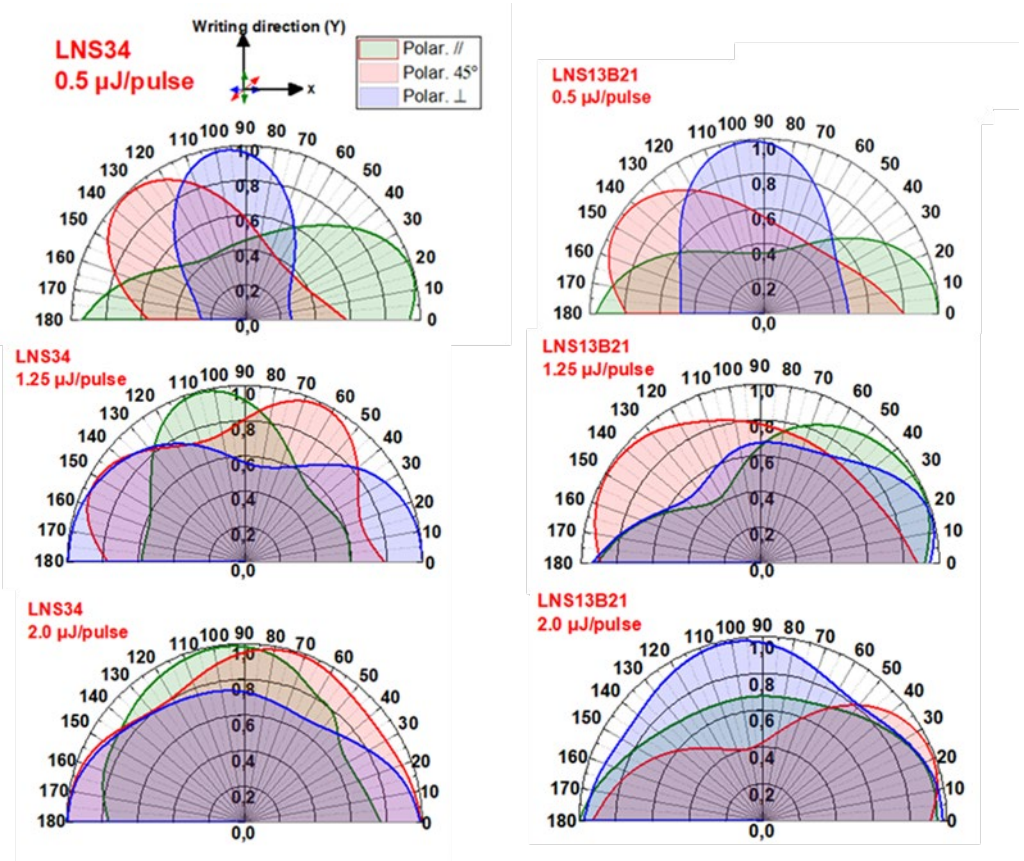

Figure 83: Polar representations for LNS34 and LNS13S21 glasses at 1.25 and 2 µJ/pulse with three laser polarization configurations indicated by double headed arrows in coordinates of the reference system: //, 45°, and ⊥.

To validate the results extracted from the polar trends at 1.25 and 2 µJ/pulse, we performed EBSD analysis inside the laser tracks cross-sections.

According to this characterization, we report the Inverse Pole Figure (IPF), a map to indicate the crystalline color part on the black background obtained through EBSD. The color in IPF is based on R3c space group of $LiNbO_3$. Three colors are

fundamental to identify axes: basic red is used for polar axis of the crystal (0 0 0 1 axis), green and blue for 0 $\bar{1}$ 1 0 and 1 $\bar{1}$ 0 0, respectively. This is the so-called red-green-blue (RGB) color model. The intermediate orientations are visualized by a RGB mixture of the primary components.

We intend to prove the role of laser polarization on the crystals growth direction through a comparison between LNS34 and LNS13B21.

Primarily, Figure 84 highlights the double width of the laser track of LNS13B21 compared to LNS34 one in case of configuration Y_y. Maps are referred to writing direction. For LNS34, we cannot put in evidence a particular orientation direction since the presence of different color in both laser tracks at two configurations. Otherwise, for LNS13B21 it is evident that, at same pulse energy equal to 1.25 μJ, green and blue color are predominant in case of laser polarization parallel of writing direction, while red color coincident with polar axis c is the most noticeable at laser polarization perpendicular to writing direction.

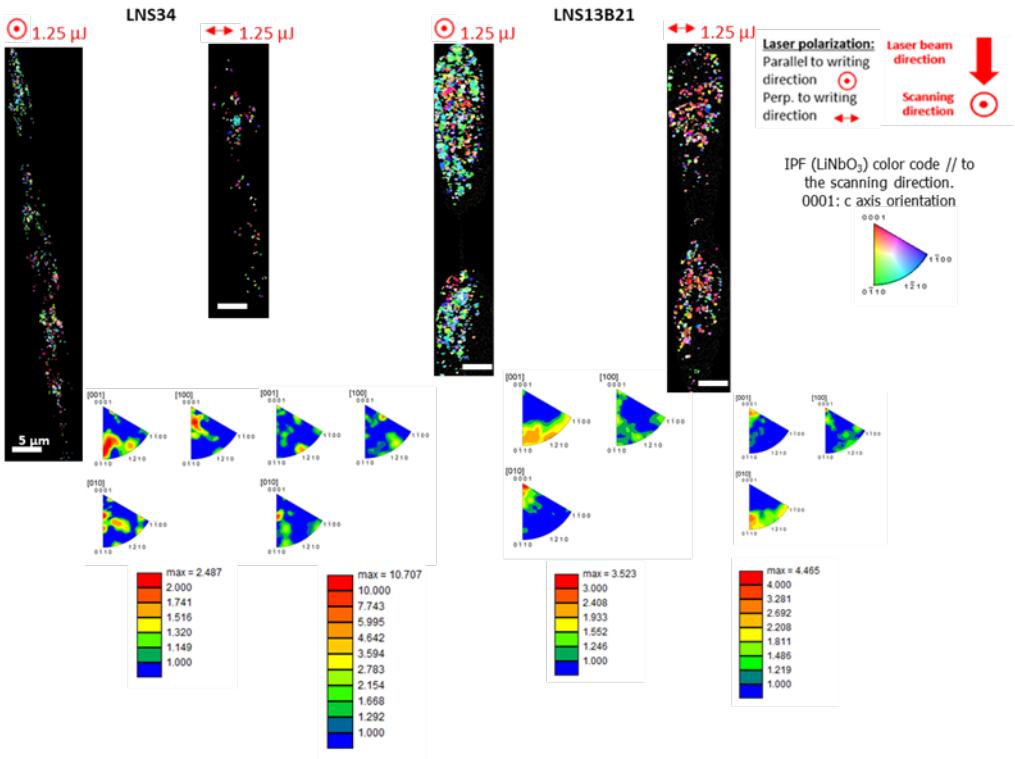

Figure 84: Inverse Pole Figure (IPF) obtained through electron backscatter diffraction (EBSD): the color in the black background represents the crystalline part for LNS34 and

LNS13B21 according Y_x and Y_y at 1.25 μJ/pulse. Other laser parameters are λ = 1030 nm; f = 200 kHz; NA = 0.6; pulse duration = 250fs; focal depth = 240 μm (in air); scanning speed = 1 μm/s.

To study the changes on the orientation directions, we reported the IPF maps related to the three reference directions used during the EBSD analysis in Figure 85.
In the scheme inside the Figure 85, it is possible to distinguish the three directions of EBSD analysis: Axis 1 (A1 on the left) which is along laser beam direction when a cross section is analyzed, and the operator corrected the alignment. Axis 3 (A3 on the right) is along scanning direction. Axis 2 (A2 in the middle) complete the reference trihedra. The laser polarization is thus the plane A2-A3.
IPF maps of LNS34 show multiple colors indicating that different orientations occur, whatever the configuration with respect to laser polarization.
Interestingly, in the case of LNS13B21, except of map referred to A1 that describe a variability of color corresponding to multiple orientation crystals direction, there is a prevalence of a particular color in case of A2 and A3: red and green have emerged at Y_y and, on the contrary green and red at Y_x, respectively. This is indicative of crystals growth with polar axis c oriented, parallel to writing direction in case of configuration Y_y and perpendicular in case of configuration Y_x.

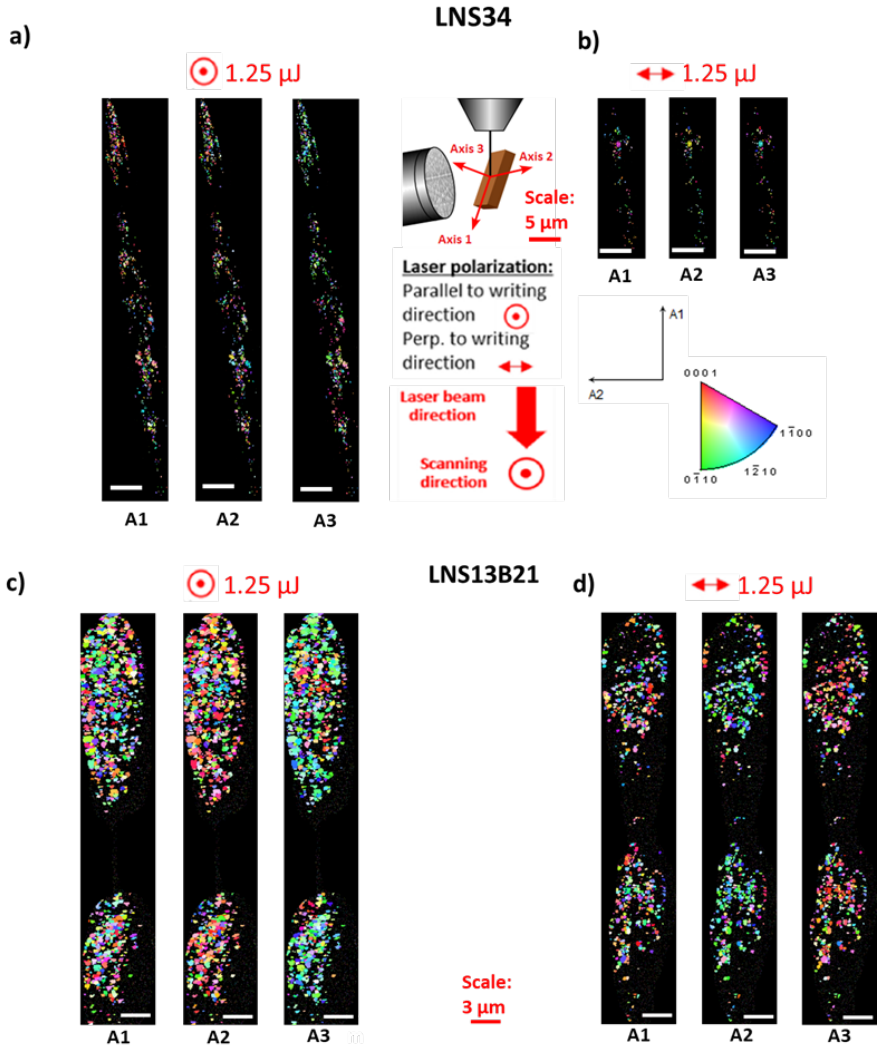

Figure 85: Inverse Pole Figure (obtained from EBDS analysis) for LNS34 at a) Y_y, and b) Y_x and for LNS13B21 sample at c) Y_y and d) Y_x, coding the crystal orientation according to the scheme reported in the figure through Axis 1 (A1 on the left), Axis 2 (A2 in the middle), and (A3 on the right) corresponding to beam direction, laser polarization, writing direction respectively, at 1.25 µJ and configurations parallel (three maps on the left) and perpendicular (three maps on the right) to laser polarization. Other laser parameters are λ = 1030 nm; f = 200 kHz; NA = 0.6; pulse duration = 250fs; focal depth = 240 µm (in air); scanning speed = 1 µm/s.

Figure 86 represents the polar figure maps, plotted in order to get a clear picture of the distribution of polar axis and to bring out the presence of multiple textures of $LiNbO_3$ crystals. We have to take into account that pole figure represents crystalline

direction or a normal plan of material in the sample reference system, while an inverse pole figure (IPF) shows a specific direction of sample within a crystalline system. The union of two different way of representation makes more complete the analysis on crystals and a clear visualization of the distribution of polar axis, to indicate the presence of two textures.

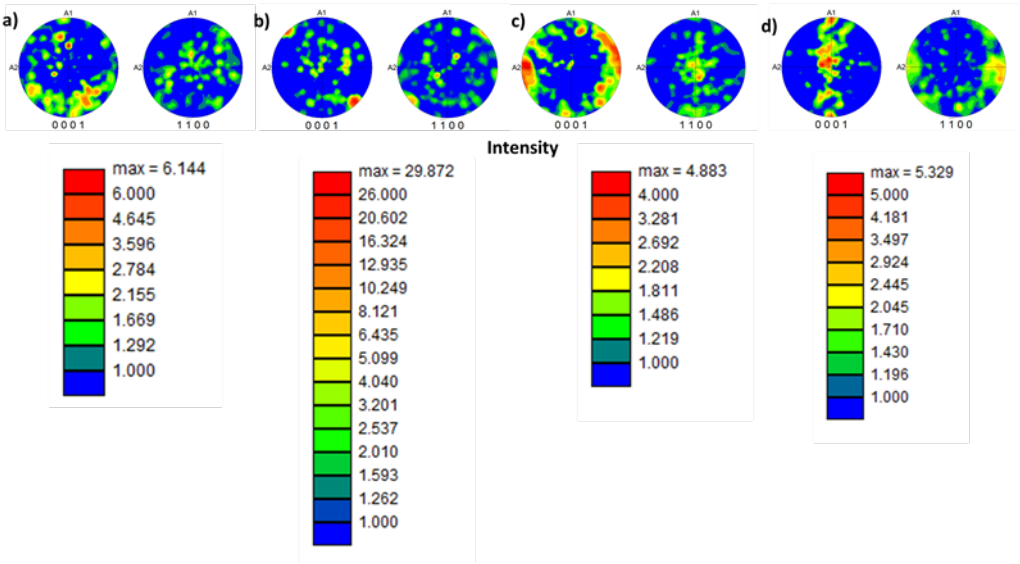

Figure 86: Polar figures referred to LNS34 at 1.25 µJ for a) Y_y, b) Y_x and LNS13B21 at 1.25 µJ for c) Y_y, d) Y_x. where A1 is the beam direction (z axis), A3 is the writing direction (y axis for Y_x and Y_y configurations), polarization is along A2 (x axis) for Y_x and along A3 for Y_y configurations.

In fact, even though in a more disordered way for LNS34, it is clear to note the presence of crystals orientation in Figure 87a and b. The organization of growth directions becomes definite in case of LNS13B21, as it is possible to see clearly in Figure 85c and d. These data have confirmed that found in previous Figure 86.
Passing through the analysis of laser tracks cross-sections at 2 µJ reported in Figure 87, it is worth to note that their width is greatly increased in both glass samples. At high pulse energy, LNS34 shows an evident tendence to assume red color in this map at Y_y. This is indicative of a distinct growth direction of polar axis c parallel to writing direction. For configuration Y_x, LNS34 exhibits a map with variable colors, and it is possible to recognize some "cluster" zone of the same color in which crystals are oriented in the same directions.
LNS13B21 highlights a multiple orientation in both configuration Y_y and Y_x. in case of Y_x, there is a denser crystals presence in correspondence of the center and the largest lower part of laser track.

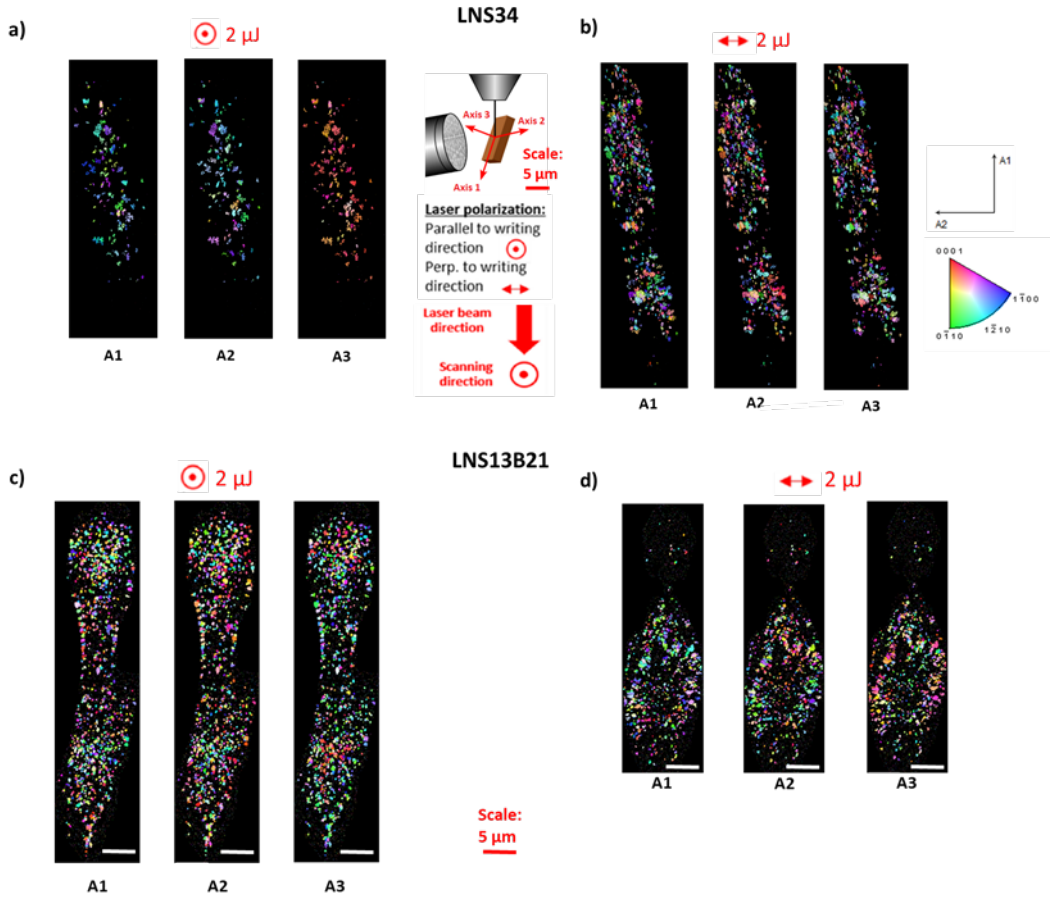

Figure 87: Inverse Pole Figure (obtained from EBDS analysis) for a) LNS34, and b) LNS13B21 sample, coding the crystal orientation according to the scheme reported in the figure through Axis 1 (A1 on the left), Axis 2 (A2 in the middle), and (A3 on the right) corresponding approximately to beam direction, laser polarization, writing direction respectively, at 2 µJ and configurations parallel (three maps on the left) and perpendicular (three maps on the right) to laser polarization. Other laser parameters are λ = 1030 nm; f = 200 kHz; NA = 0.6; pulse duration = 250fs; focal depth = 240 µm (in air); scanning speed = 1 µm/s.

The polar figures maps reported in Figure 88 point out the considerations until now presented at high pulse energy. Specifically, Figure 88a referred to LNS34 indicates two different orientations: the crystal orientation is accumulated in the polar figure center, meaning that the crystals are oriented with polar axis *c* 0 0 0 1 parallel to laser polarization (along scanning direction).

Figure 88b, referring to LNS34, displays the presence of multiple orientations in both Y_y and Y_x configurations.

The variability of orientations is even more marked in Figure 88c and d referred to LNS13B21.

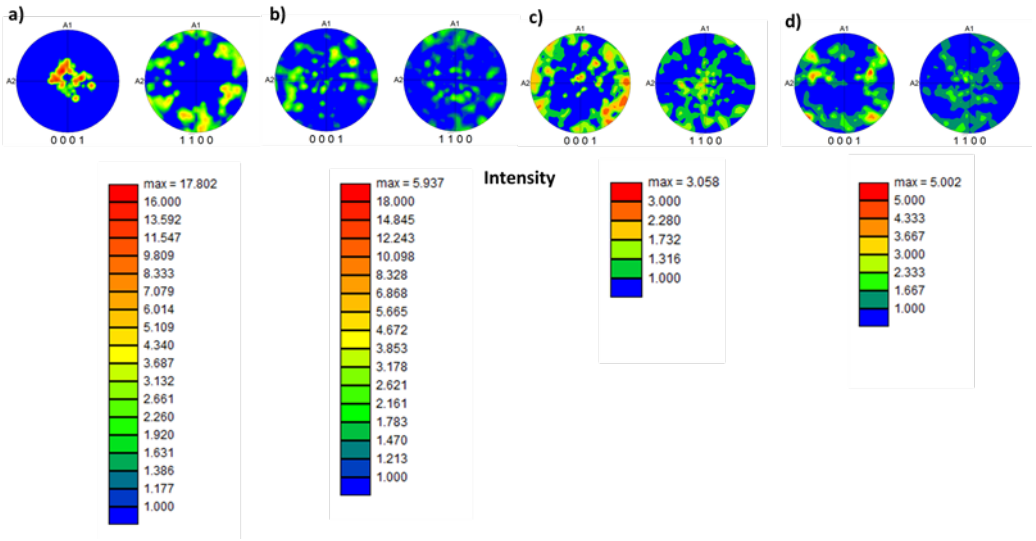

Figure 88: Polar figures referred to LNS34 at 2 µJ for a) Y_y, b) Y_x and LNS13B21 at 2 µJ for c) Y_y, d) Y_x. where A1 is the beam direction, A2 is the laser polarization, A3 is the writing direction

5.2 Investigation on nanocrystals orientation and nanogratings through scanning speed variation

This discussion intends to point out the role of scanning speed on nano-crystallization orientation and self-organized phase separation. The aim is to demonstrate the multiple links between scanning speed, crystallization, and nanogratings formation.

5.2.1 Requirements for nanocrystals precipitation

The starting point of our analysis on material response is to select suitable laser conditions for verifying the actual precipitation of orientable nanocrystals.
Starting from the LNS glass matrix, the study results have already been reported in [4]–[6], and [8]–[10].
The three laser modifications regimes, already defined in the previous section, can be described in another way to highlight other particular parameters involved in the regimes characterization taken into account in this discussion. The first regime at low pulse energies corresponds to a zone in which the material stays in glassy state modifying only refractive index and the fictive temperature, i.e., indication of

degree of disorder of glass [17], [18]. According to an average incident laser power of 0.16 W, pulse energies define the second regime with nanocrystals having the polar axis perpendicular to the writing laser polarization; then, only one texture is observed. Finally, the third regime occurs at a laser power of 0.32 W where large crystallites of the same orientation are acquired. This zone presents a part of the heat-affected volume (HAV) [16] melted and crystallizes through the action of the peripheral part of the HAV not yet melted.

Figure 89 shows the threshold energy values comparing pulse energy-repetition rate landscapes of two compositions respectively $32.5Li_2O$-$27.5Nb_2O_5$-$40SiO_2$ (mol%) in Figure 89a and $33Li_2O$-$33Nb_2O_5$-$34SiO_2$ (mol%) (the reference LNS34 in our experiments) in Figure 89b [2]. The aim is to verify if the LNS34 threshold values allow falling in the domain of nano-crystallization, looking at the results found for the glass reported in Figure 73a.

For LNS34, it is possible to note the energy thresholds detected from previous experiments in [1], and [19] (T1, T2, and T3 respectively for the three regimes 1, 2, and 3) a little lower than the ones found for $32.5Li_2O$-$27.5Nb_2O_5$-$40SiO_2$ (mol%) but the formation of the nanocrystals is confirmed [2].

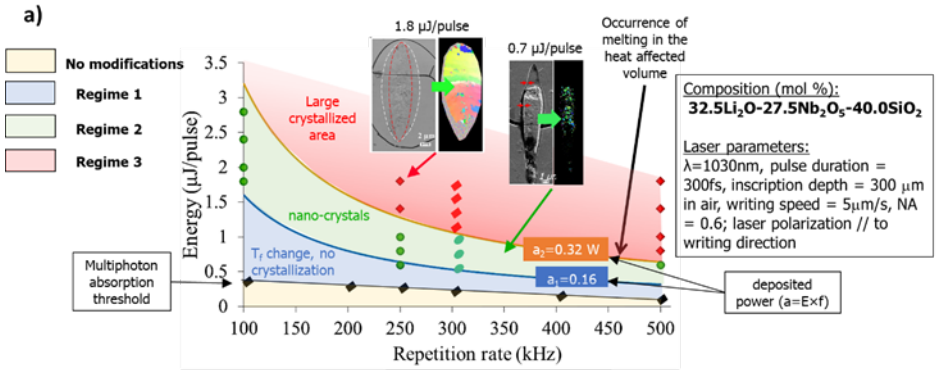

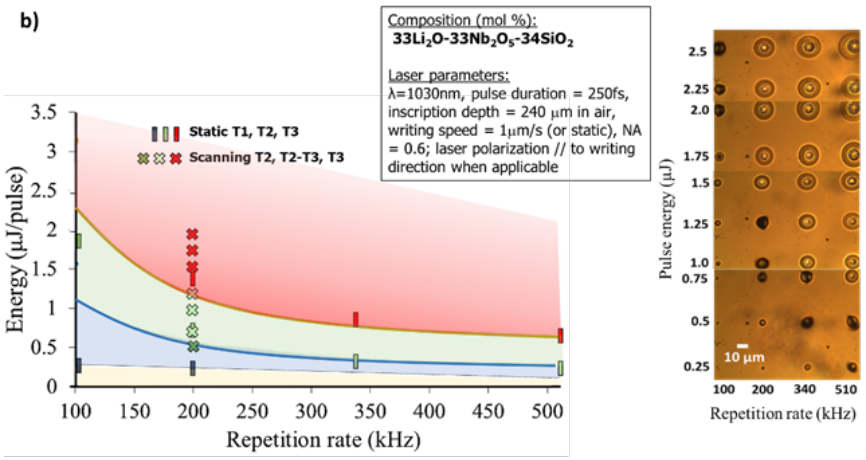

Figure 89: pulse energy-repetition rate landscape highlighting the three regimes of laser induced modifications for a) $32.5Li_2O$-$27.5Nb_2O_5$-$40SiO_2$ (mol%) [2], [3]; b) for $33Li_2O$-$33Nb_2O_5$-$34SiO_2$ (LNS34) (mol%). In addition, the trend of dots written in our experiment in static mode revealed the energy thresholds for LNS34 [2].

5.2.2 Nanogratings in LNS and LNSB

Nanogratings are composed of a crystalline phase (in our case $LiNbO_3$) and a vitreous rich-silica one (SiO_2 or SiO_2-B_2O_3), exhibiting self-assembly lamellar-like nanostructures that "grow" in the direction perpendicular to the laser polarization. Their particular characteristic is to be a subwavelength periodic structure i.e., a period smaller than wavelength (in our case 1030 nm) [6], [20]. In fact, it was discovered a nanostructure with average nanoplane distance ranges from 250 to 60 nm [10]. An attempt of comparison between LNS and LNSB nanogratings should be realized employing the same laser parameters, since this quantity is related with them [21]–[23].

Meanwhile, nanograting were found inside crystals region, but they do not necessarily cover the entire body of the laser trace, as it is possible to note in Figure 90, referred to our sample LNS13B21. Orange lines are coincident with limits that enclose the region of nano-gratings that is reduced, at increasing scanning speed, comparing with all the crystallization zone in each laser track cross-sections. Knowing that the key parameter controlling the orientation of nanostructure in silica glass is the laser polarization [24], we intend to investigate laser track cross sections, with reference to the LNS case, widely studied in the literature. In particular, LNS13B21 laser tracks reveal that it is not possible to distinguish clearly different zones as shown for LNS case.

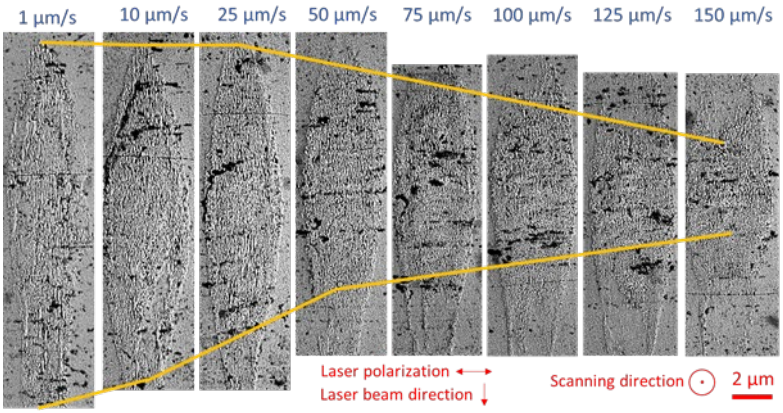

Figure 90: Scanning electron micrographs of the laser track cross sections induced by fs-laser on LNS13B21 glass sample for different scanning speed. Lamella-like nano-gratings are observed and, for comparison at different scanning speed, the upper and lower zone limits are bounded by two orange lines [2].

In the case of LNS extensively and previously studied in [4], four zones (identified with A-D) within the same laser track could be identified when laser polarization is perpendicular to scanning direction, as shown in next Figure 91.

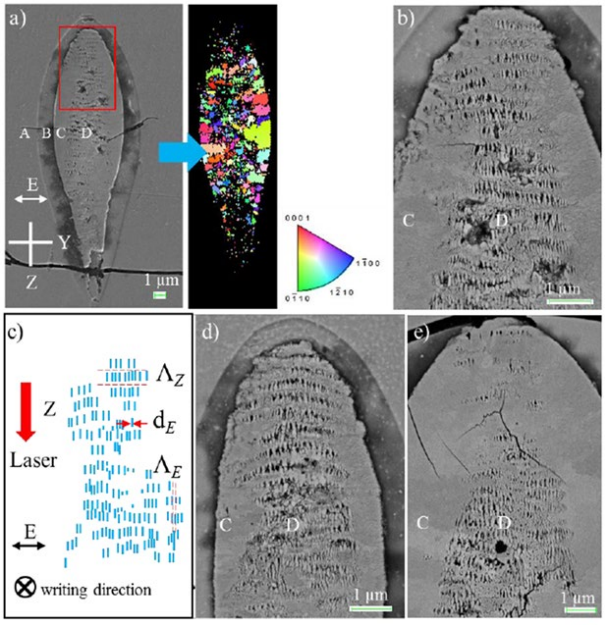

Figure 91: Morphology of the fs laser track with laser polarization, along Y direction, is perpendicular to X direction of scanning: a) SEM micrograph on left side and the

corresponding IPF coding along laser polarization direction on the right side for 1 μJ/pulse; b) this is a magnification of Figure 5.22a enclosed in the red rectangle; c) scheme of laser-induces structures, with forces and main parameters indicated: d_E is the nanostructures thickness, Λ_E is the distance between the dashes, Λ_Z is the distance between the nanostructure lines; scanning direction is along Z, also writing direction is indicated; morphology of the laser track varying the pulse energy: d) 0.8 and e) 1.4 μJ/pulse. Other fundamental parameters are: $32.5Li_2O - 27.5Nb_2O_5 - 40SiO_2$ (mol%), 1030 nm, 500 kHz, 300 fs, 5 μm/s, NA = 0.6, focal depth 300 μm in air [4].

Zone A is the non-irradiated area, Zone B is the one where it is possible to see the sensitivity to HF etching treatment to the material. In Zone C nanostructure does not present lamella-like periodic self-organization. In Zone D, crystals with disordered orientations smaller than the ones in Zone C, are found with a quasi-periodic nanostructure perpendicular to the propagation direction (Figure 91b). The head of the laser track shows the nanostructure along laser polarization direction. This is highlighted in a scheme in Figure 91c, where dashed parallel to each other with a thickness around 50 nm are marked by d_E. Other important parameters are the distance between dashed identified by Λ_E, and the distance between these structure lines marked by Λ_Z both around 100 nm (Figure 91c).
In Figure 91, different pulse energy are reported to investigate how changes the fs-laser induced nanostructure. Focusing the attention on Zone C and D at increasing pulse energy, the width of region D expands from about 3.2 to 6.2 μm, at 0.8 and 1.4 μJ/pulse in Figure 91d and e, respectively.
Nanogratings in the LNS34 glass matrix are described clearly by TEM micrographs in the following Figure 92 [3].

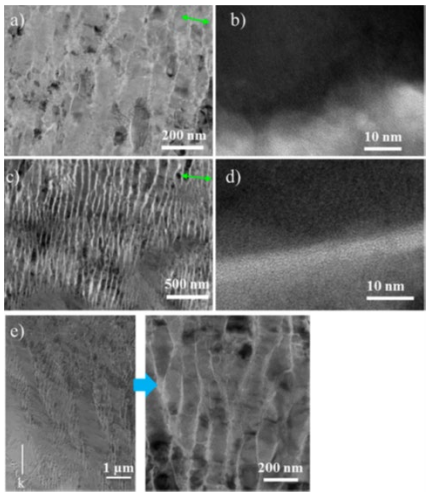

Figure 92: TEM micrographs (bright field mode of self-assembled nanostructure in LNS glass at various pulse energies (a – b) 0.7, (c – d) 1.3, and (e) 1.8 μJ/pulse. The laser

propagation direction is perpendicular to the paper plane for (a – d); nanostructure along the laser propagation direction is illustrated in (e). K is the laser propagation direction. Writing laser polarization direction is indicated by the green double arrows. The micrographs are referred to $33Li_2O – 33Nb_2O_5 – 34\ SiO_2$ (mol%), at 1030 nm, 300 fs, 300 kHz, 5 µm/s, and focus depth 350 µm [3].

Crystalline phase appears dark whereas amorphous parts are represented in white lines. The phase separation has not to be complete to reveal the presence of nanogratings.

The formation of nanogratings can occur only after a sequence of multi-pulses in conditions of regime 2. Figure 93 below is inserted to show the pulse number effect on the well-defined organization of nanogratings [25]. Figure 93a represents a nano-planes discontinuity which its evolution is reported in Figure 93b: nanogratings are shown with their complete self-organization in nanoplanes at laser polarization perpendicular to the scanning direction and 10^5 pulses/µm. The role of laser polarization orientation is highlighted in the next two micrographs of Figure 93c and d: at laser polarization parallel to the scanning direction, and increasing pulses number, the average size of nanopores diminishes in d with respect c.

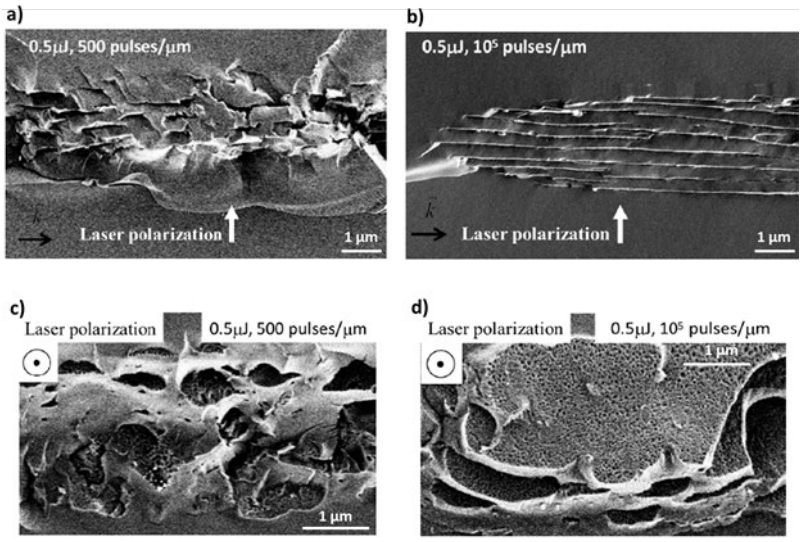

Figure 93: Field-Emission Gun Scanning Electron Microscope (FEG-SEM) secondary electron images of femtosecond laser track cross-section for the writing laser polarization (a, b) perpendicular to the scanning direction and (c, d) parallel to the scanning direction.

Other laser parameters are: pulse energy = 0.5 μm/pulse; wavelength = 1030 nm; pulse duration = 300 fs; repetition rate = 500 kHz; NA = 0.6 [25].

5.2.3 Influence of glass chemical structure and bonding on nanogratings formation

It is worth to note that light acts on nanogratings as the laser polarization is acting on their orientation. But then, is light the source of nanogratings formation or, being they already present within the material, does it simply make them evident? Or simply, does it modify what thermodynamics wanted to do: a phase separation?
Considering a suitable glass composition, fs-laser may be assimilated to a localized continuous heating source in average that induces $LiNbO_3$ crystallization, through a partly thermal process [10], [26]. Fs-laser irradiation can modify the glass homogeneity without being able to exclude at all that, even the irradiated glass, was initially not homogeneous. The presence of heterogeneities may affect the possible material devitrification [27]. It is important to foresee the role and the possible effect of preexisting defects and impurities in glass. They involved in the crystallization and the final structure of lamella-like nanogratings. The presence of nano-heterogeneities could generate a glass dissolution together with the action of fs-laser heating of the material. A consequent precipitation of nuclei generating nanomodifications could be assembled and organized gradually in nanoplanes until forming nanogratings [20]. Therefore, it can be assumed that a driving force exists, or the nanostructure skeleton is already present and drives the preliminary chemical separation [3], [10].
An attempt of explanation of the observed phenomenon starts from the analysis of the chemical glass structure. In detail, glass contains nanodomains with different chemistry and nature of the bonds. Komatsu *et al.* [27] in 2015, discussing the glass structure influence on laser-induced crystallization, proposed the existence of nanoscale strong and fragile structures within glass. In particular, nanoscale glasses fragility is a way to characterize a heterogeneous structure and bonding. A structure of glass formers (in our case SiO_2 and B_2O_3) with strong covalent polymerizable bonds coexists with a fragile one of glass modifiers (as Li_2O) with ionic bonds. The difference in electronegativity between the cations of formers and the ones of modifiers is responsible of ionic bonds between them. Because of their different bonds nature, formers crystallization is more difficult than the modifiers one. There are also the intermediates (as Nb_2O_5) that adapt their behavior, depending on the specific former of the glass lattice used. The crystallization nucleation is probably triggered from non-polymerizable ionic parts [27]. The strong domains in nanoscale were localized where we can find nanopores, while the fragile ones tend to

crystallize, after possible migration from their initial position in the glass network (maybe Li^+ and Nb^{5+}), when they are irradiated by laser light beam.
In our case, lithium enters the network in the form of modifier oxide (Li_2O) and the presence of two former oxides implies the possibility of release of more oxygen, despite the increasing number of oxides in matrix has made more difficult to predict the behavior of mobile ions.
Keeping in mind the possible role of heterogeneities, which can also be called alternatively inhomogeneities, we proceed to explore nanogratings formation.
Admittedly, it is very intriguing to delve into the origin of nanogratings. There are lots of attempts of interpretations about nanogratings generation.
We will proceed through a brief overview about the most important contributions about nanogratings interpretation, until illustrating the link between glass inhomogeneities and nanograting formation.
Shimotsuma *et al.* observed nanogratings, induced by fs-laser irradiation, in 2003 for the first time [28] in silica glass. Successively, they were found also in other glasses: doped silica [29], GeO_2 [30], [31], TiO_2 – containing silicate glasses [32], [33], and multicomponent borosilicate glasses [32], [34], [35].
The first model proposed by Shimotsuma [28] dealt with the interference of the laser field with the laser-induced plasma waves. Optical properties of the plasma and local temperature affected the nanograting period. This approach resulted incorrect at high plasma density and did not correspond with the experimental observations, excluding the strong dependence on pulse energy of nanograting period.
At this point, Taylor *et al.* [36] can be quoted about the evolution of spherically shaped nanoplasmas. They were produced by hot spots that surrounded in an inhomogeneous way the defect or color centers, allowing an anisotropic multiphoton ionization. Bhardwaj *et al.* [37] highlighted as the periodicity was determined by the lowest order optical mode of multiple nanoplasmas, that became comparable to planar metallic waveguides.
Another perspective is nanoplanes trapped in the smallest possible standing wave cavity inside material proposed by Buividas *et al.*[38].
An interesting consideration has to be made also about longitudinal periodicity of nanogratings interpreted by an interference of short-living excitons polaritons [39], [40]. This scenario needs to low electron densities, since at higher densities the

interaction between exciton and polariton is widely screened by electron plasma as soon as it starts to efficiently absorb laser energy [41].

Another approach is proposed by Liao *et al.* [42] to show how the excitation of standing plasma waves at the modified-unmodified areas interfaces plays a main role on the growth of periodic nanogratings, and their self-organization mechanism has exhibited similarities with femtosecond-laser-induced surface ripples formation [43].

Finally, we consider valid the definition of volume nanogratings (VNGs) proposed by Rudenko *et al.* as the smallest embedded structures ever created by light [44] that answers to our initial question. In his numerical investigation about nanogratings formation mechanism, he proposed an interplay of different phenomena: an interference between the incident and the scattered waves, numerous scatterings, local field enhancement and different accumulation processes resulted by multiphoton ionization [44]. The concentration of inhomogeneities is fundamental to start the nanograting creation and growth [44], [45]. He began to explain the importance of inhomogeneities, but its crucial role, as seeds for nanogratings formation, was well-defined properly by Buschlinger *et al.* [46].

Interestingly, this paper [46] is about the interaction of laser beam with nano-inhomogeneities in silica glasses [47]. Parameters of laser light and free carriers involved in nanograting formation inside homogeneous materials discussed in Bulgakova *et al.* [48] are the starting point of the treatment. Then, Buschlinger continued clearly, explaining how inhomogeneities allow to strongly amplify the local intensity and generation of plasma spots. It is worth to note that the exact shape and nature of initial inhomogeneities do not affect the ionization process [46]. This is a preliminary condition to have in mind before continuing with the investigation.

Moreover, two different regimes of local carrier densities achieved during irradiation were identified. In case of low carrier densities, ionization enhancement is concentrated around the initial region of field enhancement close to an inhomogeneity. When carrier densities become higher, a single nanoplasma creating into an inhomogeneity site expands further ionization in its surrounding area. It behaves as a seed for the growth of a structure enlarged [46]. The strong interaction regime is analogous of ionization instability typical of tunneling ionization in gases [49], [50] and that involved in ionization of transparent dielectrics [48].

As for the numerical model, refer to [46], for our purposes, we will recall only the salient points emerged from the simulation results carried out once also the

inhomogeneities were modeled. Glass as amorphous solid presents local variations of chemical structure [51] such as voids, gas inclusions [47], [52]. Voids are considered suitable model for a typical inhomogeneity [46], taking into account how laser light interacts with randomly distributed nanosized nonuniformities. In addition, previous laser irradiations on the glass could be responsible of the presence of material nonlinearities [37], [51]. It is important to noted that ionization around a void contributes to obtain the same final plasma structure as ionization around a region in which it is considered a particular enhanced ionization cross section [46].

We start the investigation from a spherical subwavelength inhomogeneity where plasma formation happens inside the sphere because of nonvanishing ionization cross section [46]. Considering a starting two-dimensional case, the inhomogeneity site gives rise to a dipole wave, and the latter interferes with the incident plane wave. It is worth to note that eventually, where the dipole resonance of the sphere approaches the excitation frequency, the plasma achieves a carrier density. This is the point in which an exponential increase of carrier density occurs [46]. Now, the scattered field is the only and actual responsible of the nearest intensity pattern.

Then, an ionized region grows into the direction of the electric field due to the abovementioned field enhancement. It is fundamental to note that because of scattering resulted by induced nanoplasma, the final structure is invariant regarding to microscopic details as shape, size, and chemical nature inside the seed inhomogeneity [46].

Figure 94 [46] represents how growth in the polarization direction becomes slow when the resulting structure is not more into subwavelength domain. Interestingly, the plasma becomes a nanoantenna whose the maximum value of reflectivity would be achieved at size of $\lambda/2n$. Then, constructive interference with the incident wave leads to have further ionization stimulated along the negative propagation direction, as shows in Figure 94b. This crucial point is characteristic by the inhibition of lateral growth of the initial structure. Therefore, there is a clear finite size in polarization direction [46].

Few successive optical cycles are necessary to have a new structure at the intensity maximum originated by reflection from the previous one. In this way, a tiny seed inhomogeneity turns out to be a starting point of a periodic plasma chain with wavelength dimensions and the growth direction is backwards against the propagation one, as represented in Figure 94c [46].

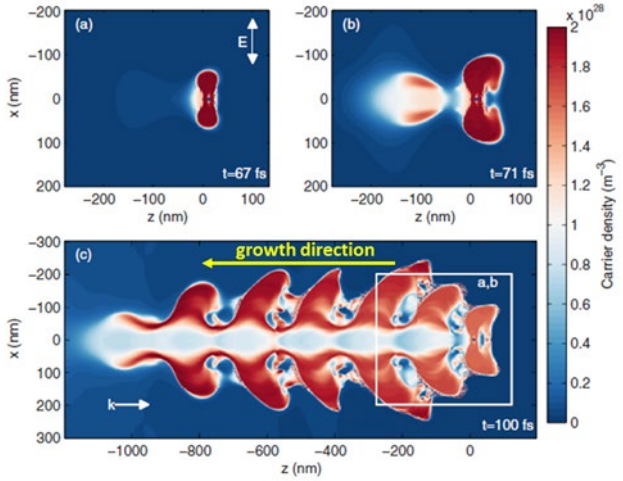

Figure 94: Plasma density (2D FDTD (Finite-difference time-domain) around a single void at the coordinate origin for different stages of structure growth. a) Plasma growth in polarization direction; b) Saturation of growth and generation of a second structure; c) Periodic plasma structure formed by subsequent growth, considering that illumination is a continuous wavelength plane wave [46].

Now, we start to explore the random distribution of the inhomogeneities in a three-dimensional volume. In the case of higher carrier densities, there is a competition of a large number of plasma structure during the growth process. The result is the onset of self-organization, well visible in the following Figure 95 [46].

We can see the same dense growth showed in 2D-case. In addition, their growth continues until they merge with their neighbors. At this point, extended plasma planes oriented perpendicularly to the polarization direction are organized. Now, a destructive interference of scattered and incident light comes into play. Then, we can see a suppression of ionization directly adjacent to each plasma plane and this occurs and after enhanced at a distance of approximately λ/n [46].

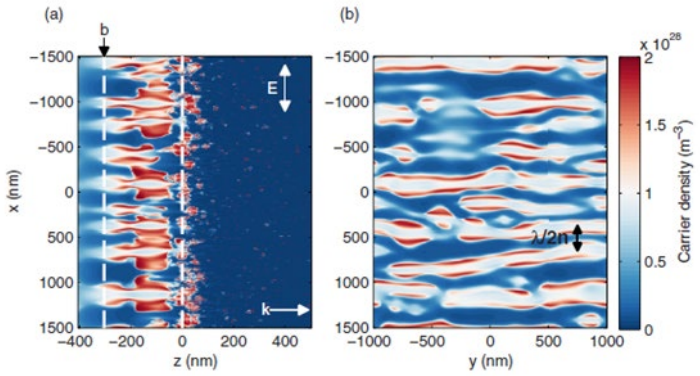

Figure 95: Carrier density generated by a plane wave normally incident on a half-space (z >0) with many inhomogeneities. The growth structures direction is backwards against the

propagation one: from the inhomogeneous/homogeneous border at z =0 and the grating has a period of ~ λ/2n = 275 nm. In a) there is a panel with polarization and laser propagation indicated, while a cut through the grating planes at z= -300 nm is reported in panel b) [46].

Since a simultaneous structures formation and a relevant interaction occur only during growth, the final period is not completely defined by the position of the intensity maximum but is also function of growth conditions, such as the density and ionization cross section of seed inhomogeneities and the excitation intensity [46]. The formation of plasma structures mainly occurs at the border of inhomogeneous region and the growth backwards into the unperturbed region at high intensity (Figure 95). There may be a growth inhibition of their neighbors where a strong suppression close to the individual structures occurs, then the period becomes as small as λ/2n. It is worth to note that even if interface is the starting point of growth, the resulting structure formation corresponds to a volume effect that is not possible to compare completely to the surface grating formation. In surface growth, there is an interference of dipole radiation initiated at a rough material surface [53], [54].

In the case of surface growth, the central point is in a "radiation remnant" incoming from polarization of a rough surface, the so-called "selvedge", represented in Figure 96 extracted by Ref. [53]. It seems like a dipole sheet of electromagnetic field. In particular, the material beneath this layer is generated by the superposition of the incident wave and the superficial waves resulting by "dipole sources" in the surface. This coincides with inhomogeneous deposited energy, and consequently the formation of the rippled patterns [48].

What can play the role of ''selvedge'' for volumetric laser energy absorption into the periodic pattern of the VNG? The ''forest fire'' model [55] of laser-induced breakdown of dielectrics [56] emerging in nanoplasma formation [36], [37] becomes another point of view to clarify the intriguing phenomenon of VNG.

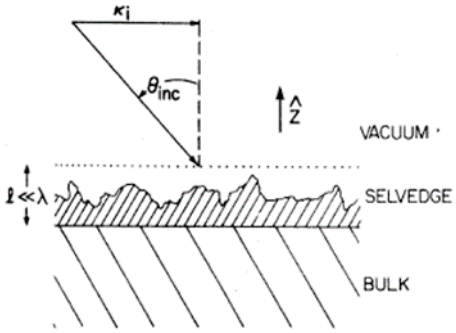

Figure 96: Scheme of the laser beam geometry incoming on rough surface indicated as "selvedge": κ_i is the wave-vector component parallel to the surface; θ_{inc} is the angle of incidence $\hat{\mathbf{Z}}$ indicates the positive direction; $l << \lambda$ is the selvedge thickness compared to laser wavelength [53]

Buschlinger concluded this treatment by arguing that the inhomogeneities on the interface are initiation points for growing densely arranged metallic plasma structures. Indeed, this process produced the self-organized period. When we compared simulation results with experimental ones, self-organization appeared as a cumulative effect and, then it needs much lower ionization rates. This model just presented included a number of inhomogeneities strongly enhanced that corresponded to a faster material ionization. Therefore, a single irradiation cycle allows to study the purely optical aspects of self-organization. Buschlinger also added that due to the influence of polarization and wavelength, optical processes can be considered dominant in nanograting formation [46].

Nevertheless, it cannot be neglected that the trigger for the nanogratings formation is photochemical, i.e., there is an interaction between laser light and inhomogeneities characterizing glass.

Eventually, this is only an attempt nanogratings interpretation based on a synergic approach to not only study nonlinear beam propagation but to take into account laser light absorption, physics of laser-induced electron plasma, thermodynamics of laser-matter interaction, chemistry, and mechanical material response. Then, this discussion allows to know where to start for exploring a new way that conjugate all these contributions towards understanding of nanogratings formation mechanism.

5.3 TTT and CCT diagrams: crystallization dynamics description by femtosecond laser modification in case study of LNS glass

Generally, to obtain a target structure with desired final properties, a thermal treatment is carried out through a heating cycle under specific temperature and pressure conditions followed by a cooling.

When a glass is invested in the crystallization process, it generally occurs that this was affected by a cooling rate determined from isothermal time-temperature transformation (TTT) or continuous cooling transformation (CCT) diagrams.

TTT diagram shows the kinetics of isothermal transformations: firstly, the material is cooled to a transformation temperature, held for a certain period, and cooled to room temperature.

Otherwise, in CCT diagram, there is continuous cooling at a constant or varying rate. Even though TTT and CCT curves are different, they are closely related to each other, and in fact, the shifting of TTT curve a little to the downward right allows to obtain the CCT diagram. Moreover, it must be considered that the time required for a reaction to begin, and the end is delayed; thus, the TTT curves are moved to longer times and lower temperatures. Figure 97, relative, for example, to slag treatment, can be considered useful to represent generally and simply the TTT and CTT diagrams in all cases. Cooling path 1 will form a glassy slag. The cooling paths 2 and 3 which are passing in the TTT diagram or the CCT diagram will form the crystalline phases. However, the kind of crystal and its morphology will be different between the two paths. The obtained microstructure can be controlled through an adequate cooling path in accordance with the purpose of utilization of slag [57].

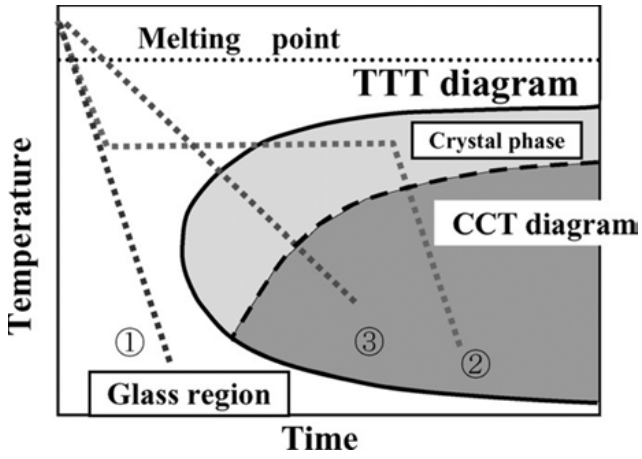

Figure 97: TTT and CCT diagrams [57]

At this point, it is necessary to discuss how a femtosecond laser would modify this diagram, in the form of thermal treatment curves on TTT and CCT diagrams, based on the contents about rationalization of the growth dynamics of Ref. [3].

The study of temperature distribution is fundamental to characterize crystallization mechanism. If we consider a low repetition rate as 100 kHz, the heat can be carried away by thermal diffusivity from the focus before arriving the next pulse at a time scale of 10 µs. Then, time left is very short, while temperature is not high enough for crystallization. The investigation around time and temperature allows to define the conditions for crystallization. The most important requirement is to measure a period between two sequential pulses smaller than thermal diffusion time; in this situation heat accumulation is found. It means a thermal diffusion time of length comparable to the beam radius (i.e., w_0^2/D_θ, where D_θ is the thermal diffusivity, and w_0 = 1 µm typically).

Firstly, the laser irradiation highlights the considerable differences between the phenomena unleashed in the laser focus area and those that occur a bit away from the focus center. The following figure 98a and b makes visible respectively spatial temperature distribution and time evolution of temperature.

The left part of Figure 98a represents also what happens when a steady state mode is reached, and, in this case, there are no large temperature variations such that the minimum and maximum do not change when the scanning speed is low enough. The average temperature is represented by the blue curve in Figure 98a. First important conclusion due to these previous considerations is that we can control temperature distribution on time and in space by employing fs laser as if it were almost a localized continuous heating source [3].

This consideration is valid also in scanning mode as long as the scanning speed is not too fast. Then another condition to be attained is that the scanning speed should

be smaller than thermal diffusion one, i.e., speed $< \frac{D_\theta}{w_0}$. This expression is around 10 cm/s, while scanning speed is not larger than 625 μm/s in our experiments on LNSB. There is another fundamental threshold value of scanning speed that corresponds to the crystallization speed. A scanning speed of the order of few μm/s is usually chosen in the range of the typical crystal-growth velocity according to the formed crystals.

Now, we move to examine the time evolution reported in Figure 98b according to the distance from the beam center of the line on the course of the scanning speed. Also in time evolution, two different trend we can describe between situation in the center of laser focus beam and away from the center. When a point is close to the center of the line, its course allows to cross the center of the beam and then encounter the largest temperature variations. Otherwise, fluctuations become marginal and the temperature variation very small [3].

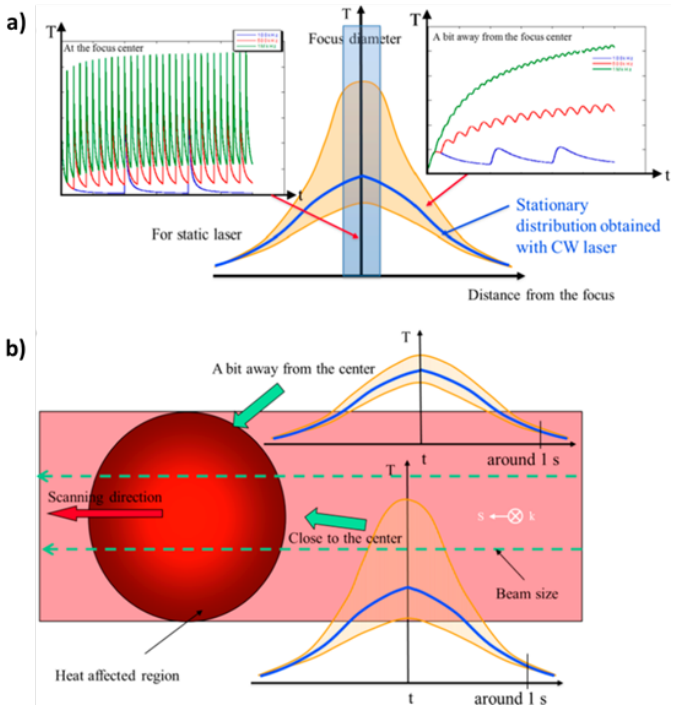

Figure 98: a) Scheme of spatial temperature distribution achieved by static laser as a function of distance from the laser focus beam. In the left side there is a representation of temperature variation at the focus center; the right side shows a position a bit away according to repetition rate. The area in blue shaded represents the approximated beam

width. Yellowish and brownish ones correspond to the amplitude of the temperature variation at the steady state; b) Time evolution of the temperature relative to a fixed point according to the distance from the focus center in scanning mode. The scanning beam, arbitrary limited, is enclosed in the red zone [3].

Now, we intend to explore what happens when CCT and TTT curves interact with the complex thermal treatment represented by laser irradiation of the glass. Always relying on the deepening about Classical Nucleation Theory (CNT) reported in the first section of Appendix, we proceed to create a link between CNT and the TTT curves obtained by integrating in time the nucleation and growth rates and we report the results schematizing in the following Figure 99a and b.

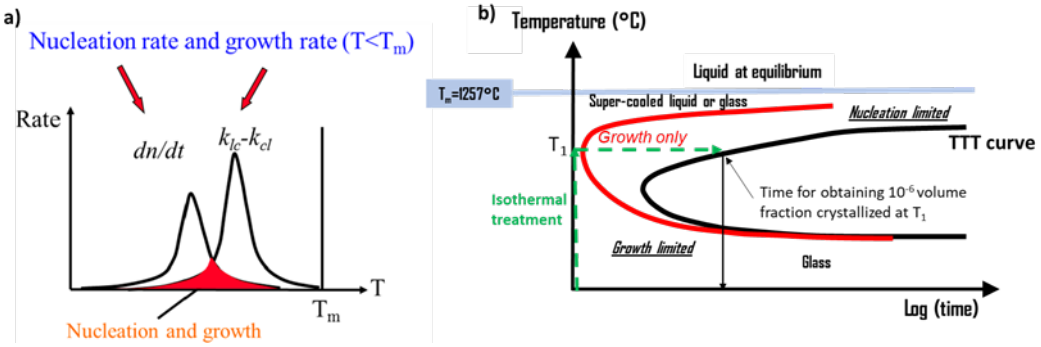

Figure 99: Scheme of the nucleation and growth rates; b) TTT curve derived by time integration of the rates [3]

The stationary nucleation rate described the number of nuclei per unit time at a given temperature and is expressed by:

$$I(T) = \frac{dn}{dt} \propto exp\left(-\frac{\Delta G_D}{k_B T}\right) exp\left(-\frac{\Delta G^*}{k_B T}\right) \qquad (46)$$

where ΔG_D is the kinetic barrier that corresponds to activation energy to cross the glass-crystal interface related to a diffusion coefficient (D); ΔG^* is the energy barrier to form a stable nucleus to grow; k_B is Boltzmann's constant, and T is the temperature.

When the temperature is higher than melting temperature (T_m), the growth is equal to zero. ΔG^* is high, when the temperature is nearby below T_m that is relevant for nucleation process, then the nucleation rate is very low. As temperature decreases, even ΔG^* diminishes and the possibility of forming seeds increases.

When the viscosity rises drastically, atom movement is limited, and the ordered crystal structures formation is prevented, and the nucleation rate decreases.

From previous considerations, we deduce that there will be an optimal temperature corresponding to the maximum nucleation rate. Otherwise, when the temperature is

almost coincident to T_g, ΔG^* decreases and nucleation rate increases considerably, and it could reach a maximum nucleation rate when ΔG^* and ΔG_D are of the same magnitude order.

The crystalline growth rate defines the critical nuclei growth with radius larger that a critical one and is given by:

$$C(T) = k_{lc} - k_{cl} = f\lambda\nu \exp\left(-\frac{\Delta G_D}{k_B T}\right)\left[1 - \exp\left(-\frac{\Delta G_V}{k_B T}\right)\right] \quad (47)$$

where k_{lc} is kinetic constant referred to liquid-crystal interface; k_{cl} is the one referred to crystal-liquid interface; f is the fraction of sites on the crystal surface, ready for the attachment; ΔG_V is the difference in free energy per unit volume between liquid or amorphous and crystalline phase; ΔG_D in this case is not necessarily the same to the nucleation activation energy reported above.

Summarizing, the crystal growth rate is larger than the nucleation one at higher temperatures. If we are dealing with homogeneous crystallization, the fraction of crystalline part x_c is a result of time integration of crystallization rate $\frac{\delta x_c}{\delta t}$.

When temperature does not depend on time (isothermal annealing), we can represent the results by time temperature transformation curve (TTT curve in black in Figure 99b).

When fs laser acts as a particular heating source, we can consider approximately a constant cooling of the melt: the temperature is decreased from T_m = 1257°C at a constant rate in the following Figure 100a.

Otherwise, when nucleation is heterogeneous, only the growth rate is to be considered and it corresponds to curve in red in Figure 100b [3].

Therefore, a continuous cooling transformation (CCT) curve is obtained by the time integration of the crystallization rate reported in Figure 100. The CCT curve is deduced from a TTT shifting a bit to the downward right.

The reason lies in the integration of the lower growth rate during the cooling process from the melt to a given temperature. Thus, the time to obtain the same amount is larger (i.e., 10^{-6}).

The importance of this kind of representation is in the fact that the transformation curve establishes a limit for the crystallization domain achieved after a time depending on laser thermal treatment curve. Moreover, a temperature domain exists below the melting temperature for which the crystallization rate is the largest.

Therefore, the evolution of the temperature during beam scanning at the different places of the irradiated area shows a sudden increase and decrease in temperature. It is important to consider two different cases reported in Figure 100b and c.
Firstly, when the maximum temperature is larger than T_m, only the part below T_m and in the decreasing stage has to be taken into account because higher temperature removes what happens in the past. Then, laser treatment time starts from the T_m. This is the case represented in Figure 100b where the transformation curve depends on the nucleation, regardless of whether it is homogeneous or not.
Otherwise, for places where maximum temperature smaller than T_m, the time origin is not well-defined and the curve of temperature in function of time is shown in Figure 100c. In this case, there is a crystallization without melting and it starts under the temperature increasing by nucleation.

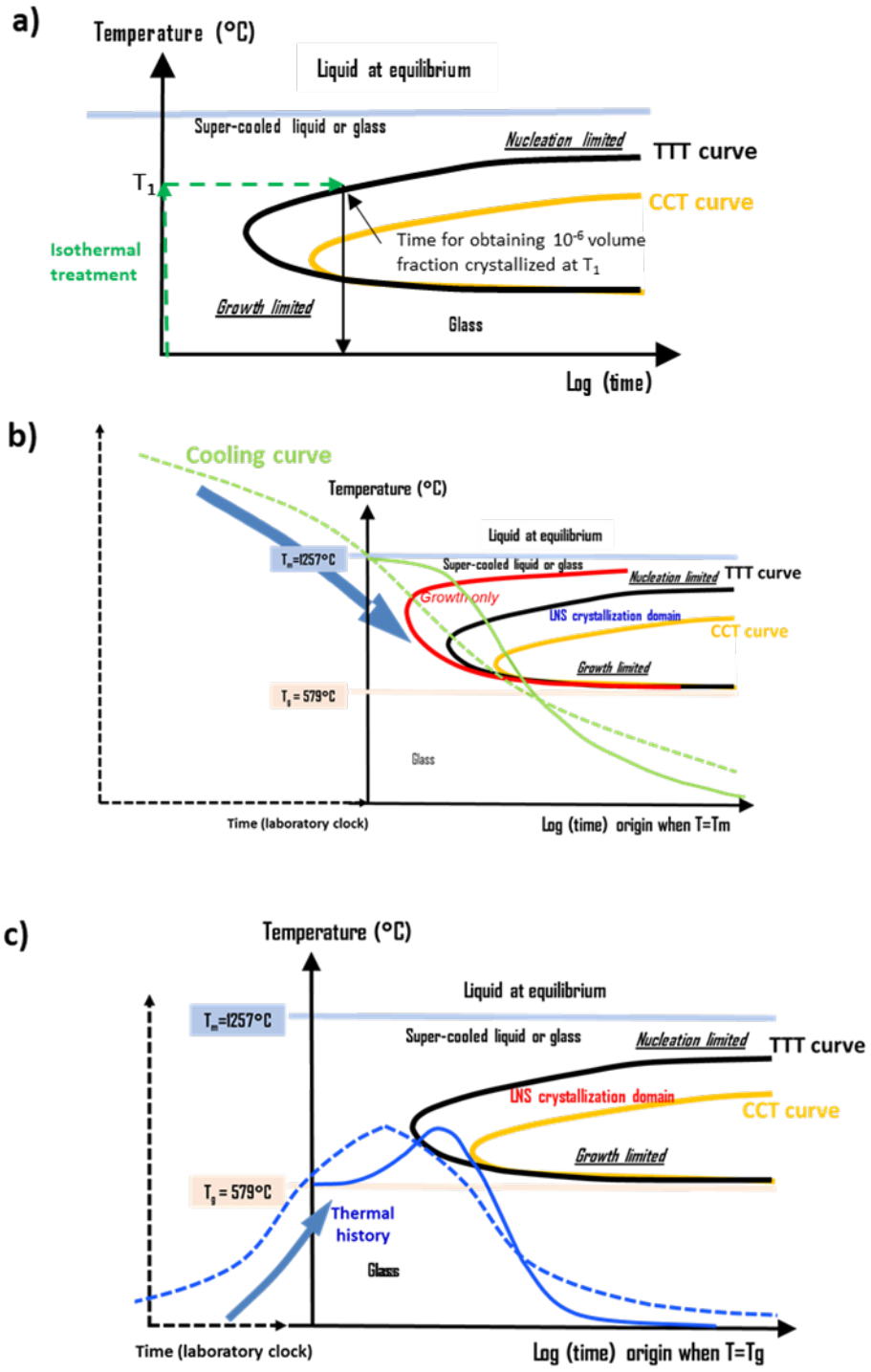
a)
Temperature (°C)
Liquid at equilibrium
Super-cooled liquid or glass
Nucleation limited
TTT curve
T1
CCT curve
Isothermal treatment
Time for obtaining 10-6 volume fraction crystallized at T1
Growth limited
Glass
Log (time)
b)
Cooling curve
Temperature (°C)
Liquid at equilibrium
Tm=1257°C
Super-cooled liquid or glass
Nucleation limited
TTT curve
Growth only
LNS crystallization domain
CCT curve
Growth limited
Tg = 579°C
Glass
Time (laboratory clock)
Log (time) origin when T=Tm
c)
Temperature (°C)
Liquid at equilibrium
Tm=1257°C
Super-cooled liquid or glass
Nucleation limited
TTT curve
LNS crystallization domain
CCT curve
Growth limited
Tg = 579°C
Thermal history
Glass
Time (laboratory clock)
Log (time) origin when T=Tg

Figure 100: a) only the TTT and CCT curves; these curves with laser thermal treatment curve b) for places experiencing maximum average T larger than T_m and c) for places at maximum temperature smaller than T_m [3]

Now, we arrived at an important point of our discussion, the interpretation of crystallization dynamics, that it will be analyzed referring to the energy quantitatively deposited on our material. Based on the amount of this energy, we can distinguish different trends of temperature time evolution.

Firstly, we are in conditions of low pulse energy that corresponds to regime 1 for LNS glass. This status during fs laser irradiation does not allow a crystallization but only some modifications of the amorphous area.

When we pass into intermediate low pulse energy corresponding to regime 2 for LNS, the following Figure 101 is useful to visualize results.

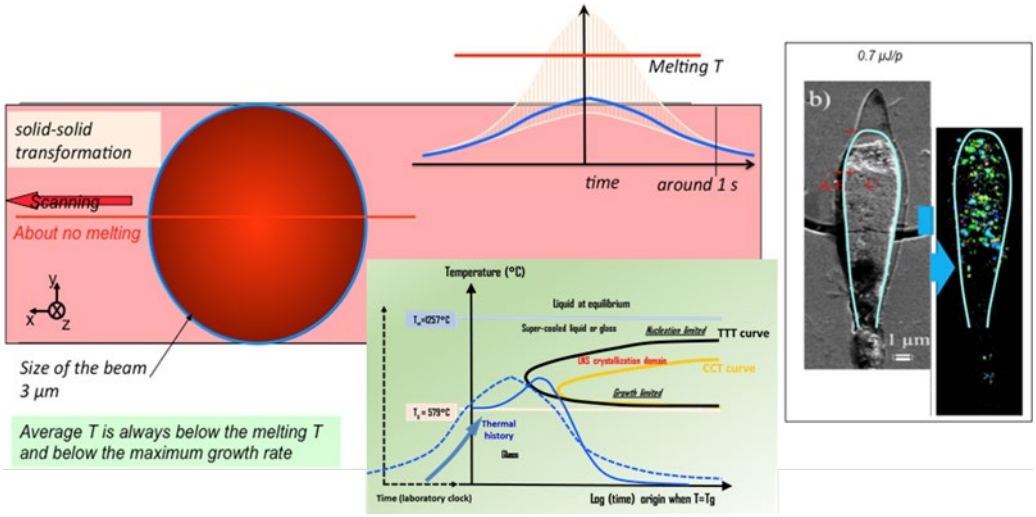

Figure 101: Time evolution of the temperature relative to a fixed point according to the distance from the focus center in scanning mode and SEM micrograph and EBSD map of the cross section of the laser track obtained at intermediate pulse energy in regime 2 for LNS glass [3]

Crystal cross-sections were strongly affected by irradiation conditions. Focusing the attention on the left side of Figure 101 above, the average temperature is always lower than T_m and below the maximum growth rate. It is worth to note that a solid transformation happens. SEM micrograph and EBSD map reveal only nanocrystals which are found throughout the volume concerned: all crystallized area was hit by beam light. Then, only the part of the spatial temperature distribution in the beam crosses the crystallization area. As it is possible to see on the figure, the growth rate is very low and consequently only nanocrystals show their actual presence everywhere after homogeneous nucleation. All nanocrystals could be oriented by

laser polarization. When pulse energy is high and ~ 2 µJ/pulse, referring to regime 3 for configuration close to parallel one for LNS glass, the results are well-defined by the following Figure 102.

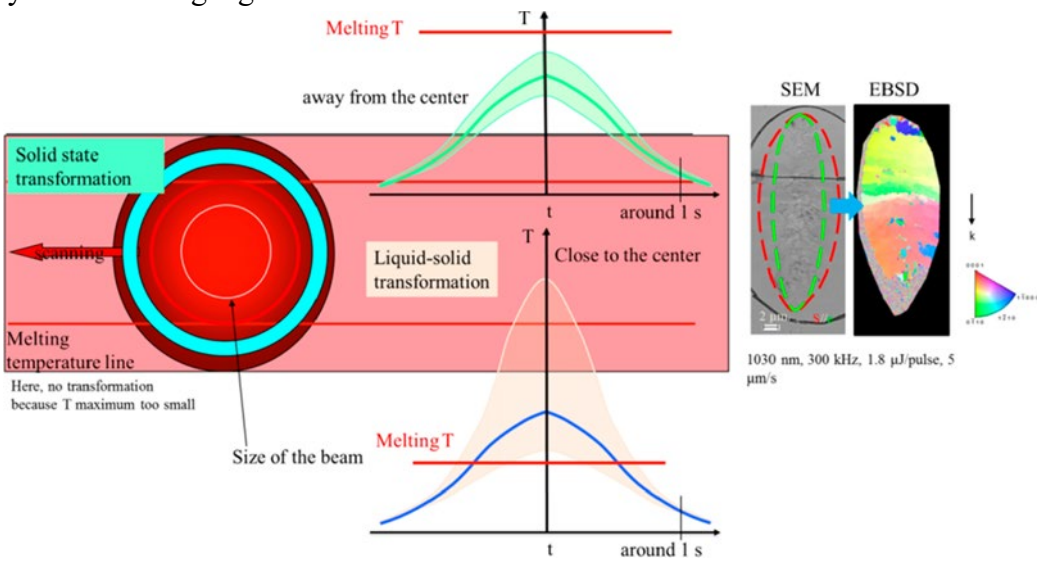

Figure 102: Time evolution of the temperature for a fixed point according to the distance from the focus center in scanning mode, and SEM micrograph and EBSD map of the cross section of the laser track obtained at high pulse energy in regime 3 for LNS glass. The green dashed line in the SEM micrograph is the beam boundary, otherwise the red dashed one highlights the crystallized volume boundary [3].

In this case, we noted that the crystallized area does not coincide with the whole zone hit by laser beam and the average temperature is higher than T_m. This particular condition is indicated by red lines and a circle in Figure 101. We noted that there is a liquid-solid transformation. Otherwise, the average temperature in the surrounding is lower than T_m, and solid-state transformation occurs. These two zones exist but it is not easy to clearly distinguish a boundary between them. To give a possible explanation of this boundary absence, the results were represented in the following Figure 103.

The crystallization begins from the periphery by homogeneous nucleation at time t_1 at lower temperature than in the center. Nucleation limits the crystallization at the center from T_m. As the laser beam irradiation proceed, the temperature in the periphery increases and nuclei growth starts, while the center crystallization waits the nucleation. The dark zone in the top is the amorphous region (corresponds to the green lines) and it generates the "bouquet" aspect. There is a growth front that propagates from the periphery toward the center following these lines. An important

parameter is the distance between two green lines in the direction of scanning where an effective growth rate emerges from the multiplication of the intrinsic growth rate and the opened time at a temperature sufficiently high. The fundamental parameter in this case is:

$$\Delta x_c = \frac{\delta x_c}{\delta t}(T_{max}) \frac{\alpha T_{max}}{\frac{dT}{dt}} \qquad (48)$$

where αT_{max} is the range of temperature on which the growth is active ($\alpha < 1$). Since the growth front lines are not parallel, the growth rate is smaller at the center. The consequence is that the cooling rate, i.e., the slope of $\frac{dT}{dt}$ is larger at the center than at the periphery.

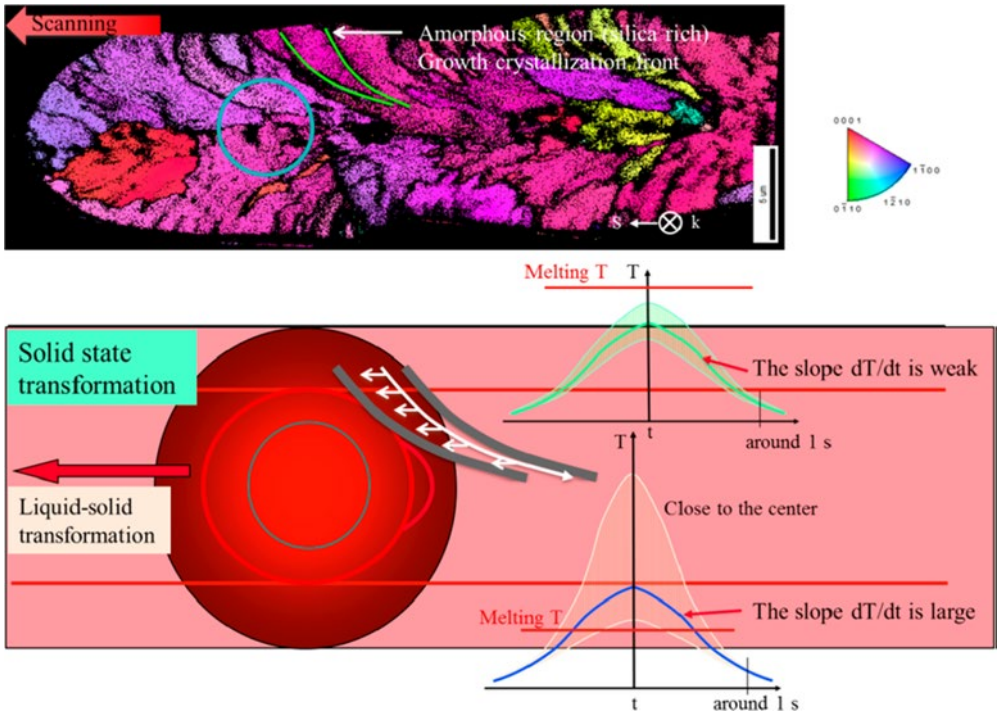

Figure 103: Interpretation of the morphology acquired by high pulse energy (regime 3 for LNS glass) in the plane perpendicular to laser propagation direction (XY plane). The blue circle reported inside the bouquet-like laser track cross-section shows the beam size inside which the temperature is almost homogeneous. The green curves represents the bouquet morphology illustrated in the map above [3].

If we detected a very high pulse energy, as 4 µJ/pulse, we are in an extreme case and the thermal-affected area is very higher than the laser beam size. The temperature is once again above T_m. It is localized by red lines and a circle in which the temperature is really far than T_m, as shown in Figure 104. A liquid-solid transformation could be expected in the central area. Otherwise, away from the

center, the maximum temperature is lower than T_m, beyond the red lines, and here, a solid-solid transformation occurs.
This case [58] is represented in the following Figure 104 in which crystallization front is illustrated in yellow curve representing the crystallization front. The c-axis is oriented along the scanning direction.

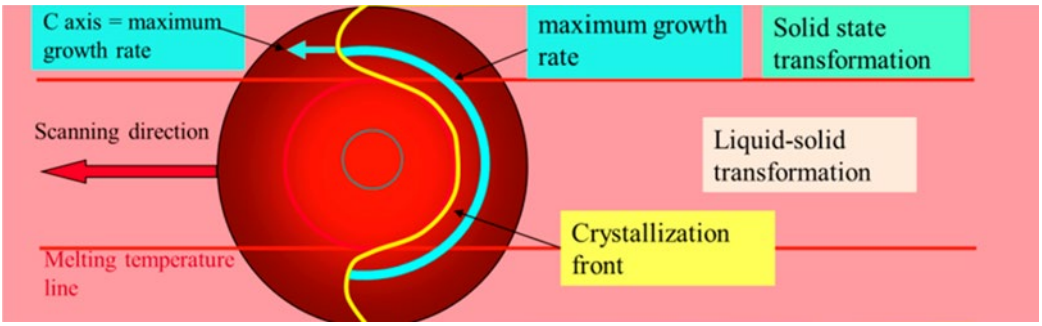

Figure 104: Time evolution of the temperature for a fixed point according to the distance from the focus center in scanning mode at very high pulse energy of 4 µJ and formed single texture interpretation [3]

It is necessary also to give an interpretation of the presence of non-crystallized area in the section of the laser traces, reported in the following Figure 105.

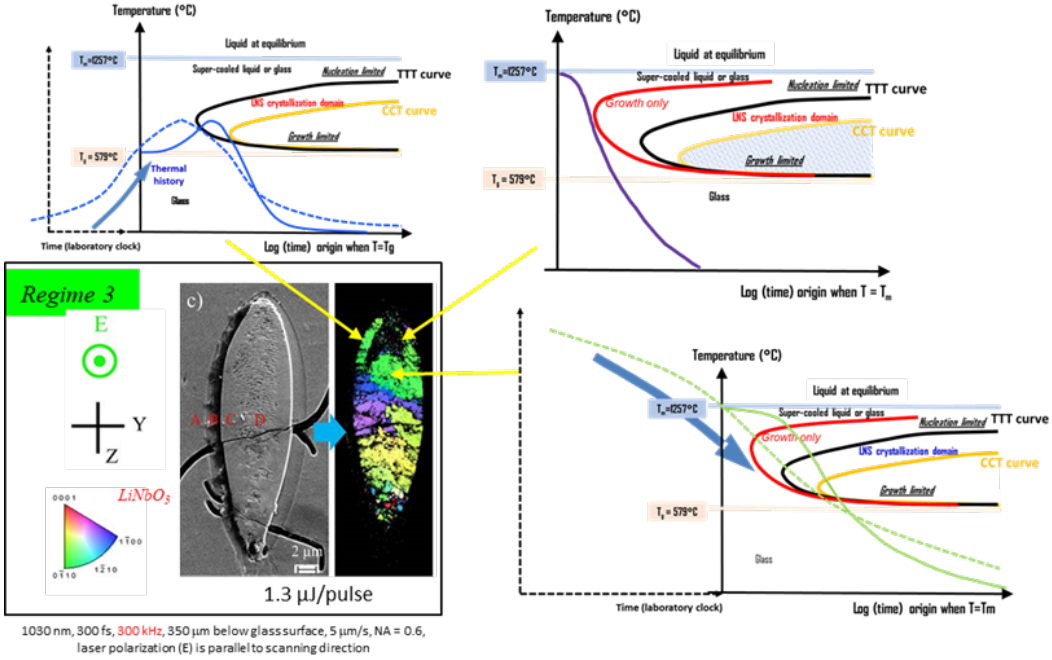

Figure 105: Interpretation of the presence of non-crystallized area in the section of laser traces [3]

There is a nonuniform morphology for parallel configuration in regime 3. Large grains are distributed throughout the width the cross section, but an amorphous area is also highlighted in the head of laser tracks. The shape is a tweezers-like zone grown by solid-solid transformation. Otherwise, the body of laser tracks is generated from a liquid-solid transformation, according to the scheme reported in Figure 105. There is another intermediate case, when the maximum temperature of the treatment curve is just slightly above the melting temperature. This is the situation in which the cooling is faster, and it could not reach the crystallization domain in the time-temperature transformation plane.
The presence of two typologies of transformations (solid-solid and liquid-solid) gives rise to inhomogeneous crystallization. In addition, nucleation and growth in the first region and only growth in the second one represent two kind of crystallization mechanisms and then, diverse crystallization rates: faster in the second than in the first one. The homogeneous case is not depending on the scanning speed as the inhomogeneous one.
Therefore, a fundamental requirement is to have the scanning speed lower than crystallization rate of the solid-solid transformation for writing a full crystallized line [3].

5.4 Laser-induced crystallization domain in LNS34 and LNS13B21

Nucleation and growth evolution obtained by laser-induced crystallization present evident differences in our samples upon addition of B_2O_3. We intend to analyze how crystallization domain changes from LNS34 to LNS13B21 [2].
Moreover, analyses are carried out to discover the effect of scanning speed on crystallization, taking into account the second series of experiments reported in Section 4.2 and the results presented below. We start focusing on the nanocrystals morphology depending on orientation, exploring the whole laser track cross-sections represented on the following Figure 106, at increasing scanning speed through SEM micrographs and IPF maps obtained in EBSD analysis.
The presence of $LiNbO_3$ nanocrystals is confirmed by EBDS analysis. The crystallization is homogeneously distributed except for central part of laser track from 1 to 100 μm/s. Probably this zone coincides with the region in which no phase separation was found. At higher scanning speed, from 125 to 175 μm/s, it is possible

to note a uniform distribution with nanocrystals concentration in the center of laser track.

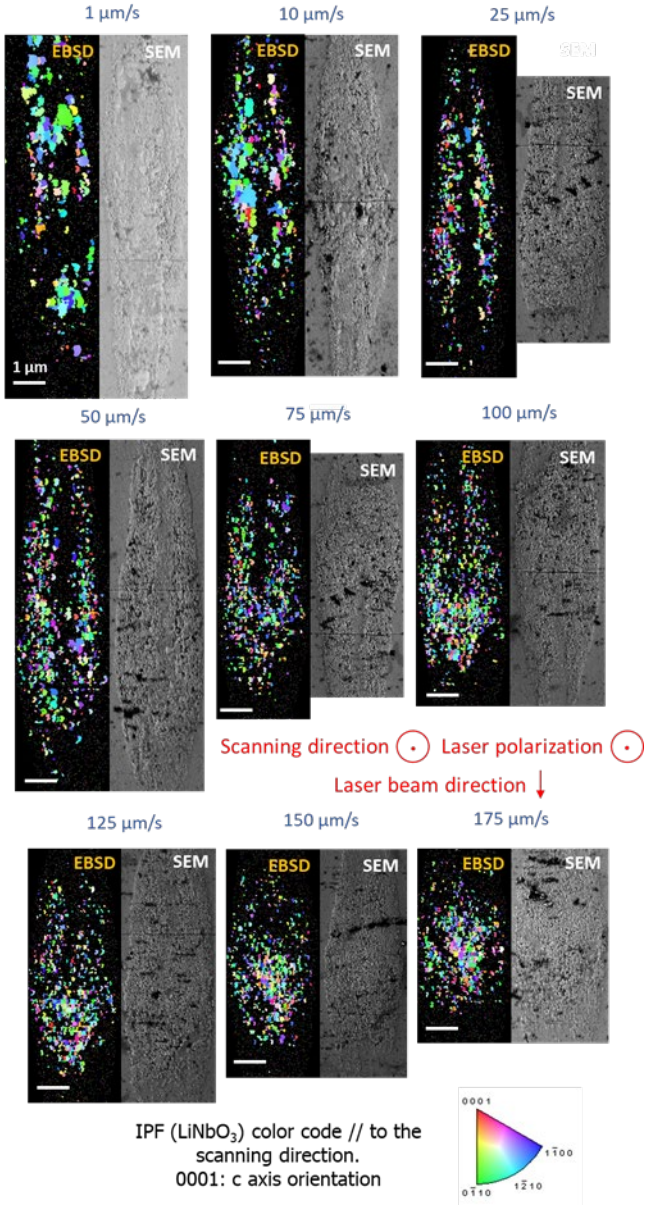

Figure 106: Morphology of laser tracks at pulse energy equal to 0.5 µJ according to polarization configuration Y_y: electron backscatter diffraction (EBSD) maps and scanning electron microscope (SEM) micrographs on the laser track cross-sections induced by fa-laser on LNS13B21 glass sample and for different scanning speeds. Other fixed parameters are: pulse energy = 0.5 µJ; configuration Y_y (laser polarization // to the scanning direction;

λ = 1030 nm; f = 200 kHz; NA = 0.6; pulse duration = 250 fs; focal depth = 240 µm (in air).

TTT diagrams are shown in the following Figure 107. Glass transition (T_g) and peak crystallization temperatures (T_p) are quite dissimilar between the two glasses. When B_2O_3 is added to the glass, the incubation time (indicated by a dashed arrow in the following Figure 107) is drastically reduced. This variation produces a displacement of the TTT curve and, consequently, an expansion of crystallization domain LNS34 to LNS13B21.

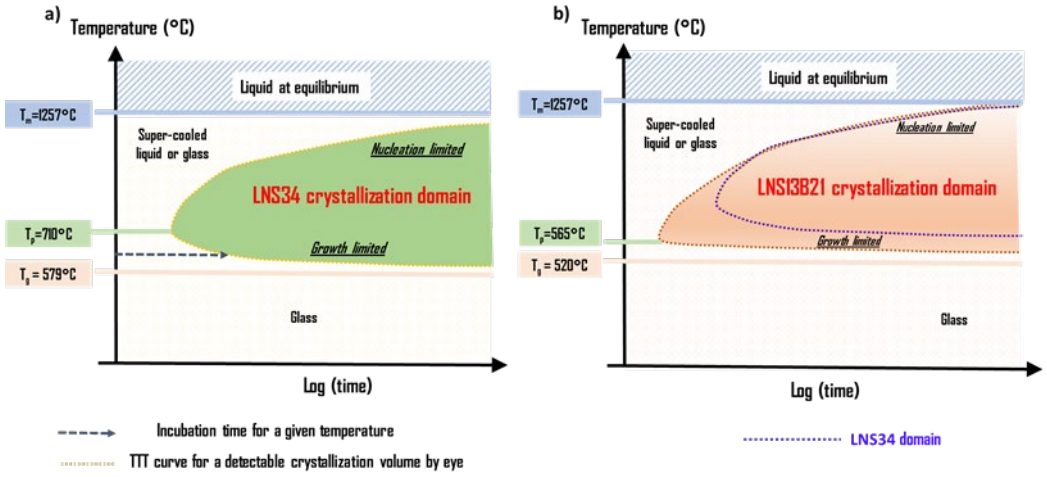

Figure 107: Representation of crystallization domain for: a) LNS, b) LNSB glasses in TTT (time – temperature – transformation) diagram; T_m: melting temperature of $LiNbO_3$, T_p: crystallization peak temperature, T_g: glass transition temperature [2]

Each of thermal treatments curves reported on the diagram corresponds to a specific laser scanning speed, as reported in Figure 108. The effect of scanning speed on the crystallization domain is represented for LNS34 (Figure 108a) and for LNS13B21 (Figure 108b). The crystallization domains are limited between glass transition temperature (T_g) on the bottom side and melting temperature (T_m) on the top side. It is important to highlight that the nucleation top side is not varied because it depends only on the thermodynamics driving force of the nuclei that we assume the same for both glasses. When B_2O_3 is added, the viscosity decreases. The growth rate increases with the strong decrease of the viscosity. These variations cause a sharp reduction in incubation time. We determine the maximum average temperature by pulse energy and repetition rate, through this formula E_p x RR. No change of the scanning speed and only a little variation of the chemical composition were taken place. When the treatment curves cross T_g, whatever the speed, the coincidence of time scales between TTT and treatment curve occurs. This

corresponds to the starting time of crystallization. In the first case, the thermal treatment at specific speed indicated by *v* is only tangent to the TTT curve. It must enter the crystallization nose during the thermal treatment to precipitate crystals. This corresponds to speed *v* for LNS34 glass.

For LNS13B21, the crystallization nose is shifted to lower time values relative to the LNS34 glass. This is in part due to the ease of nucleating and growing crystals in this glass. This leads to a decrease in the incubation time and the specific speed indicated by *v* is now completely in the crystallization domain. Consequently, in our experiments, it is possible to write at higher speeds for LNS13B21 relative to LNS34 while line crystallization until 600 µm/s. Moreover, for LNS13B21, T_p also is much lower: this leads to a shift in a crystallization domain to lower temperatures.

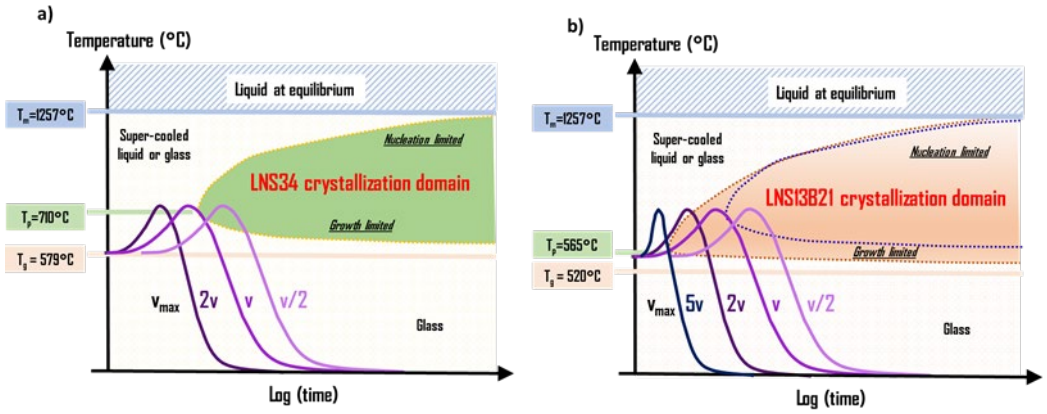

Figure 108: Scheme of the effect of the scanning speed on the crystallization for the two glasses a) LNS and b) LNSB [2]

For LNS34, if we consider a scanning speed of *v/2*, the thermal treatment curve may enter the crystallization domain; otherwise, no crystallization will happen at a scanning speed of *2v*. For LNS13B21, both incubation time and T_p are lower than LNS34 ones, and the crystallization domain is closer to the ordinate axis. The thermal treatment in correspondence of a scanning speed *v* will now penetrate the crystallization domain. Then, it is allowed a scanning speed until a value given by the experiment equal to *5v* to achieve the critical value beyond which no crystallization occurs.

Another value to be considered is the crystallization onset temperature T_x that depends on the irradiation time. Crystallization occurs when the onset value is exceeded. This is visible in Figure 109. We observed that as the scanning speed

decreases, the crystallization onset is reached at lower temperatures, as indicated by the red edge part of the diagram.

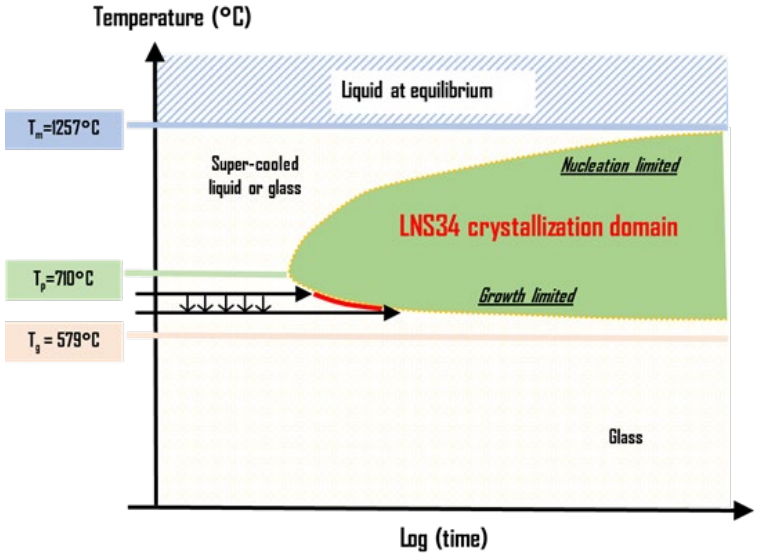

Figure 109: Scheme explaining the effect of scanning speed on the heat-affected volume (HAV) width [2]

If we examine the scheme from the point of view of thermal treatment curves, they proceed to overcome the melting temperature quite rapidly, as it is possible to see in Figure 110. The faster scanning speed to induce laser crystallization in lines occurs when increasing the mean power.

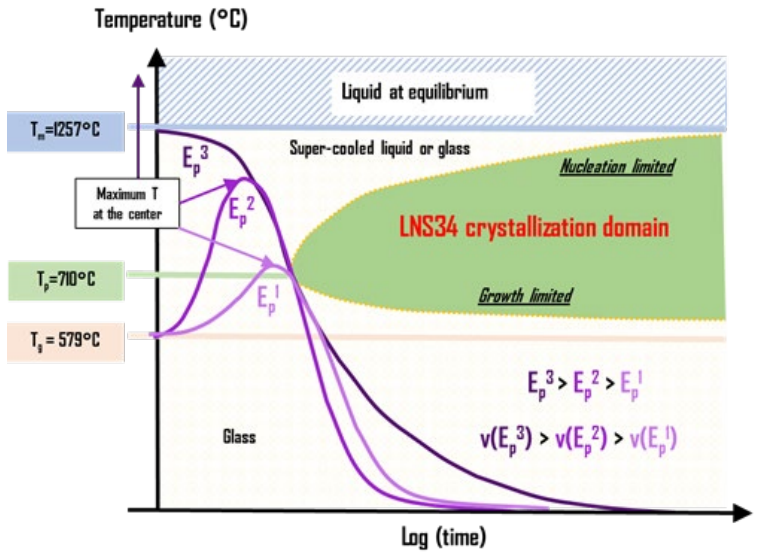

Figure 110: Scheme of the treatment curves crossing the nose of the crystallization domain: at increasing the scanning speed (v), also the energy power (E_p) must be increased to preserve the nanocrystal microstructure [2]

5.5 Boron as convenient addition in glass network

In this section, we proceed to consider briefly a boron incorporation into $LiNbO_3$ reported in [59] and [60], as an evidence, by analogy, of the advantageous choice of boron addition in glass network of $LiO_2 – Nb_2O_5 – SiO_2 – B_2O_3$.

The peculiarity of boron is the ability to act on $LiNbO_3$ crystal structure without being incorporated into crystal, because of the small radius of cation $B^{3+} \sim 0.02$ nm compared to 0.068 nm of ion radii of Li^+ and Nb^{5+}[59]. The structure of $LiNbO_3$ melt affects the process of its crystallization.

Boron has the propensity to incorporate only into tetrahedral voids of a crystal structure, specifically according to a part of groups $[BO_3]^{3-}$. It is possible to move from a bond O – O to an octahedron generated by oxygen–metal clusters MeO_6.

Me indicates metal, thus Li or Nb. This transformation implies a change of polarizability. It can control other physical properties. The characteristic optical nonlinearity and typical ferroelectricity of this material are due just to the presence of these clusters into the crystals [59].

Boron is an active chemically dopant that is able to modify crystallization temperature, viscosity, and surface tension of melts. Crystal chemistry of boron compounds is characteristic of a two-way hybridization of a boron atom, i.e., sp^2 and sp^3. The consequent formation is of triangles $[BO_3]^{3-}$ or tetrahedra $[BO_4]^{5-}$. It is one of the strongest acceptors due to the presence of a vacant orbital in the small boron atom. This donor-acceptor interaction brings the coordination number of a boron atom up to four. It is possible to form clusters of atoms that surrounds a boron atom and placed at three corners of the tetrahedron [60]. The fourth corner stays vacant with a positive electric field of particular intensity. This explains the peculiar capability of boron compounds to form strong molecular complexes. Triangles and tetrahedra of boron can be separately exhibited or polymerized between each other through a common oxygen atom. The bulky polyanions just formed are responsible of high viscosity of melts [60].

$LiNbO_3$ defects have an important role in the stability of material structure. For instance, photorefraction effect (optical damage) springs from defects with electrons placed on them generating photoelectric fields.

Covalent bonds are predominant in octahedrons occupied by niobium while lithium ion is bound with oxygen atoms only by electrostatic interaction. The major presence of covalent bonding allows to generate anion motifs in the melt, such as NbO_4 tetrahedra. These oxyanions are localized as complexes with a stable structure in $LiNbO_3$ melt. These boron-containing polyanions create stable covalent bonds with niobium containing polyanions. The consequent excess of niobium allows to increase the Li/Nb ration in the melt. The resulted grown crystal reaches the stoichiometric crystal with regard to the degree of ordering the cation sublattice. It is possible to verify a change well-illustrated in Figure 111 [61] in which is represented the presence of an antisite Nb_{Li} where Nb^{5+} cations are placed where Li^+ cations were normally found.
In fact, an antisite is defined as a site within a chemical compound in which a different atom (in our case Nb) occupies a place generally filled by another element (in our case Li). The boron inserts an additional positive charge in glass network that allows to decrease the number of Nb antisites [62], and also the one of lithium vacancies (V_{Li}).

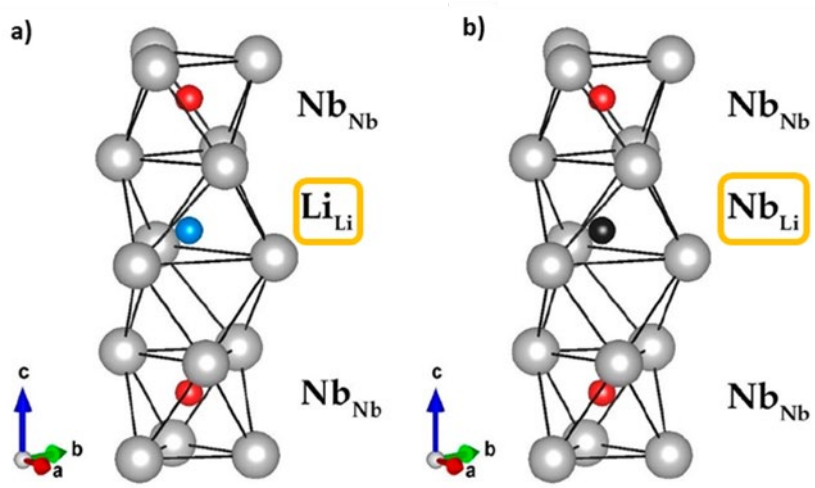

Figure 111: a) Ideal $LiNbO_3$ crystal structure with stoichiometric composition without point defects (Li_{Li}); b) nonideal $LiNbO_3$ crystal structure with Nb antisites (Nb_{Li}) [61]

5.6 Conclusions

This chapter contains a comprehensive interpretation of the results from chapter 4, starting from the investigation of the glass modifications during nanocrystals formation. Firstly, the interconnection between pulse energy and repetition rate with laser polarization direction points out the threshold values of thermal power extensively studied in case of LNS matrix. In conditions of regime 3 at high pulse

energy, LNS glass exhibits nanogratings and microcrystals oriented with scanning direction parallel to the laser polarization. Moreover, considering the increase of scanning speed, we found that the crystals size comparatively increases. It is possible to already reveal a phase separation between a glass and a crystalline zone. The SHG measurements are supported by the EBSD analysis combined with IPF maps. We have only begun the investigation of the LNSB matrix, and additional analysis will be needed in the future, as TEM for example, to have a clearer picture of the crystallization mechanisms triggered inside the material through irradiation with the femtosecond laser. The fluctuation in the nanocrystals direction observed and different aspect of nanogratings in LNS13B21 sample compared to LNS34 demonstrate the necessity of future work to clearly formulate an interpretation of its behavior. TTT and CCT diagrams are investigated extensively for LNS34. This is preliminary to report data for LNS13B21 that highlight the expansion of crystallization domain, and the crystallization onset reached at lower temperatures. Then, the boron oxide incorporation in LNS matrix allows to lower glass-making and crystallization. This leads to a fast crystallization of $LiNbO_3$. In conclusion, if we are able to control the femtosecond laser parameters, it is possible to tune the orientation and morphology of $LiNbO_3$ through the modulation of optical properties as SHG and birefringence in LNSB matrices.

5.7 Bibliography

[1] E. Muzi *et al.*, "Polarization-oriented $LiNbO_3$ nanocrystals by femtosecond laser irradiation in LiO_2–Nb_2O_5–SiO_2–B_2O_3 glasses," *Opt. Mater. Express*, vol. 11, no. 4, p. 1313, Apr. 2021, doi: 10.1364/OME.417461.

[2] E. Muzi *et al.*, "Towards a Rationalization of Ultrafast Laser-Induced Crystallization in Lithium Niobium Borosilicate Glasses: The Key Role of the Scanning Speed," *Crystals*, vol. 11, no. 3, p. 290, Mar. 2021, doi: 10.3390/cryst11030290.

[3] J. Cao, M. Lancry, F. Brisset, L. Mazerolles, R. Saint-Martin, and B. Poumellec, "Femtosecond Laser-Induced Crystallization in Glasses: Growth Dynamics for Orientable Nanostructure and Nanocrystallization," *Crystal Growth & Design*, vol. 19, no. 4, pp. 2189–2205, Apr. 2019, doi: 10.1021/acs.cgd.8b01802.

[4] J. Cao, L. Mazerolles, M. Lancry, and B. Poumellec, "Creation and orientation of nano-crystals by femtosecond laser light for controlling optical non-linear response in silica-based glasses," Université Paris-Saclay, France, 2017.

[Online]. Available: Jing Cao. Creation and orientation of nano-crystals by femtosecond laser light for controlling optical non-linear response in silica-based glasses. Material chemistry. Université Paris-Saclay, 2017. English. ﷺNNT : 2017SACLS055ﷺ. ﷺtel-01988887ﷺ

[5] J. Cao, L. Mazerolles, M. Lancry, D. Solas, F. Brisset, and B. Poumellec, "Form birefringence induced in multicomponent glass by femtosecond laser direct writing," *Opt. Lett.*, vol. 41, no. 12, p. 2739, Jun. 2016, doi: 10.1364/OL.41.002739.

[6] J. Cao, L. Mazerolles, M. Lancry, F. Brisset, and B. Poumellec, "Modifications in lithium niobium silicate glass by femtosecond laser direct writing: morphology, crystallization, and nanostructure," *J. Opt. Soc. Am. B*, vol. 34, no. 1, p. 160, Jan. 2017, doi: 10.1364/JOSAB.34.000160.

[7] J. Cao, B. Poumellec, F. Brisset, A.-L. Helbert, and M. Lancry, "Angular Dependence of the Second Harmonic Generation Induced by Femtosecond Laser Irradiation in Silica-Based Glasses: Variation with Writing Speed and Pulse Energy," *WJNSE*, vol. 05, no. 03, pp. 96–106, 2015, doi: 10.4236/wjnse.2015.53012.

[8] J. Cao, B. Poumellec, F. Brisset, A.-L. Helbert, and M. Lancry, "Tunable angular-dependent second-harmonic generation in glass by controlling femtosecond laser polarization," *J. Opt. Soc. Am. B, JOSAB*, vol. 33, no. 4, pp. 741–747, Apr. 2016, doi: 10.1364/JOSAB.33.000741.

[9] J. Cao, B. Poumellec, F. Brisset, and M. Lancry, "Pulse energy dependence of refractive index change in lithium niobium silicate glass during femtosecond laser direct writing," *Opt. Express*, vol. 26, no. 6, p. 7460, Mar. 2018, doi: 10.1364/OE.26.007460.

[10] J. Cao *et al.*, "Nanoscale Phase Separation in Lithium Niobium Silicate Glass by Femtosecond Laser Irradiation," *J. Am. Ceram. Soc.*, vol. 100, no. 1, pp. 115–124, Jan. 2017, doi: 10.1111/jace.14570.

[11] B. Poumellec, M. Lancry, R. Desmarchelier, E. Hervé, F. Brisset, and J. C. Poulin, "Asymmetric Orientational Writing in glass with femtosecond laser irradiation," *Opt. Mater. Express*, vol. 3, no. 10, p. 1586, Oct. 2013, doi: 10.1364/OME.3.001586.

[12] "M. Lancry PACRIM/GOMD May 21-26, 2017 Hawaii, USA." https://ceramics.org/wp-content/uploads/2017/05/Complete-conf-guide-PACRIM12_lo-res.pdf (accessed Oct. 21, 2021).

[13] K. Veenhuizen, S. McAnany, D. Nolan, B. Aitken, V. Dierolf, and H. Jain, "Fabrication of graded index single crystal in glass," *Sci Rep*, vol. 7, no. 1, p. 44327, Jun. 2017, doi: 10.1038/srep44327.

[14] F. Träger, Ed., *Springer handbook of lasers and optics*. New York: Springer, 2007.

[15] X. He *et al.*, "Size-controlled oriented crystallization in SiO_2-based glasses by femtosecond laser irradiation," *J. Opt. Soc. Am. B*, vol. 31, no. 2, p. 376, Feb. 2014, doi: 10.1364/JOSAB.31.000376.

[16] S. S. Mao *et al.*, "Dynamics of femtosecond laser interactions with dielectrics," *Appl Phys A*, vol. 79, no. 7, pp. 1695–1709, Nov. 2004, doi: 10.1007/s00339-004-2684-0.

[17] R. Desmarchelier, B. Poumellec, F. Brisset, S. Mazerat, and M. Lancry, "In the Heart of Femtosecond Laser Induced Nanogratings: From Porous Nanoplanes to Form Birefringence," *World Journal of Nano Science and Engineering*, vol. 5, no. 4, Art. no. 4, Nov. 2015, doi: 10.4236/wjnse.2015.54014.

[18] M. Lancry, E. Régnier, and B. Poumellec, "Fictive temperature in silica-based glasses and its application to optical fiber manufacturing," *Progress in Materials Science*, vol. 57, no. 1, pp. 63–94, Jan. 2012, doi: 10.1016/j.pmatsci.2011.05.002.

[19] B. Poumellec, M. Lancry, A. Chahid-Erraji, and P. G. Kazansky, "Modification thresholds in femtosecond laser processing of pure silica: review of dependencies on laser parameters [Invited]," *Opt. Mater. Express, OME*, vol. 1, no. 4, pp. 766–782, Aug. 2011, doi: 10.1364/OME.1.000766.

[20] S. Richter, M. Heinrich, F. Zimmermann, C. Vetter, A. Tünnermann, and S. Nolte, "Nanogratings in Fused Silica: Structure, Formation and Applications," in *Progress in Nonlinear Nano-Optics*, S. Sakabe, C. Lienau, and R. Grunwald, Eds. Cham: Springer International Publishing, 2015, pp. 49–71. doi: 10.1007/978-3-319-12217-5_3.

[21] C. Hnatovsky *et al.*, "Pulse duration dependence of femtosecond-laser-fabricated nanogratings in fused silica," *Appl. Phys. Lett.*, vol. 87, no. 1, p. 014104, Jul. 2005, doi: 10.1063/1.1991991.

[22] W. Yang, E. Bricchi, P. G. Kazansky, J. Bovatsek, and A. Y. Arai, "Self-assembled periodic sub-wavelength structures by femtosecond laser direct writing," *Opt. Express*, vol. 14, no. 21, p. 10117, 2006, doi: 10.1364/OE.14.010117.

[23] F. Zimmermann, A. Plech, S. Richter, A. Tünnermann, and S. Nolte, "The onset of ultrashort pulse-induced nanogratings: The onset of ultrashort pulse-induced nanogratings," *Laser & Photonics Reviews*, vol. 10, no. 2, pp. 327–334, Mar. 2016, doi: 10.1002/lpor.201500272.

[24] M. Lancry, B. Poumellec, J. Canning, K. Cook, J.-C. Poulin, and F. Brisset, "Ultrafast nanoporous silica formation driven by femtosecond laser irradiation: In the heart of nanogratings," *Laser & Photonics Reviews*, vol. 7, no. 6, pp. 953–962, Nov. 2013, doi: 10.1002/lpor.201300043.

[25] M. Lancry, R. Desmarchelier, K. Cook, B. Poumellec, and J. Canning, "Compact Birefringent Waveplates Photo-Induced in Silica by Femtosecond Laser," *Micromachines*, vol. 5, no. 4, pp. 825–838, Sep. 2014, doi: 10.3390/mi5040825.

[26] V. N. Sigaev *et al.*, "Second-order optical non-linearity initiated in Li2O–Nb2O5–SiO2 and Li2O–ZnO–Nb2O5–SiO2 glasses by formation of polar and centrosymmetric nanostructures," *Journal of Non-Crystalline Solids*, vol. 354, no. 10–11, pp. 873–881, Feb. 2008, doi: 10.1016/j.jnoncrysol.2007.08.033.

[27] T. Komatsu, "Design and control of crystallization in oxide glasses," *Journal of Non-Crystalline Solids*, vol. 428, pp. 156–175, Nov. 2015, doi: 10.1016/j.jnoncrysol.2015.08.017.

[28] Y. Shimotsuma, P. G. Kazansky, J. Qiu, and K. Hirao, "Self-Organized Nanogratings in Glass Irradiated by Ultrashort Light Pulses," *Phys. Rev. Lett.*, vol. 91, no. 24, p. 247405, Dec. 2003, doi: 10.1103/PhysRevLett.91.247405.

[29] M. Lancry *et al.*, "Nanogratings formation in multicomponent silicate glasses," *Appl. Phys. B*, vol. 122, no. 3, p. 66, Mar. 2016, doi: 10.1007/s00340-016-6337-8.

[30] T. Asai *et al.*, "Systematic Control of Structural Changes in GeO_2 Glass Induced by Femtosecond Laser Direct Writing," *J. Am. Ceram. Soc.*, vol. 98, no. 5, pp. 1471–1477, May 2015, doi: 10.1111/jace.13482.

[31] F. Zhang, H. Zhang, G. Dong, and J. Qiu, "Embedded nanogratings in germanium dioxide glass induced by femtosecond laser direct writing," *J. Opt. Soc. Am. B*, vol. 31, no. 4, p. 860, Apr. 2014, doi: 10.1364/JOSAB.31.000860.

[32] S. Richter *et al.*, "Laser induced nanogratings beyond fused silica - periodic nanostructures in borosilicate glasses and ULE™," *Opt. Mater. Express*, vol. 3, no. 8, p. 1161, Aug. 2013, doi: 10.1364/OME.3.001161.

[33] S. Richter *et al.*, "Ultrashort pulse induced modifications in ULE - from nanograting formation to laser darkening," *Opt. Mater. Express*, vol. 5, no. 8, p. 1834, Aug. 2015, doi: 10.1364/OME.5.001834.

[34] F. Zimmermann, A. Plech, S. Richter, A. Tünnermann, and S. Nolte, "Ultrashort laser pulse induced nanogratings in borosilicate glass," *Appl. Phys. Lett.*, vol. 104, no. 21, p. 211107, May 2014, doi: 10.1063/1.4880658.

[35] S. S. Fedotov *et al.*, "Direct writing of birefringent elements by ultrafast laser nanostructuring in multicomponent glass," *Appl. Phys. Lett.*, vol. 108, no. 7, p. 071905, Feb. 2016, doi: 10.1063/1.4941427.

[36] R. Taylor, C. Hnatovsky, and E. Simova, "Applications of femtosecond laser induced self-organized planar nanocracks inside fused silica glass," *Laser & Photon. Rev.*, vol. 2, no. 1–2, pp. 26–46, Apr. 2008, doi: 10.1002/lpor.200710031.

[37] V. R. Bhardwaj *et al.*, "Optically Produced Arrays of Planar Nanostructures inside Fused Silica," *Phys. Rev. Lett.*, vol. 96, no. 5, p. 057404, Feb. 2006, doi: 10.1103/PhysRevLett.96.057404.

[38] R. Buividas *et al.*, "Mechanism of fine ripple formation on surfaces of (semi)transparent materials via a half-wavelength cavity feedback," *Nanotechnology*, vol. 22, no. 5, p. 055304, Feb. 2011, doi: 10.1088/0957-4484/22/5/055304.

[39] S. Richter *et al.*, "On the fundamental structure of femtosecond laser-induced nanogratings," *Laser & Photonics Reviews*, vol. 6, no. 6, pp. 787–792, 2012, doi: https://doi.org/10.1002/lpor.201200048.

[40] M. Beresna, M. Gecevičius, P. G. Kazansky, T. Taylor, and A. V. Kavokin, "Exciton mediated self-organization in glass driven by ultrashort light pulses," *Appl. Phys. Lett.*, vol. 101, no. 5, p. 053120, Jul. 2012, doi: 10.1063/1.4742899.

[41] N. M. Bulgakova and V. P. Zhukov, "Continuum Models of Ultrashort Laser–Matter Interaction in Application to Wide-Bandgap Dielectrics," in *Lasers in Materials Science*, vol. 191, M. Castillejo, P. M. Ossi, and L. Zhigilei, Eds.

Cham: Springer International Publishing, 2014, pp. 101–124. doi: 10.1007/978-3-319-02898-9_5.

[42] Y. Liao *et al.*, "High-fidelity visualization of formation of volume nanogratings in porous glass by femtosecond laser irradiation," *Optica*, vol. 2, no. 4, p. 329, Apr. 2015, doi: 10.1364/OPTICA.2.000329.

[43] Y. Liao *et al.*, "Formation of nanogratings in a porous glass immersed in water by femtosecond laser irradiation," San Francisco, California, United States, Mar. 2015, p. 93500G. doi: 10.1117/12.2076905.

[44] A. Rudenko, J.-P. Colombier, and T. E. Itina, "From random inhomogeneities to periodic nanostructures induced in bulk silica by ultrashort laser," *Phys. Rev. B*, vol. 93, no. 7, p. 075427, Feb. 2016, doi: 10.1103/PhysRevB.93.075427.

[45] P. P. Rajeev *et al.*, "Transient nanoplasmonics inside dielectrics," *J. Phys. B: At. Mol. Opt. Phys.*, vol. 40, no. 11, pp. S273–S282, Jun. 2007, doi: 10.1088/0953-4075/40/11/S03.

[46] R. Buschlinger, S. Nolte, and U. Peschel, "Self-organized pattern formation in laser-induced multiphoton ionization," *Phys. Rev. B*, vol. 89, no. 18, p. 184306, May 2014, doi: 10.1103/PhysRevB.89.184306.

[47] R. H. Doremus, "Physical Solubility of Gases in Fused Silica," *Journal of the American Ceramic Society*, vol. 49, no. 9, pp. 461–462, Sep. 1966, doi: 10.1111/j.1151-2916.1966.tb13299.x.

[48] N. M. Bulgakova, V. P. Zhukov, and Y. P. Meshcheryakov, "Theoretical treatments of ultrashort pulse laser processing of transparent materials: toward understanding the volume nanograting formation and 'quill' writing effect," *Appl. Phys. B*, vol. 113, no. 3, pp. 437–449, Dec. 2013, doi: 10.1007/s00340-013-5488-0.

[49] E. S. Efimenko, A. V. Kim, and M. Quiroga-Teixeiro, "Ionization-Induced Small-Scaled Plasma Structures in Tightly Focused Ultrashort Laser Pulses," *Phys. Rev. Lett.*, vol. 102, no. 1, p. 015002, Jan. 2009, doi: 10.1103/PhysRevLett.102.015002.

[50] E. S. Efimenko and A. V. Kim, "Strongly coupled regime of ionization-induced scattering in ultrashort laser-matter interactions," *Phys. Rev. E*, vol. 84, no. 3, p. 036408, Sep. 2011, doi: 10.1103/PhysRevE.84.036408.

[51] S. Richter *et al.*, "The role of self-trapped excitons and defects in the formation of nanogratings in fused silica," *Opt. Lett.*, vol. 37, no. 4, p. 482, Feb. 2012, doi: 10.1364/OL.37.000482.

[52] M. Hasegawa *et al.*, "Positron and positronium studies of irradiation-induced defects and microvoids in vitreous metamict silica," *Nuclear Instruments and Methods in Physics Research Section B: Beam Interactions with Materials and Atoms*, vol. 166–167, pp. 431–439, May 2000, doi: 10.1016/S0168-583X(99)01026-5.

[53] J. E. Sipe, J. F. Young, J. S. Preston, and H. M. van Driel, "Laser-induced periodic surface structure. I. Theory," *Phys. Rev. B*, vol. 27, no. 2, pp. 1141–1154, Jan. 1983, doi: 10.1103/PhysRevB.27.1141.

[54] J. Z. P. Skolski, G. R. B. E. Römer, J. V. Obona, V. Ocelik, A. J. Huis in 't Veld, and J. Th. M. De Hosson, "Laser-induced periodic surface structures: Fingerprints of light localization," *Phys. Rev. B*, vol. 85, no. 7, p. 075320, Feb. 2012, doi: 10.1103/PhysRevB.85.075320.

[55] B. Drossel and F. Schwabl, "Formation of space-time structure in a forest-fire model," *Physica A: Statistical Mechanics and its Applications*, vol. 204, no. 1–4, pp. 212–229, Mar. 1994, doi: 10.1016/0378-4371(94)90426-X.

[56] L. N. Gaier * *et al.*, "Hole-assisted energy deposition in dielectrics and clusters in the multiphoton regime," *Journal of Modern Optics*, vol. 52, no. 7, pp. 1019–1030, May 2005, doi: 10.1080/09500340500067174.

[57] Y. Kashiwaya, T. Nakauchi, K. S. Pham, S. Akiyama, and K. Ishii, "Crystallization Behaviors Concerned with TTT and CCT Diagrams of Blast Furnace Slag Using Hot Thermocouple Technique," *ISIJ International*, vol. 47, no. 1, pp. 44–52, 2007, doi: 10.2355/isijinternational.47.44.

[58] A. Stone *et al.*, "Femtosecond laser-writing of 3D crystal architecture in glass: Growth dynamics and morphological control," *Materials & Design*, vol. 146, pp. 228–238, May 2018, doi: 10.1016/j.matdes.2018.03.016.

[59] N. V. Sidorov *et al.*, "Boron Influence on Defect Structure and Properties of Lithium Niobate Crystals," *Crystals*, vol. 11, no. 5, p. 458, Apr. 2021, doi: 10.3390/cryst11050458.

[60] N. V. Sidorov, N. A. Teplyakova, R. A. Titov, and M. N. Palatnikov, "Structural Features, Physicochemical, and Optical Characteristics of Lithium Niobate Crystals Grown from Boron-Doped Melts," *Tech. Phys.*, vol. 63, no. 12, pp. 1762–1770, Dec. 2018, doi: 10.1134/S1063784218120198.

[61] O. Sánchez-Dena, C. D. Fierro-Ruiz, S. D. Villalobos-Mendoza, D. M. Carrillo Flores, J. T. Elizalde-Galindo, and R. Farías, "Lithium Niobate Single Crystals and Powders Reviewed—Part I," *Crystals*, vol. 10, no. 11, p. 973, Oct. 2020, doi: 10.3390/cryst10110973.

[62] O. Sánchez-Dena, S. D. Villalobos-Mendoza, R. Farías, and C. D. Fierro-Ruiz, "Lithium Niobate Single Crystals and Powders Reviewed—Part II," *Crystals*, vol. 10, no. 11, p. 990, Oct. 2020, doi: 10.3390/cryst10110990.

Chapter 6

Sol-gel process for glass synthesis: a route towards the fabrication of $Bi_2O_3 – B_2O_3 – Fe_2O_3$

This chapter focuses on the research activity related to glass fabrication by sol-gel process finalized to laser irradiation. Then, after a process framing in the various phases of glass technology and an explanation of its main characteristics and parameters in Section 1, an overview on nanoparticles and bulk glasses produced by this method is reported in Section 2 as a short summary of the steps to explain the reasons behind the choice of $Bi_2O_3 – B_2O_3 – Fe_2O_3$ (BBF) ternary system for the host glass. The main results of this work are reported in Section 3 that is divided into five subsections. An introduction motivates the choice of the BBF system from $BiFeO_3$ before passing to a discussion around Pechini Method, and his modification adapted to our glass production. Finally, a description of the experimental results, and their outlook are presented towards future work.

6.1 Introduction and general features [1]

6.1.1 General overview of the sol-gel process

Sol-gel process ─ contraction of the terms solution-gelation ─ is a well-known bottom-up procedure to create massive materials such as net-shape or net-surface objects, films, fibers, coatings, and composites. The use of "soft chemistry" processes [1], which take place in open containers at a temperature of less than 500°C, aims to renew the solid-state chemistry. Indeed, replacing the synthesis at high temperatures that leads to the more stable product, the sol-gel route will give the kinetically favored product at lower temperature. Moreover, this route allows a wide range of products, in contrast to the traditional glass fabrication techniques which occur at very high temperature. A colloidal suspension created by condensation of precursors solution called "sol" starts to become an actual "gel", i.e., a continuous tridimensional inorganic network containing an interconnecting liquid phase by hydrolysis and condensation chemical reactions [1]. This gel is subjected to drying at a low temperature like ~ 100°C. To remove the porosity, another thermal treatment of sintering at a temperature near the glass transition (T_g). A clear scheme of sol-gel steps and a different range of products that can be fabricated is shown in Figure 112 [1].

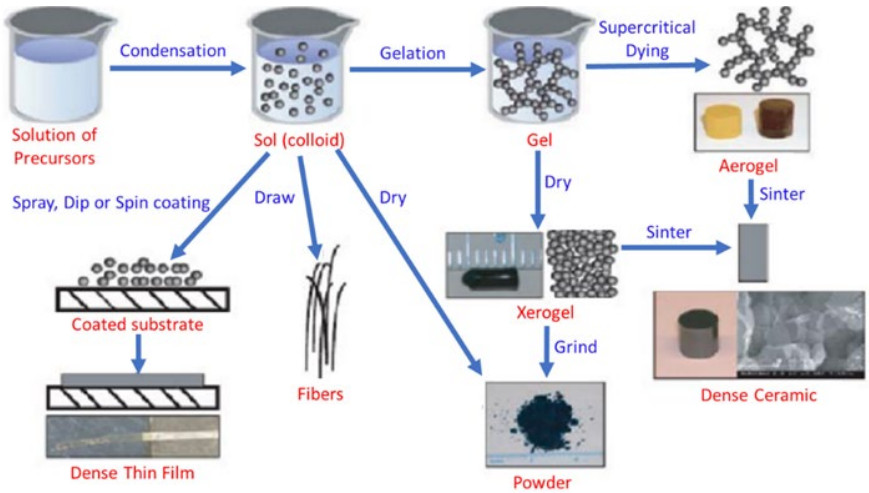

[1] The content of this paragraph is also a summary of all the sol-gel issues reported in my master thesis redacted in Italian titled "Il processo sol-gel per la sintesi del vetro: dalle nanoparticelle al bulk" (Polytechnic of Turin, 2018).

Figure 112: Scheme of sol-gel steps highlighting the variability of different final products that can be achieved (adapted from [1])

Until the 1970s, the traditional and principal method in glassmaking was the melt-quenching technique, a physical methodology that is part of first-generation glass manufacturing procedures [2]. Despite the fact that chemical vapor deposition (CVD) [3] and physical vapor deposition (PVD) [4] techniques break out as second-generation methods, the sol-gel process as a third-generation method stands out for the countless advantages it brings before and during the synthesis process [5]. For instance, there is the possibility to realize a highly pure and homogeneous component at low temperature and also the opportunity of choosing the final product shape before starting the process. Moreover, the synthesis and its parameters can be adapted according to the specific application required in various challenging domains, not only in optics, electronics, and photonics but also in energy, environment, and biomedical technology [5], [6]. In particular, sol-gel has been proven to be an enabling technology to carry out SiO_2 preforms for optical glass fibers drawing, thin-film coatings [7] of planar substrates and sensors, dye-sensitized solar cells, fibers by the incorporation of rare-earth-doped glass nanoparticles [8]–[11] and semiconductor oxide nanostructures [12], [13].
The sol-gel process is also applied to fine-grained advanced ceramics with ferroelectric, dielectric, piezoelectric, optical, electro-optical, and multiferroic properties [14], [15].
In the formation of molten glass (melt quenching), the crystalline structure is avoided through a fairly fast cooling. Indeed, in the case of traditional methods for glass production, the liquid structure is preserved through the undercooling of the melt from high temperatures. To obtain amorphous reticular structures in sol-gel materials, quick and irreversible reactions are carried out. Indeed, in the sol-gel process, the maintenance of the liquid structure is the prerogative of gelation. In addition, unlike melt quenching, it is possible to produce homogeneous and highly pure glasses, after synthesis at room temperature or less than 100° C, which culminates in gelation, with radical changes on a molecular scale, and subsequent removal of solvent and water, before the last phase of sintering at temperatures below the material melting point. It is important to note that the sol-gel process and melt quenching, both in structural terms and in terms of properties, produce very different products [1], [16], as shown in Figure 113.

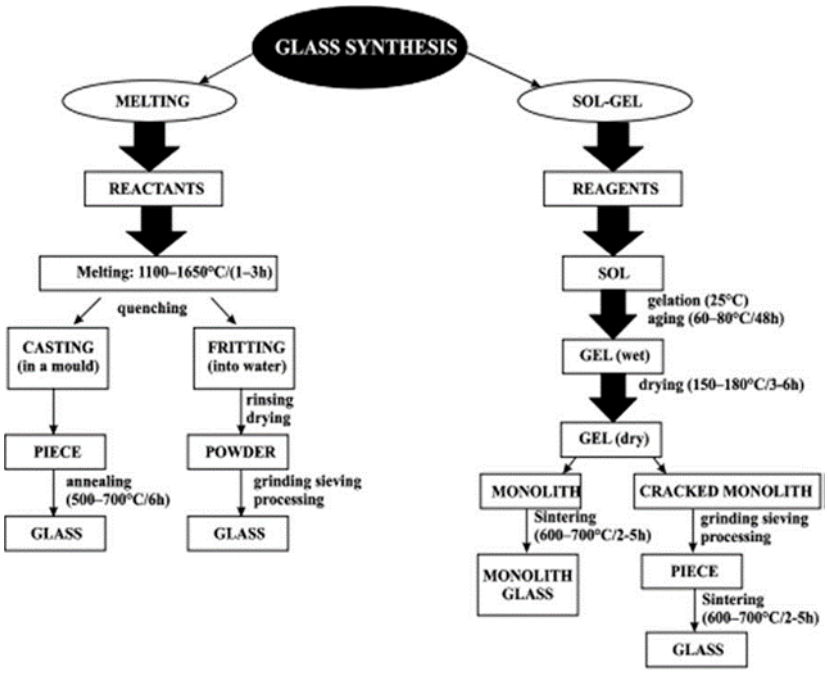

Figure 113: Comparison scheme between melt-quenching and sol-gel process for glass synthesis [16]

Below, the main advantages for the sol-gel process are reported [7], [17], [18]:

- ❖ the production of highly homogeneous multi-component gels is required in the case of glass and fiber preforms for optical applications. In addition, thanks to the control of the structure at the molecular level, we obtain glasses with unusual microstructures and also new glass-ceramics;
- ❖ dry gel microstructures can be controlled with a wide range of density, surface area, and pore size, useful in specific applications such as catalysts, transparent and impregnating insulators;
- ❖ sintered glass is produced at low temperature, around the glass transition temperature, while in normal glass production practices, the liquid temperature is exceeded by hundreds of degrees. This opens to the possibility of creating refractory glasses of high purity and homogeneity to overcome phase separation or crystallization;
- ❖ the rheological properties of the sol allow the formation of fibers, films, and composites through techniques such as spin-coating, dip-coating, injection, impregnation, or simple mixing and fusion;
- ❖ the presence of a colloidal solid-state in a liquid medium avoids pollution by dust dispersion in the synthesis stage, which is an excellent prospect for nuclear fuel applications;

- there is the possibility of controlling the kinetics of chemical reactions with low temperatures and dilution of reagents.

The sol-gel process requires a detailed study because, usually, only a limited number of parameters can be monitored, thus, making it challenging to identify the most critical variables depending on the specific properties to be obtained in the final material.

At the molecular level, the reactions of hydrolysis and condensation from the monomer to the oligomer and up to the polymer require knowledge of the different principles on which each step of the method is based.

The conversion from inorganic amorphous polymers (gelation) to glass takes place in a second passage and precisely at temperatures lower than those of fusion of the corresponding oxides.

In fact, various scientific disciplines are involved at every stage of the process [18]. Research is therefore interdisciplinary and falls not only within inorganic and organic chemistry but also within chemical engineering, material science, mineralogy, and physics, as illustrated in Figure 114 below.

sol – gel processing steps	*chemistry involved*	
precursors	organometallic chemistry, coordination chemistry, inorganic chemistry, organic chemistry,	latent monomers
	colloid chemistry, inorganic chemistry,	colloids
hydrolysis	organometallic chemistry, inorganic chemistry, physical chemistry,	
condensation	inorganic chemistry, colloid chemistry, polymer chemistry,	
gelation	colloid chemistry, inorganic chemistry, physical chemistry,	
drying densifying heating	inorganic chemistry, organic chemistry, chemical engineering,	
incorporation of organics	organic chemistry.	

Figure 114: Sol-gel steps and respective scientific discipline involved [18]

The peculiarity of the sol-gel process is the knowledge of what is introduced in the closed or open system, and at the end of the synthesis, the possibility to draw results with the appropriate characterizations carried out on the material, without having complete certainty about what happens in the intermediate passages, and it is, therefore, necessary to control all the stages, in an exhaustive and predictable way.

This is the most challenging scientific aspect in order to allow the wide diffusion of this technology at an industrial level.

6.1.2 Sol-gel typical features

The sol-gel process enables the fabrication of complex inorganics, such as ternary and quaternary oxides, characterized by a homogeneous distribution of components on the atomic scale, allowing full control of final product microstructure, even up to material nanostructure.
The following Figure 115 represents the sol-gel steps reached by chemical reactions on-going summarized in the list below [19]:

- preparation of precursors solution;
- formation of a "sol" by hydrolysis and partial condensation;
- formation of the "gel" by polycondensation of precursors solution hydrolysis;
- a possible step of aging can be added because of long gel formation and consequent variations in the composition, structure, and gel properties;
- drying if gel for production of a dense "xerogel" [20] via solvent evaporation or an "aerogel" [21] through supercritical drying;
- calcination to obtain the final product mechanically stable.

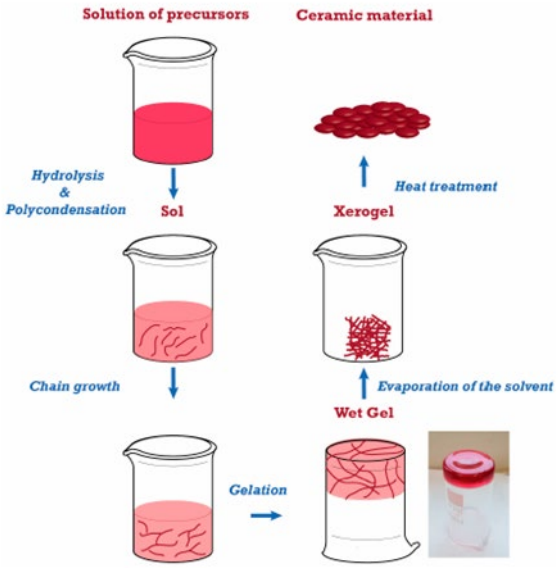

Figure 115: Scheme of different steps highlighted by hydrolysis and condensation reactions [19]

This list is only an indicative sequence of steps, but it can be manipulated according to the required final product. The sol-gel parameters control is fundamental to allow

variability of final material shapes, and below a set of main parameters to check is indicated:

- ✓ nature and concentration of precursors
- ✓ nature of the solvent (often also the process catalyst) [22]
- ✓ the pH of the solution
- ✓ nature and concentration of additives (catalysts, surfactants, nanostructure directing agents)
- ✓ pre- and post-thermal treatments of the materials
- ✓ aging time

Briefly, an overview of hydrolysis (1) and condensation (2, 3), the fundamental chemical reactions whose mechanisms regulate the sol-gel process, is shown below in Figure 116.

$$\equiv M-OR + HOH \rightleftharpoons \equiv M-OH + ROH \quad (1)$$

$$\equiv M-OH + \equiv M-OH \rightleftharpoons \equiv M-O-M\equiv + HOH \quad (2)$$

$$\equiv M-OH + \equiv M-OR \rightleftharpoons \equiv M-O-M\equiv + ROH \quad (3)$$

Figure 116: The main reactions in the sol-gel process of an alkoxide $M(OR)_4$, (1) hydrolysis of an alkoxy group, (2) condensation of two-OH species, and (3) mixed condensation of a-OH group and an alkoxy group species [19]

R is the alkyl group. Firstly, nucleophilic addition of a water molecule occurs, and secondly, alcohol (ROH) becomes a better leaving group by proton transfer [23], [24].

The nucleophilicity of the inbound group and the δ^+ of charge of element M regulate the thermodynamics of the process. The element's electronegativity, the electron-donating capacities of the OR group, and the stability of the leaving group act on M.

Furthermore, the kinetics raises with the increment of the difference (N-z), where N and z, respectively, represent the coordination number and the charge of the element M [25]. Reaction kinetics is also affected by the complexity of the alkyl chain due to the steric encumbrance that could create the alkoxide, according to a nucleophilic substitution mechanism. There is a substantial difference between the behavior of the transition metal alkoxide and the most common silicon one (N = z), where neither alcohol association nor oligomerization is noted [25], [26].

Polycondensation occurs at the same time as hydrolysis, so competition between them is often triggered. The polycondensation consists of a reaction between partially hydrolyzed alkoxide molecules and another OH-bearing species by removing water ((2) in the above Scheme) or an alkoxy group producing an alcohol molecule ((3) in the above Scheme).
These reactions of hydrolysis and polycondensation produce clusters that gradually join to form a single 3D polymeric network called gel, in which the viscosity experiences a drastic increase [27], [28]. It is a 3-dimensionally interconnected solid network with the particularity of expanding throughout a fluid medium [29]. There is a particular classification useful to distinguish different typologies of gel, depending on the supporting structure of the solid network and its bonding fashion and the most used source to prepare the solid network reported in the following Figure 117 [29]:

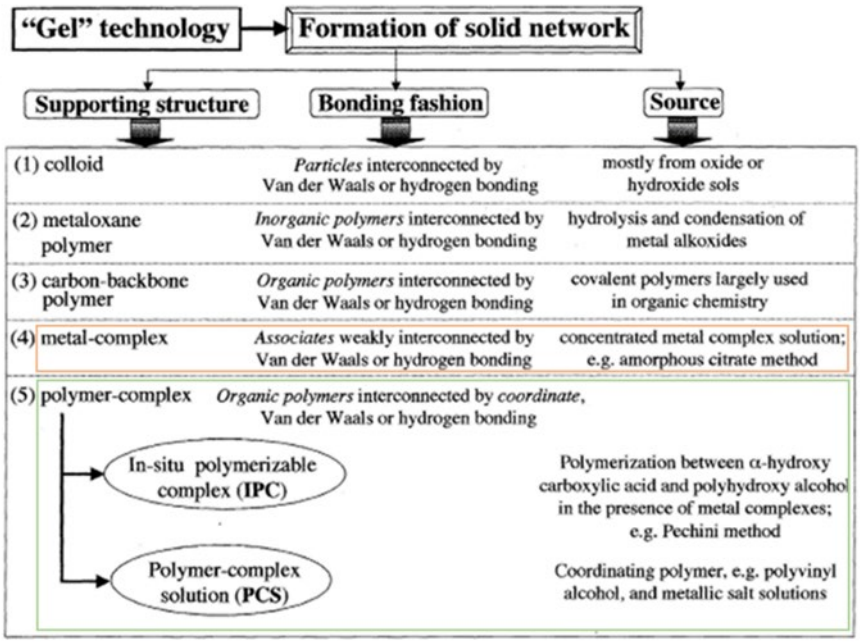

Figure 117: A typical classification of gel typologies. The attention is focused on metal- and polymer complex [29]

Focusing on metal-and polymer-complex, the difference in gel properties between the amorphous citrate method and the Pechini type in-situ polymerizable complex (IPC) is in the substitution of water with ethylene glycol. This leads to diverse chemical reactions in these two methods. The IPC method allows the formation of a rigid organic polymeric network from poly-esterification between citric acid and

ethylene glycol; otherwise, the amorphous citrate method involves the formation of weak hydrogen-bonded-like associates (see Figure 117 above).

During the synthesis of metal oxides, the rates of hydrolysis are high, since the electronegativity of the oxygen with respect to the metal is intense, and the M – O – C bonds are highly polarized. Otherwise, the rates of hydrolysis are slower for non-metal alkoxides (e.g., Si, P, Ge) [31]. During the formation of an oxides mixture, i.e., a multi-component system, gelation could occur at different times because of the different rates of hydrolysis of the precursors, and phase separation phenomena could occur through homo-condensations reactions rather than hetero-condensation. A solution to this could be introducing a basic or acidic catalyst [30] to accelerate the hydrolysis of the less reactive precursor or the addition of a chelating agent for inhibiting the most reactive precursor [23]. The control of gel properties and final product at each step of the sol-gel process makes this technique a valid alternative to others synthesis methods. A fundamental parameter is the gel time that corresponds to the duration of sol-gel transition following a significant increase in viscosity in such a way that a magnetic stir bar cannot maintain a vortex in the solution for a long time. The gel structure has to deal with the water content in the system and the nature and amount of catalyst. In general, SiO_2 can be obtained from acidic sol that forms a polymeric linear network with a low density of crossed bonds or from basic solutions characterized by clusters highly branched, as shown in Figure 118. This shows the competition between the reactions by noting the hydrolysis and condensations reactions rates as pH-dependent. In addition, steric hindrance factors define the condensation and hydrolysis rates, then the choice of the alkoxy groups affects the reactivity of silicon alkoxides $Si(OR)_4$ [19].

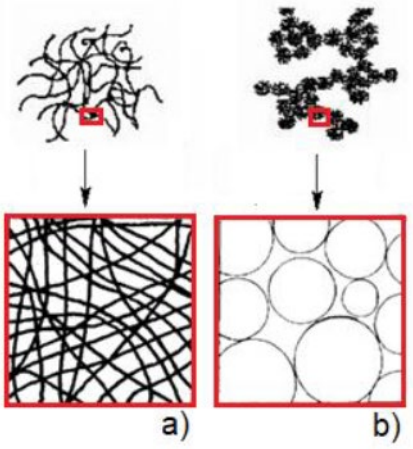

Figure 118: Representation of a gel generated by acid (a) and basic catalysis (b) [30]

Successively, gel drying occurs at 100°C to remove the solvent, primarily alcohol and water physically bound. During this step, the dry gel formed causes the deformation of its primitive porous backbone, and many cracks could be generated [23], [24], [31]. Shrinkage is induced by chemical driving force as condensation reaction and physical one as capillary pressure. The uniformity of the pressure leads to uniform network compression, and there will not be fractures. Otherwise, a pressure gradient is generated by the low permeability of the gel, and then cracks could be formed by the difference in the contraction speed between inside and outside the gel. This produces a xerogel, i.e., a product of an uncontrolled drying with disordered pores. The solution to this problem is to mitigate the possibility of warping and cracking through aging. Even though the formation of the gel has already taken place, the typical reactions of the sol-gel process continue leading to the variation of the material's chemical-physical properties. It is possible to see the phenomenon of syneresis, e.g., a shrinkage coming from the new crosslinks. This leads to an increase of gel modulus and viscosity, diminishing the successive shrinkage during drying.

In other cases, gels form aerogels with liquid pores replaced by air. These are obtained by supercritical drying (SCD) condition that has a minimal impact on the structure.

The subsequent thermal treatments are a function of the final product required. Typical temperatures in which dry gel is heated are in the range of 300-500°C to remove any residual organics. The last step is the calcination that gives rise to the most mechanically stable materials [19].

6.2 Overview on nanoparticles and bulk glasses fabricated by sol-gel process

The first approach with the sol-gel process occurred during the master thesis and then carried on in the six months pre-doctoral scholarship. During the first year of my Ph.D. activity at the Polytechnic of Turin, a development of the sol-gel process for glass formation was carried on starting with a single-component process. This activity predicted a progressive increase in the number of components until the synthesis of three-component glasses.

In particular, the research was firstly focused on the sol-gel synthesis of nanoparticles up to bulk silica glass [32], whose selected results are represented in Figure 119 a, b, and c. After an exploration of the behavior of silica glass, mainly aimed at finding the best catalyst for sol-gel hydrolysis and condensation, an

exploration of the acetic acid role as reagent and solvent in the synthesis process was also effectuated [33].

In addition, the incorporation of glass nanoparticles doped with rare earths and active glasses, i.e., special silica-based glasses for applications in photonics doped with neodymium, was also studied. In this last case, silica nanoparticles and bulk glass synthesis allowed us to monitor how macrostructure and nanostructure changed by introducing different amounts of neodymium as a dopant into the silica network and, samples were then characterized through DLS, FESEM, and XRD.

The starting point was to obtain silica nanoparticles that are suitable for common photonic devices. The subsequent incorporation of rare earth in the glass structure, as neodymium oxide, allows obtaining active glasses for advanced applications. The choice of neodymium is due to a maximum emission intensity in comparison with other rare earths [34]. Nanostructure change analysis by introducing a different amount of neodymium oxide in a silica network was the scope of the experiments. The investigation was then extended to neodymium-doped bulk glass, adopting a new methodology based on acetic acid used as solvent, reagent, and catalyst in the complete absence of water [35]. The neodymium incorporation in the glass matrix has been demonstrated by FESEM analysis [36]. Different amount of neodymium is revealed in products aged at room temperature and heated at high temperature by thermal oven treatment, as reported in Figure 119d, e, and f. Future perspective is to detect lifetime in fluorescence analysis to confirm the optical properties of doped glasses. Furthermore, the next step will be to find an application that can take advantage of the variability of neodymium concentration in a silica glass network [37], [38]. Another experiment is to synthesize neodymium-doped silica bulk glass [39], and an example of the samples obtained are shown in Figure 119g.

Finally, during an interesting tutoring activity on two-components sol-gel synthesis, the fabrication of aluminosilicate glasses through the sol-gel process [40]–[43] for fiber Bragg grating glass sensors was also explored to realize $SiO_2 – Al_2O_3$ glasses of different compositions (mol%) and the products of 90% – 10% and 50% – 50% respectively are reported in Figure 119h.

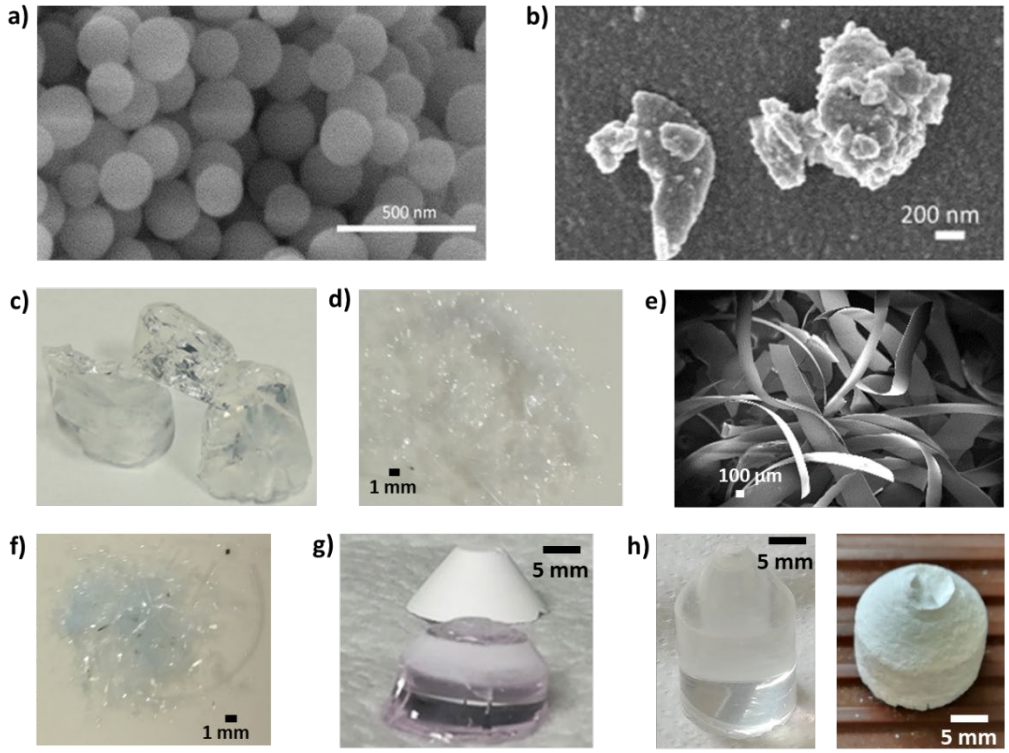

Figure 119: Overview of various products obtained by sol-gel synthesis in Polytechnic of Turin: a) pure silica nanoparticles (basic synthesis at room temperature inspired by Stöber method with tetramethyl orthosilicate (TEOS), H_2O, C_2H_5OH and NH_4OH); b) small nanoparticles and aggregates found after pure silica bulk glass synthesis based on TEOS and use of CH_3COOH as solvent and catalyst; c) final transparent silica bulk glass obtained by same synthesis process of b) after thermal treatment at 600°C for 2h at 1°/min; d) fiber-shape silica glass doped with neodymium ($Nd(NO_3)_3{\cdot}6H_2O$, 0.5% mol) (molar ratio 1 : 4 : 4 = TEOS : CH_3COOH : H_2O) after calcination at 600°C for 2h; e) FESEM image of sample d) at 100X; e) fiber-shape silica glass doped with neodymium ($Nd(NO_3)_3{\cdot}6H_2O$, 1.5% mol) (molar ratio 1 : 4 : 4 = TEOS : CH_3COOH : H_2O) after calcination at 600°C for 2h; g) allumino-silicate bulk glasses at 90% SiO_2 – 10% Al_2O_3 and 50% SiO_2 – 50% Al_2O_3 respectively; h) neodymium doped silica bulk glass after aging at T_{room} for 24 days realized only with TEOS, CH_3COOH and $Nd(NO_3)_3 \cdot 6H_2O$ (2,3% wt)

6.3 Towards a new synthesis route of $Bi_2O_3 – B_2O_3 – Fe_2O_3$

6.3.1 Introduction

The background acquired through the fabrication of two-components materials leads to proceed towards a sol-gel glass synthesis of $Bi_2O_3 – B_2O_3 – Fe_2O_3$ (BBF)

ternary system, following precisely the modified Pechini method to be discussed later in this paragraph. First of all, this configuration is really interesting with respect to its multiferroicity, and consequently, the characterizing properties as well as the resulting applications.

This "*multiferroic*" family, whose name was introduced by H. Schmid in 1994 [44], belongs to multifunctional materials that show the coexistence of ferroelectric, ferromagnetic, or antiferromagnetic orders in single or multiphase materials [47]. A distinct advantage is the possibility to control magnetic properties by an electric field, and then the magnetic state is complemented with the electric state. For example, the bismuth-based compounds are the typical lone-pair ferroelectrics. The lone-pair mechanism is generated by an anisotropic distribution of unbonded valence electrons around the host ion, as outlined in Figure 120. The peculiarity is that the ferroelectricity of $BiFeO_3$ is observed at room temperature. Specifically, a pair of Bi^{3+} valence electrons in the *6s* orbital is not included in *sp* hybridization and creates a local dipole. This gives rise to a spontaneous polarization [46] of 100 $\mu C \cdot cm^{-2}$ below the Curie temperature.

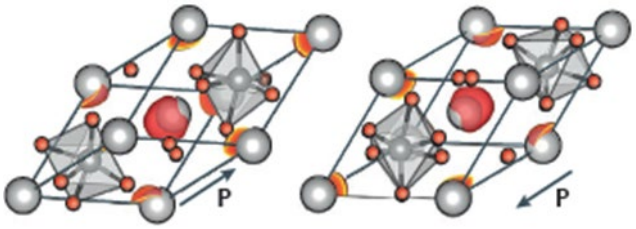

Figure 120: Mechanism promoting the coexistence of magnetic and electric long-range order: the case of lone - pair in $BiFeO_3$. The two Bi^{3+} electrons shift away from the Bi^{3+} ion generating the ferroelectricity and towards FeO_6 octahedra, giving rise to a spontaneous polarization P along the [111+ direction. Lone - pair is represented by the red isosurface of electron localization function of $BiFeO_3$ [45]

Furthermore, the selection of the BBF system is revealed attractive for advanced application due to multiferroic characteristics.

In recent years, there has been a growing number of studies on multiferroic transition metal oxide glasses [47]–[49] because of their technological uses in electronics, optics, tunable solid-state lasers, and optical telecommunication.

This material is suitable for many applications in data storage, sensors, and devices for spintronics [46]. It is difficult to prepare $BiFeO_3$ for incongruently melting at 934°C that makes hard solid-state synthesis and preferential evaporation of Bi_2O_3

at high temperatures. The easy appearance of second phases $Bi_2Fe_4O_9$ and $Bi_{25}FeO_{40}$ bringing impurities makes the synthesis of this material even more challenging [50].

Otherwise, a long-range periodic antiferromagnetic structure appears below the Néel temperature equal to 643°C. $BiFeO_3$ is the only room-temperature single-phase multiferroic material among the lone-pairs ones. It presents large and robust electric polarization and pronounced magnetoelectric coupling.

A summary box of terminology and clear schemes about multiferroics is shown in the following Figure 121 [45].

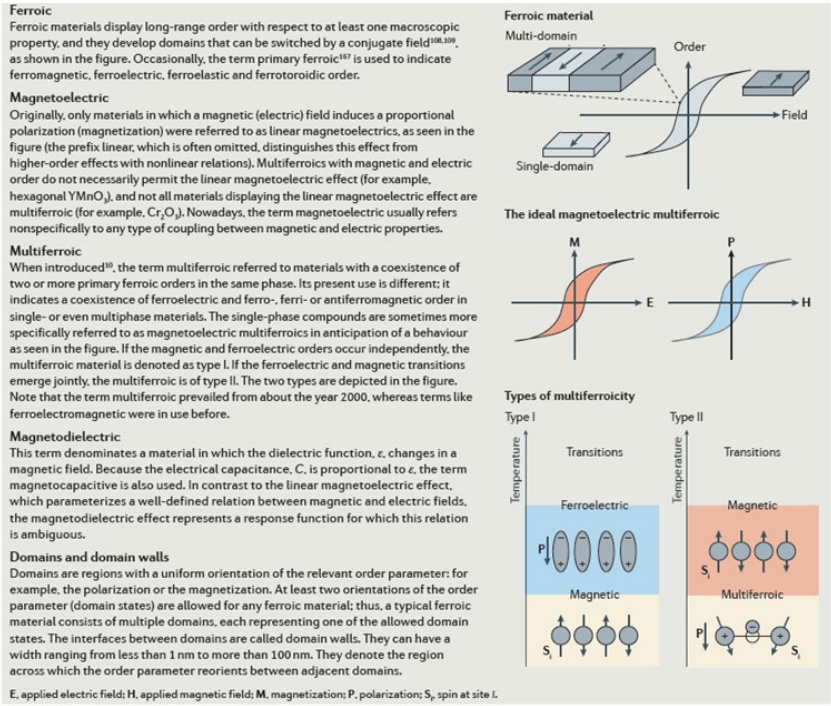

Figure 121: Clear terminology and schemes referred to multiferroics [45]

The multiferroic materials for advanced applications [47] have to be synthesized in a phase-pure form not to reduce their typical properties since it is a big challenge to produce them without impurities. The choice of BBF glasses for specific applications in photonics [51] is also challenging because the presence of iron makes reddish the mixture of the oxide, and then it is necessary to explore optical transparency [52], being a required condition for laser irradiation.

6.3.2 A brief overview of bismuth ferrite ($BiFeO_3$) and BBF system

Initially, the synthesis of $BiFeO_3$ [53] nanoparticles [54], [55] was preliminary to

that of a ternary glass. Ferroelectricity and antiferromagnetism coexist in the multiferroic bismuth ferrite, $BiFeO_3$, then this is chosen as a preliminary two-component synthesis product according to this Ref. [56], before proceeding with BBF fabrication.

$BiFeO_3$ is a perovskite with space group R3c suitable for specific applications as information storage, sensors, and actuators. The peculiarity is a magnetoelectric coupling at room temperature [57]. The Bi^{3+} lone electron pair provides a stereochemical activity that gives its ferroelectric order ($T_C \sim 830°C$). The impurities like $Bi_2Fe_4O_9$, Bi_2O_3, and $Bi_{25}FeO_{39}$ that can appear during synthesis are removed by the action of nitric acid leaching after the calcination of mixed bismuth and iron oxides.

Diverse wet chemical syntheses can be employed [58], but only nearly pure-phase materials were fabricated [59]. Different modified Pechini methods have been employed, with various polybasic carboxylic acids as complexing agents with or without ethylene glycol addition as polymerization agents [60], [61], [62]. This is the rationale behind the choice of starting with binary compounds to achieve $BiFeO_3$ production.

The original Pechini synthesis with citric acid and ethylene glycol allowed the production of both phase-pure materials [62] and secondary phases [63]. The presence of the OH-group is crucial for forming phase pure $BiFeO_3$, while the presence of COOH groups is not significant [65]. Ethylene glycol was employed as a solvent for a successful experiment in much larger quantities than when it is used only for polymerization reaction in an aqueous solution.

A suitable choice of nature and quantity of precursors and organic additives is fundamental. There is a case in which nitrates and citrates became precursors reported in [64]. Self-combustion of the gel during calcination could happen in combination with the evaporation of large amounts of decomposition gases, like CO [65]. The risk, in this case, stems from the formation of metallic bismuth: this phase segregation leads to a loss of homogeneity during calcination, even if the metal is readily subjected to oxidization in the later stages of calcination. The nitrates of bismuth and iron are the most common cations precursors [60], and also, in this work, their choice is confirmed.

The properties of the BBF oxides are based on the action of each oxide typology on the glass network.

B_2O_3 is the former oxide with peculiar characteristics like a strong electronegativity element that forms a very small cation B^{3+} (ionic radius 0.27Å). In an aqueous

solution, boron is characterized by two co-ordinates, tetrahedral in borate $[B(OH)]^-$, trigonal in boric acid B(OH). Both forms are stable in the monomer state, borate at pH > 11, boric acid at pH 7. Them, in the presence of B_2O_3 as a glass former, glasses are produced over a large range of compositions. B_2O_3 presents a special anomaly that consists of the transformation of triangles BO_3 in tetrahedra BO_4, explained in Ref. [66], which has to be taken into account when boron oxide is used in sol-gel synthesis.

Fe_2O_3 is the modifier oxide, easy to crystallize and to be complexed by citric acid, but its high melting point is a disadvantage for the sol-gel process.

Bi_2O_3 is the intermediate oxide, not a good glass network former because of a relatively small amount of field strength (0,53) of Bi^{3+} ion, has low solubility in water; as a preliminary step, it will be dissolved in concentrate HNO_3 before introduction in the synthesis container to ease the interaction with other metal oxides during the synthesis process.

The interesting review of [67] and the chapter [68] were the starting point to understand the Pechini method before proposing a new synthesis protocol.
protocol.

6.3.3 Pechini method overview

The original Pechini method was proposed in 1967 for depositing a dielectric film of titanates and niobates of lead and alkaline-earth elements to product capacitors [54]. It consists of a particular procedure of sol-gel synthesis of multi-component finely dispersed oxide materials, including the formation of complexes and production of an intermediate polymer gel [69]. Then, metal complexes are employed to prepare bulk materials, nano-crystalline powders, and thin films. The main sequence of steps for Pechini's method is to proceed with an intensive blending of different cations in a solution, a controlled transformation in gel, removal of the polymer matrix, and a production of a homogeneous oxide material. A suitable amount of metal salts alkoxides, according to the molar ratio required for a particular product, is introduced into a solution of citric acid and ethylene glycol. Citric acid was selected as a chelating agent for its cheapness and availability [70], [71].

The formation of citric complexes is needed to balance the difference in individual behavior of ions in solution and to create a better distribution of ions preventing the separation of components at successive later stages. The chemical reaction of polycondensation of citric acid and ethylene glycol begins above 100°C, producing

a citrate gel. When the temperature exceeds 400°C, oxidation, and pyrolysis of polymer matrix start, leading to the formation of X-ray amorphous oxide and/or carbonate precursor. Further thermal treatments contribute to the formation of the required final product with a high degree of homogeneity and dispersion. The most important key parameter is pH, and its control influences the extent of cation binding to the citrate. The optimization is made by introducing ammonia, ammonium hydroxide, or a similar base to control pH. It is necessary to check the solution acidity to prevent the precipitation of individual hydroxides in the case of multi-component synthesis. The formation of a covalent network is a consequence of poly-esterification between citrate and ethylene glycol. The ceramic phase is visible after decomposition or combustion of organics [19], [69].

Nowadays, Pechini's method is widely employed in a vast range of domains synthesizing dielectric, fluorescent and magnetic materials, high-temperature superconductors, and catalysts. Its peculiar simplicity, quite complete independence of the process conditions from the chemistry of positive ions contained in the final material, and a low temperature of precursor treatment, without sintering, producing nanocrystal powders of refractory oxides [69] constitute the main advantages.

Few shortfalls of this method consist of ethylene glycol toxicity, significant volumes of organic reagents per unit of product mass, the partial regeneration of one of the components during pyrolysis of polymer gel (e.g., copper, lead, zinc, ruthenium, etc.), and a lack of stability of citric complexes of some elements (bismuth, silicon, etc.) [69].

The chemical Pechini reactions have been described in Figure 122 [29]. In particular, this is the In-Situ Polymerizable Complex (IPC) method that joins the metal-complex formation with the "in-situ" polymerization of organics.

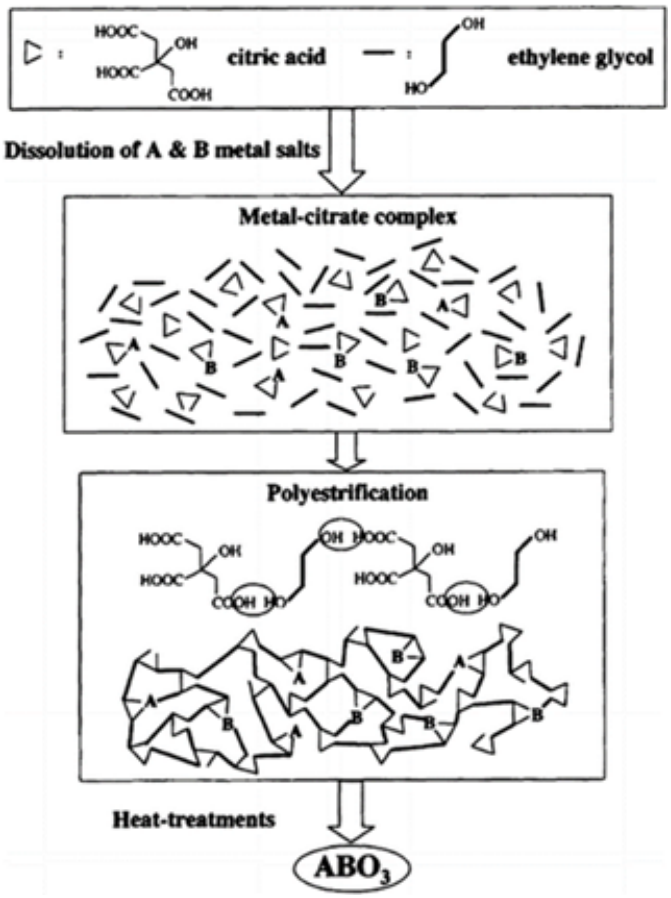

Figure 122: Pechini-type in-situ polymerizable complex (IPC) method: illustration of the chemical reaction between a polybasic carboxylic acid chelate and ethylene glycol during the formation of a complex perovskite oxide [29]

The choice of precursors is fundamental to form a homogenous multi-component gel without any phase segregation, related to the ability of metal cations to move. For this reason, the IPC method allows immobilizing the individual metal citric acid complexes in a rigid polymer network, maintaining the original stoichiometric ratio of metal ions upon polymerization. The polymeric resin with randomly branched polymers is obtained with metal cations uniformly distributed. Oxide powder is the product after thermal treatment of polymeric resin at high temperatures above 300°C and, consequently, polymer decomposition.

This method shows advantages with respect to the solid-state reaction technique in chemical homogeneity, composition control, high purity, and a possible crystallization at low temperature (i.e., also at 400°C) [29].

Although in the evolution of the original Pechini method, many other carboxylic acids and polyols have replaced citric acid and ethylene glycol over the years, in

this work, we chose to finalize the synthesis with citric acid focusing on other parameters explored and motivated later together with the way to solve the instability of bismuth citric complex.

6.3.4 The modified Pechini method for BBF synthesis

The modified Pechini process, adopted in this thesis work among the various $BiFeO_3$ synthesis reported in classification in Figure 123, represents a route for oxide materials starting with a homogeneous aqueous solution with the desired cation precursors inside in stoichiometric ratio. After the introduction of particular additives, the solution is converted to a rigid crosslinked polymer, hindering segregation of the cations by chemical reactions and evaporation. The polymer is further converted to a homogeneous oxide powder or film by a successive series of heat treatments [68].

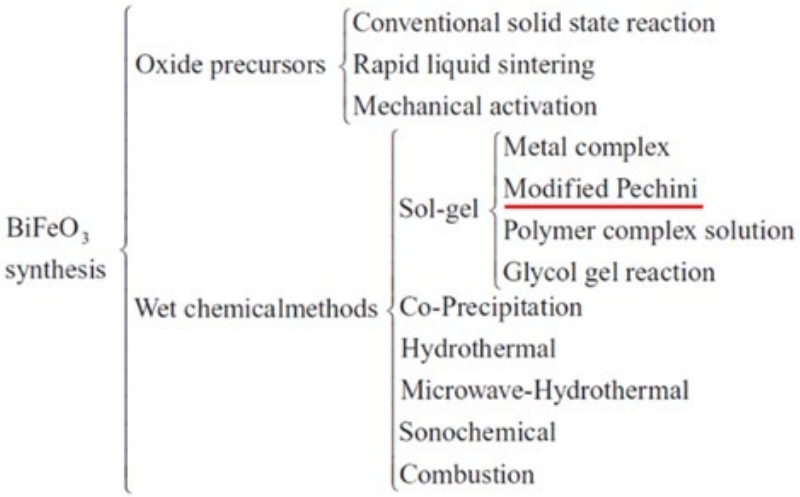

Figure 123: Synthesis methods scheme analyzed in the review highlighting the Modified Pechini as the one chosen in this work [67]

The modified Pechini method differs from the original by a diverse chelating agent that can be used. The creation of metal complexes through the reaction between metal cations and chelating agents leads to a growing polymer net that can reduce segregations during thermal treatments in which the polymer decomposition process can occur at high temperatures. The dehydration process is really a reaction of esterification between carboxylic acid and alcohol. To form a tetramer molecule, the resulting product of ester shows an alcoholic group in its left and

one carboxylic acid group in its right end, so this former can continue the chain reaction with another di-carboxylic acid and the latter with another di-alcohol [67].

The use of water provides a route attractive for environmental reasons, being simple and versatile for many different applications as thin films or coatings. There are no limitations to the number of cations involved in solution formation, and this method becomes interesting and challenging the more complex the product is.

The syntheses of this work were realized following this Scheme of the Pechini method reported in Figure 124 [68].

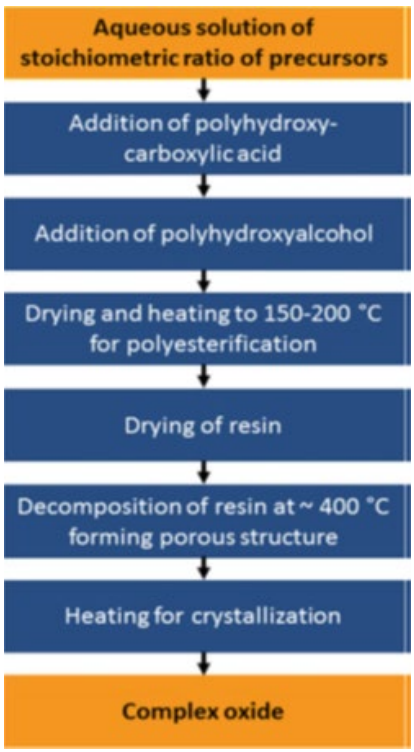

Figure 124: Flowsheet showing the Modified Pechini method steps [68]

In detail, the chemistry of the three main steps of the modified Pechini process is described below.

1) preparation of a stable aqueous solution of precursors

The first requirement is the stability of the aqueous chelated solution with the cation precursors. They have to be soluble in water or aqueous solutions with chelating agents, and then typical precursors are hydroxides, alkoxides, acetates, chlorides,

citrates, and nitrates. The cheapest are nitrates, also used for their high solubility. The concentration of cations is generally in the range from 0.1 to 1 M. It is critical to mix cations in the correct stoichiometric ratio. Citric acid is the most common tribasic hydroxyl carboxylic acid. Then, the degree of protonation of citric acid depends on the pH with three pKa values equal to 3.13, 4.76, and 6.39. The middle carboxylic group is the most acidic for the electron withdrawing power of the α-OH group, forming the strongest complexes with metal cations.
The complexes stability is a function of pH and concentration; even the bases can form complexes, but they are weaker than the ones created under acidic conditions. In addition, other important factors for stability [72] of chelate complexes are cation charge, size, and the number of valence electrons.
Typically, citric acid is added in excess according to molar ratio citric acid: cation from 1 to 3 [73], [74]. This ratio is fundamental to reaching a successful synthesis. Another essential condition is to study the proper introduction order of cations and chelating agents, following the rule that the cation forming the most stable chelates is introduced firstly and the one creating the least stable lastly [72].
The polymerization into a resin is obtained easily with the suitable addition of polyalcohol, like ethylene glycol, in the minimum amount necessary to esterification reaction. This issue was very controversial in the past [75], [76], but nowadays, it is common to introduce it in the same molar ratio as carboxyl acid.
The pH of the solution and the presence of protonated carboxylic groups affect the poly-esterification reaction [70], [71]. In a few cases, nitric acid has to be added in solution to catalyze the polymerization dependent on the original pH, or the base addition is necessary to increase the pH avoiding the precipitation of salts in solution [77].

2) drying and heating of the solution to form a solid polymeric resin

The first thermal treatment of cation precursors stable aqueous solution is drying at temperatures in the range of 110-150°C to remove water. It is essential is to avoid salts precipitation, which may affect the homogeneity of the final product. Since the viscosity increases during drying, the solution is finally turned into a polymeric-like resin. It is also possible to predict some precipitation that can occur before synthesis, as guaranteed by the sol-gel process in general. Basic cations precipitate as nitrates, chlorides, acetates, and chelates from a chelating agent during water evaporation. It can be noted a large increase of volume, by further heating of polymeric resin, due to release of water from hydrated chelates, decomposition of

complex anions from the precursors and the organics. The presence of foam avoids the segregation of cations during the process for a long diffusion path created by the gas development. It is possible to see some reactions that make the aqueous precursors' solution a brittle voluminous spongy-like material [68].

3) *decomposition/combustion of the resin to produce an amorphous oxidefollowed by crystallization of the desired oxide phase*

The third step is decomposition to remove the organics from the polymeric resin. Thermal decomposition for the resin typically occurs at 400°C. Each system has a typical crystallization temperature even low than 400°C. The decomposition process is exothermic, simultaneously at the crystallization; then, it is also challenging to find the actual crystallization temperature [78]. If there is a metastable phase, it could become a thermodynamically stable phase [79]. There could be a possible formation of carbonates from the decomposition of organics during the preparation of very basic cation oxides.

When the required product is a thin film on a substrate, it could be obtained by classical spin or dip coating. Successively, the drying of precursor film on a hot plate and the decomposition step of organic additives and complex anions from the precursors are the two stages, sometimes performed at the same time by a unique rapid thermal process. The type of nucleation to form the microstructure depends on pyrolysis temperature, heating rate, and crystallization temperature [85]. The thickness of each deposition can be established from a few to hundreds of nanometers by changing the viscosity of the solution or the spinning or dipping speed [86], [87]. The thickness could be increased by repeating the deposition many times.

Some inconveniences can result from incorrect stoichiometry because of the presence of crystallization water in nitrates and adsorbed water to be dried before use. Another phenomenon to avoid is the precipitation of the crystalline phase before the formation of the polymeric resin, considering the complexation of the less-soluble salts. It can be solved by varying the cation precursor or the chelating agent.

Some red-ox reactions between the organics and the cations can also occur in some cases give elemental metal like Bi, which could be solved with the same variation above [80].

6.3.5 Towards successful composition: focus on three experiments

The preliminary stage for three-component synthesis is to study the ternary phase

BBF diagram in Figure 125, in which there are also the terns of compositions already explored.
Glass compositions found by Hashimoto and Qiu enclosed in the yellow region are reported together with compositions in which there was crystallization [46].
The presentation of three main experiments at the end of the paragraph will explain how this composition was logically chosen.

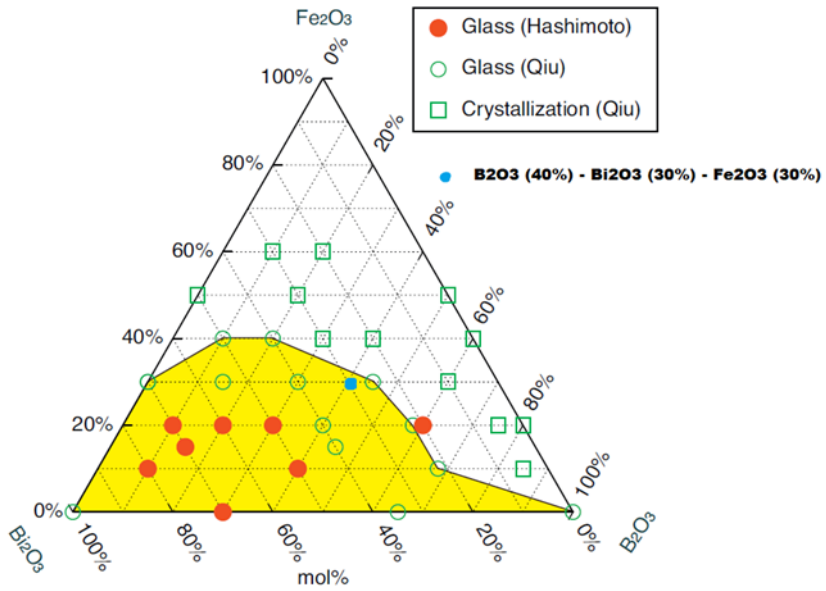

Figure 125: Glass-forming region for Bi_2O_3 - B_2O_3 - Fe_2O_3 system enclosed in yellow [81]: the final and successful composition is reported in light blue point

A first preliminary synthesis test with binary system Bi-Fe was performed. For producing bismuth ferrite ($BiFeO_3$), the modified Pechini sol-gel method was employed using citric acid as the chelating agent. A fundamental step is the definition of a binary composition for the first experiment preparation with Bi_2O_3 and Fe_2O_3 for $BiFeO_3$ nanoparticles following the synthesis reported in Ref. [56].
The reagents used in the present work were analytical grade bismuth nitrate pentahydrate ($Bi(NO_3)_3 \cdot 5H_2O$), iron nitrate nonahydrate ($Fe(NO_3)_3 \cdot 9H_2O$), citric acid ($C_6H_8O_7$), ethylene glycol ($C_2H_6O_2$) and acetic acid (CH_3COOH).
Below, the description of various synthesis steps in detail before proceeding with the BBF ternary system.
The stoichiometric proportion of $Bi(NO_3)_3 \cdot 5H_2O$ and $Fe(NO_3)_3 \cdot 9H_2O$ were initially dissolved in 400 ml deionized water with an individual concentration of 0.025 M. The solution was stirred for about 30 minutes to obtain a clear solution. When the

solution was transparent, 0.02 mole of citric acid ($C_6H_8O_7$) as the chelating agent was added to the solution to complex the metal cations.
The solution was then stirred and heated at 70-75°C for 8-10 hours until to form a transparent blackish-red sol. The temperature control was effectuated by a suitable probe to have for all the processes a temperature constant as shown in Figure 126.

Figure 126: Solution of first attempt with a probe to maintain a constant temperature of 75°C during the process

The pH of the solution was maintained in a range of 1-2 by adding NH_4OH dropwise.
This first attempt has been interrupted at this point for the following explained reasons:

1) The solution has never become transparent after 30 minutes
2) A test with equimolar concentrations between precursor salts and citric acid is required
3) It is necessary to verify if there will be complete salts solubility in water, and the solution will become transparent
4) In the modified Pechini process, water must be evaporated to form the polymeric resin.

Six actions for the modified Pechini method employed in this research work were necessary during the synthesis process to obtain the polymeric resin:

- Solution of a suitable HNO_3 concentration to dissolve $Bi(NO_3)_3 \cdot 5H_2O$ and also to act on the difficult stability of the bismuth salt
- The proper molar ratio between citric acid and metals that it has to be not

more than 2

- Definition of introduction precursors order based on stability complexes with citric acid
- Control of pH by ammonia
- Control of temperature
- Control of the amount of H_2O and NH_3

Successively according to the reasons and actions necessary explained above, the three most important experiments for BBF system synthesis will be illustrated below in a detailed way.

1. First experiment with boric acid as a precursor of boron oxide

A composition of 60% B_2O_3 – 30% Bi_2O_3 – 10% Fe_2O_3 (mol%) is the first that provides small preliminary results for the synthesis of a ternary glass, and the procedure is explained below and reported in Figure 127.

The methodology presents some modifications of Ref. [56] used for the nanoparticles of $BiFeO_3$. After preparation of a nitric acid aqueous solution 2M and the successive addition of suitable moles of $Bi(NO_3)_3 \cdot 5H_2O$ in a falcon vial, another aqueous solution with citric acid is stirred in a graduate cylinder. In another falcon vial, a solution with a suitable molar ratio of $Fe(NO_3)_3 \cdot 9H_2O$ and H_3BO_3 is made. It is necessary to proceed by the addition before of $Bi(NO_3)_3 \cdot 5H_2O$ solution and successively the citric acid solution. Only at this point, the solution was heated at 75°C to form a transparent blackish-red sol, maintaining the pH of the solution between 1-2 by adding ammonia solution dropwise and keeping revolution per minute under control as the water evaporates. The solution does not become blackish red, but it remains yellow opaque. Only an increase in viscosity is visible when the solution has reached the volume of approximately 1 ml. There are no analyses of this sample. Then, the choice of another composition was the next step to solve precipitates formation in the bottom of the container and a few amounts of B_2O_3 former oxide.

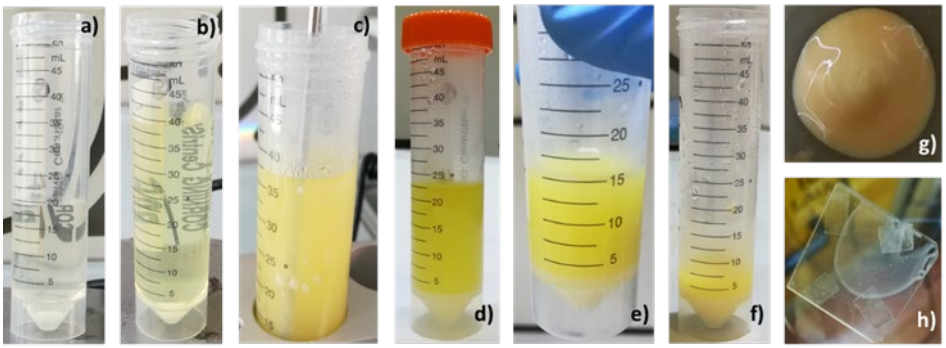

Figure 127: Sample in a falcon vial a) before the addition of Fe and B component; b) after the introduction of all the precursors; c) in the beginning of its heating at 75°C; d) solution after a few hours of heating; e), f) suspension after heating not finished yet, some white precipitates are visible in the bottom of the vial; g) suspension at the end of the process is dark yellow not red; h) thin-film deposed on glass slide after synthesis to check its consistency

2. A second experiment with boric acid as a precursor of boron oxide

A new composition is prepared by 40% B_2O_3 – 30% Bi_2O_3 – 30% Fe_2O_3 (mol%), with these two following crucial actions necessary in this experiment compared to the previous one:

1. addition of boron excess due to the difficulty of the boron oxide to enter the glass network
2. Fast addition of the citric acid moles equal to the sum of one of the three precursors to avoid the formation of precipitates.

The main process steps are shown in Figure 128. The solution became blackish-red and jellified after 5 hours. The temperature was maintained between 70 – 80°C during all the processes until the formation of a red polymeric resin. Finally, it is deposited by spin coating on a glass surface, as shown in Figure 128g.

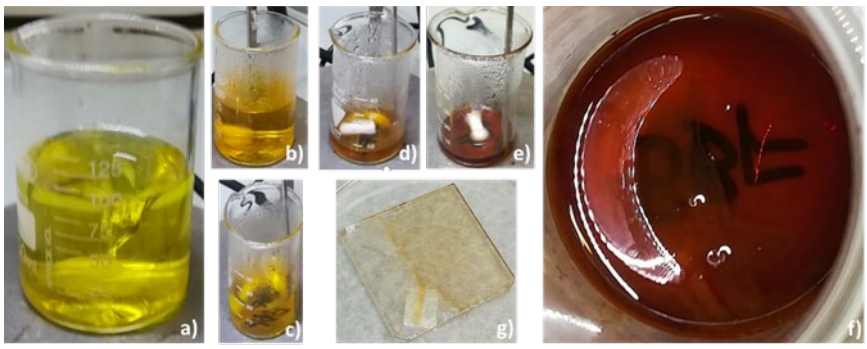

Figure 128: a) yellow and transparent solution after citric acid addition; b) solution at 70°C with starting change of color to red; c) solution at 75°C; d) last 10 ml of solution at 80°C; e), f) red resin at the final stage; g) glass slide with solution after spin coating at 2000 rpm

After ten days, a few red aggregates on the glass surface are to be checked for their possible crystalline nature that has to be avoided before laser irradiation, as highlighted in Figure 129.

Figure 129: Few red aggregates on the glass that probably indicate a surface crystallization

A TG-DTA analysis of the resin is done and represented in Figure 130. This is a preliminary step before carrying out further analysis necessary to identify the highlighted peaks. The drastic weight reduction at 200°C corresponds to the removal of the liquid component.

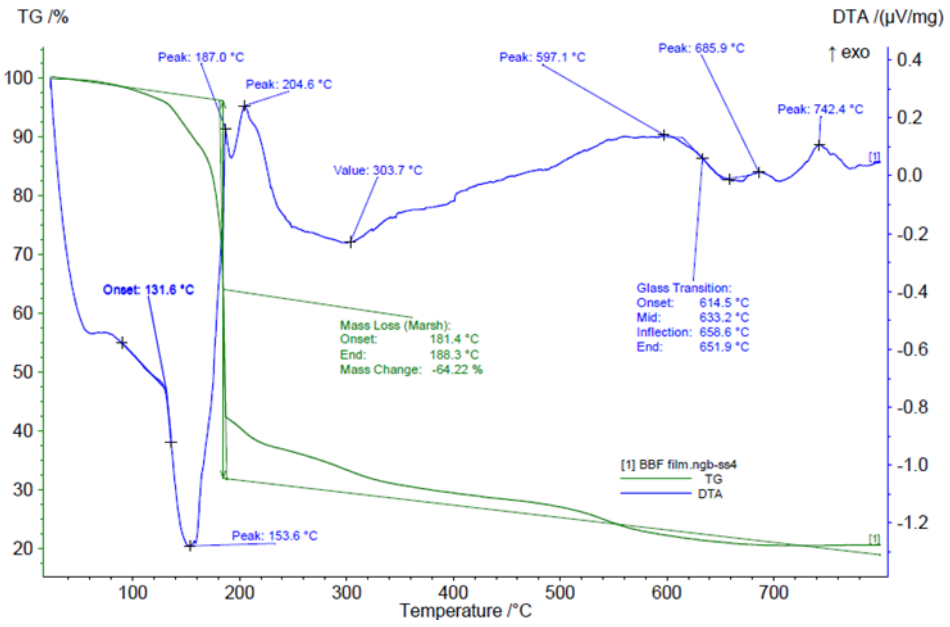

Figure 130: TG-DTA analyses of red polymeric resin

3. *Third experiment with boric acid as a precursor of boron oxide*

The same previous composition and two necessary actions indicated above in the precedent experiment were used in this last one, with the results summarized in Figure 131. The solution became blackish-red and jellified after 3 hours and 30 min.

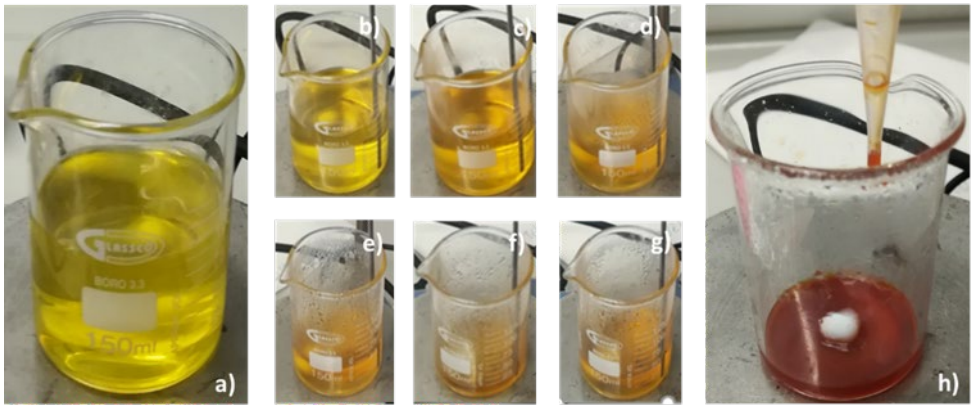

Figure 131: yellow and transparent solution after citric acid addition; b) solution at 38°C; c) solution at 66°C; d) solution at 70°C; e), f) solution at 76°C; g) solution at 78°C; h) red resin in the end of synthesis

During the increase of the sample viscosity in the final step, the resin was trasferred in a mold by Pasteur pipette as shown in Figure 132b. Part of the resin was heated at 100°C for 7 hours, resulting in the aspect shown in Figure 132g.

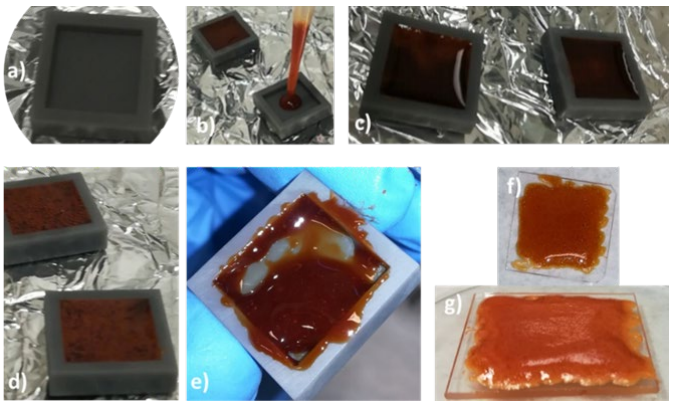

Figure 132: a) mold; b) transfer of solution in the mold by Pasteur pipette; c) full molds; d) full dry mold; e) consistency of resin in the mold; part of resin was spread on two glass slides after spin coating at 2000 rpm, and this is the resin aspect f) before and g) after thermal treatment at 100°C for 7 hours

6.3.6 Activity outlook and future improvements

An important remark is that, even though promising results have been achieved, it is not yet possible to complete the synthesis, and the steps carried out have been highlighted in Figure 133:

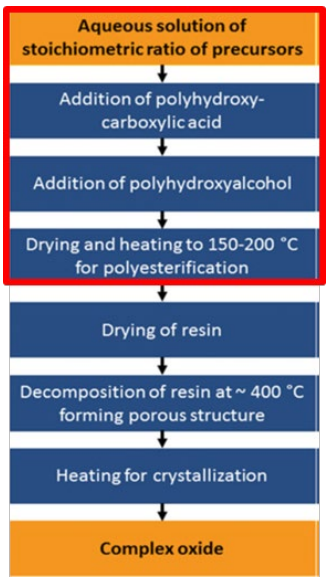

Figure 133: Modified Pechini method steps carried out, highlighted in red rectangle [68]

Indeed, it is possible to proceed with an XRD analysis of the resin to ensure that there was no surface crystallization of heterogeneous type. Further heat treatments and thin-film depositions with spin coaters are desirable to control optical transparency, a limiting parameter for future laser irradiation. After further analysis, another experiment with the same composition would be carried out to verify the repeatability of the process. The objective is to make this procedure an innovative synthesis protocol for the ternary system 40% B_2O_3 - 30% Bi_2O_3 - 30% Fe_2O_3.
To conclude, the composition control that the sol-gel methodology allows on nanoscale is a guarantee to have a glass in optimal condition, without having an early crystallization before proceeding with laser irradiation. Moreover, the sol-gel method has the possibility of obtaining composition not attainable with melt quenching in particular for multiferroics. Sol-gel could be also more convenient for applications, since the sol can be spin coated on a substrate allowing to form a thin film of the material to be modified. That would allow integration of the femtosecond modified structure on e.g., waveguides in silicon photonics.

6.4 Conclusions

This chapter relates on the chemical synthesis process of sol-gel, that works better for multiferroic materials as Bi_2O_3 – B_2O_3 – Fe_2O_3 (BBF). The possibility of a detailed parameters control allows to prefer this chemical technique over the

conventional melting quenching one. A sol becomes a gel after several steps, starting from the nanoparticles formation and up to a bulk material after multiple thermal treatments. The exploration of the peculiarities of ternary glassy system chosen provides the reasons to select the modified Pechini method as the best sol-gel process for BBF material. Three main steps can be identified: 1) preparation of a stable aqueous solution of precursors; 2) drying and heating of the solution to form a solid polymeric resin, and 3) decomposition/combustion of the resin to produce an amorphous oxide followed by crystallization of the desired oxide phase. The suitable choice of initial chemical composition is studied through ternary phase diagram, focusing the attention to be at the limit of the crystallization zone without, in fact, going beyond it. Three different key experiments are reported to explain the logical process followed to setup the best synthesis for BBF. Six actions are revealed fundamental: preparation of a solution with a suitable HNO_3 concentration to dissolve Bi $(NO_3)_3 \cdot 5H_2O$ and also to act on the difficult stability of the bismuth salt; verification that the molar ration between citric acid and metals is not greater than 2; definition of introduction precursors order based on stability complexes with citric acid; control of pH by NH_3, of temperature and of the amount of H_2O and NH_3. It was not possible to finish the Pechini process to synthesize a material suitable and ready for femtosecond irradiation but, so far, the results about resin production have been encouraging.

6.5 Bibliography

[1] A. Chládová, J. Wiener, J. M. Luthuli, and V. Zajícová, "Dyeing of glass fibres by the sol gel method," *AUTEX Research Journal*, vol. 11, p. 7, 2011.

[2] I. A. Rahman and V. Padavettan, "Synthesis of Silica Nanoparticles by Sol-Gel: Size-Dependent Properties, Surface Modification, and Applications in Silica-Polymer Nanocomposites—A Review," *Journal of Nanomaterials*, vol. 2012, pp. 1–15, 2012, doi: 10.1155/2012/132424.

[3] Z. Huang, Y. Huang, L. Zheng, and G. Zhang, "Effects of precursors on silica particle generation in CVD synthesis for fused silica glass," *Journal of Non-Crystalline Solids*, vol. 499, pp. 86–94, Nov. 2018, doi: 10.1016/j.jnoncrysol.2018.07.020.

[4] L. Geyao, D. Yang, C. Wanglin, and W. Chengyong, "Development and application of physical vapor deposited coatings for medical devices: A review," *Procedia CIRP*, vol. 89, pp. 250–262, 2020, doi: 10.1016/j.procir.2020.05.149.

[5] D. A. Barcelos, D. C. Leitao, L. C. J. Pereira, and M. C. Gonçalves, "What Is Driving the Growth of Inorganic Glass in Smart Materials and Opto-Electronic

Devices?," *Materials*, vol. 14, no. 11, p. 2926, May 2021, doi: 10.3390/ma14112926.

[6] S. Pooyan and P. O. Box, "Sol-gel process and its application in Nanotechnology," p. 5, 2005.

[7] J. D. Mackenzie, "Applications of the sol-gel process," *Journal of Non-Crystalline Solids*, vol. 100, no. 1–3, pp. 162–168, Mar. 1988, doi: 10.1016/0022-3093(88)90013-0.

[8] W. Stöber, A. Fink, and E. Bohn, "Controlled growth of monodisperse silica spheres in the micron size range," *Journal of Colloid and Interface Science*, vol. 26, no. 1, pp. 62–69, Jan. 1968, doi: 10.1016/0021-9797(68)90272-5.

[9] A. Lukowiak, J. Lao, J. Lacroix, and J.-M. Nedelec, "Bioactive glass nanoparticles obtained through sol–gel chemistry," *Chem. Commun.*, vol. 49, no. 59, p. 6620, 2013, doi: 10.1039/c3cc00003f.

[10] V. McGahay and M. Tomozawa, "Phase separation in rare-earth-doped SiO2 glasses," *Journal of Non-Crystalline Solids*, vol. 159, no. 3, pp. 246–252, Jan. 1993, doi: 10.1016/0022-3093(93)90230-U.

[11] P. Lopez-Iscoa *et al.*, "Design, Synthesis, and Structure-Property Relationships of Er3+-Doped TiO2 Luminescent Particles Synthesized by Sol-Gel," *Nanomaterials*, vol. 8, no. 1, p. 20, Jan. 2018, doi: 10.3390/nano8010020.

[12] K. Sarkar *et al.*, "Custom-Made Morphologies of ZnO Nanostructured Films Templated by a Poly(styrene-block-ethylene oxide) Diblock Copolymer Obtained by a Sol-Gel Technique," *ChemSusChem*, vol. 6, no. 8, pp. 1414–1424, Aug. 2013, doi: 10.1002/cssc.201300291.

[13] S. Hilliard *et al.*, "Mesoporous thin film WO_3 photoanode for photoelectrochemical water splitting: a sol–gel dip coating approach," *Sustainable Energy Fuels*, vol. 1, no. 1, pp. 145–153, 2017, doi: 10.1039/C6SE00001K.

[14] A. Choi, "SOL-GEL PROCESSING AND CHARACETRIZATION OF ADVANCED CERAMIC MATERIALS," *J Aust. Ceram. Soc.*, p. 5, 2006.

[15] G. Panomsuwan and H. Manuspiya, "A comparative study of dielectric and ferroelectric properties of sol–gel-derived BaTiO3 bulk ceramics with fine and coarse grains," *Appl. Phys. A*, vol. 124, no. 10, p. 713, Oct. 2018, doi: 10.1007/s00339-018-2126-z.

[16] G. Kaur, G. Pickrell, N. Sriranganathan, V. Kumar, and D. Homa, "Review and the state of the art: Sol-gel and melt quenched bioactive glasses for tissue

engineering: Review and State of the Art Of Bioactive Glasses," *J. Biomed. Mater. Res.*, vol. 104, no. 6, pp. 1248–1275, Aug. 2016, doi: 10.1002/jbm.b.33443.

[17] J. Wenzel, "Trends in sol—gel processing: Toward 2004," *Journal of Non-Crystalline Solids*, vol. 73, no. 1–3, pp. 693–699, Aug. 1985, doi: 10.1016/0022-3093(85)90389-8.

[18] H. Schmidt, "Chemistry of material preparation by the sol-gel process," *Journal of Non-Crystalline Solids*, vol. 100, no. 1–3, pp. 51–64, Mar. 1988, doi: 10.1016/0022-3093(88)90006-3.

[19] S. Esposito, "'Traditional' Sol-Gel Chemistry as a Powerful Tool for the Preparation of Supported Metal and Metal Oxide Catalysts," *Materials*, vol. 12, no. 4, p. 668, Feb. 2019, doi: 10.3390/ma12040668.

[20] G. Guzel Kaya and H. Deveci, "Synergistic effects of silica aerogels/xerogels on properties of polymer composites: A review," *Journal of Industrial and Engineering Chemistry*, vol. 89, pp. 13–27, Sep. 2020, doi: 10.1016/j.jiec.2020.05.019.

[21] A. Soleimani Dorcheh and M. H. Abbasi, "Silica aerogel; synthesis, properties and characterization," *Journal of Materials Processing Technology*, vol. 199, no. 1–3, pp. 10–26, Apr. 2008, doi: 10.1016/j.jmatprotec.2007.10.060.

[22] "The role of solvent in sol-gel processing of silica glass."

[23] D. Levy and M. Zayat, "The Sol-Gel Handbook," p. 1557.

[24] L. L. Hench and J. K. West, "The sol-gel process," *Chem. Rev.*, vol. 90, no. 1, pp. 33–72, Jan. 1990, doi: 10.1021/cr00099a003.

[25] C. J. Brinker and G. W. Scherer, "CHAPTER 2 - Hydrolysis and Condensation I: Nonsilicates," in *Sol-Gel Science*, C. J. Brinker and G. W. Scherer, Eds. San Diego: Academic Press, 1990, pp. 20–95. doi: 10.1016/B978-0-08-057103-4.50007-6.

[26] C. J. Brinker and G. W. Scherer, "CHAPTER 3 - Hydrolysis and Condensation II: Silicates," in *Sol-Gel Science*, C. J. Brinker and G. W. Scherer, Eds. San Diego: Academic Press, 1990, pp. 96–233. doi: 10.1016/B978-0-08-057103-4.50008-8.

[27] C. J. Brinker and G. W. Scherer, "CHAPTER 4 - Particulate Sols and Gels," in *Sol-Gel Science*, C. J. Brinker and G. W. Scherer, Eds. San Diego: Academic Press, 1990, pp. 234–301. doi: 10.1016/B978-0-08-057103-4.50009-X.

[28] C. J. Brinker and G. W. Scherer, "CHAPTER 5 - Gelation," in *Sol-Gel Science*, C. J. Brinker and G. W. Scherer, Eds. San Diego: Academic Press, 1990, pp. 302–355. doi: 10.1016/B978-0-08-057103-4.50010-6.

[29] “Kakihana M., Yoshimura M. Synthesis and characterization of complex multicomponent oxides prepared by polymer complex method // Bull. Chem. Soc. Jpn. 1999. V. 72. P. 1427–1443.”

[30] E. J. A. Pope and Mackenzie, J.D., “Sol-gel processing of silica: The role of the catalyst.,” *Journal of Non-Crystalline Solids*, vol. 87, pp. 185–198, 1986.

[31] C. J. Brinker and G. W. Scherer, “CHAPTER 8 - Drying,” in *Sol-Gel Science*, C. J. Brinker and G. W. Scherer, Eds. San Diego: Academic Press, 1990, pp. 452–513. doi: 10.1016/B978-0-08-057103-4.50013-1.

[32] J.-L. R. Noguès and W. V. Moreshead, “Porous gel-silica, a matrix for optically active components,” *Journal of Non-Crystalline Solids*, vol. 121, no. 1–3, pp. 136–142, May 1990, doi: 10.1016/0022-3093(90)90119-7.

[33] B. Karmakar, G. De, D. Kundu, and D. Ganguli, “Silica microspheres from the system tetraethyl orthosilicate-acetic acid-water,” *Journal of Non-Crystalline Solids*, vol. 135, no. 1, pp. 29–36, Oct. 1991, doi: 10.1016/0022-3093(91)90439-D.

[34] E. J. A. Pope and J. D. Mackenzie, “Nd-doped silica glass I: Structural evolution in the sol-gel state,” *Journal of Non-Crystalline Solids*, vol. 106, no. 1–3, pp. 236–241, Dec. 1988, doi: 10.1016/0022-3093(88)90266-9.

[35] M. N. Muralidharan, C. A. Rasmitha, and R. Ratheesh, “Photoluminescence and FTIR studies of pure and rare earth doped silica xerogels and aerogels,” *J Porous Mater*, vol. 16, no. 6, pp. 635–640, Dec. 2009, doi: 10.1007/s10934-008-9243-6.

[36] S. Duhan, P. Aghamkar, and M. Singh, “Synthesis and Characterization of Neodymium Oxide in Silica Matrix by Solgel Protocol Method,” *Research Letters in Physics*, vol. 2008, pp. 1–4, Aug. 2008, doi: 10.1155/2008/237023.

[37] M. Zawadzki and L. Kępiński, “Synthesis and characterization of neodymium oxide nanoparticles,” *Journal of Alloys and Compounds*, vol. 380, no. 1–2, pp. 255–259, Oct. 2004, doi: 10.1016/j.jallcom.2004.03.053.

[38] S. Narang, S. Rani, P. Aghamkar, and S. Kumar, “Structural investigations on Nd-doped silica nanocomposites: effect of sintering temperature and dopant concentration,” *Philosophical Magazine Letters*, vol. 94, no. 8, pp. 503–513, Aug. 2014, doi: 10.1080/09500839.2014.939734.

[39] S. S. Wang, Y. Zhou, Y. L. Lam, C. H. Kam, Y. C. Chan, and X. Yao, “Fabrication and characterisation of neodymium-doped silica glass by sol-gel process,” *Materials Research Innovations*, vol. 1, no. 2, pp. 92–96, Sep. 1997, doi: 10.1007/s100190050026.

[40] F. J. Klug, S. Prochazka, and R. H. Doremus, "Alumina-Silica Phase Diagram in the Mollite Region," *Journal of the American Ceramic Society*, vol. 70, no. 10, pp. 750–759, 1987, doi: https://doi.org/10.1111/j.1151-2916.1987.tb04875.x.

[41] H. El Hamzaoui *et al.*, "From porous silica xerogels to bulk optical glasses: The control of densification," *Materials Chemistry and Physics*, vol. 121, no. 1–2, pp. 83–88, May 2010, doi: 10.1016/j.matchemphys.2009.12.043.

[42] S. Liu, V. Boffa, D. Yang, Z. Fan, F. Meng, and Y. Yue, "Clarifying the gel-to-glass transformation in Al2O3-SiO2 systems," *Journal of Non-Crystalline Solids*, vol. 492, pp. 77–83, Jul. 2018, doi: 10.1016/j.jnoncrysol.2018.03.049.

[43] P. Melnikov, V. A. Nascimento, I. V. Arkhangelsky, and L. Z. Zanoni Consolo, "Thermal decomposition mechanism of aluminum nitrate octahydrate and characterization of intermediate products by the technique of computerized modeling," *J Therm Anal Calorim*, vol. 111, no. 1, pp. 543–548, Jan. 2013, doi: 10.1007/s10973-012-2566-1.

[44] H. Schmid, "Multi-ferroic magnetoelectrics," *Ferroelectrics*, vol. 162, no. 1, pp. 317–338, Jan. 1994, doi: 10.1080/00150199408245120.

[45] M. Fiebig, T. Lottermoser, D. Meier, and M. Trassin, "The evolution of multiferroics," *Nat Rev Mater*, vol. 1, no. 8, p. 16046, Aug. 2016, doi: 10.1038/natrevmats.2016.46.

[46] J. Wang *et al.*, "Epitaxial $BiFeO_3$ Multiferroic Thin Film Heterostructures," *Science*, vol. 299, no. 5613, pp. 1719–1722, Mar. 2003, doi: 10.1126/science.1080615.

[47] R. M. Thankachan and R. Balakrishnan, "Synthesis Strategies of Single-Phase and Composite Multiferroic Nanostructures," in *Synthesis of Inorganic Nanomaterials*, Elsevier, 2018, pp. 185–211. doi: 10.1016/B978-0-08-101975-7.00008-7.

[48] S. Wohlrab, H. Du, M. Weiss, and S. Kaskel, "Foam-derived multiferroic $BiFeO_3$ nanoparticles and integration into transparent polymer nanocomposites," *Journal of Experimental Nanoscience*, vol. 3, no. 1, pp. 1–15, Mar. 2008, doi: 10.1080/17458080801935597.

[49] J. Ma, J. Hu, Z. Li, and C.-W. Nan, "Recent Progress in Multiferroic Magnetoelectric Composites: from Bulk to Thin Films," *Adv. Mater.*, vol. 23, no. 9, pp. 1062–1087, Mar. 2011, doi: 10.1002/adma.201003636.

[50] S. M. Selbach, M.-A. Einarsrud, and T. Grande, "On the Thermodynamic Stability of $BiFeO_3$," *Chem. Mater.*, vol. 21, no. 1, pp. 169–173, Jan. 2009, doi: 10.1021/cm802607p.

[51] J. Lin, M. Yu, C. Lin, and X. Liu, "Multiform Oxide Optical Materials via the Versatile Pechini-Type Sol–Gel Process: Synthesis and Characteristics," *J. Phys. Chem. C*, vol. 111, no. 16, pp. 5835–5845, Apr. 2007, doi: 10.1021/jp070062c.

[52] H. Hosono, T. Kinoshita, Y. Ikuta, K. Kajihara, and M. Hirano, "Optical transparency of SiO 2 glass in vacuum ultraviolet region and defect formation by F 2 laser," Boulder, CO, Apr. 2001, p. 223. doi: 10.1117/12.425069.

[53] C. Tabares-muñoz, J.-P. Rivera, and H. Schmid, "Ferroelectric domains, birefringence and absorption of single crystals of $BiFeO_3$," *Ferroelectrics*, vol. 55, no. 1, pp. 235–238, Apr. 1984, doi: 10.1080/00150198408015377.

[54] R. Ramesh, "Emerging routes to multiferroics," *Nature*, vol. 461, no. 7268, pp. 1218–1219, Oct. 2009, doi: 10.1038/4611219a.

[55] S. Vijayanand, H. S. Potdar, and P. A. Joy, "Origin of high room temperature ferromagnetic moment of nanocrystalline multiferroic BiFeO3," *Appl. Phys. Lett.*, vol. 94, no. 18, p. 182507, May 2009, doi: 10.1063/1.3132586.

[56] M. H. Rizvi, "SYNTHESIS AND SIZE DEPENDENT PROPERTIES OF MULTIFERROIC BiFeO3 NANOPARTICLES.," p. 97.

[57] G. Catalan and J. F. Scott, "Physics and Applications of Bismuth Ferrite," *Adv. Mater.*, vol. 21, no. 24, pp. 2463–2485, Jun. 2009, doi: 10.1002/adma.200802849.

[58] J. K. Kim, S. S. Kim, and W.-J. Kim, "Sol–gel synthesis and properties of multiferroic BiFeO3," *Materials Letters*, vol. 59, no. 29–30, pp. 4006–4009, Dec. 2005, doi: 10.1016/j.matlet.2005.07.050.

[59] S. Shetty, V. Palkar, and R. Pinto, "Size effect study in magnetoelectric BiFeO3 system," *Pramana - J Phys*, vol. 58, no. 5–6, pp. 1027–1030, May 2002, doi: 10.1007/s12043-002-0211-4.

[60] S. M. Selbach, M.-A. Einarsrud, T. Tybell, and T. Grande, "Synthesis of $BiFeO_3$ by Wet Chemical Methods," *J American Ceramic Society*, vol. 90, no. 11, pp. 3430–3434, Nov. 2007, doi: 10.1111/j.1551-2916.2007.01937.x.

[61] Q.-H. Jiang, C.-W. Nan, and Z.-J. Shen, "Synthesis and Properties of Multiferroic La-Modified BiFeO3 Ceramics," *J American Ceramic Society*, vol. 0, no. 0, pp. 060601012420007-???, Jun. 2006, doi: 10.1111/j.1551-2916.2006.01062.x.

[62] M. Popa, D. Crespo, J. M. Calderon-Moreno, S. Preda, and V. Fruth, "Synthesis and Structural Characterization of Single-Phase $BiFeO_3$ Powders from

a Polymeric Precursor," *J American Ceramic Society*, vol. 90, no. 9, pp. 2723–2727, Sep. 2007, doi: 10.1111/j.1551-2916.2007.01779.x.

[63] S. Ghosh, S. Dasgupta, A. Sen, and H. Sekhar Maiti, "Low-Temperature Synthesis of Nanosized Bismuth Ferrite by Soft Chemical Route," *J American Ceramic Society*, vol. 88, no. 5, pp. 1349–1352, May 2005, doi: 10.1111/j.1551-2916.2005.00306.x.

[64] A. Hardy, S. Gielis, H. Van den Rul, J. D'Haen, M. K. Van Bael, and J. Mullens, "Effects of precursor chemistry and thermal treatment conditions on obtaining phase pure bismuth ferrite from aqueous gel precursors," *Journal of the European Ceramic Society*, vol. 29, no. 14, pp. 3007–3013, Nov. 2009, doi: 10.1016/j.jeurceramsoc.2009.05.018.

[65] A. Hardy *et al.*, "Gel Structure, Gel Decomposition and Phase Formation Mechanisms in the Aqueous Solution–Gel Route to Lanthanum Substituted Bismuth Titanate," *J Sol-Gel Sci Technol*, vol. 33, no. 3, pp. 283–298, Mar. 2005, doi: 10.1007/s10971-005-6378-7.

[66] H. Doweidar, "Consideration of the boron oxide anomaly," *J Mater Sci*, vol. 25, no. 1, pp. 253–258, Jan. 1990, doi: 10.1007/BF00544216.

[67] J. Silva, A. Reyes, H. Esparza, H. Camacho, and L. Fuentes, "$BiFeO_3$: A Review on Synthesis, Doping and Crystal Structure," *Integrated Ferroelectrics*, vol. 126, no. 1, pp. 47–59, Jan. 2011, doi: 10.1080/10584587.2011.574986.

[68] T. O. L. Sunde, T. Grande, and M.-A. Einarsrud, "Modified Pechini Synthesis of Oxide Powders and Thin Films," in *Handbook of Sol-Gel Science and Technology*, L. Klein, M. Aparicio, and A. Jitianu, Eds. Cham: Springer International Publishing, 2016, pp. 1–30. doi: 10.1007/978-3-319-19454-7_130-1.

[69] "Pechini method." https://eng.thesaurus.rusnano.com/wiki/article2075 (accessed Aug. 02, 2021).

[70] L.-W. Tai and P. A. Lessing, "Modified resin–intermediate processing of perovskite powders: Part I. Optimization of polymeric precursors," *J. Mater. Res.*, vol. 7, no. 2, pp. 502–510, Feb. 1992, doi: 10.1557/JMR.1992.0502.

[71] L.-W. Tai and P. A. Lessing, "Modified resin–intermediate processing of perovskite powders: Part II. Processing for fine, nonagglomerated Sr-doped lanthanum chromite powders," *J. Mater. Res.*, vol. 7, no. 2, pp. 511–519, Feb. 1992, doi: 10.1557/JMR.1992.0511.

[72] M. Sletnes, S. L. Skjærvø, M. Lindgren, T. Grande, and M.-A. Einarsrud, "Luminescent Eu3+-doped NaLa(WO4)(MoO4) and Ba2CaMoO6 prepared by the modified Pechini method," *J Sol-Gel Sci Technol*, vol. 77, no. 1, pp. 136–144, Jan. 2016, doi: 10.1007/s10971-015-3837-7.

[73] M.-L. Fontaine, C. Laberty-Robert, A. Barnabé, F. Ansart, and P. Tailhades, "Synthesis of La2−xNiO4+δ oxides by polymeric route: non-stoichoimetry control," *Ceramics International*, vol. 30, no. 8, pp. 2087–2098, Jan. 2004, doi: 10.1016/j.ceramint.2003.11.013.

[74] C. Nityanand, W. B. Nalin, B. S. Rajkumar, and C. M. Chandra, "Synthesis and physicochemical characterization of nanocrystalline cobalt doped lanthanum strontium ferrite," *Solid State Sciences*, vol. 13, no. 5, pp. 1022–1030, May 2011, doi: 10.1016/j.solidstatesciences.2011.01.026.

[75] M. P. Pechini, "Method of preparing lead and alkaline earth titanates and niobates and coating method using the same to form a capacitor," US3330697A, Jul. 11, 1967 Accessed: Aug. 02, 2021. [Online]. Available: https://patents.google.com/patent/US3330697A/en

[76] M. Kakihana, M. M. MIlanova, M. Arima, T. Okubo, M. Yashima, and M. Yoshimura, "Polymerized Complex Route to Synthesis of Pure Y2Ti2O7 at 750°C Using Yttrium-Titanium Mixed-Metal Citric Acid Complex," *J. Am. Ceram. Soc*, vol. 79 [6], pp. 1673–1676, 1996.

[77] C. Chu and B. Dunn, "Preparation of High-Tc Superconducting Oxides by the Amorphous Citrate Process," *J American Ceramic Society*, vol. 70, no. 12, p. C-375-C–377, Dec. 1987, doi: 10.1111/j.1151-2916.1987.tb04924.x.

[78] T. O. L. Sunde *et al.*, "Transparent and conducting ITO thin films by spin coating of an aqueous precursor solution," *J. Mater. Chem.*, vol. 22, no. 31, p. 15740, 2012, doi: 10.1039/c2jm32000b.

[79] B. Schumm, P. Wollmann, J. Fritsch, J. Grothe, and S. Kaskel, "Nanoimprint patterning of thin cadmium stannate films using a polymeric precursor route," *J. Mater. Chem.*, vol. 21, no. 29, p. 10697, 2011, doi: 10.1039/c1jm10886g.

[80] N. M. Leonard, L. C. Wieland, and R. S. Mohan, "Applications of bismuth(III) compounds in organic synthesis," p. 25, 2002.

[81] T. Hashimoto, M. Hamajima, H. Ohta, H. Nasu, A. Ishihara, and Y. Nishio, "Fe2O3-Bi2O3-B2O3 glasses as lithium-free nonsilicate pH responsive glasses – Compatibility between pH responsivity and hydrophobicity," *Materials Research Bulletin*, vol. 50, pp. 385–391, Feb. 2014, doi: 10.1016/j.materresbull.2013.11.038.

Chapter 7

Conclusions and future outlooks

Two goals have been pursued in this Ph.D. thesis, in the context of the NANOMAX project: 1) the fabrication of advanced optical glasses and 2) their 3D-nanostructurating by femtosecond laser for photonic applications. Below, the most relevant results achieved will be summarized as preliminary conclusion before outlining future outlooks in the following section.

7.1 Main achievements

Firstly, the synthesis of bulk glasses following two different techniques, sol-gel, and melt quenching, has been carried out.
On the one hand, the multiferroic Bi_2O_3 - B_2O_3 - Fe_2O_3 (BBF) glass was chosen, proposing an innovative sol-gel process carried out by modified Pechini approach, after the study of different methodologies extensively explored in literature. Even though promising results have been achieved, it has not been possible to complete the synthesis and extend the work to femtosecond laser irradiation yet. Then, after acting on the control of multiple parameters (precursors concentration, molar ratio of citric acid/metallic ions, precursors introduction order, pH, temperature, amount of H_2O and NH_3), the perspective is to make this procedure an emerging synthesis protocol for the ternary system of composition 40% B_2O_3 - 30% Bi_2O_3 - 30% Fe_2O_3.

On the other hand, this thesis work has significantly investigated the laser-matter interaction through fs-laser induced modifications inside Li_2O – Nb_2O_5 – SiO_2 – B_2O_3 (LNSB) glasses, fabricated by conventional melt quenching method. First, the work was conducted on a reference glass in the ternary Li_2O – Nb_2O_5 – SiO_2 (LNS)

system. Evolution in morphology, crystallization, and nanostructure upon fs-laser irradiation have been examined through polarized light microscopy, chemical analysis, and optical properties measurements (birefringence, index variation, second harmonic generation, SHG). Laser polarization dependent nanocrystal orientation and oriented nanostructure formation found for LNS were also confirmed in the case of LNSB. New potentials were revealed, including enhanced the optical properties such as birefringence, along with tunable SHG.

These findings may facilitate the integration of functionalized 3D glass-based optical devices for photonic applications (e.g., frequency convertors, light modulators, phase optical elements, photonic circuits).

Regarding the five objectives proposed in Chapter 1 and below reported, we intend to verify them qualitatively and quantitatively:

1) Clarify how three threshold regimes of LNSB glasses vary with the four laser parameters considered in this thesis work;
2) Determine the chemical distribution and the evolution of glass nanostructure as a function of B_2O_3 content in the glass matrix;
3) Control of both size and orientation of laser-induced nonlinear $LiNbO_3$ nanocrystals;
4) Investigate relationships between fs laser-induced modifications and macroscopic optical properties;
5) Investigate the driving effects / mechanisms behind the fs laser-induced properties in LNSB glasses compared with LNS ones.

Initially, melt-quenching technique was used to fabricate optical oxide glasses. The selection of glass compositions required to allow the control of the variation of laser-induced optical properties and, most of all, the variation of volume fraction of active phase crystalline dispersed within the glass matrix.

3D modifications were studied in four glass compositions, and varying four main laser parameters: pulse energy, repetition rate, light polarization and scanning speed. Studying the transformations in a pulse energy - repetition rate landscape, complemented with variation of laser polarization and scanning speed, energy threshold values for LNSB were found slightly lower than LNS ones [1].

These values allow to investigate the static crystallization ones by detection of SHG varying pulse energy and repetition rate. Green light emerged from the sample is a first criterion to be validated for a nonlinear crystals precipitation. In addition, we found that incubation time, as fundamental parameter characteristic of the static dots irradiation, is drastically reduced in LNSB samples compared to LNS ones.

Specifically, at a delivered power of 100 mW, LNS13B21 reveals an incubation time equal to ~1 second, that becomes of ~10 seconds for LNS20B14, until ~20 seconds for both LNS27B7 and LNS34 [2]. This has demonstrated that incubation time varies in function of glass compositions.

Nanocrystals size and orientation SHG measurements validated by EBSD analysis have confirmed the presence of nanocrystals and the role of polarization effect. Comparing 0.5 and 1.25 μJ/pulse, we found a strong modulation at low pulse energy and the presence of two textures is characteristic of two minima identified for configuration Y_x but not for Y_y, at increasing pulse energy. Differences are evident for each glass composition, as the pulse energy increases. But it is difficult to draw definitive conclusions about trends as the amount of B_2O_3 increases. A preferential orientation of c polar nanocrystals axis perpendicular to laser polarization is revealed at 0.5 μJ/pulse [2]. We have noted that, at increasing pulse energy, addition of B_2O_3 made very difficult to classify a trend referred to a particular pulse energy value in a unique way for all the four glass compositions. Unpredictable effects have been reported with B_2O_3 addition on the shape of the SHG curves and on the formation or not of two crystals textures. Then, in more depth, it was necessary to verify by EBSD maps some correspondence with SHG measurements, highlighting firstly nanocrystals precipitation and secondly large zones with the same textures at highest pulse energy. Fs-laser has modified the material into its bulk bringing out the birefringence characteristic of $LiNbO_3$. We have studied the aspect of the irradiated lines by retardance measurements at increasing of scanning speed: the LNS13B21 has highlighted an enhancement of the maximum response, precisely twice larger than the one of LNS34 [1].

In addition, we stated that the light created the smallest self-organized structure, i.e., the nanogratings that are considered responsible of the birefringent response of the irradiated lines.

Furthermore, as shown in comparison between LNS13B21 and LNS34, the B_2O_3 addition in glass network also affected the chemical distribution and the evolution of glass nanostructure. We have discovered a phase separation into nanogratings revealed by SEM-EDS, varying scanning speed. It is not possible to highlight a specific trend at increasing scanning speed, but it is necessary to explore deeply the nanogratings morphology and structure.

Finally, we have studied how femtosecond laser modified CCT and TTT diagrams, focusing the attention on time and temperature, as conditions to define the crystallization. In fact, we have characterized crystallization mechanisms by studying the spatial temperature distribution and the time evolution of the temperature, considering the laser as a localized continuous heating source. Then,

nucleation and growth rates entered to play into the CCT and TTT curves. Upper limit is constituted by melting temperature and lower limit is defined by glass transition temperature. The consequence of B_2O_3 addition is an expansion of crystallization domain.

Specifically, no crystallized lines at 1 μJ/pulse and 200 kHz were detected at scanning speed beyond ~100 μm/s for LNS34 and beyond ~600 μm/s for LNS13B21. In conclusion, SiO_2 substitution with B_2O_3 in increasing quantities (from 7% to 21% mol) leads to a fast crystallization of $LiNbO_3$ nanocrystals induced by fs-laser irradiation [1] .

7.2 Future outlooks

This section contains the specific guidelines towards new scientific and technological developments based on this Ph.D. work. The next steps to take for the advancement of this research should address the points listed below:

1) Femtosecond laser irradiation of $B_2O_3 – Fe_2O_3 – Bi_2O_3$ (BBF);
2) In-depth investigation of the differences between the crystallization rates of LNS and LNSB glass matrices;
3) Modeling of Fourier heat equation to give further insight in the heat dynamics of the heat affect zone;
4) Synthesis, irradiation, and characterization of following ternary glass matrix $Li_2O–Nb_2O_5–B_2O_3$, starting from studying B_2O_3-containing glass behavior.

Regarding sol-gel synthesis, it is possible to proceed with an XRD analysis of the dried gel to ensure that there was no surface crystallization of heterogeneous type. Further heat treatments and thin-film depositions with spin coaters are desirable to control optical transparency, a limiting parameter for future laser irradiation. After further analysis, another experiment with the same composition would be carried out to verify the repeatability of the process. The objective is to make this procedure an innovative synthesis protocol of the ternary system BBF to irradiate with femtosecond laser.

Then, in the future we consider making other attempts to find glass matrices that do not promote crystallization upon glass fabrication, while enabling fast crystallization during laser irradiation. The results obtained are to be deepened by adding detailed analyses to find the amount and nature of the elements present. Li^+ could easily migrate and remain on the surface, Nb^{5+} instead in depth but there are analyses to be made to validate this, for example by TEM. Also, the chemical

migration is to be investigated carefully to verify the presence and the amount of Li^+ on the surface by XPS analysis.

It is important to verify phase separation and obtain further SHG measurements on samples with increasing scanning speed. During the in-depth analysis of nanostructure, it is fundamental also to focus on a new investigation of nanogratings. Connected with nanogratings formation, we intend also to start from a preliminary examination of heterogeneities in glass before irradiation by SEM, to verify if they could be some trigger points for nanogratings.

Considering the fact that boron does not enter into $LiNbO_3$ network and the small radius of the B^{3+} cation, it could be attractive to analyze if boron is present really only in the vitreous lamellas of nanogratings.

Indeed, more in-depth spectroscopic (e.g., Raman spectroscopy) analysis could provide information on the different phase changes and the structure of the modified glass.

It cannot make a general declaration in a comprehensive way about how temperature affects boron coordination; it is necessary a more accurate and in-depth analysis using spectroscopic properties (e.g., Raman spectroscopy).

It would be necessary to make other measurements of SHG with varying scanning speed, not only on LNS34 and LNS13B21 but also on the "intermediate" compositions LNS27B7 and LNS20B14, to study the simultaneous effect of the composition of the glass and the scanning speed on the SHG.

Furthermore, it would be very useful to collect further EBSD maps for all the four glass compositions to verify how the nanostructure changes varying glass composition and also scanning speed.

Further modeling work, in particular using the Fourier heat equation, is required to study the temperature distribution and evolution during irradiation, which could be very interesting to highlight a detailed comparison between LNS and LNSB.

Heat equation modeling could also become a further tool to promote the choice and to select a suitable composition of this following glass matrix $Li_2O–Nb_2O_5–B_2O_3$. The first reason of this preference is chemical: boron addition in glass network is advantageous for crystal nanostructure. We found and started to demonstrate this statement employing the quaternary glass matrix $Li_2O–Nb_2O_5–SiO_2–B_2O_3$. We could foresee the relevant benefit in having a glass matrix free from SiO_2, even though a cautious synthesis is to be made for the boron easy propensity to a surface crystallization after quenching. It is necessary a thorough study of $Li_2O–Nb_2O_5–B_2O_3$ phase diagram to choose a suitable composition also to foster fs-laser induced crystallization.

This work is pioneering for future development in different research fields, suggesting a multidisciplinary approach to be adopted: nonlinear optics (nanogratings and specific applications), material chemistry, laser-oriented crystallization of glass materials, plasma, and quantum physics, nonequilibrium thermodynamics. By combining the choice of laser parameters with a suitable glass composition based on the nonlinear optical properties expected, it is possible to address towards the specific optical and photonic applications to be achieved.

7.3 Bibliography

[1] E. Muzi *et al.*, "Towards a Rationalization of Ultrafast Laser-Induced Crystallization in Lithium Niobium Borosilicate Glasses: The Key Role of the Scanning Speed," *Crystals*, vol. 11, no. 3, p. 290, Mar. 2021, doi: 10.3390/cryst11030290.

[2] E. Muzi *et al.*, "Polarization-oriented $LiNbO_3$ nanocrystals by femtosecond laser irradiation in LiO_2–Nb_2O_5–SiO_2–B_2O_3 glasses," *Opt. Mater. Express*, vol. 11, no. 4, p. 1313, Apr. 2021, doi: 10.1364/OME.417461.

Appendix

A - Classical Nucleation Theory (CNT)

This model proposed by Gibbs is a theory about nucleation of a new thermodynamic phase, liquid, or crystal. Thermal fluctuation of the chemical composition is the cause of homogeneous nucleation in the liquid phase or glass.
In case of formation of a spherical nucleus, change in free energy corresponds to the sum of surface term (positive) and bulk term (negative) as:

$$\Delta G_T = 4\pi r^2\gamma + \frac{4}{3}\pi r^3 \Delta G_V \qquad \text{(A49)}$$

Where ΔG_T is the total free energy change, r is the radius of the nucleus, γ is the specific surface free energy of the critical nucleus-melt interface, and ΔG_V is the difference between the free energies of crystal and liquid per unit volume.
In super-cooled liquid, ΔG_V is associated with the liquid-crystal transformation, given as:

$$\Delta G_V = \Delta H_V - T\Delta S_V \qquad \text{(A50)}$$

$$\Delta H_V = -L_v \qquad \text{(A51)}$$

Where ΔH_V (< 0) is the change of volume enthalpy, L_v is latent heat, T is the temperature, and ΔS_V is the change of entropy.
If ΔH_V, corresponding to the release heat during the crystallization, is constant, at T_m, $\Delta G_V = 0$:

$$\Delta G_V = \frac{\Delta H_V \Delta T}{T_m} \qquad \text{(A52)}$$

$$\Delta T = T_m - T \qquad \text{(A53)}$$

In correspondence of critical nucleus radius (r^*), the total free energy reaches the maximum and the one with the highest value of ΔG^*.

When $\frac{d\Delta G_T}{dr} = 0$, we obtain:

$$r^* = \frac{-2\gamma}{\Delta G_v} \qquad \text{(A54)}$$

$$\Delta G^* = \frac{16\pi\gamma^3}{3(\Delta G_v)^2} \qquad \text{(A55)}$$

when $r < r^*$, the nuclei are not stable; when $r > r^*$, the nuclei are stable, and they continue to grow.

The requirement for crystallization is that the nuclei have to overcome the thermodynamic barrier for nucleation, precisely the ΔG^*.

The free energy trend and the variation of critical nuclei radius r^* are represented in the following Figure A134.

The classical homogeneous nucleation theory wants to give a thermodynamic description of initial stage of nucleation from embryo to nucleus with a little larger size than r^*[1]. The change of parent phase in the system is negligible due to the largeness in volume and mass comparing that of nuclei. The nucleation curve reported in Figure A134a passes through a single maximum point at r^*.

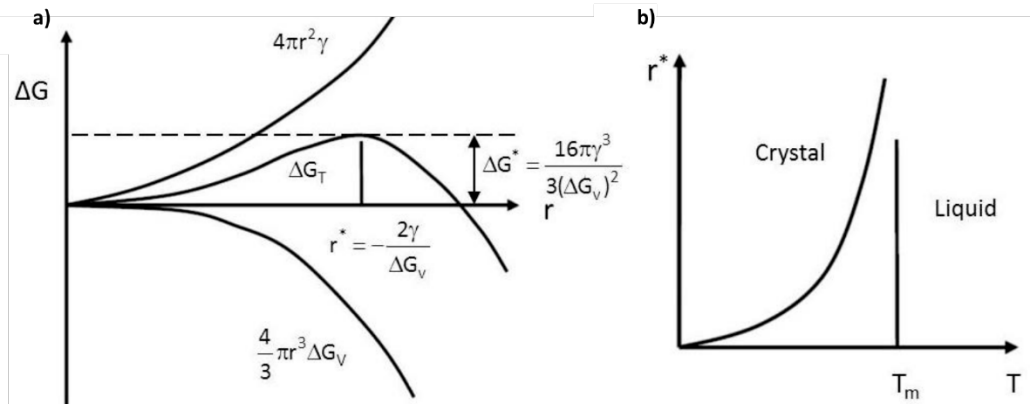

Figure A134: a) The free energy change associated with homogeneous nucleation of a sphere of radius r in which the $T < T_m$; b) variation of r^* critical with the under-cooling of the melt [2].

There is a relationship between the number of embryos with radius r^* per volume (N^*) and the number of molecules per volume (N):

$$N^* = N\,exp\left(-\frac{\Delta G^*}{k_B T}\right) \qquad \text{(A56)}$$

N^* can be defined also as the germs' formation rate and the agglomeration rate of molecules on the seed.

The germ-matrix interface crossing affects the atom diffusion, considering a diffusion layer. The rate of nuclei formation at r^* size corresponds to:

$$\frac{dn}{dt} = N^* K\,exp\left(-\frac{\Delta G_D}{k_b T}\right) \propto exp\left(\frac{\Delta G_D + \Delta G^*}{k_b T}\right) \qquad \text{(A57)}$$

Where ΔG_D is the activation energy to cross the glass-crystal interface (kinetic barrier), ΔG^* is the energy barrier to form a nucleus stable to grow, and k_B is Boltzmann's constant (1.38×10^{-23} J/K).

T affects the size of r*. Because ΔG_v is a function of ΔT, we obtain:

$$r^* \propto (\Delta T)^{-1} \qquad \text{(A58)}$$

$$\Delta G \propto (\Delta T)^{-2} \qquad \text{(A59)}$$

Then, r* increases with T, when $T < T_m$, as represented in Figure A134b. When T is close to T_m, ΔG^*, that play a dominant role in the nucleation rate (very low), is high. Otherwise, the diffusion term is high at this temperature. When T and ΔG^* decrease, the possibility of seeds formation increases. Moreover, the viscosity of material increases sharply, restricting atom movement, inhibiting the ordered crystal structures formation, and thus decreasing the nucleation rate.
There is an optimal T for the maximum nucleation rate. When T is close to T_g, ΔG^* decreases and nucleation rate increases sharply, reaching a possible maximum when ΔG^* and ΔG_D are of the same magnitude order.
The utility of this CNT model is to determine the crystallization in glasses. It must always be taken into account that there is an evident discrepancy between the calculated and the experimental results, which may be explained that the real practice of solidification of glassy alloys often involves heterogeneous nucleation [3].
A heterogeneous nucleation occurs when the process starts at some preferred sites than at other ones. If it compares to the homogeneous one, there is an effect mainly because diminishes thermodynamic barrier, leading to a decrease of the contribution of the effective surface energy to the work of critical cluster formation [4].
The growth process, shown in the following Figure A135, can be represented by a reversible reaction and the growth rate is thus given by [2]:

$$k_{lc} - k_{cl} = k_0 \exp\left(-\frac{\Delta G_a}{k_B T}\right) - k_0 \left[\exp\left(-\frac{\Delta G_a - \Delta G_v}{k_B T}\right)\right] = k_0 \exp\left(-\frac{\Delta G_a}{k_B T}\right)\left[1 - \exp\left(-\frac{1}{k_B T}\frac{v L_v (T_m - T)}{T_m}\right)\right] \qquad \text{(A60)}$$

where ΔG_a is the positive surface term of free energy.
As represented in Figure A135b, when T is equal or larger than T_m, the growth rate is 0. Below T_m, at higher temperature, crystal growth rates exhibit higher than nucleation rates. The nucleation occurs at lower temperature than crystals growth. Then, cooling a melt will meet the growth regime before the formation of nuclei.

Considering crystal growth happens after nuclei, crystallization on cooling occurs in the overlap zone, shown by red zone in Figure A135b.
If glass is heated, the crystallization is not limited to the above overlap zone anymore. In addition, chemical composition has an influence on crystal growth [5]. If we want to obtain nanosized crystal in glass, the temperature has to be low enough to stay in the nucleation zone, and then to prevent growth. A glass volume crystallization is obtained, if the temperature necessary for nucleation is maintained a time long enough and successively a temperature for growing is achieved.

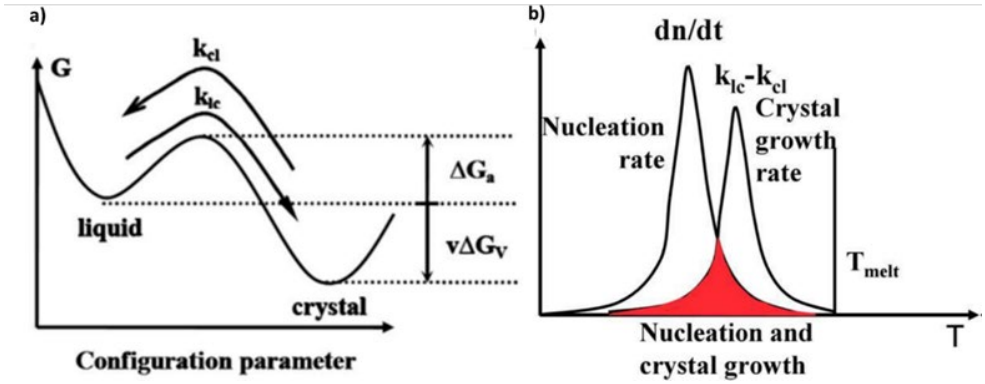

Figure A135: a) Scheme of free energy according to configurational parameter; b) a superimposition of the nucleation and growth [2]

B - Generic microscopic model of the origin of optical nonlinearity

When a light wave passes through a material medium, its electric field acts on the electronic clouds, or more schematically on the electrons of atoms (or molecules), moving the barycenter from their respective nuclei and thus inducing electrical dipole moment, as shown in Figure A136.

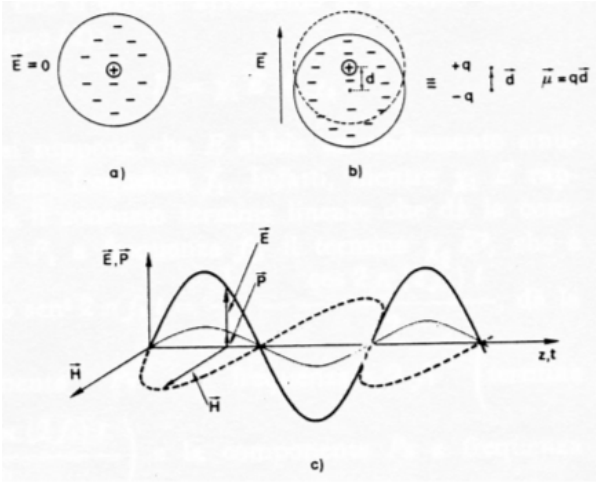

Figure A136: a) material medium without electric field; b) material medium with electric field that induces an electrical dipole moment; c) electromagnetic wave representation [6]

In conductors the charges are free to move through the material giving rise to a weak electric current. In dielectric materials instead the charges are localized and can be schematized as bound oscillators with a certain elasticity, as shown in Figure A137.

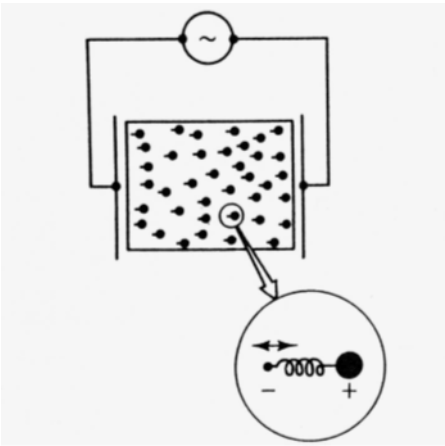

Figure A137: Scheme of dielectric materials as bound oscillators [6]

In low intensity, the electric field associated with the wave causes a slight displacement of the particles from their equilibrium position and generate an oscillating induced polarization. Because nuclear charges have much larger mass of electrons follows that, at optical frequencies, only the negative charge undergoes a significant shift and contributes. The induced polarization resulting propagates with the field to the same optical frequency and radiates field in the medium.
Neglecting the positive ion displacement and for one-dimensional case, the single electron position varies according to this following equation of motion:

$$m\left[\frac{d^2x}{dt^2} + 2\Gamma\frac{dx}{dt} + \Omega^2 x + \left(\xi^{(2)}x^2 + \xi^{(3)}x^3 + \ldots\right)\right] = -eE(t) \qquad \text{(A61)}$$

where x is displacement from the equilibrium position, Ω is the resonance oscillator frequency, e the electron charge and Γ indicates the dissipation. The equation right term represents the force applied to the electron from the wave field generating the oscillations. Neglecting the anharmonic terms $\xi^{(2)}x^2 + \xi^{(3)}x^3 + \ldots$, and considering only the harmonic response generated from an electric field of this following form:

$$E(t) = E_0 cos\,(\omega t) = \frac{1}{2}E_0[exp(-i\omega t) + exp\,(i\omega t)] = \frac{1}{2}E_0[exp(-i\omega t) + c.c.] \qquad \textit{(A62)}$$

where ω is the optical pulsation and *c.c.* indicates the conjugate complex term. The solution of (A63) is to be searched in the form of $x(t) = \frac{1}{2}[\tilde{x}_0 \exp(-i\omega t) + c.c.]$, where $\tilde{x}_0$ is a complex quantity including both amplitude and phase responses. Substituting this expression and the (A64) in (A63) a linear equation is obtained and solving it, electron displacement in function of time results expressed in the following form:

$$x(t) = \frac{1}{2}\left[\frac{-eE_0}{m}\,\frac{exp\,(-i\omega t)}{\Omega^2 - \omega^2 - 2i\Gamma\omega} + c.c.\right] \qquad \text{(A63)}$$

This results in dipole momentum induced equal to $P(t) = -ex(t)$ and, if N corresponds to the number of oscillators per unit volume, the polarization induced in medium is equal to:

$$P(t) = -Nex(t) \qquad \text{(A64)}$$

Then, the polarization dependence with respect to the field is linear by the complex susceptibility $\tilde{\chi}(\omega)$ giving:

$$P(t) = \frac{1}{2}\,\varepsilon_0\tilde{\chi}(\omega)\,E_0 exp(-i\omega t) + c.c. \qquad \text{(A65)}$$

where:

$$\tilde{\chi}(\omega) = \frac{Ne^2}{\varepsilon_0 m} \cdot \frac{1}{\Omega^2 - \omega^2 - 2i\Gamma\omega} \qquad \text{(A66)}$$

The trend of the susceptibility real and imaginary part is shown in the following Figure A138.

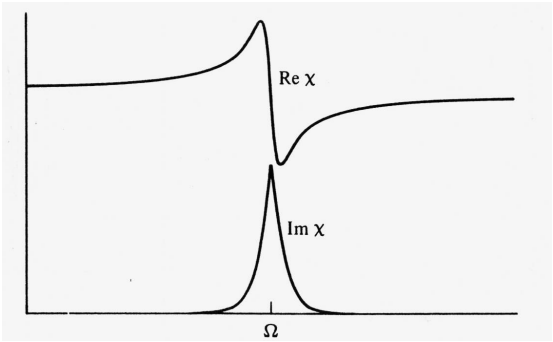

Figure A138: Diagram of real and imaginary part of susceptibility [6]

The polarization induced in medium oscillates at same frequency of incident optical field, radiates in medium and modifies the wave propagation. The medium losses are included in imaginary part $\tilde{\chi}(\omega)$ that considering the component of $\vec{P}$ in quadrature with the field $\vec{E}$.
The dielectric constant is given by the following expression:

$$\tilde{\varepsilon}(\omega) = \varepsilon_R(\omega) + j\varepsilon_I(\omega) \qquad \text{(A67)}$$

Remembering that the complex refractive index of a material is defined by

$$\tilde{n} = n + j\kappa \qquad \text{(A68)}$$

where n and κ, called refractive index and extinction coefficient, determine the refractive and absorbent properties of the material. In this case, the following expressions apply:

$$\varepsilon_R = n^2 - \kappa^2 \qquad \text{(A69)}$$

$$\varepsilon_I = 2n\kappa \qquad \text{(A70)}$$

from which it is possible to derive the trend, or dispersion, of n and κ in function the pulse ω of the electromagnetic wave.
Considering the anharmonic terms $m\left[\left(\xi^{(2)}x^2 + \xi^{(3)}x^3 + \ldots\right)\right]$ where $\xi^{(2)}$ and $\xi^{(3)}$ are constant, the potential of attraction $V(x)$ in symmetric media is expressed by:

$$V(x) = \frac{m}{2}\Omega^2 x^2 + \frac{m}{4}\xi^{(3)} x^4 + \ldots \qquad \text{(A71)}$$

In symmetric media, in which is it possible to determine a symmetric center in the structure, the electron potential energy is to be reflected in the medium symmetry. Due to the symmetry of the material, *V(x)* includes only the even exponential terms of the equation in x, in such way that *V(x)= V(-x)*.
The elastic force exerted on the electron is therefore equal to:

$$F(x) = -\frac{\partial V}{\partial x} = -m\Omega^2 x - m\xi^{(3)} x^3 \qquad \text{(A72)}$$

In non-centrosymmetric media, in which the condition *V(x)= V(-x)* is not verified, the potential may contain also odd exponential terms:

$$V(x) = \frac{m}{2}\Omega^2 x^2 + \frac{m}{3}\xi^{(2)} x^3 + \ldots \qquad \text{(A73)}$$

In which corresponds this elastic force:

$$F(x) = -\frac{\partial V}{\partial x} = -m(\Omega^2 x - m\xi^{(2)} x^2 + \ldots) \qquad \text{(A74)}$$

To find the expression of the nonlinear polarization, consider the case where the forcing electric field is the sum of two different pulsation fields:

$$E(t) = E_1 \cos(\omega_1 t) + E_2 \cos(\omega_2 t) \qquad \text{(A75)}$$

In this case the equation of nonlinear harmonic oscillator is reduced to:

$$\frac{d^2x}{dt^2} + 2\Gamma \frac{dx}{dt} + \Omega^2 x + \xi^{(2)} x^2 = -e \cdot mE(t) \qquad \text{(A76)}$$

Generally, small values of nonlinear term are more interesting in nonlinear optics applications. Precisely, the electric field forcing term does not cause the particle ionization undergone the field generating the breaking of the material.
Then, the previous equation solution may be expressed, in according to a perturbative approach, in this way:

$$x(t) = x^{(1)}(t) + x^{(2)}(t) \qquad \text{(A77)}$$

in which $x^{(1)}(t)$ is the solution of (A78) without considering the anharmonic term, whilst $x^{(2)}(t)$ is considered as a small correction for the $x^{(1)}(t)$. By replacing the (A79) in the (A78), developing and eliminating the terms that satisfied the harmonic oscillator, it is obtained:

$$\ddot{x}^{(2)}(t) + 2\Gamma\dot{x}^{(2)}(t) + \Omega^2 x^{(2)}(t) = -\xi^{(2)}(t)x^{(1)^2}(t) \qquad \text{(A78)}$$

from which the $x^{(2)}(t)$ satisfies a differential equation not homogeneus where the source term is the square of the linear solution.

Similarly, the first order solution that compares in (A79) is expressed as:

$$x^{(1)}(t) = \frac{1}{2}\left[\tilde{x}^{(1)}(\omega_1)e^{-i\omega_1 t} + \tilde{x}^{(2)}(\omega_2)e^{-i\omega_2 t} + c.c.\right] \quad \text{(A79)}$$

The solution of (A80) is searched in the following form:

$$x^{(2)}(t) = \frac{1}{2}\left[\tilde{x}^{(2)}(\omega_1+\omega_2)e^{-i(\omega_1+\omega_2)t} + \tilde{x}^{(2)}(\omega_1-\omega_2)e^{-i(\omega_1-\omega_2)t} + \tilde{x}^{(2)}(2\omega_1)e^{-i2\omega_1 t} + \tilde{x}^{(2)}(2\omega_2)e^{-i2\omega_2 t} + c.c.\right] \qquad \text{(A80)}$$

Replacing (A76), (A81) and (A82) in the (A80) and if the terms oscillate at the same pulse, the following expressions are obtained for the complex amplitudes:

$$x^{(2)}(\omega_1 \mp \omega_2) = -\frac{1}{2}\frac{\xi^{(2)}(e/m)^2}{(\Omega^2-\omega_1^2-2i\Gamma\omega_1)(\Omega^2-\omega_2^2-2i\Gamma\omega_2)} \cdot \frac{E_1E_2}{[\Omega^2(\omega_1+\omega_2)-4i\Gamma((\omega_1\pm\omega_2)]} \qquad \text{(A81)}$$

And generally:

$$x^{(2)}(2\omega_k) = -\frac{1}{2}\frac{\xi^{(2)}(e/m)^2}{(\Omega^2-\omega_k^2-2i\Gamma\omega_k)(\Omega^2-4\omega_k^2-4i\Gamma\omega_k)} \cdot E_k^2 \qquad \text{(A82)}$$

$$k = 1,2$$

We noted that the second order solution leads to the generation of different pulsation from forcing ones. In particular, the presence of sum and difference pulsation $(\omega_1 \pm \omega_2)$ and second harmonic pulsation $(2\omega_k)$.
Even though this approach is very simplified because the total field in the (A77) should include all the terms of the field effectively in the medium, also those eventually generated in the nonlinear process.
After this excursus, the polarization induced is expressed:

$$P(t) = -Nex(t) = -Ne\left[x^{(1)}(t) + x^{(2)}(t)\right] \qquad \text{(A83)}$$

that it may be which can be schematically rewritten as:

$$P(t) = P_L(t) + P_{NL}(t) \qquad \text{(A84)}$$

where the linear term $P_L(t)$ and the nonlinear one $P_{NL}(t)$ appear.
Then, this simple model may predict that the polarization induced in a dielectric medium for high intensities of field has to contain nonlinear terms that oscillates at new optical pulse.
In the following Figure A139, a nonlinear dependence of the electric field polarization could generate a polarization induced that in presence of a weak electric field may be considered linear, whilst becomes nonlinear depending on the applied field amplitude for high field values.
In the case shown in Figure A139b, the polarization contains in addition to the input frequency ω also components at frequencies 2ω, 3ω, ..., and zero frequency continuous component.

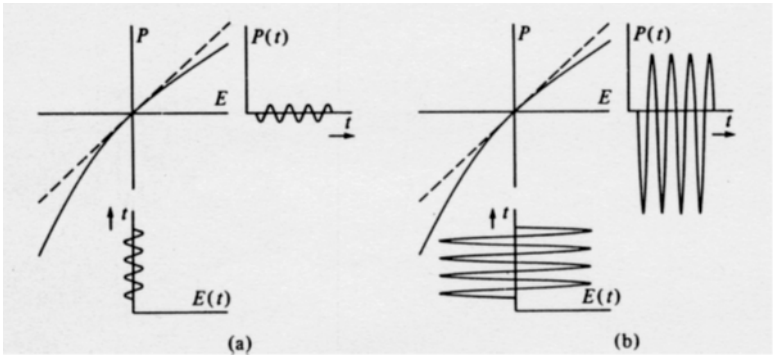

Figure A139: Schematic representations of polarization and electric field in function of time at a) input frequency ω and b) at frequency 2ω, 3ω,….[6]

This model should be tridimensional and the susceptibilities χ are tensorial variables, connected to the field component along the reference cartesian axes. Then, the problem becomes vectorial and the (2.4.4.24) may be rewritten as:

$$\vec{P}(t) = \vec{P}_L(t) + \vec{P}_{NL}(t) \qquad \text{(A85)}$$

where $\vec{P}_L(t)$ is the linear term and $\vec{P}_{NL}(t)$ is the nonlinear one.
If the nonlinear term of the polarization is inserted into wave equation, it becomes the source term and it will then give rise to radiation of electromagnetic field at all frequencies at which it oscillates.
From the previous expressions, it is possible to note that when the forcing frequencies ω_k $(k = 1,2)$ or one of their linear combination $\pm\omega_k \pm\omega_j$ $(k,j=1,2)$ coincide with the resonance oscillator frequency Ω, the linear susceptibility $\chi^{(2)}$ becomes very high. Comparing $\chi^{(2)}$ with $\chi^{(3)}$, it is noted that high values of linear susceptibility are necessary to have high values of nonlinear one. Then, optical

nonlinearities are high in proximity to system-specific resonances, where the extinction coefficient is high. This is relevant for the photonic applications where there will be the tendency to maximize the nonlinear response.
However, operating under a resonance regime is likely to increase optical absorption, limiting the transmittance of the device and the ability to cascade many of them.
Fixed then the wavelength, or the pulsation, at which the device must operate, a nonlinear material, whose resonance frequencies characteristics are such that the nonlinear response is sufficiently high, and absorption is negligible, is chosen.
A nonlinear phenomenon is present in case of anisotropic material, as a glass ceramic in which crystals and glass matrix coexist. The glass is an isotropic material and then it is not subjected on effects of second order nonlinearity as second harmonic signal. It is necessary to transform the glass into a glass ceramic to be able to detect a non-linear response to laser irradiation. There is a connection between crystal properties and physical ones: in this case the appearance of non-linear terms of χ (physical property) shows how centrosymmetric crystal property has been broken. $\chi^{(2)}$ vanishes identically for a material possessing a center of inversion symmetry (a centrosymmetric medium). Non-centrosymmetric and centrosymmetric medium exhibit potential curve and polarization signal completely different, and this may explain the role of material symmetry in nonlinear optics, as illustrated in the following Figure A140.

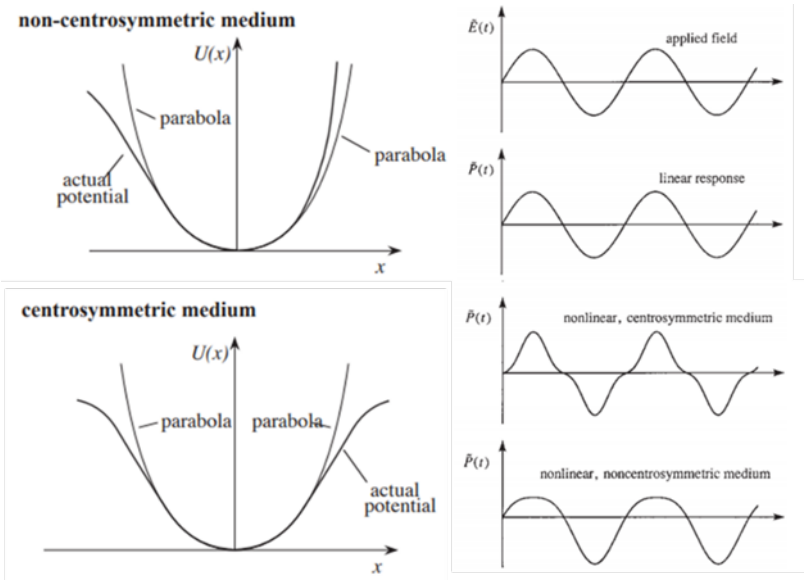

Figure A140: how potential curve (U) changes in non-centrosymmetric and centrosymmetric medium, the signal of the electric field and the curves of the respective polarization signals (Lorentz atomic model) [7]

C - Second harmonic generation

Second harmonic generation (SHG) is a nonlinear optical effect, in which the frequency of incident light is doubled. Virtual energy transition and not the absorption of the photons involves SHG, and the energy is conserved, as shown in Figure A141.

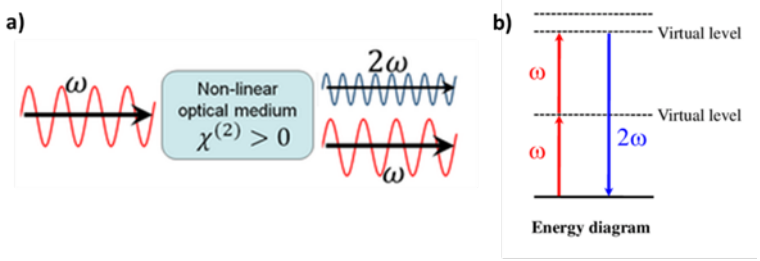

Figure A141: Scheme of SHG phenomenon from two different points of view: a) non-linear optical medium diagram and b) virtual energy diagram

SHG effect originates when an intense light as laser interacts with a matter, precisely a non-centrosymmetric structure, the vibrating electric field of the incident beam leads to the polarization of the matter, reemitting light at ω_i (the original frequency) and $2\omega_i$ (the doubled frequency or half the wavelength), as shown in Figure A142.

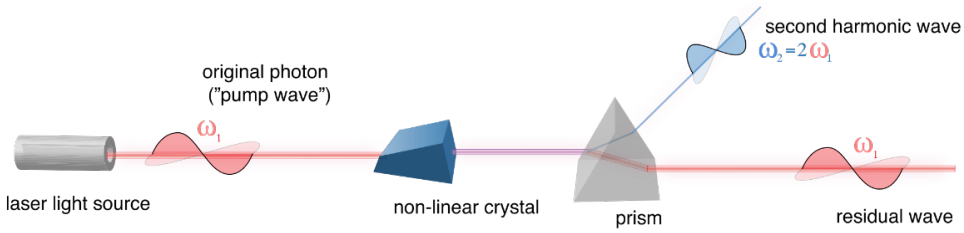

Figure A142: SHG scheme

The χ coefficients of terms higher than the first are such as to contribute to polarization only for electric fields of very large size. This explains why nonlinear phenomena were not observed prior to the development of lasers, which provide high intensities. It is possible to estimate the second-order coefficients, and therefore the intensity necessary to observe the phenomenon, exploiting considerations on the electronic behavior of the atom.
Wave propagation problems, energy transfer, and boundary conditions are dealt with using Maxwell's equations. Macroscopic differential form is given by:

$$\nabla \times \vec{E} = -\frac{\partial \vec{B}}{\partial t} \quad \text{(A86)}$$

$$\nabla \times \vec{H} = \vec{J} + \frac{\partial \vec{D}}{\partial t} \quad \text{(A87)}$$

$$\nabla \cdot \vec{D} = \rho \quad \text{(A88)}$$

$$\nabla \cdot \vec{B} = 0 \quad \text{(A89)}$$

Where $\vec{E}$ is the electric field vector, $\vec{B}$ is the magnetic flux density, $\vec{H}$ is the magnetic field vector, $\vec{J}$ is the current density vector, $\vec{D}$ is the electric flux density, and ρ is the sources for the electromagnetic field (volume charge density). For the source free region $J = 0$ and $\rho = 0$.

The constitutive relations are the following:

$$\vec{D} = \varepsilon_0 \vec{E} + \vec{P} \quad \text{(A90)}$$

$$\vec{E} = \mu_0 \vec{H} + \vec{M} \quad \text{(A91)}$$

Where ε_0 is the vacuum permittivity, $\vec{P}$ is the induced electric polarization, μ_0 is the vacuum permeability, and $\vec{M}$ is the induced magnetic polarization. For nonmagnetic matter $\vec{M} = 0$.

Considering the above equations, it is possible to write:

$$\nabla \times \nabla \times \vec{E} = -\mu_0 \varepsilon_0 \frac{\partial^2 \vec{E}}{\partial t^2} - \mu_0 \frac{\partial^2 \vec{P}}{\partial t^2} \quad \text{(A92)}$$

Where c is the speed of light in vacuum, $\mu_0 \varepsilon_0 = 1/c^2$

Several simplifications are assumed to solve the above equation:

1) The $\vec{P}_{NL}$ is treated as a small perturbation to the total induced polarization, considering the nonlinear effects are relatively weak in matter;

2) $\nabla \times \nabla \times \vec{E} = \nabla(\nabla \cdot \vec{E}) - \nabla^2 \vec{E} = -\nabla^2 \vec{E}$. Then, we write:

$$\nabla^2 \vec{E} = \frac{1}{c^2} \frac{\partial^2 \vec{E}}{\partial t^2} - \mu_0 \frac{\partial^2 \vec{P}}{\partial t^2} \quad \text{(A93)}$$

This equation can be translated in the Fourier domain:

$$\nabla^2 \tilde{E}(\omega) = \frac{\omega \varepsilon(\omega)}{c^2} \tilde{E}(\omega) + \frac{\omega^2}{c^2} \tilde{P}_{NL}(\omega) \quad \text{(A94)}$$

Where ε is the dielectric constant. The temporal variation of electric field at ω and 2ω are neglected, and the wave at second harmonic frequency will follow the wave equation:

$$\nabla^2 \tilde{E}(2\omega) = \frac{\omega\varepsilon(2\omega)}{c^2} \tilde{E}(2\omega) + \frac{\omega^2}{c^2} \tilde{P}^{(2)}(2\omega) \quad \text{(A95)}$$

Considering low conversion efficiency, the amplitude of $\vec{E}_\omega$ remains essentially constant over the interaction length, L, the intensity of SHG is given by:

$$I_{2\omega}(L) = \frac{(2\omega)^2}{8\varepsilon_0 c^3} \frac{|\chi^{(2)}|^2}{n_\omega^2 n_{2\omega}} L^2 \left(\frac{\sin(\frac{\Delta kL}{2})}{(\Delta kL/2)} \right)^2 I_\omega^2 \quad \text{(A96)}$$

$$I_\omega^2 = \frac{1}{2} \varepsilon_0 c n_\omega \left| \vec{E}_\omega \right|^2 \quad \text{(A97)}$$

$$\Delta k = k_{2\omega} - 2k_\omega = \frac{2\omega(n_\omega - n_{2\omega})}{c} \quad \text{(A98)}$$

$$L_c = \frac{\pi}{\Delta k} \quad \text{(A99)}$$

Where L is the nonlinear matter length, Δk is the wave vector mismatch, k is the wave vector of the electric field, and L_c is the coherence length where the SHG efficiency reaches the maximum (SHG intensity oscillates as a function of L, with period L_c).

Phase matching

Phase matching occurs when generated and propagating wave present a constant phase relationship indicated by Δk = 0. Efficient SHG in homogeneous media comes from decreasing Δk. There are many methods to achieve phase matching. Precisely, for birefringent phase matching (BPM), certain angle θ, the ordinary polarized fundamental and the extraordinary polarized second harmonic own the same refractive index, achieving Δk = 0. In that case, BPM is sensitive to the propagation angle and this kind phase matching is known as critical phase matching.

Another technique, noncritical phase matching can be used, in which the beams propagate down one of the axes of the nonlinear crystal and the temperature of the crystal is adjusted (generally, n_e is much more temperature sensitive that n_o, indicating a phase matching condition can be achieved). In this case a material with spatially modulated nonlinear properties can be used instead of a homogeneous nonlinear crystal material. This is the basis quasi-phase matching, which can be achieved by periodic poling of nonlinear crystal materials.

SHG can also be obtained from the random distributed nanocrystals because the emission from a nanocrystal can lose its phase relation with the order nano-crystals due to multiple scattering. Vigouroux et al. [8] have observed isotropic bulk SHG signals in lithium niobium silicate glass ceramics. It is fundamental to study the

radial distribution of the $LiNbO_3$ crystalline in spherulite domains: a macroscopic 10-15 µm c-axis oriented poly-crystallite with consecutive domains spatially radiating incoherent SHG signal. Because spherulites are sparsely distributed in the matrix with distances larger than the coherence length, i.e., 8-10 µm, they radiate uncorrelated SHG field. The total SHG intensity is the sum of the individual contribution.

SHG is forbidden in the bulk of centrosymmetric matter within the dipolar approximation. However, this symmetry is broken at the interface between two centrosymmetric media, allowing for SHG. At a surface or interface, the bulk symmetry is broken, allowing the second order nonlinear process even in a centrosymmetric matter.

D - Trends of SHG intensity for all the four glass compositions: curves and polar representations

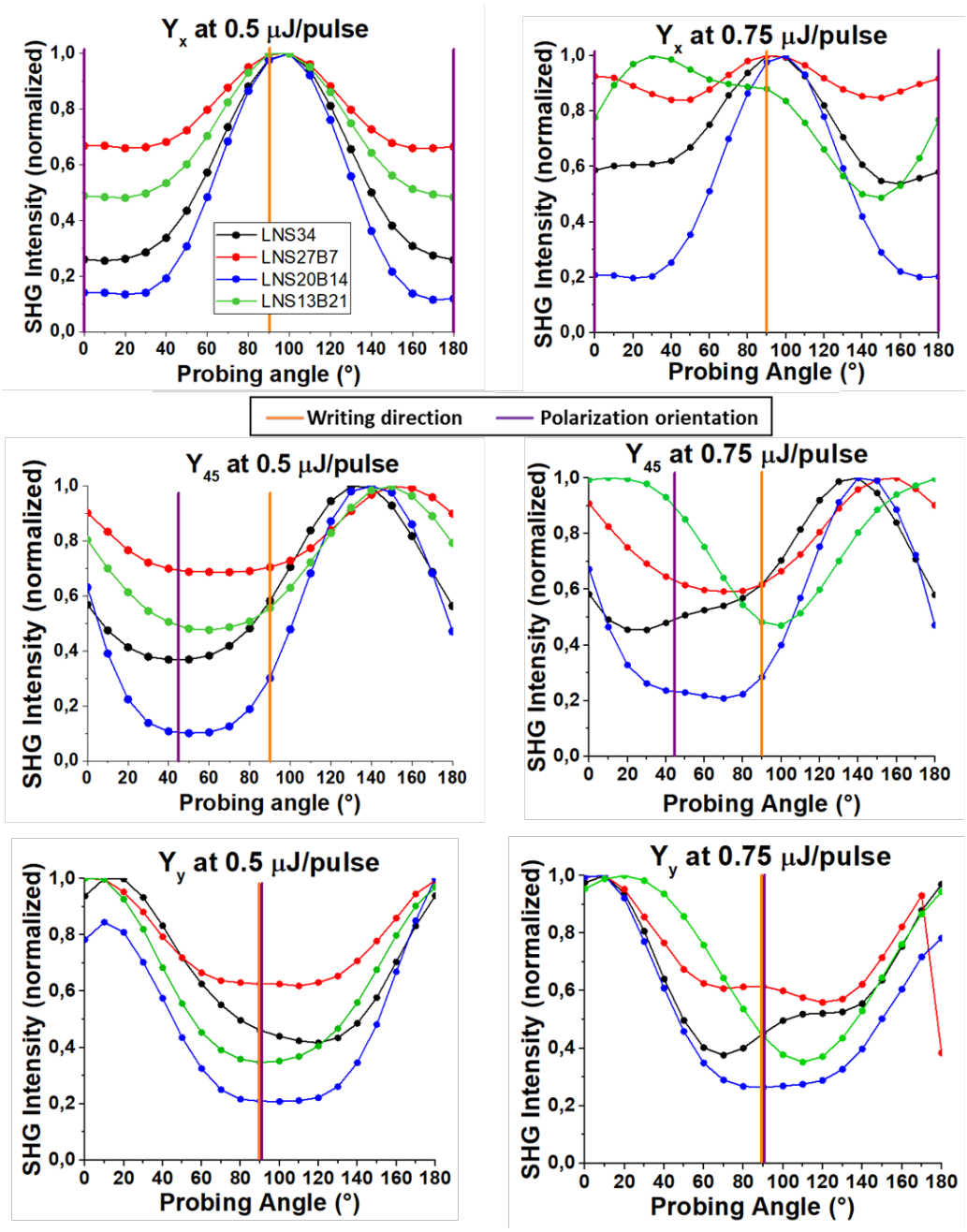

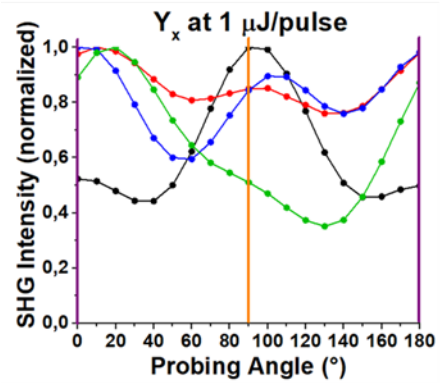
Y$_x$ at 1 μJ/pulse
SHG Intensity (normalized)
Probing Angle (°)

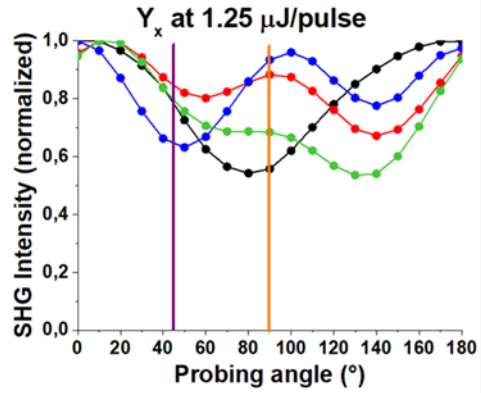
Y$_x$ at 1.25 μJ/pulse
SHG Intensity (normalized)
Probing angle (°)

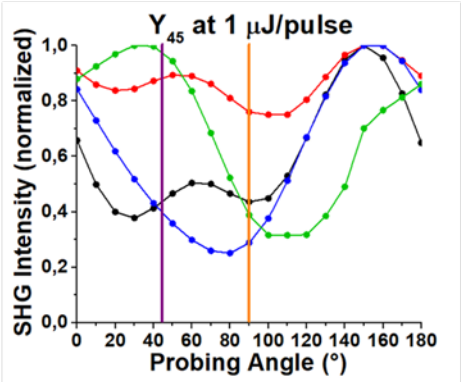
Y$_{45}$ at 1 μJ/pulse
SHG Intensity (normalized)
Probing Angle (°)

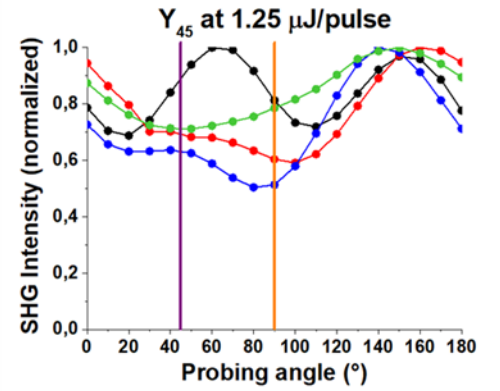
Y$_{45}$ at 1.25 μJ/pulse
SHG Intensity (normalized)
Probing angle (°)

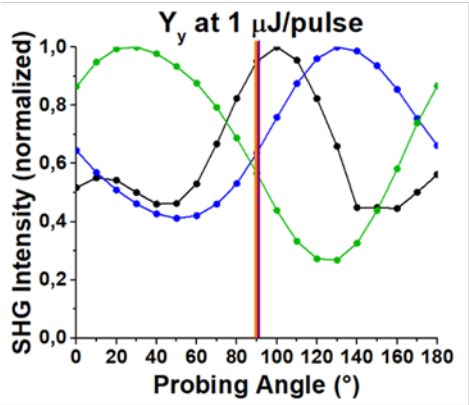
Y$_y$ at 1 μJ/pulse
SHG Intensity (normalized)
Probing Angle (°)

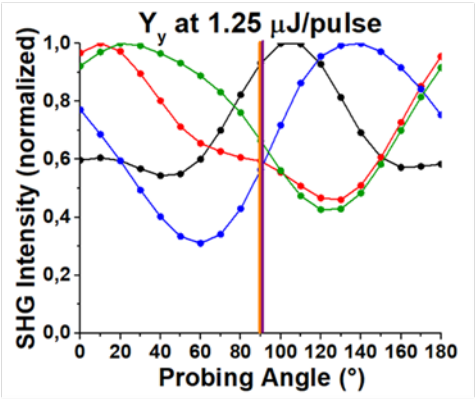
Y$_y$ at 1.25 μJ/pulse
SHG Intensity (normalized)
Probing Angle (°)

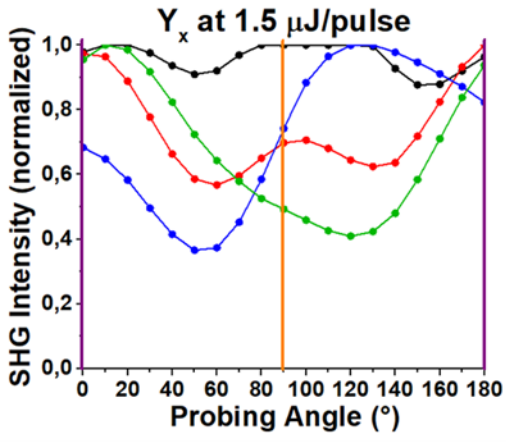
Y$_x$ at 1.5 μJ/pulse
SHG Intensity (normalized)
Probing Angle (°)

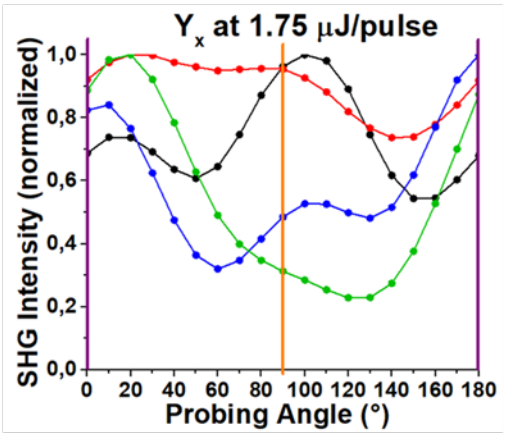
Y$_x$ at 1.75 μJ/pulse
SHG Intensity (normalized)
Probing Angle (°)

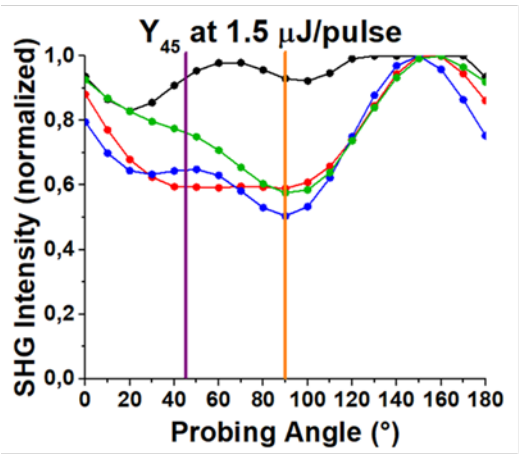
Y$_{45}$ at 1.5 μJ/pulse
SHG Intensity (normalized)
Probing Angle (°)

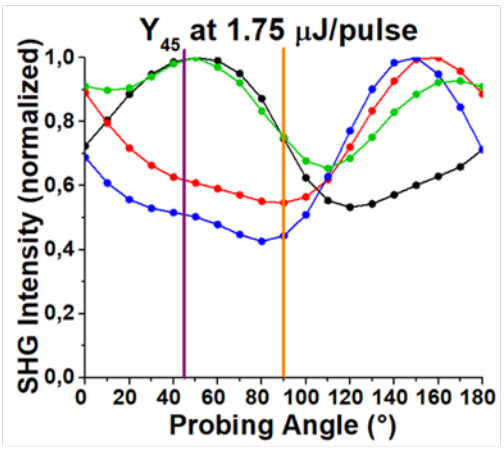
Y$_{45}$ at 1.75 μJ/pulse
SHG Intensity (normalized)
Probing Angle (°)

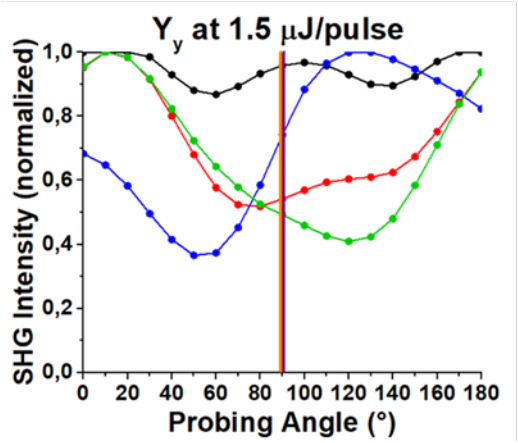
Y$_y$ at 1.5 μJ/pulse
SHG Intensity (normalized)
Probing Angle (°)

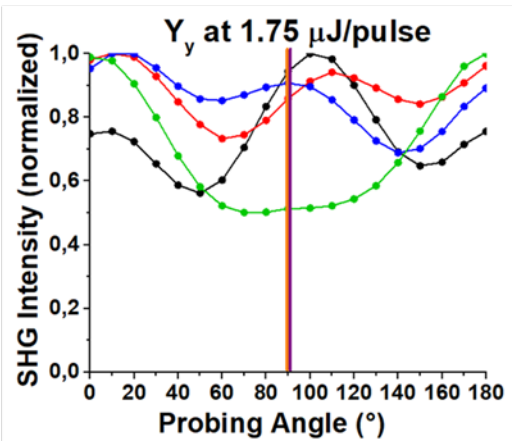
Y$_y$ at 1.75 μJ/pulse
SHG Intensity (normalized)
Probing Angle (°)

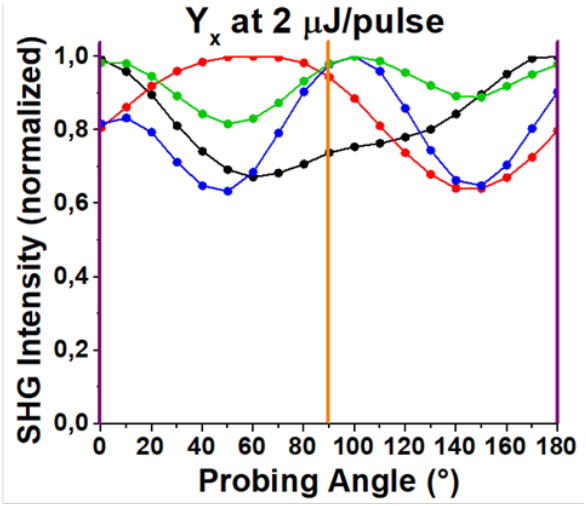
Y x at 2 μJ/pulse
SHG Intensity (normalized)
0,0
0,2
0,4
0,6
0,8
1,0
0 20 40 60 80 100 120 140 160 180
Probing Angle (°)

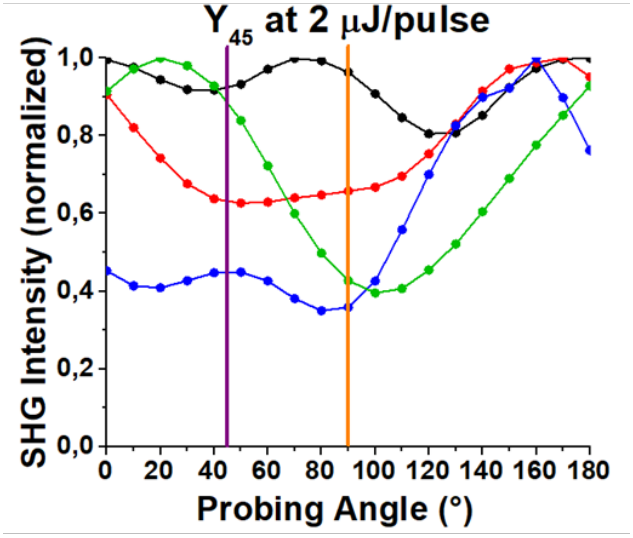
Y 45 at 2 μJ/pulse
SHG Intensity (normalized)
0,0
0,2
0,4
0,6
0,8
1,0
0 20 40 60 80 100 120 140 160 180
Probing Angle (°)

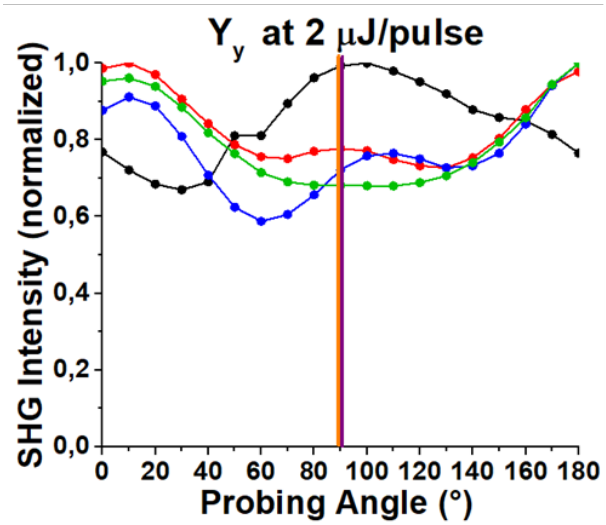
Y y at 2 μJ/pulse
SHG Intensity (normalized)
0,0
0,2
0,4
0,6
0,8
1,0
0 20 40 60 80 100 120 140 160 180
Probing Angle (°)

LNS34

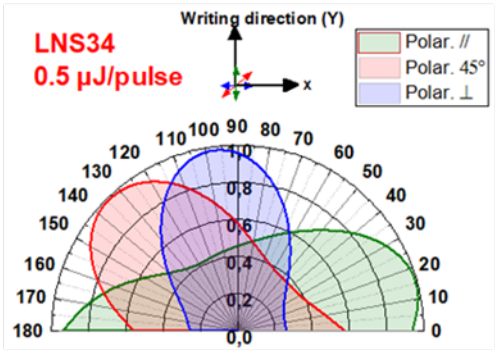
LNS34
0.5 µJ/pulse
Writing direction (Y)
x
Polar. //
Polar. 45°
Polar. ⊥

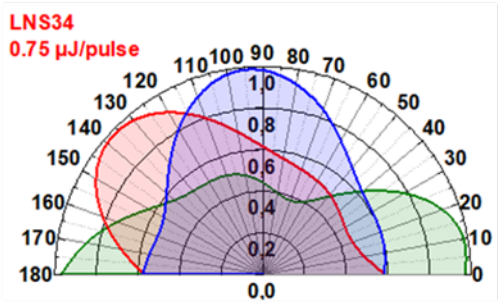
LNS34
0.75 µJ/pulse

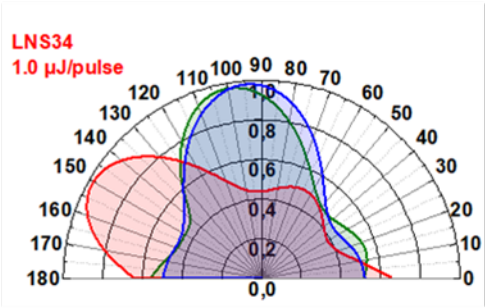
LNS34
1.0 µJ/pulse

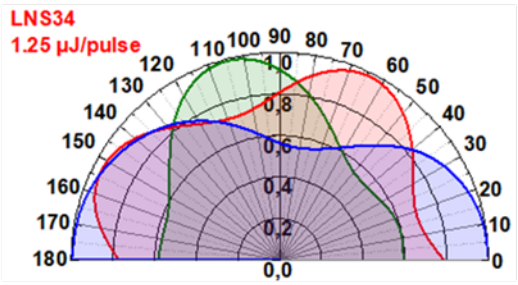
LNS34
1.25 µJ/pulse

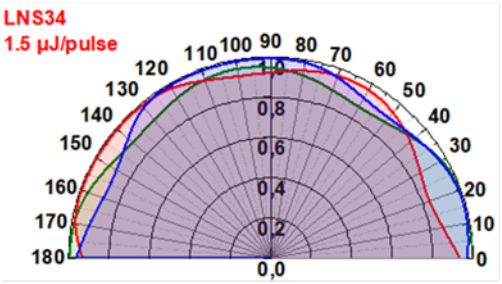
LNS34
1.5 µJ/pulse

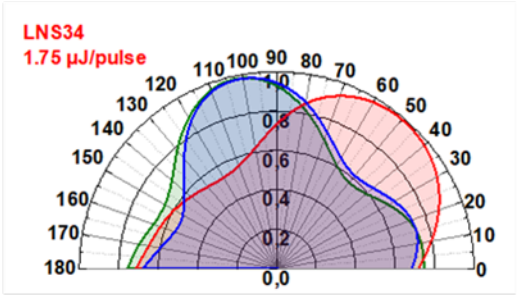
LNS34
1.75 µJ/pulse

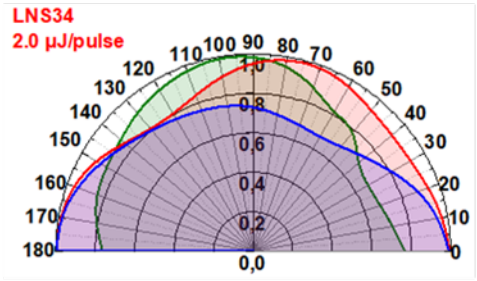
LNS34
2.0 µJ/pulse

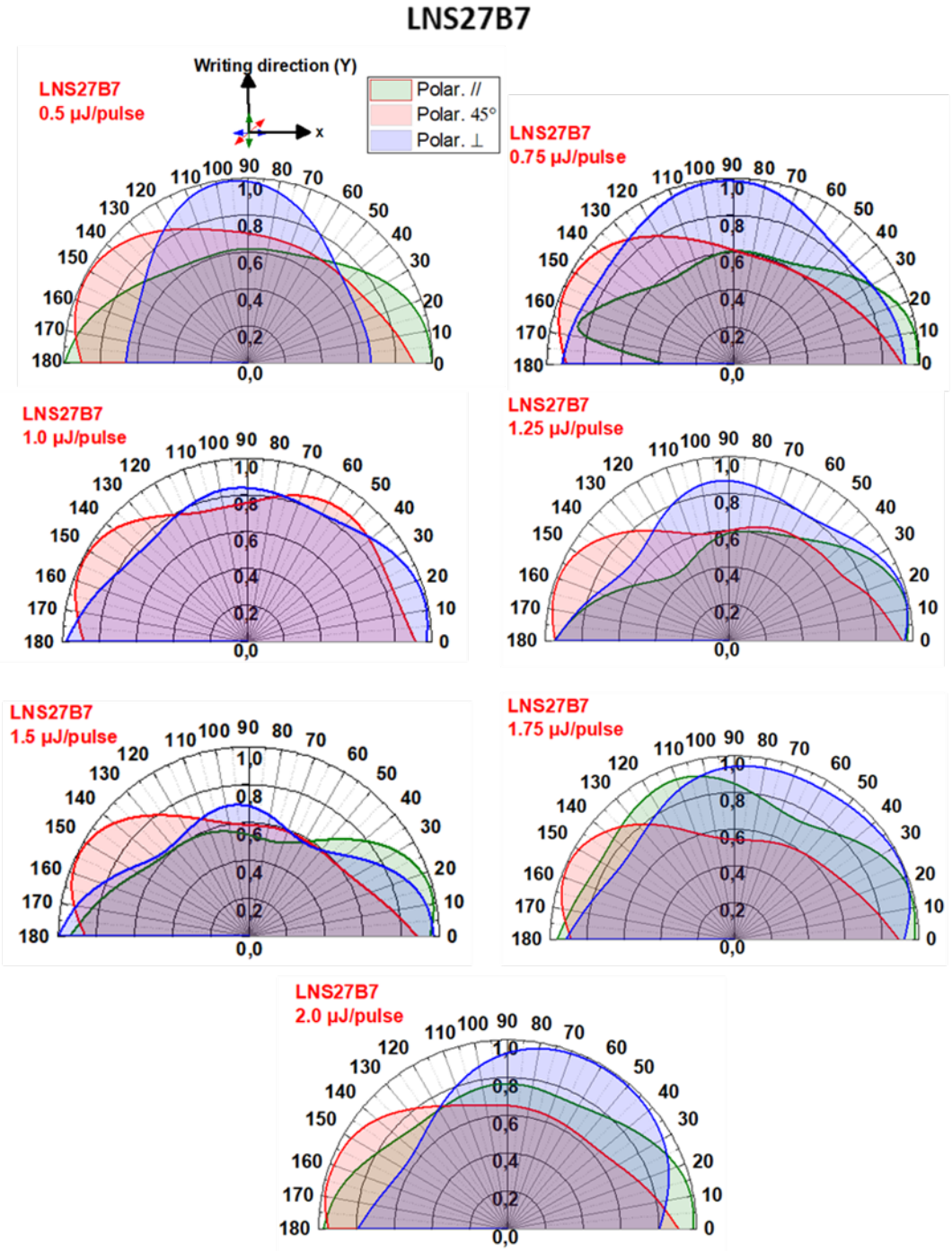
LNS27B7
Writing direction (Y)
x
Polar. //
Polar. 45°
Polar. ⊥
LNS27B7
0.5 µJ/pulse
LNS27B7
0.75 µJ/pulse
LNS27B7
1.0 µJ/pulse
LNS27B7
1.25 µJ/pulse
LNS27B7
1.5 µJ/pulse
LNS27B7
1.75 µJ/pulse
LNS27B7
2.0 µJ/pulse

LNS20B14

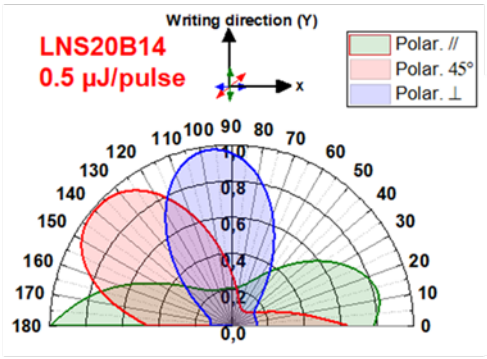
Writing direction (Y)
LNS20B14
0.5 µJ/pulse
Polar. //
Polar. 45°
Polar. ⊥
x

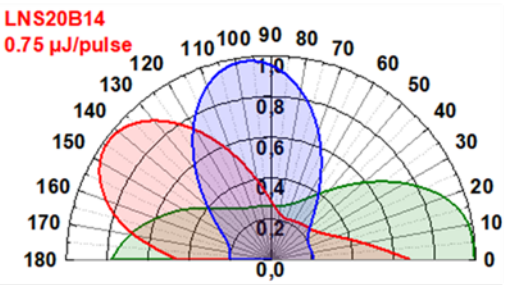
LNS20B14
0.75 µJ/pulse

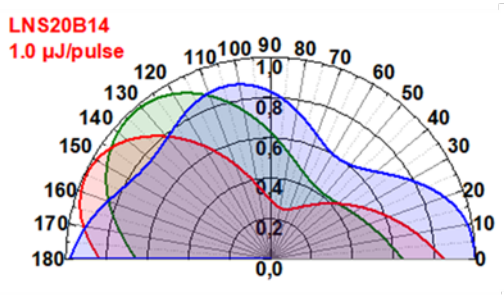
LNS20B14
1.0 µJ/pulse

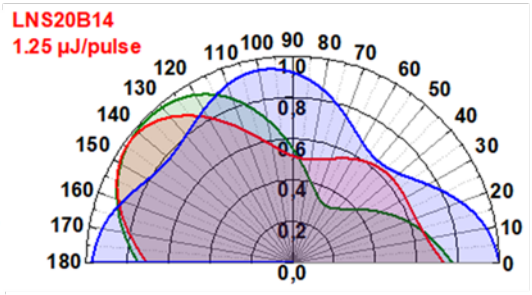
LNS20B14
1.25 µJ/pulse

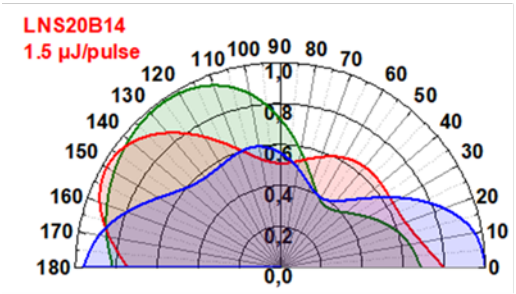
LNS20B14
1.5 µJ/pulse

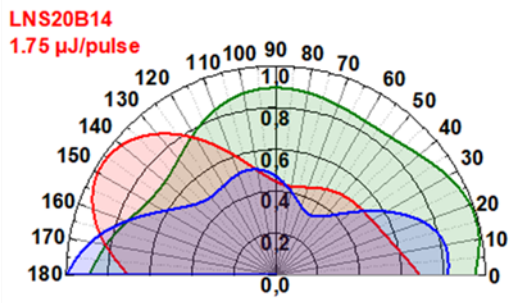
LNS20B14
1.75 µJ/pulse

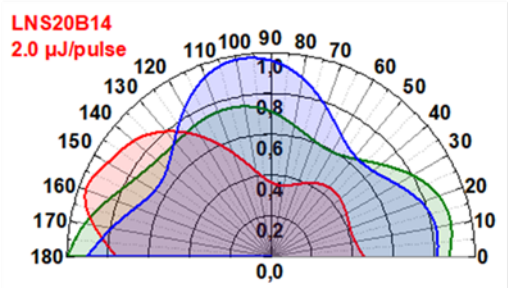
LNS20B14
2.0 µJ/pulse

LNS13B21

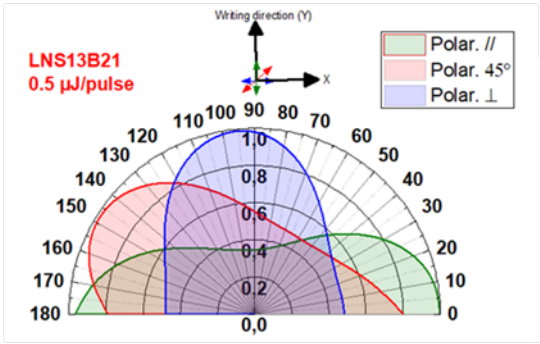
Writing direction (Y)
X
Polar. //
Polar. 45°
Polar. ⊥
LNS13B21
0.5 µJ/pulse

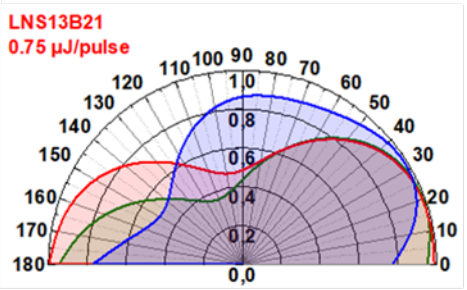
LNS13B21
0.75 µJ/pulse

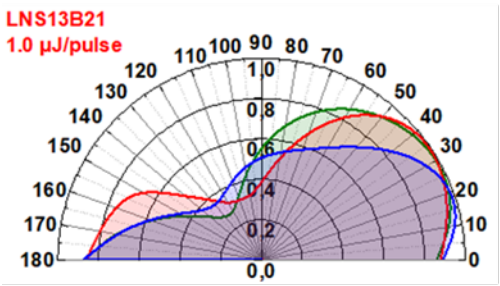
LNS13B21
1.0 µJ/pulse

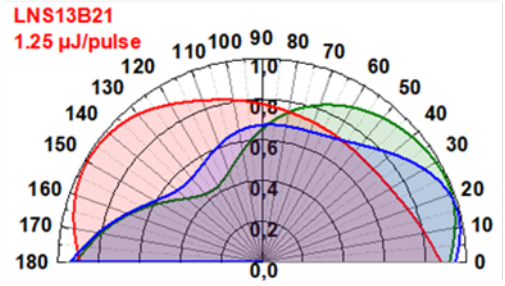
LNS13B21
1.25 µJ/pulse

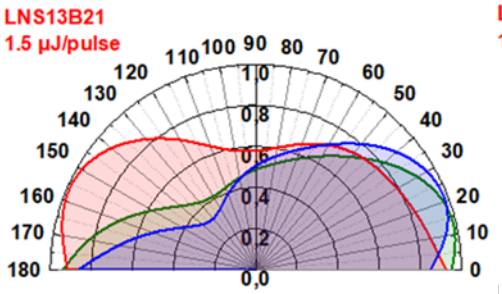
LNS13B21
1.5 µJ/pulse

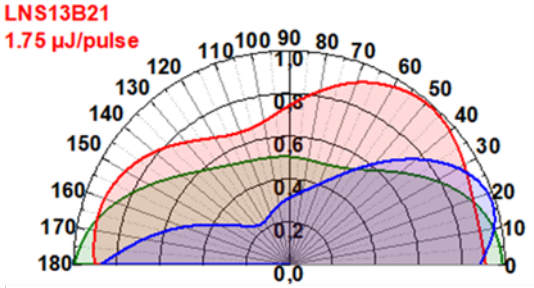
LNS13B21
1.75 µJ/pulse

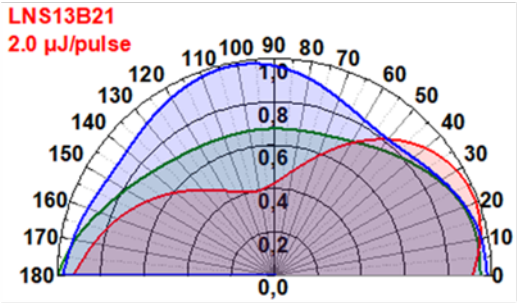
LNS13B21
2.0 µJ/pulse

E - Quantitative Phase Microscopy (QPM)

Quantitative Phase Microscopy (QPM) uses a partially coherent illumination and ordinary transmission microscope to extract non-interferometric quantitative phase data. This technique can recover phase even in the presence of amplitude modulation, making it significantly more powerful than existing methods of phase microscopy. Another peculiarity of this technique is the production of quantitative images of the profile of the sample without phase unwrapping. Also, the spatial resolution is in the range of micrometer with the sensitivity on the order of 10^{-4}. An example of QPM technique phase information of the line written in pure silica by femtosecond laser irradiation is shown in the next Figure A143. Those lines images derived from an integration of the whole picture using MATLAB code. In this case, the background level is quite homogenous, and its fluctuations are on the order of +/-0.005 rad. The phase in the line center is positive while it becomes negative on the border. Also, the uncertainty of this measurement is less than 5%.

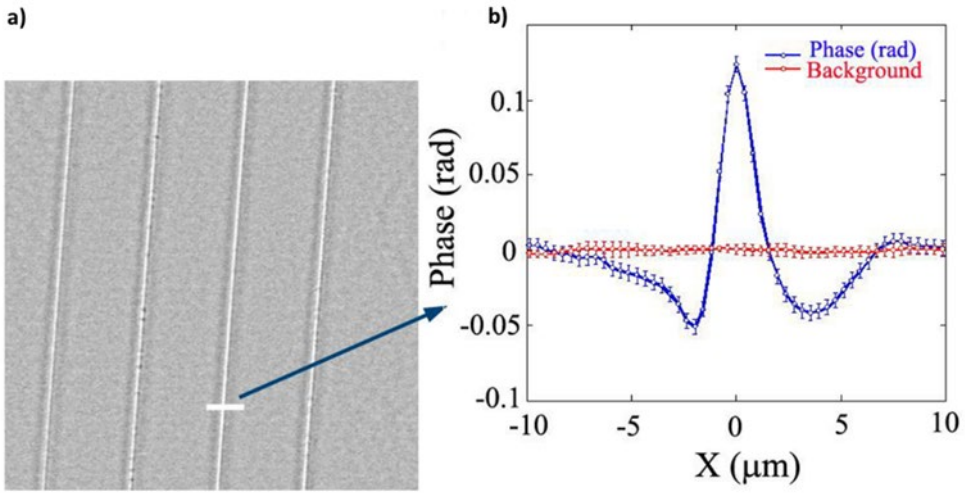

Figure A143: Quantitative phase measurement of the written lines with a line spacing of 50 μm in pure silica: a) phase image and b) profile (line's cross section)

A set of three images was captured by the camera mounted on the microscope: one in-focus (I_0) and the other two very slightly positively/negatively (I_+/I_-) defocused images. The scheme was reported in the next Figure A144. The images were converted into intensity data by a computer code. There is a transport of intensity equation that represents the propagation of light field along the optical axis z in microscope:

$$\frac{2\pi}{\lambda}\frac{\partial I(\vec{r})}{\partial z} = -\nabla\left(I(\vec{r})\nabla\varphi\left(\frac{\vec{r}}{M}\right)\right) \qquad \text{(A100)}$$

where $\vec{r} = (x, y)$ is a two-dimensional vector in the transverse plane, I is the intensity distribution of the image and M is the magnification of the microscope. The differential information of the propagation of the field on the left side of the previous equation is given by:

$$\frac{\partial I(\vec{r})}{\partial z} \approx \frac{I_+ - I_-}{2\Delta z} \qquad \text{(A101)}$$

where Δz is the defocus distance. The transport of intensity equation can be solved by a specific algorithm. This technique is based on coherent illumination, even if there is a partially coherent illumination source in QPM systems that provides same results to the coherent case. The irradiance distribution of the illumination source shows inversion symmetry. A motorized stage (Physic Instrument) was used for translating the microscope objective to capture the de-focused images. IATIA Ltd creates the image acquisition and the algorithm for phase map calculation in QPM system. The refractive index variation of the laser modified region is given by:

$$\Delta n = \frac{\Delta\varphi\lambda}{2\pi d} \qquad \text{(A102)}$$

where λ is the wavelength of 515 nm (green filter) used by IATIA software to calculate the quantitative phase image, d is the thickness of the modified region and $\Delta\varphi$ is the phase variation between the modified and bulk of the material measured from QPM.

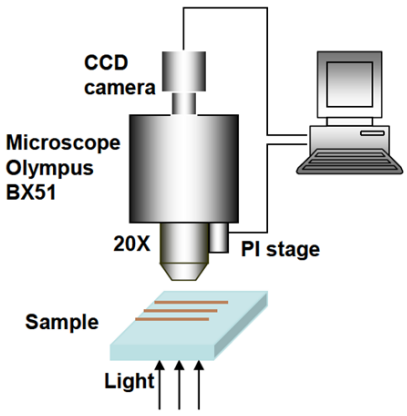

Figure A144: Schematic of quantitative phase microscopy setup

An example of QPM measurement of the waveguide structures, specifically type-I modifications, is reported in the next Figure A145. A 20X objective and an 8-bit mega-pixel CCD camera captured the three bright field images. The NA of the

condenser was set to be 80% NA of the objective. We can obtain different typologies of information: the phase of modified structure is shown in a) and represented in b); the differential interference contrast (DIC) image was emulated by the calculated phase information of the structure in c).

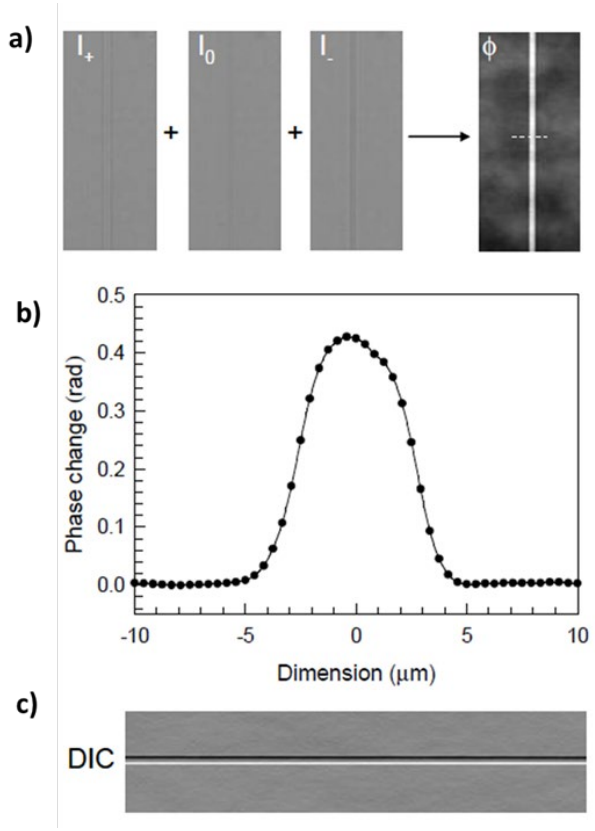

Figure A145: QPM measurement provides different information: a) three bright field images: one in-focus (I_0) and the other two very slightly positively/negatively (I_+/I_-) defocused images were captured to calculate the quantitative phase image φ; b) Quantitative phase change information of the arrow in cross the waveguide structure; c) DIC image of the waveguide structure using the calculated phase information from a) [9]

Bibliography

[1] K. Wasai, G. Kaptay, K. Mukai, and N. Shinozaki, "Modified classical homogeneous nucleation theory and a new minimum in free energy change 1. A new minimum and Kelvin equation," *Fluid Phase Equilibria*, p. 8, 2007.

[2] H. Zeng, B. Poumellec, C. Fan, G. Chen, A. Erraji-Chahid, and M. Lancry, "Preparation of Glass-Ceramics with Oriented Nonlinear Crystals: A Review," in *Advanced in Materials Science Research*, Nova Science, 2012, pp. 89–134.

[3] S. B. Lee and N. J. Kim, "Kinetics of crystallization in continuously cooled BMG," *Materials Science and Engineering: A*, vol. 404, no. 1–2, pp. 153–158, Sep. 2005, doi: 10.1016/j.msea.2005.05.038.

[4] V. M. Fokin, E. D. Zanotto, N. S. Yuritsyn, and J. W. P. Schmelzer, "Homogeneous crystal nucleation in silicate glasses: A 40 years perspective," *Journal of Non-Crystalline Solids*, vol. 352, no. 26–27, pp. 2681–2714, Aug. 2006, doi: 10.1016/j.jnoncrysol.2006.02.074.

[5] M. Shimizu *et al.*, "Formation mechanism of element distribution in glass under femtosecond laser irradiation," *Opt. Lett.*, vol. 36, no. 11, p. 2161, Jun. 2011, doi: 10.1364/OL.36.002161.

[6] "Capitolo 3 - introduzione all'ottica nonlineare.pdf."

[7] R. W. Boyd, *Nonlinear optics*, 3rd ed. Amsterdam; Boston: Academic Press, 2008.

[8] H. Vigouroux *et al.*, "Crystallization and Second Harmonic Generation of Lithium Niobium Silicate Glass Ceramics," *Journal of the American Ceramic Society*, vol. 94, no. 7, pp. 2080–2086, 2011, doi: https://doi.org/10.1111/j.1551-2916.2011.04416.x.

[9] W. Yang, "Femtosecond laser writing in transparent materials," University of Southampton, United Kingdom, 2008.

Research Article Vol. 11, No. 4 / 1 April 2021 / Optical Materials Express 1313
Optical Materials EXPRESS

Polarization-oriented $LiNbO_3$ nanocrystals by femtosecond laser irradiation in LiO_2–Nb_2O_5–SiO_2–B_2O_3 glasses

ELISA MUZI,[1,2,*] MAXIME CAVILLON,[1] MATTHIEU LANCRY,[1] FRANÇOIS BRISSET,[1] BENJAMIN SAPALY,[1] DAVIDE JANNER,[2] AND BERTRAND POUMELLEC[1]

[1]Institut de Chimie Moléculaire et des Matériaux d'Orsay (ICMMO), Université Paris-Saclay, CNRS, 91405 Orsay, France
[2]Department of Applied Science and Technology (DISAT), Politecnico di Torino, 10129 Torino, Italy
*elisa.muzi@universite-paris-saclay.fr

Abstract: This work investigates the role of a B_2O_3 addition (up to 21 mole %) into a lithium niobium silicate glass matrix, focusing on the orientational dependency of second harmonic generation (SHG), induced after femtosecond laser irradiation. We detected the sharp emission of light at 515 nm, characteristic of SHG, in both static and scanning configurations, using pulse energy, repetition rate, and laser polarization as varying parameters. Among the results to highlight, the SHG signature appears within a few seconds in highly doped B_2O_3 glass, i.e., one order of magnitude smaller than in B_2O_3-free glass. Additionally, we found that the orientability of the polar axis of $LiNbO_3$ nanocrystals by writing laser polarization can be obtained in glasses when SiO_2 is substituted with B_2O_3. These preliminary results open the door to the fabrication of crystal / glass based photonic devices with lower laser power deposited and much faster crystallization kinetics.

1. Introduction

Femtosecond (fs) laser direct writing (FLDW) is a powerful and versatile tool enabling a large variety of optical components to be fabricated in transparent materials such as glasses (e.g. Bragg gratings, waveguides, graded index lenses, birefringent optics) [1–3]. In addition to surface modifications, the femtosecond laser irradiation has allowed the 3D-nanostructuring of optical properties induced by permanent effects on material structure. By controlling the fs-laser parameters (e.g. pulse energy, repetition rate, scanning speed, polarization), it becomes possible to induce crystallization inside a glass substrate with a high spatial selectivity (few tens of μm^3 or less). Some examples of crystals induced by FLDW in glasses can be found in the recent review of Komatsu et al. [4], among which we can cite β-BaB_2O_4 [5], $Ba_2TiSi_2O_8$ [6], or $LiNbO_3$ [7]. A particular focus is about fs-laser crystallization of $LiNbO_3$ in silicate matrix, a crystal that allows many applications in different fields because of its properties: ferroelectricity, pyroelectricity, piezoelectricity and a large second order susceptibility. In particular, because of its axial symmetry, the second order susceptibility tensor ($\chi^{(2)}$) of $LiNbO_3$ crystal is such that its nonlinear coefficient value along the polar axis (d_{33} = 34.4 pm/V [8,9]) is much greater than the nonlinear coefficients values along the other axes (d_{31} = 4.88 pm/V, d_{22}=2.58 pm/V [8,9]). Therefore, it presents an angular dependence of $\chi^{(2)}$-related processes, such as second harmonic generation (SHG). This translates into a modulation of the SHG signal during FLDW that occurs when the crystals can be oriented along the direction of laser polarization.

To produce crystallization by FLDW, the typical glass matrix used in previous works is composed of 33%Li_2O – 33%Nb_2O_5 – 34%SiO_2 (LNS) (molar %) [7,10]. Although interesting results have been published, the impact of the glass matrix has not been studied extensively yet.

#417461 https://doi.org/10.1364/OME.417461
Journal © 2021 Received 11 Dec 2020; revised 11 Feb 2021; accepted 24 Feb 2021; published 31 Mar 2021

Optical Materials EXPRESS

In particular, if SiO_2 is partially substituted with B_2O_3, the impact on the crystallization rate can drastically increase, unlocking in such a way the industrial potential of this direct writing technique. Indeed, the incorporation of B_2O_3 into the glass matrix is of interest as it is expected to lower the glass transition temperature and, thus, to improve the kinetics of $LiNbO_3$ crystallization compared for LNS glass [11–14].

In this work, we report on the impact of $LiNbO_3$ crystallization by FLDW by adding a significant amount of B_2O_3 in the glass matrix (through modification of the starting glass batch composition). We revealed the creation of polarization dependent $\chi^{(2)}$ by the SHG detection and confirmed this is related to $LiNbO_3$ nanocrystals by electron backscattered diffraction (EBSD) measurements. As a reference, we start with the crystallization of a typical LNS glass. We,

then, intend to analyze the impact on fs-laser irradiation on glass crystallization, when SiO_2 is partly substituted with B_2O_3. More specifically, we aim at determining whether it is possible to induce tunable SHG angular modulation in these glassy matrices and to identify the orientation of the laser-induced nanocrystals in these borosilicate glass matrices compared to LNS glass (i.e., B_2O_3-free glass).

2. Method

Four glasses, with increasing B_2O_3 content up to 21%, were fabricated using melt-quenching technique. Compositions and labels are reported in the Table 1. A powder mixture of 30 grams per batch composed of SiO_2 (99.9%, SERLABO), H_3BO_3 (99.5%, PROLABO), Li_2CO_3 (99.9%,

SIGMA ACS reagent) and Nb_2O_5 (99.5%, STREM CHEMICALS) powders in stoichiometric amount, was first homogenized using acetone. The mixed powder was then placed inside a platinum crucible and dried at 200°C for 2 hours before increasing the temperature at a heating rate of 5°C/min up to 1000°C. The mixed powder remained at this temperature for 1 hour. After that, to obtain the melting, the temperature was increased to 1400°C for LNS34 and 1350°C for LNS27B7, LNS20B14, LNS13B21 at a heating rate of 10°C/min. Finally, the molten mixture was quenched between two metal plates preheated at around 350°C and maintained at this temperature for about 30 minutes.

Table 1. Glass labels and batch compositions

Glass label	Glass batch composition (mol%)
LNS34	33% LiO_2 – 33% Nb_2O_5 – 34% SiO_2
LNS27B7	33% LiO_2 – 33% Nb_2O_5 – 27% SiO_2 – 7% B_2O_3
LNS20B14	33% LiO_2 – 33% Nb_2O_5 – 20% SiO_2 – 14% B_2O_3
LNS13B21	33% LiO_2 – 33% Nb_2O_5 – 13% SiO_2 – 21% B_2O_3

The obtained glasses had the shape of a slab of about 1 mm thickness. For laser irradiation, samples were double side polished to reach optical quality and then they were placed on the FLDW system that comprises a motorized translation stage and a commercial femtosecond laser (Satsuma, Amplitude Systèmes Ldt, $\lambda = 1030$ nm, pulse duration = 250 fs). Each irradiation was performed by focusing the laser beam approximately 240 µm below the sample top surface using a 0.6 numerical aperture (NA) aspheric lens. We choose this focusing depth to avoid any surface ablation when scanning over long distances and to avoid heterogenous nucleation preferentially triggered at the surface.

The translation stage enables a displacement in the XY plane, while the laser beam propagation direction is along the Z direction as depicted in Fig. 1(a). Three different laser polarization configurations referenced relative to the laser writing direction, along the Y-axis, were used: parallel: parallel (Y_y), at 45° (Y_{45}) and perpendicular (Y_x) to it. The SHG intensity was recorded in transmission using a spectrometer (Jaz, Ocean Optics) equipped with a multimode optical fiber

Optical Materials EXPRESS

and a coupling lens to maximize light collection from the sample. A more detailed description of the setup is reported in Ref. [7].

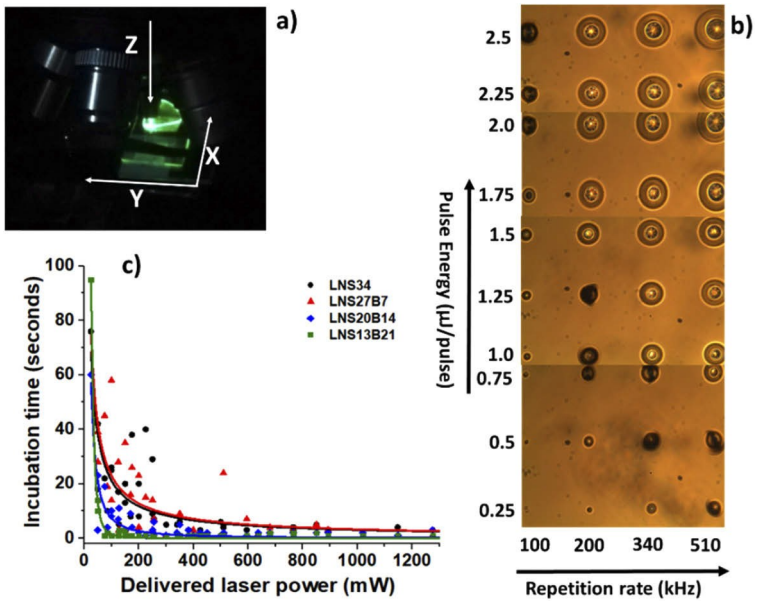

Fig. 1. a) Typical image of SHG detected after few seconds under static irradiation that corresponds to the end of the incubation time; b) Optical microscope image in transmission and white light of static irradiation until the onset of SHG of LNS34 glass sample with varying laser parameters; c) Incubation time as a function of the power (in mW) delivered by the laser in static conditions for four glass compositions. Laser conditions used: λ = 1030 nm, NA = 0.6, f = 200 kHz, focus depth = 240 µm in air. In Fig. 1(c), each data set was fitted with a power law (ax^b); the latter only serves as a guide-to-the-eye.

We started by performing a static irradiation to investigate the influence of laser parameters during laser-induced crystallization. This experiment, carried out on each sample, served to determine the incubation time as a function of glass composition. The incubation time is the time taken, upon fs-laser irradiation, until the observation of the SHG signal ($\lambda_{SHG} = \lambda/2 = 515$ nm) and is indicative of the early birth of non-centrosymmetric crystals, typically $LiNbO_3$ is expected in our case [7]. At this stage, only two laser parameters were varied, i.e., the pulse energy, ranging from 0.25 to 2.5 µJ, in steps of 0.25 µJ and the laser repetition rate, with values of 100 kHz, 200 kHz, 340 kHz, and 510 kHz. The laser polarization was fixed along the X-axis that is defined by the plane of laser compressor. The minimum incubation time to induce crystallization, found from the above experiments, is also needed for writing lines structures. First the laser was set in static mode for the minimum incubation time until green light was detected; then the laser scanning was started. Line writing parameters were set at a fixed repetition rate of 200 kHz and writing speed of 1 µm/s using different pulse energies (0.25 µJ to 2.0 µJ, step of 0.25 µJ). This was repeated for the three different laser polarization configurations to assess their influence on the crystal orientation, namely parallel (Y_y), at 45° (Y_{45}) and perpendicular (Y_x).

For each written line, we measured the SHG intensity in the XY plane according to the azimuthal angle (θ) of the probe beam polarization, up to 180° starting from the polarizer reference position in correspondence of 0°, i.e., along X. The probe beam propagation direction was set perpendicular to the XY plane and its electric field direction was parallel to this plane.

In our samples, the SHG intensity was measured in transmission mode with the fundamental beam (1030 nm) propagating perpendicularly to the sample XY plane at pulse energy = 0.1 µJ/pulse.

Optical Materials EXPRESS

The spot size (diameter) of the probing beam was approximately 30 μm, well overlapping each laser track during SHG measurements. The repetition rate during the measurement was set at 100 kHz. The transmitted SHG light (515 nm) was recorded after passing an IR low pass filter mounted before the spectrometer collector.
Finally, to investigate the correlation between the laser induced microstructure and the SHG response, we proceeded with an analysis at field-emission scanning electron microscope (FEG- SEM ZEISS SUPRA 55 VP) with electron backscattered diffraction (EBSD) detector (TSL-EDAX Velocity Camera and OIM Analysis software).

3. Results and discussion

In Fig. 1, we report respectively: a) the SHG signal detected upon irradiation, b) the laser induced modifications observation under optical microscope with varying conditions, and c) incubation times measured for each glass sample under static irradiation. In particular, Fig. 1(b) illustrates the dependence of the laser affected zone on both pulse energy (E_p) and repetition rate (RR). As the deposited power ($P = RR$ x E_p) increases, the area of the modified region becomes wider than the spot size, which is characteristic of thermal accumulation in and around the focal spot (of radius w_0 1.2λ/(2NA) 1 μm). Figure 1(c) shows that the measured incubation time decreases as the delivered power P increases. For similar experimental conditions, these measurements clearly indicate the tendency for LNS13B21 glass to crystallize at a much higher rate compared to other glasses. For example, at a delivered power of 100 mW, LNS13B21 sample exhibits an incubation time of 1 second, while it is of 10 seconds for LNS20B14 and 20 seconds for both LNS27B7 and LNS34, as represented in Fig. 1(c). In term of laser-affected volume, we observe that both laser track width and length (measured within the cross section) increase along with the pulse energy. This behavior is characteristic of more heat deposited inside the glass upon irradiation and it is in agreement with results from Fig. 11 in Ref. [7].
To assess the effect of the orientation of the writing laser polarization on the crystals, we investigated the angular dependency of the SHG intensity. All the measured values, as a function of the azimuthal orientation of the probing linear polarization, were normalized relative to their highest value as shown in Fig. 2. Here we compared two writing configuration schemes: Y_x and Y_{45}. In particular, we choose to represent those relative to two characteristics pulse energies, i.e.,
0.5 μJ and 1.25 μJ, because of important SHG trends variations that are visible in Fig. 2(a) and 2(b), for the four investigated glasses. For the lowest energy value, a strong SHG modulation is found with an azimuth-θ of 90° for all glasses. For pulse energy of 1.25 μJ, the evidence of SHG "directionality" is strongly reduced for all four samples, as it is more easily visible from the polar representations referring to LNS1B21 sample, reported in Fig. 2(c). Here we note the occurrence of a second maximum on the SHG(θ) curve along the polarization direction.
More specifically, from Fig. 2, we observe that at the lowest energy (0.5 μJ/pulse), the normalized SHG intensity (I/I_{max}) follows a sinusoidal behavior with a strong contrast (I_{max}- I_{min})/(I_{max}+I_{min}) up to 0.9 for LNS20B14. We note a maximum for a direction perpendicular to the laser polarization i.e., 90° and 135° for Y_x and Y_{45} configurations, respectively. In contrast the minimum SHG is found for a probing angle perpendicular to the maximum one. This is in agreement with Ref. [10], where the polar axis of $LiNbO_3$ is oriented perpendicularly to the laser polarization. Interestingly, this behavior is preserved even after a large substitution of SiO_2 with B_2O_3.
As the pulse energy is increased, from 0.5 to 1.25 μJ, the SHG intensity profile becomes more "isotropic", which could be caused by the presence of several crystalline textures with different orientations [15]. Indeed, from Fig. 2(c) we can see that the low energy texture (population leading to SHG_{max} for θ perpendicular to writing polarization) is still appearing at 1.25 μJ. However, there is another contribution that appears in the SHG(θ) response, and is indicative of a second texture (i.e., a second population of $LiNbO_3$ crystals with a preferential orientation).

Optical Materials EXPRESS

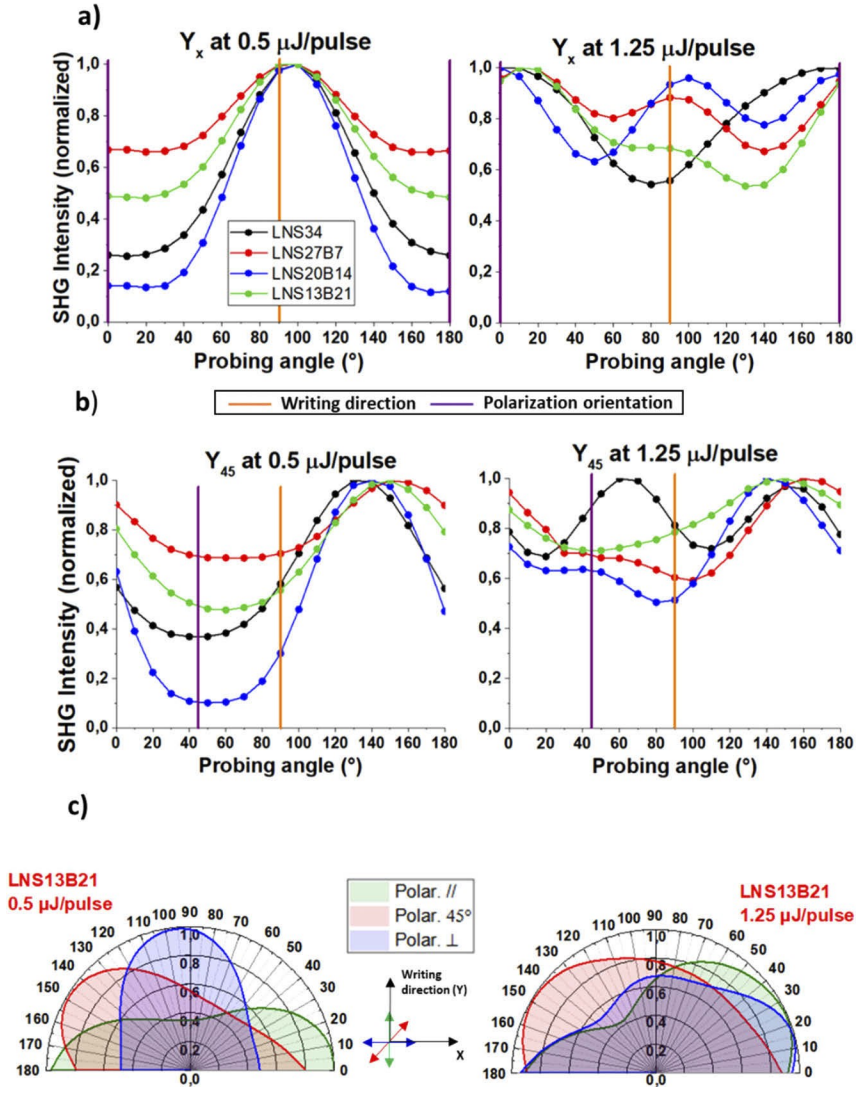

Fig. 2. Normalized SHG intensity for four glass compositions as a function of probing polarization angle in the XY plane as defined in the text, a) for the four glass samples, configuration Y_X at two pulse energies: 0.5 µJ/pulse and 1.25 µJ/pulse; b) same as a) but for the Y_{45} configuration. Both the writing direction and the laser polarization during writing are reported on each graph; c) polar representations for LNS13B21 glass for 0.5 µJ/pulse and 1.25 µJ/pulse with three configurations: Y_y, Y_{45} and Y_x (the polarization orientations with respect to writing direction are indicated by double headed arrows in the coordinates of the reference system).

Optical Materials EXPRESS

This is also clear with the configuration Y_{45} for which there is no maximum in the direction of writing.
One could expect the minima and maxima of the SHG modulation to be positioned exactly 90° apart from the laser polarization. However, a slight departure from this angle is observed, and

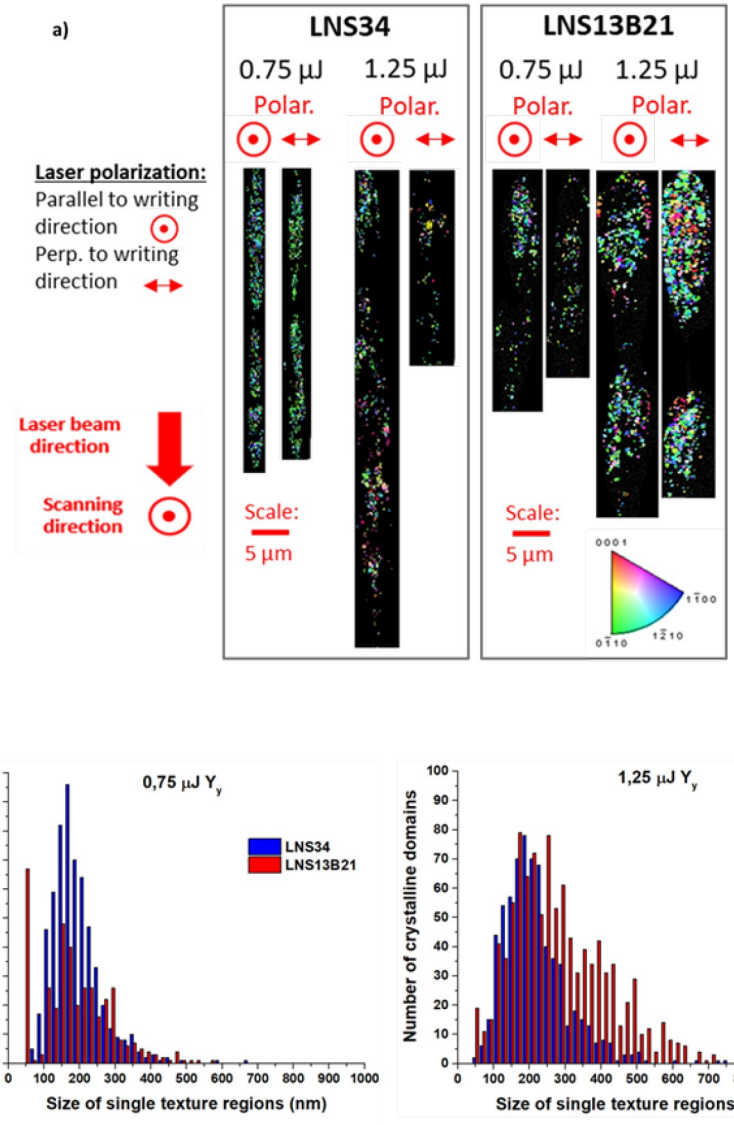

Fig. 3. a) Electron Back Scatter Diffraction (EBSD) micrographs of the laser track cross sections for both LNS34 and LNS13B21 glass samples, for two pulse energies (0.75 µJ/pulse and 1.25 µJ/pulse) and with laser polarization either parallel or perpendicular to the scanning direction. The inverse pole figure (IPF) color code is based on $LiNbO_3$ space group, with coding along the laser polarization direction; b) Size distribution of single texture regions for LNS34 and LNS13B21 for the Y_y configuration and two different pulse energies (0.75 µJ and
1.25 µJ). Irradiation conditions: λ = 1030 nm, NA = 0.6, f = 200 kHz, focus depth = 240 µm in air, writing speed = 1 µm/s.

Optical Materials EXPRESS

may be due to an asymmetric orientational writing effect as previously observed at low speeds (1 µm/s, similar to this work) in LNS glass [15].
Finally, to validate the presence of the $LiNbO_3$ crystals and to study their orientation inside the laser track cross sections, electron backscattered diffraction (EBSD) analysis was performed on LNS34 and LNS13B21 samples [16,17]. The results are presented in Fig. 3(a).
We first observed that $LiNbO_3$ nanocrystals were effectively precipitated. Secondly, from the inverse pole figure (IPF) color code, the crystal c axis (along the 0001 direction) is found to be oriented perpendicular to the laser polarization (absence of red color on the EBSD map).
This is obviously the case at the lowest pulse energy, whereas at higher energies crystal c axis orientation is observed to vary and be only partially oriented along the polarization direction. Note that these observations are in agreement with the SHG experiments: at low pulse energies the crystals are well oriented with their c axis perpendicular to the writing laser polarization and corresponding to a maximum SHG contrast with a nearly single texturation. However, at higher pulse energies, a part of the nanocrystals population exhibit c axis orientation along the polarization leading to a more spatially distributed (hence isotropic) SHG response.
From the EBSD data (Fig. 3(a)) we could distribution of single texture regions of nanocrystals (assuming they are spherical) within the investigated laser track area. In Fig. 3(b), we report this distribution for LNS34 and LNS13B21 for the Y_y configuration and two different pulse energies (0.75 µJ and 1.25 µJ). At the highest pulse energy (1.25 µJ in this comparison) we observe the tendency to form larger regions with same textures compared to the low energy conditions (0.75
µJ, 20 nm – 300 nm diameter range).

4. Conclusion

In this work, we demonstrated that tunability of SHG in lithium niobate silicate glass can be extended to the borosilicate glass family, through an adequate control of the laser parameters. More specifically, the substitution of SiO_2 with B_2O_3 is found to be advantageous as it promotes faster crystallization of $LiNbO_3$ crystals while preserving the tunability of SHG. The latter is related to the larger SHG response along the c axis of the crystals, which is preferentially aligned perpendicular to the laser polarization at low pulse energy. Currently, the $LiNbO_3$ orientation is understood as being due to alignment of the larger linear susceptibility matrix element (to c axis) with the electric field [18]. We also observe that LNS13B21 glass exhibits a shorter incubation time and thus likely a faster crystal growth with respect to LNS34 that may explain the larger crystals at 1.25 µJ, and more experiments are ongoing to confirm this hypothesis. Several key properties of the written structures related to photonic devices fabrication will be investigated in the future, including refractive index changes and birefringence response.

Funding. Compagnia di San Paolo (Joint Research Program); Agence Nationale de la Recherche (CHARMMMAT ANR-11-LABX-0039).

Acknowledgments. This work was supported by the French National Research Agency under the program CHARMMMAT ANR-11-LABX-0039-grant. Elisa Muzi and Davide Janner also acknowledge financial support from Compagnia di S. Paolo through the Joint Research Program.

Disclosures. The authors declare no conflicts of interest.

References

1. R. R. Gattass and E. Mazur, "Femtosecond laser micromachining in transparent materials," Nat. Photonics **2**(4), 219–225 (2008).
2. J. Habel, T. Boilard, J. S. Freniere, F. Trepanier, and M. Bernier, "Femtosecond FBG written through the coating for sensing applications," Sensors **17**(11), 2519 (2017).
3. T. T. Fernandez, M. Sakakura, S. M. Eaton, B. Sotillo, J. Siegel, J. Solis, Y. Shimotsuma, and K. Miura, "Bespoke photonic devices using ultrafast laser driven ion migration in glasses," Prog. Mater. Sci. **94**, 68–113 (2018).
4. T. Komatsu and T. Honma, "Laser patterning and growth mechanism of orientation designed crystals in oxide glasses: A review," J. Solid State Chem. **275**, 210–222 (2019).

Optical Materials EXPRESS

5. K. Miura, J. Qiu, T. Mitsuyu, and K. Hirao, "Space-selective growth of frequency-conversion crystals in glasses with ultrashort infrared laser pulses," Opt. Lett. **25**(6), 408–410 (2000).
6. B. Zhu, Y. Dai, H. Ma, S. Zhang, G. Lin, and J. Qiu, "Femtosecond laser induced space-selective precipitation of nonlinear optical crystals in rare-earth-doped glasses," Opt. Express **15**(10), 6069–6074 (2007).
7. J. Cao, M. Lancry, F. Brisset, L. Mazerolles, R. Saint-Martin, and B. Poumellec, "Femtosecond laser-induced crystallization in glasses: growth dynamics for orientable nanostructure and nanocrystallization," Cryst. Growth Des. **19**(4), 2189–2205 (2019).
8. M. J. Weber, ed., *CRC Handbook of Laser Science and Technology* (CRC Press, 1986), Vol. Optical materials, Part 1: Nonlinear Optical Properties/Radiation damage.
9. R. S. Klein, G. E. Kugel, A. Maillard, and K. Polgar, "Considerations of angular acceptance and non- linear optical coefficient measurements by second harmonic generation in $LiNbO_3$ crystals," Ferroelectrics **296**(1), 57–66 (2003).
10. J. Cao, L. Mazerolles, M. Lancry, F. Brisset, and B. Poumellec, "Modifications in lithium niobium silicate glass by femtosecond laser direct writing: morphology, crystallization, and nanostructure," J. Opt. Soc. Am. B **34**(1), 160–168 (2017).
11. M. P. Fernandes Graca and M. Almeida, "Glass ceramics with para, anti or ferroelectric active phases", in *Advances in Ceramics - Electric and Magnetic Ceramics, Bioceramics, Ceramics and Environment* (IntechOpen, 2011).
12. A. Faeghi-Nia, V. K. Marghussian, and E. Taheri-Nassaj, "Effect of B_2O_3 on crystallization behavior and microstructure of $MgO–SiO_2–Al_2O_3–K_2O–F$ glass–ceramics," Ceram. Int. **33**(5), 773–778 (2007).
13. G. Ferlat, A. P. Seitsonen, M. Lazzeri, and F. Mauri, "Hidden polymorphs drive vitrification in B_2O_3," Nat. Mater. **11**(11), 925–929 (2012).
14. W. Vogel, *Glass Chemistry* (Springer-Verlag, 1994).
15. J. Cao, B. Poumellec, F. Brisset, A. L. Helbert, and M. Lancry, "Angular dependence of the second harmonic generation induced by femtosecond laser irradiation in silica-based glasses: variation with writing speed and pulse energy," World J. Nano Sci. Eng. **05**(03), 96–106 (2015).
16. B. Poumellec, M. Lancry, C. Fan, A. Erraji-Chahid, and P. Kazansky, "Asymmetric orientational femtosecond laser writing detected in several properties in various glasses," Advances in Optical Materials, OSA Technical Digest (CD) (Optical Society of America, 2011), paper AIFB2.
17. K. Veenhuizen, D. N. Sean McAnany, B. Aitken, V. Dierolf, and H. Jain, "Fabrication of graded index single crystal in glass," Sci. Rep. **7**(1), 44327 (2017).
18. J. Cao, B. Poumellec, F. Brisset, A.-L. Helbert, and M. Lancry, "Tunable angular-dependent second- harmonic generation in glass by controlling femtosecond laser polarization," J. Opt. Soc. Am. B **33**(4), 741–747 (2016).

crystals

MDPI

Article

Towards a Rationalization of Ultrafast Laser-Induced Crystallization in Lithium Niobium Borosilicate Glasses: The Key Role of the Scanning Speed

Elisa Muzi [1,2], Maxime Cavillon [1,*], Matthieu Lancry [1], François Brisset [1], Ruyue Que [1], Diego Pugliese [2], Davide Janner [2] and Bertrand Poumellec [1]

[1] Institut de Chimie Moléculaire et des Matériaux d'Orsay (ICMMO), Université Paris-Saclay, CNRS, 91405 Orsay, France; elisa.muzi@universite-paris-saclay.fr (E.M.); matthieu.lancry@universite-paris-saclay.fr (M.L.); francois.brisset@universite-paris-saclay.fr (F.B.); ruyue.que@universite-paris-saclay.fr (R.Q.); bertrand.poumellec@universite-paris-saclay.fr (B.P.)

[2] Department of Applied Science and Technology (DISAT) and RU INSTM, Politecnico di Torino, 10129 Torino, Italy; diego.pugliese@polito.it (D.P.); davide.janner@polito.it (D.J.)

* Correspondence: maxime.cavillon@universite-paris-saclay.fr

Abstract: Femtosecond (fs)-laser direct writing is a powerful technique to enable a large variety of integrated photonic functions in glass materials. One possible way to achieve functionalization is through highly localized and controlled crystallization inside the glass volume, for example by precipitating nanocrystals with second-order susceptibility (frequency converters, optical modulators), and/or with larger refractive indices with respect to their glass matrices (graded index or diffractive lenses, waveguides, gratings). In this paper, this is achieved through fs-laser-induced crystallization of $LiNbO_3$ nonlinear crystals inside two different glass matrices: a silicate (mol%: $33Li_2O$-$33Nb_2O_5$-$34SiO_2$, labeled as LNS) and a borosilicate (mol%: $33Li_2O$-$33Nb_2O_5$-$13SiO_2$-$21B_2O_3$, labeled as LNSB). More specifically, we investigate the effect of laser scanning speed on the crystallization kinetics, as it is a valuable parameter for glass laser processing. The impact of scanning energy and speed on the fabrication of oriented nanocrystals and nanogratings during fs-laser irradiation is studied. Fs-laser direct writing of crystallized lines in both LNS and LNSB glass is investigated using both optical and electron microscopy techniques. Among the main findings to highlight, we observed the possibility to maintain crystallization during scanning at speeds ~5 times higher in LNSB relative to LNS (up to ~600 µm/s in our experimental conditions). We found a speed regime where lines exhibited a large polarization-controlled retardance response (up to 200 nm in LNSB), which is attributed to the texturation of the crystal/glass phase separation with a low scattering level. These characteristics are regarded as assets for future elaboration methods and designs of photonic devices involving crystallization. Finally, by using temperature and irradiation time variations along the main laser parameters (pulse energy, pulse repetition rate, scanning speed), we propose an explanation on the origin of (1) crystallization limitation upon scanning speed, (2) laser track width variation with respect to scanning speed, and (3) narrowing of the nanogratings volume but not the heat-affected volume.

Keywords: femtosecond laser; crystallization; silicate glasses

Citation: Muzi, E.; Cavillon, M.; Lancry, M.; Brisset, F.; Que, R.; Pugliese, D.; Janner, D.; Poumellec, B. Towards a Rationalization of Ultrafast Laser-Induced Crystallization in Lithium Niobium Borosilicate Glasses: The Key Role of the Scanning Speed. *Crystals* **2021**, *11*, 290. https://doi.org/10.3390/cryst11030290

Academic Editor: Alessandro Chiasera

Received: 24 February 2021
Accepted: 10 March 2021
Published: 15 March 2021

1. Introduction

As the world is progressively evolving towards a photonic future, there is a need for miniaturization and functionalization of photonic devices (including photonic chips, wavelength converters, lenses, retardation waveplates, waveguides, etc.) [1]. In this context, femtosecond (fs)-laser irradiation in glass materials is an attractive way to functionalization [2,3]. By using temporal ultra-short laser pulses (e.g., 10–1000 fs) with very high intensities (up to 10–100 TW/cm^2), highly selective local modifications (few μm^3 in volume) can be achieved thanks to multiphotonic absorption of the laser light.

Different kinds of materials modifications can be obtained, depending on the glass material considered, as well as laser parameters (e.g., pulse energy, repetition rate, and scanning speed). For instance, in silica glass, both positive and negative index contrasts can be achieved [4,5]. The glass response to fs-laser is manifold, and includes, for instance, formation of defects, densification, fictive temperature changes, stress fields, crystallization, and so forth. The latter (crystallization) is a promising pathway in the functionalization of optical devices. The precipitation in glasses of several crystals has drawn interest for their nonlinear, or electro-optic properties, among which we can cite Fresnoite (barium or strontium-based [6]), barium borate (BaB_2O_4) [7], $LaBGeO_5$ [8,9], or again Lithium niobate ($LiNbO_3$) [10], but many others exist (see, for instance, [11] for an extended and thorough review).

Given the plethora of crystals that can be induced from glasses, it is therefore important to comprehend the mechanisms that may lead to property tunability. In this work, we investigate the role played by scanning speed (v) vs. the energy during the crystallization process, and specifically draw our attention to nano-crystallization orientation and self-organized phase separation (so called nanogratings). From an application standpoint, the goal is to provide means to target future glass fabrication in order to maximize scanning speed and property response (e.g., second harmonic generation i.e., SHG, birefringence), while keeping scattering losses as low as possible. From a fundamental perspective, this work aims to better understand the mechanisms that drive light-matter structuring in these glasses. More specifically, we intend to highlight links between scanning speed and the resulting structuring (crystallization, its size and orientation distribution, and nanograting formation). To conduct this study, two glasses were fabricated with the melt-quenching technique, with the following batch composition (mol%): $33Li_2O$-$33Nb_2O_5$-$34SiO_2$ (labeled as LNS), and $33Li_2O$-$33Nb_2O_5$-$13SiO_2$-$21B_2O_3$ (labeled as LNSB). The addition of B_2O_3 is known to lower the crystallization temperature and increase the crystallization rate. Subsequently, each glass sample was irradiated by fs-laser while laser parameters are varied (scanning speed, pulse energy, and laser polarization).

In the subsequent Introduction Sections 1.1–1.4, we provide a brief discussion on several important points that will give the reader context in order to better comprehend the Results and Discussion Sections. First, we discuss background information on oriented crystallization in lithium niobium silicate glasses. Secondly, we consider the role played by the incubation time and its impact on the time-temperature-transformation (TTT) crystallization diagram in LNS glass. Then, the temperature profile evolution (in space and time) after laser irradiation inside the glass is addressed, as well as the impact of pulse temporal overlapping. Finally, we highlight the choice of laser parameters, using a pulse energy-repetition rate landscape, which are prerequisites to induce oriented nano-crystallization.

1.1. Oriented-Crystallization of $LiNbO_3$ Induced by Fs-Laser in Lithium Niobium Borosilicate Systems

In a series of papers [10,12–16], our group has extensively investigated fs-laser-induced crystallization in lithium niobium silicate (generically labeled as LNS) glass, and more specifically the material response upon laser parameter changes including pulse energy (E_p), pulse repetition rate (f), and laser polarization direction (with respect to the scanning direction). Among these studies, it was pointed out that precipitated nanocrystals inside LNS could be oriented in space through a control of laser polarization. At low pulse energies (typ. ~0.5 µJ/pulse as per this paper), a maximum SHG optical response was observed perpendicularly to the writing laser polarization direction, no matter its orientation. This SHG response was attributed to the crystallization of $LiNbO_3$ nanocrystals, the latter having their polar axes perpendicular to the laser polarization. This texturing of $LiNbO_3$ nanocrystals was later confirmed by electron backscatter diffraction (EBSD). At slightly higher pulse energies (typ. ~1.25 µJ/pulse as per this paper), a second texture appeared, indicating that $LiNbO_3$ polar axis was partly oriented in the direction of laser polarization in these conditions. The existence domain of this texture still must be confirmed. These

results are in agreement with previous results [17]. Very recently ([18]), we reported that B_2O_3 incorporation into LNS glass preserved the dynamical modifications yielding to SHG response, while keeping its polarization-dependence. This added an important parameter, namely the laser polarization, to the engineer's toolbox for optical device elaboration and tuning.

1.2. Incubation Time and Temperature-Time-Transformation (TTT) Curve in Static Mode

In the same previous work [18] as described above, we observed that the addition of B_2O_3 drastically reduced the incubation time with respect to B_2O_3-free (i.e., LNS) glass. The incubation time is the time taken, upon fs-laser irradiation, until the observation of the SHG signal. The variation of the incubation time with respect to the average laser power and upon the addition of B_2O_3 to the glass produces a displacement of the time-temperature-transformation (TTT) curve. Using results from [18], the incubation time is represented in Figure 1a, while the TTT curve for LNS is reported in Figure 1b.

Now, to further pinpoint the decrease in the incubation time when adding B_2O_3 into LNS glass, and to make the link with the TTT diagram, we must consider the temperature distribution upon (pulsed) laser irradiation. For a single pulse with a given pulse energy (E_p), the associated thermal deposition (transfer to the lattice vibrations) leads to a temperature distribution profile T(r, t). The latter is as wide as the beam waist diameter immediately after the pulse is deposited, which corresponds to the period start as defined by t_1 in Figure 1c. Following this initial step, the T profile broadens very rapidly due to heat diffusion following a bell shape, and consequently, the maximum temperature (at the center) conversely decreases since the amount of heat given to the system is constant. Finally, at the end of a period, T slowly reaches a minimum value, T_{min}, towards the end of the period. This temperature profile evolution is illustrated in Figure 1c.

Now in the multipulses regime, at radius r including the center, the temperature T(r, t) oscillates between T_{max} (r, N) and T_{min} (r, N) [19]. N corresponds to the number of pulses deposited before the time t, and τ_p is the period of the pulses. When T(r, t) is computed within one time period, it is clear that close to the center ($r < 3w_0$, w_0 being the width of the beam at $1/e$) and for weak time overlapping pulses ($\tau_p >> \tau_D$, the heat diffusion time) there is no crystallization:

(1) neither at the beginning of the period, T is too high (several thousand degrees) during a short time
(2) nor at the end of the period, T is too low during a long part of the period (specifically when the pulse time overlapping is small).

So, the "active part" of the period is between T_{max} and T_{min}. Consequently, our reasoning is based on the averaged power delivered within a pulse time period. The average temperature $\overline{T}$ (the mathematical expression can be found in Appendix A Equations (A2) and (A3)) appears to be a function of the averaged power $\overline{P} = E_p \cdot f$ and of the number of pulses N. Note that $\overline{T}$ is constant within each period.

For a given $\overline{P}$, the $\overline{T}$ distribution is thus a bell shape curve around the beam axis that does not oscillate anymore but slowly evolves with respect to time i.e., N. Now looking at the TTT diagram in Figure 1b, several scenarios can be envisioned. First, if maximum $\overline{T}$ is just above the crystallization onset temperature, T_x, and if the irradiation time is at least equal to the incubation time, crystallization will occur. Now, if the maximum $\overline{T}$ increases slightly (though an increase of $\overline{P}$) approaching to T_p (crystallization temperature peak), a larger area will be above T_x and crystallize. Finally, if $\overline{T}_{max} > T_p$, there will be a radius $r > 0$ where $T = T_p$ that will crystallize first rather than the center of the bell. The apparent incubation time measured with the laser is thus a uniform decreasing function on $\overline{T}$ and so on $\overline{P}$ (see Section 4.3) as in Figure 1a.

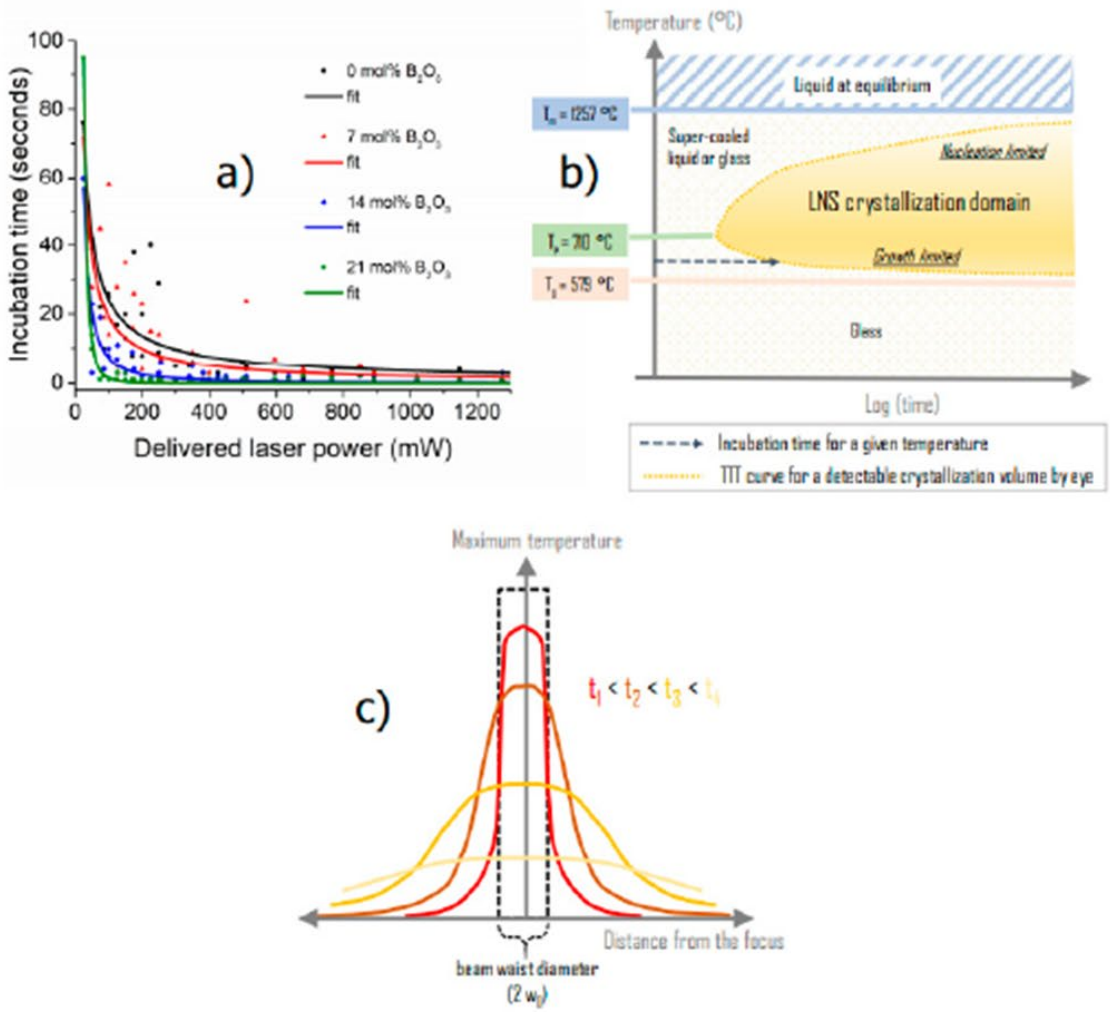

Figure 1. (**a**) Evolution of the incubation time as a function of LNSB glass composition. The results are recalled from [18]. (**b**) Representation of the crystallization domain for LNS glass in TTT (time-temperature-transformation) scheme; T_p: crystallization peak temperature, T_g: glass transition temperature. (**c**) Scheme of the temperature spatial distribution T(r, t) evolution after pulse deposition inside the glass, and as time evolves. We note that as the maximum temperature decreases with time, the width of the distribution increases (the heat energy in the system remains constant). As a side note, the beam waist radius w_0 is typ. around 1 to 1.5 µm.

1.3. Heat Accumulation (Multi-Pulse Irradiation) Considerations and Impact on Crystallization

Within heat accumulation regime, the spatial temperature profile evolution (Figure 1c) described above for a single pulse is expected to be modified by subsequent pulses while the contributions from the former ones are not vanished yet. This will influence the temperature distribution in space. The time needed to reach a steady state of overlapping pulses (in time) can be associated with a minimal number of pulses, labeled as $N_{ssm}(r)$ in Appendix A (Equation (A5)). In this case, a memory effect is at play from one pulse to the other. It seems that growth of nanocrystals and nanogratings is of such category. This may also explain that the incubation time is dependent on the average power and not only on pulse energy. Several key features can be extracted from modeling heat deposition and

temperature profile in multi-pulse regime (see Appendix A for more details regarding the hypotheses and the calculations used):

(1) *when there is no pulse overlap in time*; typ. when the pulse period (τ_P) is greater than a few hundreds of the diffusion time ($\tau_D \sim w_0^2/4D_T$, w_0 is the beam waist radius at 1/e and D_T is the thermal diffusivity):
   - E_p (and more specifically the absorbed part of E_p) sets the temperature amplitude (T_0 in Appendix A, $T_0 = 3 \cdot A \cdot E_p/(4 \cdot \pi \cdot \rho \cdot C_p \cdot w_0^3)$) and this is not dependent on the thermal conductivity. On the contrary, the shape of T(r, t) is from the solution of the Fourier's equation with one pulse and is defined by w, f and the thermal diffusivity D_T.
   - Note that f/v controls the density of pulses per µm (P_D) or the pulse overlap in space. P_D is ranging from <2000 to 200,000 pulses/µm in this present work. Moreover, the number of pulses deposited punctually is given by $2w_0P_D$ (w_0 is the beam radius).

(2) *when there is an important overlap between pulses in time (typ. $\tau_P < \tau_D/10$)*:
   - The average power $\overline{P} = E_p \cdot f$ controls the temperature amplitude that is now dependent on the thermal conductivity κ, i.e., $\frac{A \cdot E_p \cdot f \cdot \alpha}{2\pi\kappa}$ with α being the absorption coefficient. The profile in space and time is close to the solution of the Fourier's equation with a continuous wave (CW) laser source [20] and the width of the distribution is simply dependent on α.
   - Note that as in the previous situation, f/v controls the density of the pulses per µm (or their overlap in space) ≡ duration of irradiation per point ($=\tau_P \cdot 2w_0 \cdot f/v$).

(3) *when the pulse overlap is intermediate (typ. $\tau_P - \tau_D$)*: An average approximation may be considered for the temperature.
   - Case n°1: $\overline{T}(r, N) = \int_{\text{period N}} \frac{T(r,t)}{\tau_p} dt$: this corresponds to an average temperature during the total pulse period, numbered N.
   - Case n°2: we can say that below a given temperature (T_{min}), no effect happens (e.g., below T_g for a crystallization, but another T_{min} can be used for another process depending on the kinetics involved). No effect occurs also above a given T_{max} (e.g., T_m or liquidus temperature in the case of crystallization). Consequently, the average temperature is bound as in the next expression $\overline{T}(r, N) = \frac{1}{(t_2 - t_1)} \int_{t_1(r,N)}^{t_2(r,N)} T(r, t) dt$ where $t_1(N) = \inf(T_{max}(r, N), T_m)$ and $t_2(N) = \sup(T_g, T_{min}(r, N))$. It is worth pointing out that for this suggestion, $t_2(r, N) - t_1(r, N) < \tau_p$. Note: sup(.,.) and inf(.,.) mean the largest and the smallest values of the quantities in the brackets.

Therefore, the important parameter to consider is the pulse overlapping in time. It is ruled by the ratio $R_t = t_p/t_D$. For the glasses to be considered in this study, $R_t = 18$ as $D_T = 9 \cdot \times 10^{-7}$ m²/s either for LNS or LNSB glasses. The number of overlapping pulses is around 10^{-15} (see Appendix A Equation (A5)). This means that pulses deposited between 10 and 15 time periods before the last pulse have a negligible contribution to the pulse's summation. Note that our experiments herein are rather in the conditions of weakly overlapping pulses. Consequently, from the beginning of irradiation and after 10–15 pulses, a steady state is reached where T oscillations become repetitive. However, in most of the observed phenomena, the relevant quantity is the average temperature $\overline{T}(r, N)$ that becomes time independent after 15 pulses. It is written $\overline{T}(r, \infty)$ in Appendix A Equation (A4) (for instance) and its time-independent shape is thus very convenient to discuss the effect of thermal treatment in scanning mode with a laser.

In this work, we will mostly focus on the effect played by the scanning speed. As shown above, the latter plays a different role than the pulse energy (E_p). It must be pointed out that the heat diffusion speed ($\sim 4D_T/w_0$, i.e., a few 10 m/s in our experimental conditions) is much larger than the scanning speed (typ. <1 mm/s). Consequently, the scanning speed is expected to have a negligible effect on the temperature distribution profile.

1.4. Phase Separation Induced by Fs-Laser in Lithium Niobium Silicate Glass and Choice of Laser Parameters in This Study

In addition to precipitate oriented nano-crystals in LNS glass, it is possible to induce laser polarization-oriented phase separation upon laser irradiation under the form of lamellar-like structures perpendicular to the laser polarization [13]. These lamellas are quasi-periodic and form an array of crystalline phase ($LiNbO_3$-rich) and glass phase (SiO_2-rich) at the sub-wavelength scale [13]. A direct consequence of this re-organization is the appearance of measurable form birefringence, which can be characterized under an optical microscope with polarized light through optical retardance measurements [13,21].

To study the effect of scanning speed on this phase separation, we first need to find the adequate laser conditions to fall within the domain of orientable nanocrystals. In a previous publication on LNS glass with a close composition to the LNS glass used herein, three laser-induced modification regimes were stated [14] as highlighted in Figure 2a using a Ep–f landscape. There is a first regime at low pulse energies where the material remains in a vitreous state. In this regime, both the refractive index and the etching rate are modified (isotropically), which is associated with a change of fictive temperature (a parameter characterizing the degree of disorder in glass). A second regime appears at higher pulse energies (in fact above an averaged incident laser power of 0.16 W), where nano-crystallization is observed, and that is textured such that the polar axis of the nanocrystals is perpendicular to the writing laser polarization. Then, increasing the pulse energy, a third regime appears (above an average incident power around 0.32 W) where larger crystallized zones with the same orientation appear. In this case, a part of the heat-affected volume (HAV) is melted and crystallizes driven by the peripheral part of the HAV that has not melted. In our conditions and as will be detailed in the Materials and Methods Section, we used two pulse energies: 0.5 and 1.0 µJ/ pulse (at f = 200 kHz), which correspond to 0.1 and 0.2 W, respectively. For completeness, based on previous experiments carried out in the samples investigated herein [18], we could identify the thresholds (T1, T2, T3) for the 3 regimes. Therefore, in Figure 2b we place the thresholds on a similar E_p–f landscape found for LNS. It is worth pointing out that the LNSB glass would exhibit slightly lower threshold values. With the experimental conditions considered in this paper, we are in the regime of oriented nano-crystals formation.

Finally, in [12], the effect of the scanning speed in regime 2 has not been investigated deeply but pointed nevertheless an effect. At an energy of 1.4 µJ, the orientable possibility was seen for 25 µm/s with the polar axis perpendicular to the laser polarization; but for 10 µm/s there was another texture with the polar axis parallel to the laser polarization [17]. On the other hand, at high pulse energies (4.2 µJ), the authors from [22] obtained a perfect single texture (a third one with the polar axis aligned along the direction of scanning) in the whole heat-affected volume (HAV) for speeds lower than about 25 µm/s. However, at this pulse energy, the laser track width is a bit large for a single-mode waveguide (25 µm). Nevertheless, these works showed that controlling the scanning speed may enable the control of nano-/micro-crystallization of the laser track.

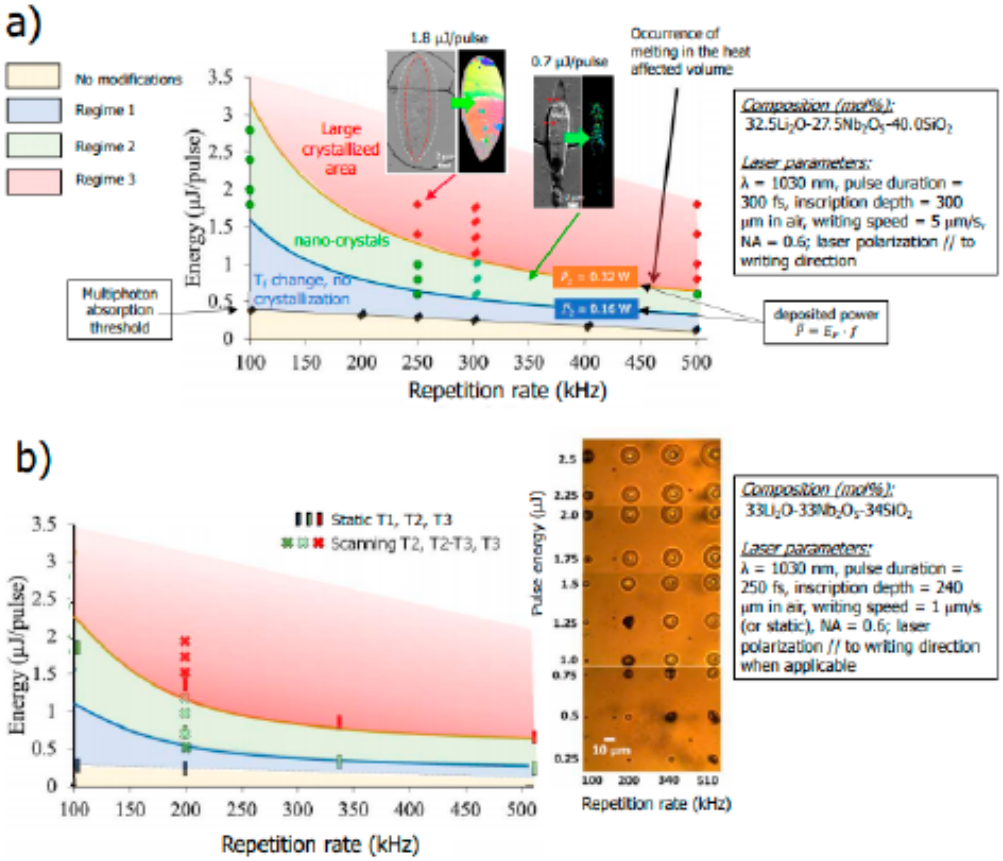

Figure 2. (**a**) The three regimes of laser induced modifications in the pulse energy—repetition rate plane (E_p–f). The scheme on the left is for a LNS glass with a close composition than the one used in this paper ([12]). (**b**) Regimes established from results obtained with the glass composition and pulse duration used in the present paper. We note that the energy thresholds are a bit lower for the LNSB glass. N.B., the mention "static" means no beam scanning (dot production, the relevant parameter is the duration of irradiation) contrarily to "scanning" (the relevant parameter is the scanning speed).

2. Materials and Methods

The two glasses investigated in this work were fabricated using the conventional melt-quenching technique. These glasses are the same as the ones used in Ref. [18]. The targeted compound concentration (in mol%) of each glass is: $33Li_2O$-$33Nb_2O_5$-$34SiO_2$ (labeled as LNS) and $33Li_2O$-$33Nb_2O_5$-$13SiO_2$-$21B_2O_3$ (labeled as LNSB). Briefly, powders of Li_2O_3, SiO_2, and Nb_2O_5 (and H_3BO_3 for LNSB glass) were crushed together in acetone to homogenize the powder mixture. Subsequently, each powder batch was placed inside a platinum crucible and dried at 200 °C for ~2 h. Following this, the temperature was increased up to 1400 °C (LNS) and 1350 °C (LNSB) and set at these temperatures for 1.5 h. Then, the molten mixture was quenched between two metal plates preheated at around ~350 °C and maintained at this temperature for about 30 min. The quenched glass formed a plate about 1-mm thick. Finally, few pieces of each glass sample were polished on top and bottom surfaces until optical roughness was reached. Each glass sample was thus placed on a motorized translation stage and subsequently irradiated using a femtosecond laser (Satsuma, Amplitude Systèmes Ltd. Pessac, France, λ = 1030 nm, pulse duration = 250 fs, numerical aperture (NA) = 0.6). Each irradiation was performed with the laser focal point

situated approximately 240 µm (in air) below the sample top surface. The translation stage enables a displacement in the XY plane, while the laser beam direction is along the Z direction. The experimental setup is displayed in Figure 3. Here, the reference in the direction of writing laser polarization is given by +X in the XY plane (illustrated by e in Figure 3); the scanning direction is identified as S in the same figure.

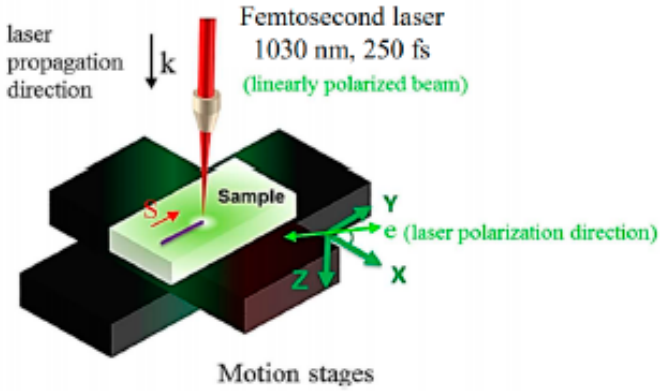

Figure 3. Experimental laser setup, and convention for the reference on the sample and its relation to the reference on the laser. S and e correspond to the scanning direction and the polarization direction, respectively. Note: in this work, Yy configuration corresponds to e parallel to S (e is along Y), and Yx configuration to e perpendicular to S (e is along X).

Lines were written in the plane perpendicular to the laser propagation direction (i.e., the XY plane) at various scanning speeds (from 5 to 600 µm/s). A half-wave plate placed along the beam path controlled the linear polarization. 5 mm-long lines (at f = 200 kHz) were written inside each glass sample (LNS and LNSB), using two laser polarization configurations: parallel (labeled as Yy), and perpendicular (labeled as Yx) to the laser scanning direction (being along the Y axis, or S). Other parameters were varied, including pulse energy (0.5 and 1.0 µJ), and scanning speed. At this point, it is worth to point out that prior to each scanning, the sample was irradiated with a static beam with a time at least equal to the incubation time. The minimum scanning speed was set to 1 µm/s, and the maximum scanning speed was determined once no green light could be detected during the irradiation. This green light is characteristic of SHG induced by $LiNbO_3$, and no light detected was indicative that no more crystallization occurred during the inscription (typically at speeds of few hundreds of µm/s at a pulse energy of 1 µJ).

To investigate the differences of the lines inscribed in both LNS and LNSB and when scanning speed is varied, we used an Olympus BX51 optical microscope (Olympus). A first observation was done under white light to gain general insights on the laser track transparency, homogeneity, and dimensions. A second analysis was performed under polarized light to detect birefringence, characteristic of textured nano-scale phase separation, and neutral axis directions. Using a first-order (full wave) retardation waveplate, the slow and fast axes of the lines (if birefringent) have been determined. Finally, we measured the linear retardance (R) at the center of the irradiated lines, using the De Sénarmont compensator technique. R is proportional to the birefringence (B) through the relation $R = B \times L$, where L is the thickness of the birefringent object.

Finally, to better comprehend the origin of the differences observed in optical microscopy, the laser track cross-sections of the LNSB sample (at different speeds and for 0.5 µJ/pulse) were brought under a field-emission gun scanning electron microscope (Carl Zeiss Microscopy GmbH). (FEG-SEM ZEISS SUPRA 55 VP) equipped with an electron backscatter diffraction (EBSD) detector. The samples were side polished perpendicularly to

the scanning direction and until the laser-cross section was exposed. Crystalline texture, size, and nano-/micro-texturing could be observed.

3. Results

3.1. Effect of Scanning Speed: Optical Microscope Observation under White Light Illumination (Transmission Mode)

In Figure 4a, the optical microscope images of some sections of the inscribed lines (Yx configuration, in transmission mode, top view, and upon white light illumination) for LNS and LNSB samples are displayed. At this point, it is worth pointing out that the black lines (at low speeds, typ. < 25 µm/s) were associated with a bright and well visible green light observation during the laser irradiation and the brown colored lines with less vivid green light intensity (although still visible). Finally, for the nearly transparent lines (at the highest scanning speeds), no green light could be detected during the irradiation. Detection of SHG is a direct indication if $LiNbO_3$ crystals were precipitated during laser scanning. As can be seen from Figure 4, the samples are lightly colored (orange). Absorption spectra were recorded and are presented in Appendix B, Figure A1. They revealed a linear absorption tail starting below 500 nm and a cutoff wavelength in the UV region at around 350 nm for both glasses. However, no absorption band is detected at the laser wavelength that could be a source of strong linear absorption. From Figure 4a, a very different behavior is observed with respect to each glass sample. For LNS at 0.5 µJ/pulse no crystallization could be detected at scanning speeds above ~50 µm/s, and there was a sharp transition between crystallized lines to no crystallization. For LNSB glass, crystallization was detected up to ~225 µm/s for the same pulse energy regime and configuration. Additionally, the transition regime from dark lines to transparent ones was incremental. Comparison made between LNS and LNSB for a higher pulse energy (1.0 µJ) shows no crystallization at scanning speeds beyond ~100 µm/s for LNS glass and beyond ~600 µm/s for LNSB. Moreover, the line width fluctuates in a periodic fashion for LNS whereas it is very weak for LNSB. This is rather similar to what has been reported in [23] using a CW laser 1080 nm, 1.4–1.8 W, NA = 0.8, at the surface.

Finally, the averaged heat-affected volume (HAV) width for each line is reported in Figure 4b, for Yy and Yx configurations. In both LNS and LNSB, increasing the pulse energy causes, on the first order, an increase of the HAV width. For LNSB glass at low pulse energy, the laser track thickness slowly decreases as the scanning speed increases. On the other hand, at 1.0 µJ/pulse, the laser track width increases and reaches a maximum at around 150–250 µm/s, then progressively decreases.

3.2. Birefringence Measurements and Polarization-Dependent Orientation

Based on the previous observation under optical microscopy, we could classify three (3) types of line inscription regimes: one at low speed (lines appear dark, little to no light passing through them), one at medium speed (brownish lines, with light passing through them), and one at high speed (no detectable crystallization, and light fully passing through them). These three-speed regimes are reported in Figure 5a for lines written in LNSB using increasing speeds: 1, 75, and 350 µm/s. To further investigate the differences between these speed regimes, we used different illumination conditions:

(1) transmission with natural light; we see rough modifications
(2) transmission with crossed polarizer (P) and analyzer (A) (polarized light)
(3) same as (2) with a full waveplate inserted with its orientation perpendicular to the scanning direction; see Figure 5a.

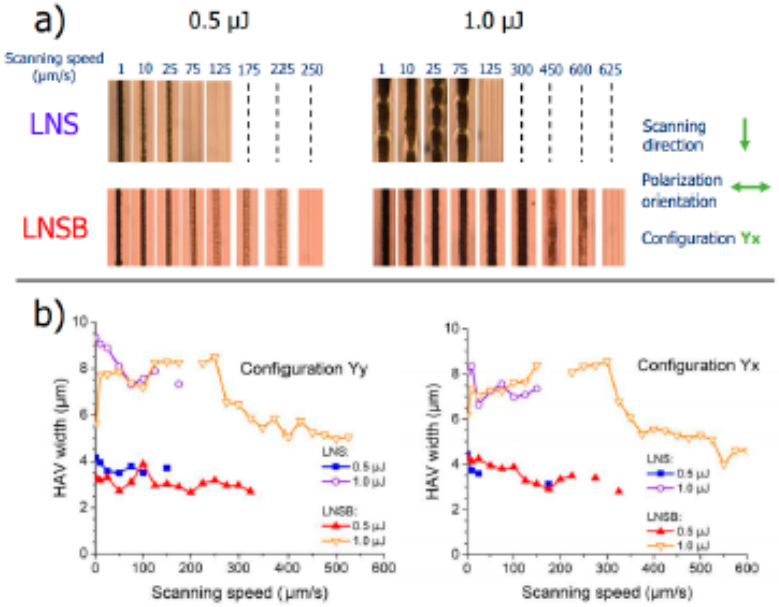

Figure 4. (**a**) Optical microscope images of lines inscribed by fs-laser in silicate (LNS) and borosilicate (LNSB) glasses at various scanning speeds and for two pulse energies: 0.5 and 1.0 µJ (Yx configuration). (**b**) Heat-affected volume (HAV) width as a function of scanning speed, measured from optical microscope images in LNS and LNSB glass samples, for 0.5 and 1.0 µJ, and in both Yy and Yx configuration modes. Other (fixed) parameters are: $\lambda = 1030$ nm; $f = 200$ kHz; NA = 0.6; pulse duration = 250 fs; focal depth: 240 µm (in air).

In (2): the background (glass) whatever the sample orientation appears dark due to glass isotropy. The lines are also dark when they are placed parallel to either P or A. On the contrary, when the lines (low and medium speed regime) were rotated at any other angle than parallel (//) to P or A, light passes through them, with a maximum at an angle of 45° with respect to both A and P axes (with a precision of ±5°). This feature was maximized for the medium speed regime (75 µm/s in Figure 5a) indicating that the orientations of the neutral axes are parallel and perpendicular to the line scanning direction.

In (3): with the insertion of a full retardation waveplate and the neutral axes at 45° from A and P, we distinguish the slow axis from the fast axis. When the slow axis of the line is parallel or perpendicular to the slow axis of the full retardation plate (at 550 nm), it appears blue or yellow, respectively. Here, whatever the investigated configurations, the slow axis of the written line is found perpendicular to the writing laser polarization. This agrees with [21], and is attributed to (i) the formation of quasi-periodic lamellas with two different refractive indices, and (ii) not to the birefringence related to the oriented $LiNbO_3$ nanocrystals contained in one of the lamellas.

Finally, retardance (R) was quantitatively measured at the center of each irradiated line as reported in Figure 5b,c. In LNS glass, the retardance arises from the formation of a sub-wavelength and lamellar-like structure with periodic alternation of $LiNbO_3$-rich regions (crystallized) with $LiNbO_3$-poor (glass rich) ones, leading to form birefringence, hence retardance [21].

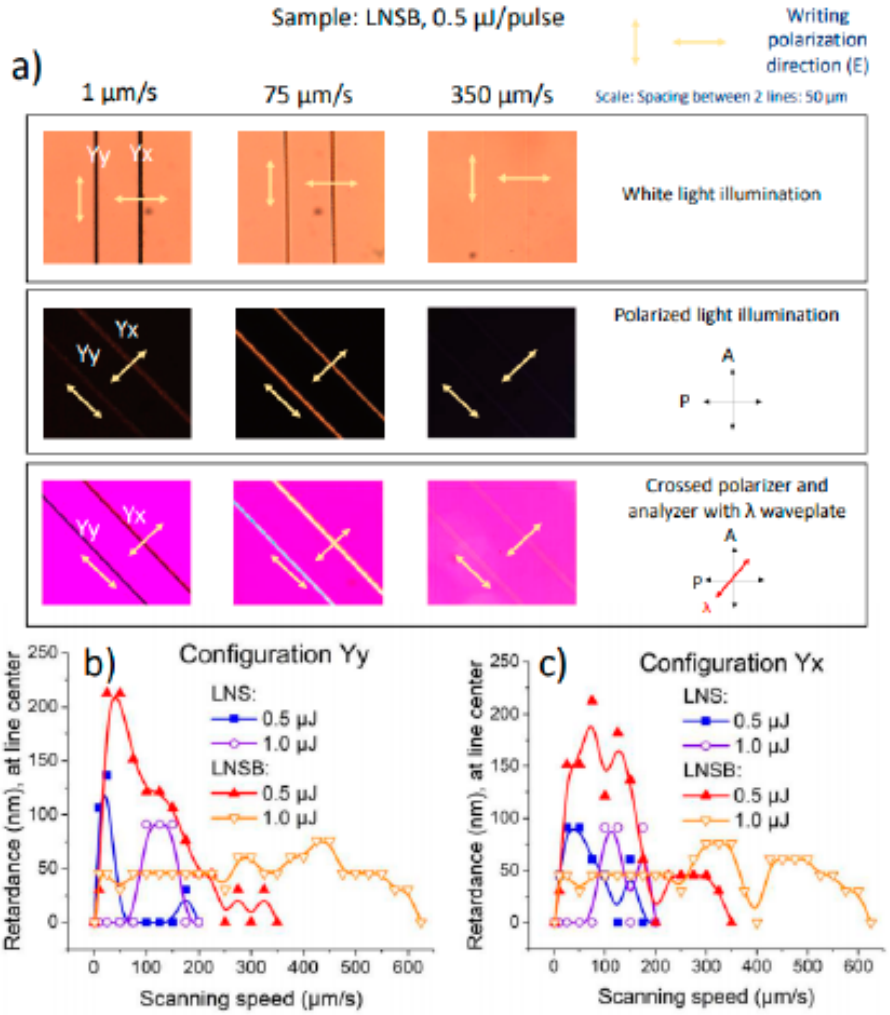

Figure 5. (**a**) Optical microscope images, under different illumination conditions, of lines written at different scanning speeds (1, 75, and 350 μm/s) for LNSB glass sample at a pulse energy of 0.5 μJ. P = polarizer; A = analyzer. Other (fixed) parameters are: λ (fs-laser wavelength) = 1030 nm; f = 200 kHz; NA = 0.6; pulse duration = 250 fs; focal depth: 240 μm (in air). Retardance (in nm) measured for (**b**) Yy and (**c**) Yx configurations at 550 nm at the center of the irradiated lines as a function of scanning speed, for both LNS and LNSB glasses, at pulse energies of 0.5 and 1.0 μJ.

From Figure 5b,c, we observe general trends with respect to the retardance of the lines. At the lowest speed (1 μm/s) the measured retardance is null and this for each glass and at every pulse energy (either 0.5 or 1.0 μJ). Now, in LNSB, as the scanning speed is progressively increased, the retardance also increases, until it reaches a maximum. Lowering the pulse energy (going from 1.0 to 0.5 μJ) results in the enhancement of the retardance. In LNSB, this increase approximately corresponds to a factor of 4 (up to 200 nm). At 0.5 μJ retardance disappears beyond 350 μm/s, whereas for 1.0 μJ it is roughly constant until 600 μm/s. For LNS, the maximum is always roughly 100 nm. However, if retardance increases just from a few μm/s until 50 μm/s at 0.5 μJ, it starts to increase the latter by 1.0 μJ but both exhibit a steep decay at 200 μm/s. Although at higher speeds the lines are not crystallized, at low speeds crystallization occurs. Therefore, the low-speed regime exhibits a birefringent response, but the white light is scattered as it travels through the

cross-section due to the presence of large crystallites along the laser track. Finally, no writing polarization effect is detected on the retardance amplitude, and the maximum retardance response found for LNSB is about twice larger compared to LNS.

3.3. Investigation of Scanning Speed Effect on the Laser Track Morphology in LNSB Glass

To better understand the various trends observed when the scanning speed is varied, we investigated the morphology and nanostructure using scanning electron microscope imaging and electron backscatter diffraction (EBSD). In Figure 6a, we report the laser track cross-section (for 0.5 µJ/pulse, Yy configuration) SEM micrographs and EBSD diffraction pattern images taken in LNSB sample, at three different speeds: 1, 10, and 75 µm/s. As one can rotate the lamellas by rotating the laser polarization, the choice of Yy configuration was decided for investigating the crystallization in the plane of the lamellas (see for instance [14]). We first confirm the presence of $LiNbO_3$ nanocrystals, and no other crystalline phase was detected, i.e., all Kossel's figures were indexed. Secondly, we observe that the crystallization is rather homogeneously distributed. As it has been seen before in a similar analysis performed on SiO_2 [24], there are some regions that are not phase separated. We can suppose that this is the case at the center of the laser track, especially for 25 and 50 µm/s. However, we cannot completely rule out the possibility to partially investigate some areas that are between two crystalline zones, hence they would appear amorphous. We observe a concentration of nanocrystals at the laser track center in the head as the speed increases, whereas at a low speed we observe larger regions of similar crystalline orientation, i.e., similar color in the inverse pole figure (IPF). The average size of the regions of the same orientation (single texture) as a function of scanning speed is reported in Figure 6b (in magenta), along with the error bar, which corresponds to the standard deviation (providing information of the size distribution). Additionally, we also report the evolution of the number of regions as a function of scanning speed. This figure emphasizes the observation of larger crystalline domains with the same orientation in the low-speed regime relative to the high-speed one. Interestingly, beyond 25 µm/s, we observe a plateauing in the crystalline size evolution (averaged size centered at 100 nm) with a narrower distribution (small standard deviation). This is also accompanied with a rather constant number of a single texture region: approximately 600 to 800 regions from 10 to 175 µm/s, while this number drops to 300 for the lowest scanning speed (1 µm/s).

Lastly, in Figure 6c, the pole figures of $LiNbO_3$ c axis reveal a dominant texture, where the c axis is found preferentially perpendicular to the laser polarization for all laser tracks. This is consistent with previous works (see for instance [10,18]). However, we observe that, as the scanning speed increases, the preferential orientation of the c axis becomes less contrasted.

In addition, SEM imaging was performed on the laser track cross-section of LNSB sample but this time in the Yx configuration. This allows seeing any lamellar-like nanostructuring as already suspected based on the observation of birefringence. This variety of nanogratings, previously observed in LNS glass ([13]) within the crystallized region, "grow" perpendicularly to the laser polarization. The SEM micrographs reported in Figure 7 show some interesting features worth pointing out. First, the observed crystallized volume becomes smaller as the scanning speed increases (in yellow). Additionally, the length, but not so much the width, of the region where lamella-like structuring is observed, framed by the orange dashed line, progressively decreases as the scanning speed increases. At low speeds (<25 µm/s), there is a complete overlap between the crystallized and lamellas regions, while it is much reduced at higher speeds. Similar observations have been reported in [12]. At low pulse energy (0.5 µJ/pulse), the lamella area also coincides with the crystallized one. But when energy is increased, the lamella area becomes smaller with respect to the crystallized one, i.e., the overlap is reduced. Note that lamellas forming nanogratings are resulting from direct interaction with the laser light whereas crystallization is not.

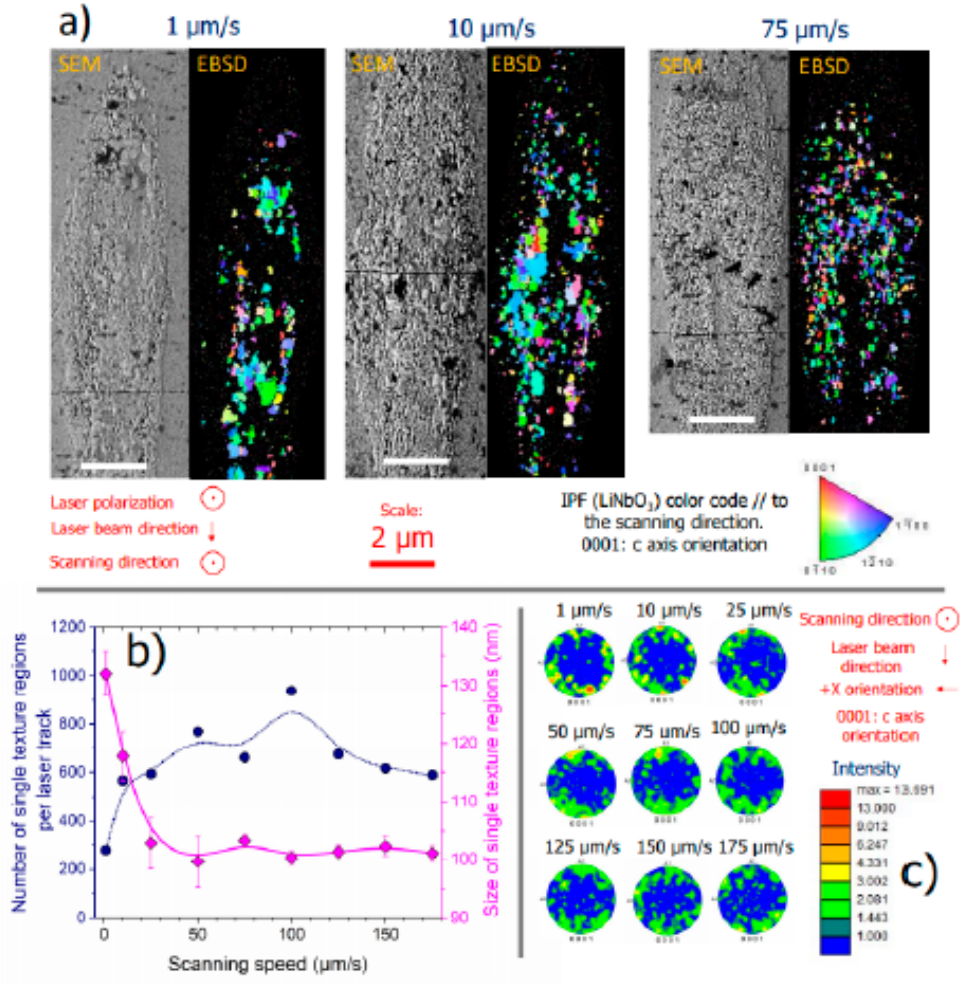

Figure 6. (**a**) Scanning electron microscope (SEM) micrographs and electron backscatter diffraction (EBSD) maps on the laser track cross-sections induced by fs-laser on LNSB glass sample and for different scanning speeds. Other (fixed) parameters are: pulse energy = 0.5 µJ; configuration = Yy (laser polarization // to the scanning direction); λ = 1030 nm; f = 200 kHz; NA = 0.6; pulse duration = 250 fs; focal depth: 240 µm (in air). (**b**) Number of single texture regions and their averaged diameter (assuming a spherical shape) as a function of scanning speeds, extracted from EBSD data, i.e., (**a**). (**c**) Pole figure of the $LiNbO_3$ c axis (labeled as 0001), also extracted from the EBSD data.

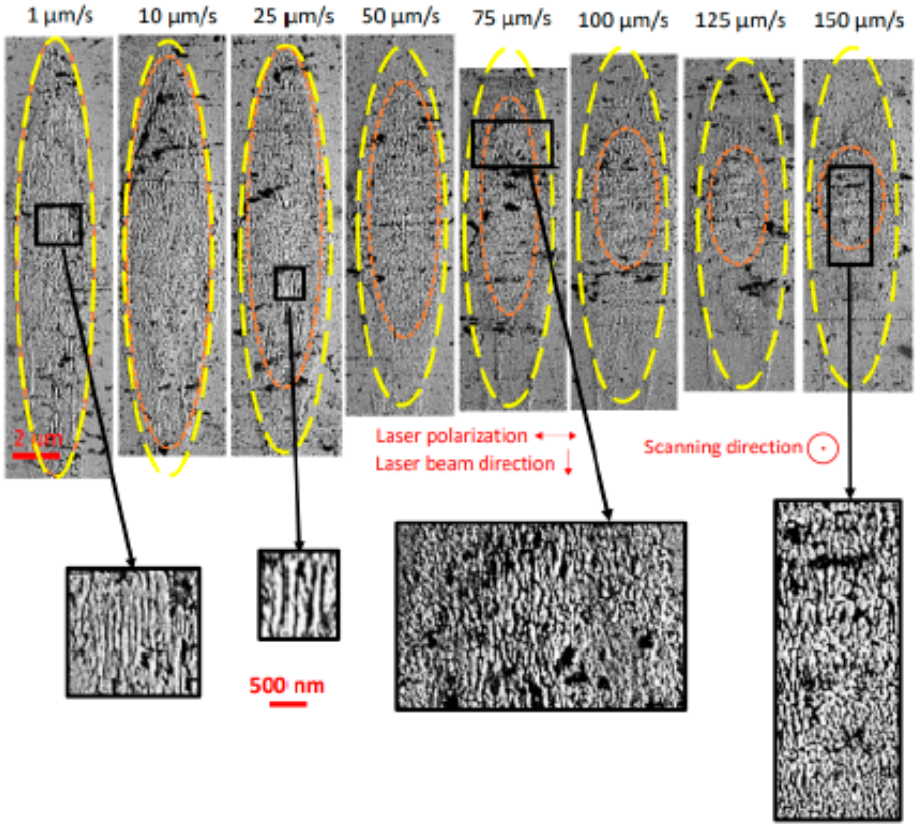

Figure 7. Scanning electron micrographs of the laser track cross-sections induced by fs-laser on LNSB glass sample and for different scanning speeds. The surrounded areas are (i) in yellow: area where crystallization within the laser track, associated with crystallization, is detected; and (ii) in orange: area where lamella-like nanogratings are observed (see for example insets). Other (fixed) parameters are: pulse energy = 0.5 µJ; configuration = Yx (laser polarization ⊥ to the scanning direction); λ = 1030 nm; f = 200 kHz; NA = 0.6; pulse duration = 250 fs; focal depth: 240 µm (in air). N.B. the crystallized volumes (in yellow) are similar to the ones in the Yy configuration (Figure 6).

4. Discussion

4.1. Temperature and Its Distribution Profile during Irradiation in LNS and in LNSB Glasses

The laser energy deposition inside the material is achieved through a nonlinear—multiphotonic—absorption effect. The absorbed energy is then redistributed in the lattice in form of heat, typically in a Gaussian-like shape (in space). After a short stage of non-linearity, the absorbed energy proportion is independent of the pulse energy [25]. One advantage of using a converging beam is that the absorption is triggered in-depth and then controllable.

In pulsed regime, the time for the instantaneous temperature to reach a steady state for our compounds and laser conditions can be shown from the Fourier's equation to be around 270-τ_D (see Appendix A), with $\tau_D = w_0^2/4D_T$, w_0 ~1 µm) and D_T(LNS) = 9 × 10^{-7} m^2/s [21]. This gives $\tau_D \approx 0.28$ µs and thus 76 µs to reach the steady state or 15 pulses in our conditions (200 kHz). This is indicative that we have a weak temporal overlapping between pulses, and that we are close to the so-called "single pulse regime" discussed in the Introduction. Moreover, the thermal diffusivity $D_T = \kappa/\left[\rho C_p\right]$, where κ is the thermal conductivity, ρ the density, and C_p the heat capacity, should not be drastically

different when moving from LNS to LNSB. Indeed, the partial substitution of 21 mol% SiO_2 with B_2O_3 into the glass system is not expected to change the thermal diffusivity by much (see for instance Table 8.20 in Ref. [26]). Additionally, the ρ and C_p values, extracted from Sciglass software, are ρ(LNS, 20 °C) = 3482 kg/m^3, C_p(LNS, 20 °C) = 629.2 J/(kg·K), ρ(LNSB, 20 °C) = 3535 kg/m^3, and C_p(LNSB, 20 °C) = 657.8 J/(kg·K). The ρC_p product differs only by 6% between the two glasses.

Consequently, the spatial temperature distribution profiles, for both LNS and LNSB glasses, are very similar for a given set of conditions. This is in good agreement with our experimental results where the HAV widths appear not to vary much with the chemical composition (Figure 4).

4.2. Nucleation and Growth in LNS and LNSB Glasses: Tendencies and Comparisons

One interesting parameter to investigate differences in crystallization kinetics between the two glasses is the reduced glass transition temperature, T_{gr}, defined as $T_{gr} = T_g(K)/T_L(K)$, where T_g is the glass transition temperature and T_L is the liquidus temperature (or the melting temperature). To get T_g values, we ran differential scanning calorimetry (DSC) scans on the samples (LNS and LNSB), in addition to two other glasses with an incremental amount of B_2O_3. The results are reported in Figure 8. The T_g could not be easily distinguished for LNS glass, and therefore we took the value provided by Sciglass ($T_g \approx 579.1$ °C). On the other hand, we obtained $T_g \approx 520$ °C for LNSB glass with 21 mol% of B_2O_3. For both glasses, we used $T_L = 1257$ °C (corresponding to the melting temperature of $LiNbO_3$ as in [27]); we obtained T_{gr}(LNS) ≈ 0.56 and T_{gr}(LNSB) ≈ 0.52. Additionally, and for completeness, we observe that the progressive addition of B_2O_3 shifts down the crystallization peak to lower temperatures: by about 150 °C between LNS and LNSB with 21 mol% B_2O_3.

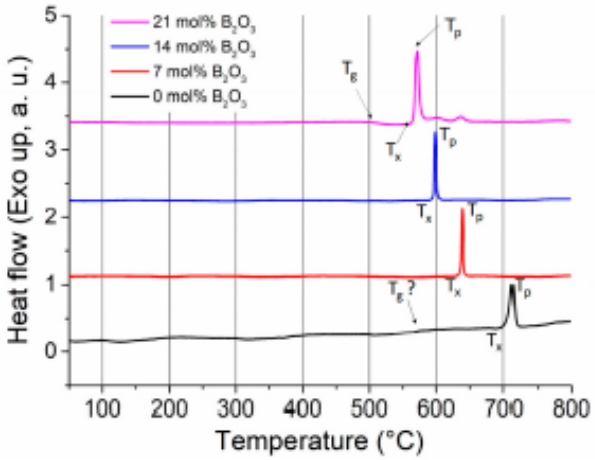

Figure 8. Differential scanning calorimetry (DSC) scans for four glasses with an increasing amount of B_2O_3 in the batch composition; in mol%: $33Li_2O$-$33Nb_2O_5$-(34–x)SiO_2-xB_2O_3, with x = 0, 7, 14, and 21. Heating rate was 10 °C/min. Black curve corresponds to LNS, while the pink curve to LNSB. T_g = glass transition temperature; T_p = crystallization peak temperature; T_x = onset of crystallization temperature.

The T_{gr} values are only indicative and further work (including viscosity measurements) is required to more precisely ascertain these values, such as melting temperatures (which in glass can be defined as the temperature for which the viscosity reaches log (viscosity, Pa·s) = 1). This will be important in the future, since the melting temperature of LNSB glass is lower than LNS, and this would have the tendency to shift the T_{gr} value of LNSB slightly to higher values. Aside from these caveats, the differences of T_{gr} between

the glasses can be, at least quantitatively, compared to the maximum nucleation rate (I_{max}) and time lag of nucleation (incubation time) reported in Figure 4.3 of [28]. Interestingly, these observed differences in T_{gr} can lead up to several orders of magnitude higher I_{max} values for LNSB relative to LNS, while the incubation time is correspondingly two orders of magnitude lower [28,29]. The detection of SHG (through intense green light detection) for LNSB is much faster than for LNS upon laser irradiation (up to 20× faster) [18] and indicates a faster nucleation rate. Additionally, by looking at Figure 2 from [29], the maximum growth rate can be crudely estimated. For LNS, it would be in the 100 µm/s range, while it would be higher for LNSB by an order of magnitude. Once again, these trends agree well with the experimental observations. At a pulse energy of 1.0 µJ, crystallization (through SHG observation) is observed up to 100 µm/s in LNS, while it is detected up to 600 µm/s in LNSB. For completeness, T_{gr} is determined for a glass but excluding migration of chemical species. If the latter occurs (e.g., in $Sr_2TiSi_2O_8$ glasses as in [30] or other silicate glasses [3]), the situation becomes more complex and growth will become composition-dependent and temperature-dependent.

Another interesting point to highlight is that the net crystal growth rate in glass is directly related to the mobility of the atoms, i.e., the diffusion coefficient (Wilson–Frenkel's theory [31]), which, in turn, is proportional to the inverse of the viscosity through the Stoke–Einstein's relation [28]. Moreover, incorporation of B_2O_3 into the silicate glass melt is known to decrease viscosity [26]. Another observation is that the LNSB glass yielded to some occasional surface crystallization upon cooling, whereas it was not observed for LNS glass. These are the first indications of the more pronounced tendency to crystallize for LNSB relative to LNS. Additionally, we can estimate the Hruby Criterion $k_H = (T_x - T_g)/(T_m - T_x)$, which is indicative of the tendency of glass to crystallize (especially upon heating) [32]. In this criterion, T_x stands for the onset crystallization temperature, T_g the glass transition temperature, and T_m the melting temperature (here taken as T_m of $LiNbO_3$). For LNSB, $T_g \approx 520$ °C and $T_x \approx 560$ °C. For LNS, $T_g \approx 579.1$ °C (Sciglass) and $T_x \approx 700$ °C (see for instance Ref. [33]). This yields to $k_H \approx 0.06$ for LNSB and $k_H \approx 0.22$ for LNS. The smaller k_H value for LNSB (≈4 times lower) with respect to LNS indicates its higher tendency to crystallization.

4.3. What Does Limit Crystallization as the Scanning Speed Is Increased?

To answer this question, let us first briefly recall what has been learned from the Introduction:

- The incubation time t_i at a given temperature is the time for the glass to produce a volumetric number of nanocrystals that gives rise to detectable SHG intensity. This time provides information on the TTT curve that binds the domain of crystallization in the frame of homogeneous nucleation assumption [34] (see Figure 1b).
- The spatial temperature distribution T(r, t(N)) (Figure 1c) has a maximum directly related to the pulse energy (E_p), the heat capacity (C_p) and the irradiated volume (width and length): this situation is valid for pulses with no overlapping in time.
- An average curve can be obtained by averaging the T(r, t(N)) curve on the period of the pulse $\overline{T}(r, N) = \int_{\tau_p} \frac{T(\tau, t(N))}{\tau_p} dt$. This curve becomes stationary after about $270\tau_D$ or $N > N_{sstn}(0) = 15$ pulses (see Appendix A Equation (A5)).
- A time-averaged temperature curve is a convenient mean to consider the temperature spatial distribution, and to understand the effective incubation time (t_{eff}) obtained from laser irradiation. This last is close to the shortest one in the possible crystallization range from T_g to the maximum average temperature (T_{max}) controlled by the average light power $\overline{P}$: $t_{eff}(E_p \cdot f) = \min_{t_i}(\overline{T})_{(T_g \le T_x \le \overline{T} \le T_{max} \le T_m)}$ where $t_i(T)$ is the domain boundary in Figure 1b.

Thus, for low-average power ($\overline{P}$), $\overline{T}$ is close to T_g, t_{eff} is large, but as $\overline{P}$ increases, t_{eff} decreases drastically until a value defined by the TTT curve (at the T_p temperature), and then slows down weakly for further increase of $\overline{P}$. This explains the shape of the curve shown in Figure 1a.

When the beam is moving (let us say along x), considering that the steady state is rapidly reached, $\overline{T}(x - vt, y, z, \infty)$ is a bell shape curve moving. Considering one point in the material, its temperature travels along this curve, increasing and decreasing: this is the local treatment and the bell shape that we know in space is translated in time domain. This is what we call the thermal treatment curve.

Following these previous considerations and based on our results, in Figure 9 we sketch the TTT diagrams for LNS (Figure 9a) and LNSB (Figure 9b), considering the differences in T_g, T_x, T_p, t_{eff} while T_m is assumed constant. On this figure, several heat treatments (heating-cooling curves) are drawn: note that the mean power is fixed so the maximum T is a constant and will not change as a function of scanning speed, as discussed earlier. Consider first the diagram of Figure 9a, which is for LNS glass. The scanning speed (v) is chosen so that the heat treatment does not reach the crystallization domain. Now, if we consider scanning at a speed of v/2, the treatment may penetrate the crystallization domain (i.e., the nuclei have time to form and to grow). Reversely, at higher scanning speeds (e.g., 2v in the sketched diagram) no crystallization will be detected. The situation is different for LNSB as the incubation time is much shorter and T_p much lower. This has the effect of shifting the crystallization domain to lower temperature and closer to the ordinate axis, as illustrated in Figure 9b. Therefore, for the same scanning speed v, the treatment curve will now penetrate the crystallization domain. It is thus possible to increase the scanning speed until a value given by the experiment (i.e., 5v) to reach the critical value beyond which the crystallization stops.

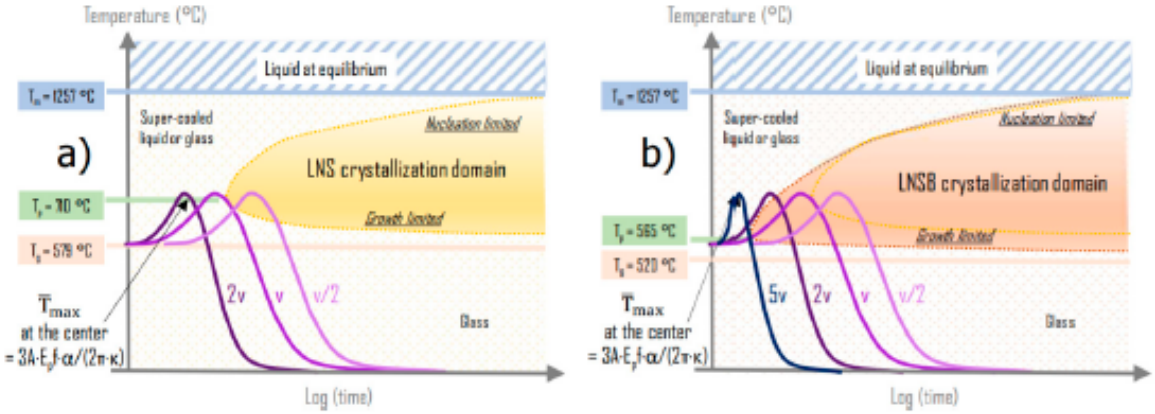

Figure 9. Scheme of the effect of the scanning speed on the crystallization for the two glasses ((**a**) LNS and (**b**) LNSB) investigated in this paper. (1) The crystallization domains are sketched based on the following rules: they are limited by the T_g on bottom side and T_m on top side; the nucleation top side is not changed because it only depends on the thermodynamics driving force of the nuclei that we assume the same for both glasses [34]. However, the growth rate is increasing with the strong decrease of the viscosity. These changes lead to a strong decrease of the incubation time. (2) The maximum average temperature is defined by pulse energy and the repetition rate ($E_p \cdot f$). It does not change on the scanning speed (v) and very little on the chemical composition. Whatever the speed, the coincidence of the time scales between TTT and treatment curve is fixed when the treatment curves cross T_g, considered to be the starting time for crystallization (what happens below T_g is expected to have insignificant effect on the crystallization kinetics).

4.4. Evolution of The Heat Affected Volume (HAV) Width and Length with Respect to the Scanning Speed V

Based on our previous discussion, we can now understand better the evolution of HAV width with respect to the scanning speed (as observed in Figure 4, for instance). To observe crystallization, the temperature should overcome T_x, and this temperature is slightly dependent on the time of irradiation (or the equivalent in laser irradiation:

the number of pulses). This can be visualized from Figure 10: when the heat treatment time increases, the crystallization is possible at slightly lower temperatures (see the red portion in the TTT diagram). Consequently, the slight decrease of the HAV width with v observed in Figure 4b is attributed to the combination of (1) incubation time to reach the crystallization growth boundary at a given temperature and (2) the decrease of deposited pulse density when v is increased. There is also the possibility that a smaller number of pulses yields to less created defect levels absorbing in the bandgap [5], decreasing the energy transfer from the light through linear absorption thus decreasing T and HAV width.

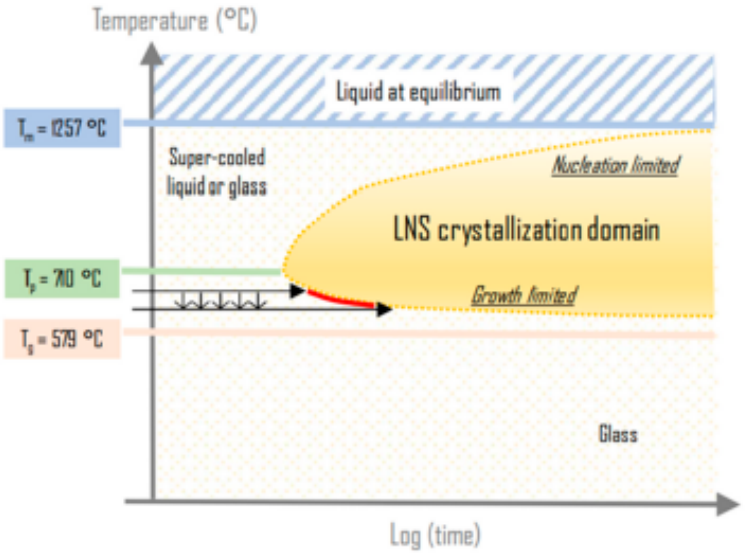

Figure 10. Sketch explaining the effect of scanning speed on the heat-affected volume (HAV) width. As the scanning speed decreases, the number of pulses deposited for a given volume increases. Consequently, the crystallization onset is reached at lower temperatures.

The length (or depth) of the HAV after the steady state is, like the width (defined by the beam waist w_0), defined by the light absorption length (i.e., $1/\alpha$ at $1/e$ with α being an effective absorption coefficient beyond the non-linear absorption stage [25]). Additionally, the related diffusion time (say τ_{Dz}) is ~$1/4{\cdot}\alpha^2 D_T$. As $1/\alpha >> w_0$ (at least by a factor of 10), $\tau_{Dz} >> \tau_{Dr}$ and the steady-state temperature along the beam propagation axis would be reached much later (2 or 3 order of times later) than along the radial direction. The total number of pulses deposited punctually (at f = 200 kHz) is above 400,000 (for v = 1 µm/s) and 4000 (for v = 100 µm/s). This is larger than the pulses needed to reach the steady-state temperature (~1500). In this case, the length follows a similar effect than for the width, so the length is shortened with the speed increase.

This is not the case at speeds such as v = 500 µm/s, for which the number of pulses deposited is only 800. Therefore, the steady state is not reached, and the temperature is smaller than the steady state one, decreasing even more the length at $\overline{T}(r, N) = T_x$.

4.5. Nanogratings Region Inside The HAV Area, but Not Always Coinciding with It

In Figure 7, we highlighted the difference between the HAV area and the area where lamellas were present. At low speed (<25 µm/s) and low energy (0.5 µJ/pulse), both regions coincide but it is no more the case when either the energy or the speed are increased (>25 µm/s).

We mentioned before that the HAV dimensions are related to the T distribution because HAV boundary is defined by a minimum T for inducing an effect (e.g., T_x for crystallization).

When the temperature amplitude increases, the temperature shape distribution (related to the diffusion time) remains the same. However, the radius where T reaches T_x is pushed further out. On the other hand, the width of the nanograting region (where there are lamellas) does not change much. Indeed, it is defined by the width of the beam since nanogratings are enabled by a light-plasma interaction.

At low energy and low speed, the top of the temperature distribution penetrating the crystallization domain (as speed v/2 in Figure 9a) may define a minimum width and coincides with the width of the beam. At higher energy, the amplitude of the T distribution increases and the HAV width becomes larger than the beam width. When the speed is increased, the T distribution does not change much, but the lamellar-structured volume is likely to shrink. The latter can be explained making the following arguments:

(1) The length and the number of the nanoplanes increase with the deposited pulses number ($2w_0 \cdot P_D$) above some number that is why the birefringence is also increasing [35].

(2) The form birefringence increases also with the pulse energy above a threshold. We can thus assume that the self-organized volume depends on the dose ($I(x,y,z) \cdot P_D \cdot D_0$), where I(x,y,z) is the local light intensity, and D_0 is a dose threshold above which self-organization structures appear.

(3) If we note that $I(x, y, z) = I(x, y, z_0) \cdot \exp(-\alpha(z - z_0))$, where z_0 is the depth where nanostructure begins to appear [36], (4) therefore, the extension of the self-organized volume is defined by local dose above the minimum dose D_0, i.e., $P_D \cdot I(x, y, z_0) \cdot \exp(-\alpha(z - z_0)) \geq D_0$ or $z - z_0 \leq \frac{1}{\alpha} \ln\left(\frac{P_D \cdot I(x,y,z_0)}{D_0}\right)$. Hence, when v increases, P_D decreases, and thus the self-organized volume as it is observed experimentally.

4.6. Phenomenological Link between Birefringent Response and Scanning Speed

By investigating the microstructure and crystal size and distribution inside the laser track (Figure 6), we observe that larger crystallized domains made up by $LiNbO_3$ nanocrystals with the same orientation are present at low speeds (<25 µm/s) and can reach up to several hundreds of nm in size. These "particles" with a size around λare strongly scattering light resulting in "black" lines in natural light transmission as we observe in Figure 5a. On the other hand, increasing the scanning speed will avoid crystallites to grow, and they will only be a few ten percent (in size) of the microscope light wavelength (550 nm). Interestingly, we observed that this size distribution of crystallized domains is rather similar for lines written at speeds > 50 µm/s in LNSB (Figure 6). Under optical microscopy, there is strong light scattering but nevertheless some light still passes through them. This tuning of scanning speed may be an efficient way to control photonic device scattering losses related to the crystals' size. From Figure 7, the presence of lamellar-like structures is taken responsible of the birefringent response of the inscribed lines [21]. The volume occupied by the lamellar-like structure becomes smaller as the scanning speed increases (and the retardance decreases). Maximizing this lamellar-like structuring would therefore bring higher retardance values and low speeds may be preferred. However, an associated low speed tradeoff is the formation of larger regions with single texture, which ultimately would cause light scattering as well. Therefore, there exists a sweet spot in the medium speed range regime where the laser track retardance response is maximized. This sweet spot is much wider for LNSB relative to LNS: typ. by a factor of 4 or 5 as it can be seen in the retardance measurements reported in Figure 5b,c.

5. Conclusions

In this work, fs-laser irradiation on two glasses, LNSB ($33Li_2O$-$33Nb_2O_5$-$13SiO_2$-$21B_2O_3$) and LNS ($33Li_2O$-$33Nb_2O_5$-$34SiO_2$), was performed. The effect of scanning speed on crystallization was investigated in various writing conditions. Experimentally, we determined that the beam scanning speed limit is 32 ± 12 µm/s for LNS and 237 ± 12 µm/s for LNSB at 0.5 µJ/pulse, and 112 ± 12 µm/s for LNS and 612 ± 12 µm/s for LNSB at 1.0 µJ/pulse. In the conditions used, faster crystallization (>5×) can be achieved when SiO_2 is substituted with B_2O_3 (here 21 mol% substitution).

Based on SEM-EBSD analysis, we observed that both the width and the length of the crystallized volume change slightly as the scanning speed is varied. We have determined the orientation distribution of the nanocrystals by SEM-EBSD. We found that a preferential texture with $LiNbO_3$ c axis perpendicular to laser polarization could be preserved when scanning speed was increased, but its contrast decreased. In addition, while the width of the nanogratings region does not change much, the length is drastically reduced when the scanning speed increases.

By using a simple approach based on temperature distribution averaged on a pulse time period, along with its characteristics in a stationary state, we showed that the irradiations were performed in the regime of weak time overlapping between pulses or heat accumulation: only 15 pulses are needed to reach 94% of the temperature steady-state value. Key results can be summarized as follows:

- We identified the variations of the thermal properties (T_x, T_p, incubation time) with respect to the glass chemical compositions. From these data, we deduced the variation of the crystallization domain in the time-temperature framework. The lower part of the crystallization domain in the TTT diagram (growth limited) is shifted to lower temperatures when B_2O_3 is added to the glass matrix. As a result for LNSB, the minimum incubation time is reduced by a factor larger than 5 with respect to LNS.
- We stated that the effective incubation time is better translated by a number of pulses whatever the repetition rate and is a function of the average laser power (rather than pulse energy only) and the number of pulses (equivalent to irradiation duration).
- We specified the concepts of spatial pulse overlap (pulse density that means irradiation time) and time pulse overlap, which govern the heat accumulation and the average temperature.
- We explained the scanning speed limit to induce crystallized lines as follows: there exists an effective irradiation time that is related to the width of the average temperature spatial distribution, and that is translated in the temporal domain during scanning. When the heat treatment time becomes smaller than the incubation time, crystallization cannot occur. Interestingly, we can deduce that faster scanning speeds while preserving the nano-crystallization are possible when the mean power is increased as illustrated in Figure 11.
- We explained the weak decrease of the HAV width when the scanning speed is increased (or the decrease of dot diameter with the decrease of the irradiation time in static irradiation) by the decrease of the incubation time with the increase of the onset temperature T_x. Crystallization starts thus at a higher temperature and this corresponds to a radius closer to the center. Two processes explain the length decrease: the same phenomena as above but in addition the decrease of the temperature amplitude due to a smaller absorption coefficient for smaller pulse densities.
- The width of the nanograting region coincides with HAV at low speeds and low energy because only a small part of the T distribution (in fact the top) is touching the crystallization domain. Assuming that these self-organized structures are dependent on the light dose ($I(x,y,z)\cdot P_D$) above a threshold dose (D_0), when the speed is increased, the local dose decreases on all points of the irradiated volume. Consequently, the volume where the dose overcomes D_0 also decreases.

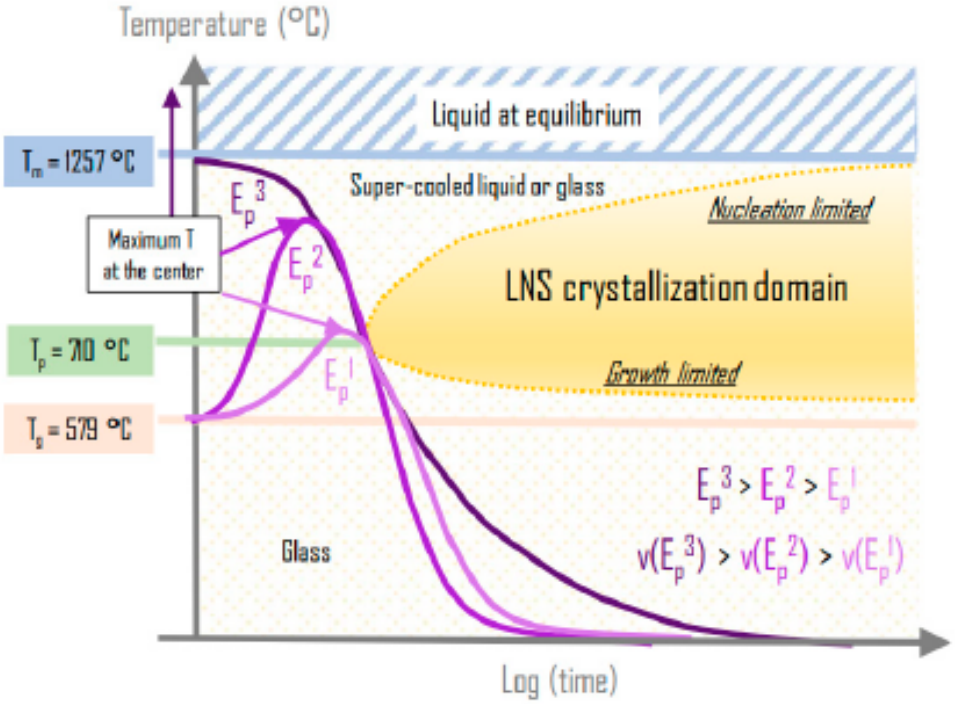

Figure 11. The figure shows the possibility of increasing the scanning speed in preserving the nanocrystal microstructure. The objective is that the treatment curve crosses the nose of the crystallization domain. If the speed is increased, the mean power must be increased in relation. Quite rapidly, the treatment curve overcomes the melting temperature, and the mechanism evolves from solid-solid to liquid-solid crystallization.

Finally, we observed that birefringence response of the inscribed line is a function of scanning speed. This is related to the variation of the nanograting region volume as explained above. On the contrary, the crystallized volume varied only weakly with the scanning speed, as well as the nanocrystal density. As a matter of fact, the latter is defined by the average temperature distribution, which is fixed by both pulse energy and repetition rate. However, the contrast of orientation is larger for low speed and this is likely to be due to the larger volume taken by nanogratings.

Author Contributions: Conceptualization, E.M., M.C., M.L. and B.P.; Data curation, E.M.; Formal analysis, E.M., M.C., R.Q. and B.P.; Funding acquisition, M.C. and B.P.; Investigation, E.M., M.C. and F.B.; Methodology, E.M., M.C. and R.Q.; Project administration, M.C. and B.P.; Resources, D.P. and B.P.; Supervision, M.C. and B.P.; Validation, M.C. and B.P.; Visualization, E.M.; Writing—original draft, E.M., M.C. and B.P.; Writing—review & editing, E.M., M.C., M.L., D.P., D.J. and B.P. All authors have read and agreed to the published version of the manuscript.

Funding: This work was supported by the French National Research Agency under the program CHARMMMAT ANR-11-LABX-0039-grant.

Institutional Review Board Statement: Not applicable.

Informed Consent Statement: Not applicable.

Data Availability Statement: Via corresponding author.

Conflicts of Interest: The authors declare no conflict of interest.

Appendix A

Foreword: the formulas below are deduced from the Fourier's equation with temperature independent and uniform coefficients, of a fs multipulse irradiation with the

hypothesis that the pulse energy is deposited in a time short enough before active thermal diffusion with a spherical geometry around the focus. This simplified model is enough for reasoning and allows to manage simple expressions. After a while corresponding to a number of pulses N_{ss}, the system reaches a steady state, beyond which the temperature at the distance r from the center of the focus oscillates between $T_{min}(r, \infty)$ and $T_{max}(r, \infty)$ within the period [19,37]. In addition, when the temperature is averaged on the period, there is no more time dependence arising from the pulsed character and discussions on the structural modifications are rendered easier. We point out that a paper will be published in the near future that will extensively describe the subsequently established equations that express analytically the results obtained numerically in Refs. [19,37] and other references. To help the Reader, the designation, definition, and units of each variable employed in the equations below are listed in Table A1 at the end of Appendix A.

The instantaneous temperature increase (T) from the room temperature at time t and distance r from the center of the beam can be shown to be [38]:

$$\frac{T(r,t)}{T_0} = \sum_{\substack{n=0 \\ N-1 = integer\ part\ (t/\tau_p)}}^{N-1} \frac{1}{\left[1+\left(\frac{t}{\tau_p}-n\right)\cdot R\tau\right]^{3/2}} \cdot \exp\left[-\frac{(r/w_0)^2}{1+\left(\frac{t}{\tau_p}-n\right)\cdot R\tau}\right] \quad (A1)$$

with $\tau_p = 1/f$, $\tau_D = w_0^2/4D_T$, $R\tau = \tau_p/\tau_D$, $T_0 = 3\cdot A\cdot E_p/(4\cdot\pi\cdot\rho\cdot C_p\cdot w_0^3)$, f is the pulse repetition rate, w_0 is a beam waist radius (at 1/e). Performing an averaging on the period, we get the average temperature expression:

$$\frac{\overline{T}(r,N)}{T_0} = \frac{1}{\tau_p}\int_{\frac{t}{\tau_p}-N-1}^{\frac{t}{\tau_p}-N} \sum_{n=0}^{N-1} \frac{1}{\left[1+\left(\frac{t}{\tau_p}-n\right)\cdot R\tau\right]^{3/2}} \cdot \exp\left[-\frac{(r/w_0)^2}{1+\left(\frac{t}{\tau_p}-n\right)\cdot R\tau}\right]\cdot dt \quad (A2)$$

That can be expressed as

$$\frac{\overline{T}(r,N)}{T_0} = \frac{w_0\cdot\sqrt{\pi}}{r\cdot R\tau}\cdot\left[\mathrm{erf}\left(\frac{r}{w_0}\right) - \mathrm{erf}\left(\frac{r/w_0}{\sqrt{1+N\cdot R\tau}}\right)\right] \quad (A3)$$

This quantity increases at the beginning of the irradiation and reaches a steady state limit that is:

$$\frac{\overline{T}(r,\infty)}{T_0} = \frac{w_0\cdot\sqrt{\pi}}{r\cdot R\tau}\cdot\mathrm{erf}\left(\frac{r}{w_0}\right) \text{ and } \frac{\overline{T}(0,\infty)}{T_0} = \frac{2}{R\tau} \quad (A4)$$

This one is reached at the level of ε after a number of pulses $N_{sssn}(r)$ for a distance r:

$$N_{sssn}(r) = \frac{1}{R\tau}\left[\left(\frac{r/w}{\varepsilon\sqrt{\pi}\cdot\mathrm{erf}\left(\frac{r}{w_0}\right)}\right)^2 - 1\right]. \text{ At the center } N_{sssn}(0) = (1/\varepsilon^2 - 1)/R\tau \quad (A5)$$

This means for $\varepsilon = 6\%$, f = 200 kHz, $D_T = 9\cdot10^{-7}$ m^2/s, $\tau_D = 0.28\mu$s, $R\tau = 18$, $N_{sssn}(0) \approx 15$ pulses or $270\cdot\tau_D$.

We note that the maximum temperature according to the radius is at the center and has the value:

$$\overline{T}(0,\infty) = \frac{3A\cdot E_p\cdot f}{8\pi\cdot\kappa\cdot w_0} \quad (A6)$$

N.B.: for cylindrical geometry, the expression of the maximum temperature is slightly modified with the introduction of an absorption coefficient resulting from non-linear absorption. We read:

$$T_0 = \frac{A\cdot E_p\cdot\alpha}{\pi\rho\cdot C_p\cdot w_0^2} \quad \overline{T}(0,\infty) = \frac{A\cdot E_p\cdot f\cdot\alpha}{2\pi\kappa} \quad (A7)$$

Table A1. Parameters, definitions and units used in the above equations.

Parameters	Definitions	Units
A	Fraction of reflected light by the plasma	none
α	Light absorption coefficient	μm^{-1}
ε	A small quantity for computation needs	none
τ_p	Pulse period	µs
τ_D	Heat diffusion time $\tau_D = \frac{w_0^2}{4D_T}$	µs
$R\tau$	τ_p/τ_D	none
w_0	Beam waist radius (at 1/e)	µm
D_T	Thermal diffusivity $D_T = \frac{\kappa}{\rho \cdot C_p}$	m^2/s
κ	Thermal conductivity	W/(m·K)
E_p	Pulse energy	J
f	Pulse repetition rate	MHz
ρ	Density	kg/m^3
C_p	Specific heat capacity	J/(kg·K)

Appendix B

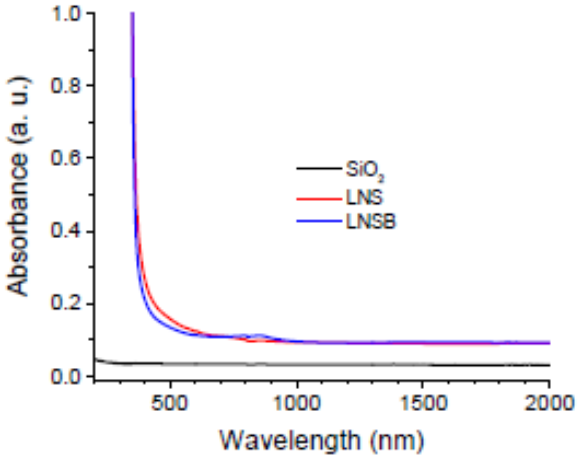

Figure A1. Absorption spectra for LNS, LNSB, with SiO_2 (Suprasil) added as a reference. The data were taken using a Cary5000 spectrophotometer. There is no specific absorption band situated at 1030 nm that could cause a drastic multiphoton absorption difference between the two silicate glasses.

References

1. Karabchevsky, A.; Katiyi, A.; Ang, A.S.; Hazan, A. On-chip nanophotonics and future challenges. *Nanophotonics* **2020**, *9*, 3733–3753. [CrossRef]
2. A round-up of recent papers in the field of photonics published by the physical sciences division of the Nature Publishing Group. *Nat. Photonics* **2008**, *2*, 251. [CrossRef]
3. Fernandez, T.; Sakakura, M.; Eaton, S.; Sotillo, B.; Siegel, J.; Solis, J.; Shimotsuma, Y.; Miura, K. Bespoke photonic devices using ultrafast laser driven ion migration in glasses. *Prog. Mater. Sci.* **2018**, *94*, 68–113. [CrossRef]

4. Bricchi, E.; Kazansky, P.G. Extraordinary stability of anisotropic femtosecond direct-written structures embedded in silica glass. *Appl. Phys. Lett.* **2006**, *88*, 111119. [CrossRef]
5. Stoian, R.; Mishchik, K.; Cheng, G.; Mauclair, C.; D'Amico, C.; Colombier, J.-P.; Zamfirescu, M. Investigation and control of ultrafast laser-induced isotropic and anisotropic nanoscale-modulated index patterns in bulk fused silica. *Opt. Mater. Express* **2013**, *3*, 1755. [CrossRef]
6. He, X.; Poumellec, B.; Liu, Q.; Brisset, F.; Lancry, M. One-step photoinscription of asymmetrically oriented fresnoite-type crystals in glass by ultrafast laser. *Opt. Lett.* **2014**, *39*, 5423–5426. [CrossRef]
7. Miura, K.; Qiu, J.; Mitsuyu, T.; Hirao, K. Space-selective growth of frequency-conversion crystals in glasses with ultrashort infrared laser pulses. *Opt. Lett.* **2000**, *25*, 408–410. [CrossRef]
8. McAnany, S.D.; Veenhuizen, K.J.; Kiss, A.M.; Thieme, J.; Nolan, D.A.; Aitken, B.G.; Dierolf, V.; Jain, H. Evolution of glass structure during femtosecond laser assisted crystallization of LaBGeO5 in glass. *J. Non-Cryst. Solids* **2021**, *551*, 120–396. [CrossRef]
9. Lipatiev, A.S.; Lipateva, T.O.; Lotarev, S.V.; Okhrimchuk, A.G.; Larkin, A.S.; Presnyakov, M.Y.; Sigaev, V.N. Direct Laser Writing of $LaBGeO_5$ Crystal-in-Glass Waveguide Enabling Frequency Conversion. *Cryst. Growth Des.* **2017**, *17*, 4670–4675. [CrossRef]
10. Cao, J.; Poumellec, B.; Brisset, F.; Helbert, A.-L.; Lancry, M. Tunable angular-dependent second-harmonic generation in glass by controlling femtosecond laser polarization. *J. Opt. Soc. Am. B* **2016**, *33*, 741. [CrossRef]
11. Komatsu, T. Design and control of crystallization in oxide glasses. *J. Non-Cryst. Solids* **2015**, *428*, 156–175. [CrossRef]
12. Cao, J.; Lancry, M.; Brisset, F.; Mazerolles, L.; Saint-Martin, R.; Poumellec, B. Femtosecond Laser-Induced Crystallization in Glasses: Growth Dynamics for Orientable Nanostructure and Nanocrystallization. *Cryst. Growth Des.* **2019**, *19*, 2189–2205. [CrossRef]
13. Cao, J.; Poumellec, B.; Mazerolles, L.; Brisset, F.; Helbert, A.-L.; Surble, S.; He, X.; Lancry, M. Nanoscale Phase Separation in Lithium Niobium Silicate Glass by Femtosecond Laser Irradiation. *J. Am. Ceram. Soc.* **2016**, *100*, 115–124. [CrossRef]
14. Cao, J.; Mazerolles, L.; Lancry, M.; Brisset, F.; Poumellec, B. Modifications in lithium niobium silicate glass by femtosecond laser direct writing: Morphology, crystallization, and nanostructure. *J. Opt. Soc. Am. B* **2016**, *34*, 160. [CrossRef]
15. Cao, J.; Mazerolles, L.; Lancry, M.; Solas, D.; Brisset, F.; Poumellec, B. Form birefringence induced in multicomponent glass by femtosecond laser direct writing. *Opt. Lett.* **2016**, *41*, 2739–2742. [CrossRef]
16. Cao, J.; Poumellec, B.; Brisset, F.; Lancry, M. Pulse energy dependence of refractive index change in lithium niobium silicate glass during femtosecond laser direct writing. *Opt. Express* **2018**, *26*, 7460–7474. [CrossRef]
17. Cao, J.; Poumellec, B.; Brisset, F.; Helbert, A.-L.; Lancry, M. Angular Dependence of the Second Harmonic Generation Induced by Femtosecond Laser Irradiation in Silica-Based Glasses: Variation with Writing Speed and Pulse Energy. *World J. Nano Sci. Eng.* **2015**, *5*, 96–106. [CrossRef]
18. Muzi, E.; Cavillon, M.; Lancry, M. Controlled Orientation of Second Harmonic Generation Induced by femtosecond laser Crystallization in Li_2O-Nb_2O_5-SiO_2-B_2O_3 glasses. *Opt. Mater. Express* **2021**, in press.
19. Eaton, S.M.; Zhang, H.; Herman, P.R.; Yoshino, F.; Shah, L.; Bovatsek, J.; Arai, A.Y. Heat accumulation effects in femtosecond laser-written waveguides with variable repetition rate. *Opt. Express* **2005**, *13*, 4708–4716. [CrossRef] [PubMed]
20. Lax, M. Temperature rise induced by a laser beam. *J. Appl. Phys.* **1977**, *48*, 3919–3924. [CrossRef]
21. Cao, J. *Creation and Orientation of Nano-Crystals by Femtosecond Laser Light for Controlling Optical Non-Linear Response in Silica-Based Glasses, Material Chemistry*; Université Paris Saclay (COmUE): Paris, France, 2017.
22. Veenhuizen, K.; McAnany, S.; Nolan, D.; Aitken, B.; Dierolf, V.; Jain, H. Fabrication of graded index single crystal in glass. *Sci. Rep.* **2017**, *7*, srep44327. [CrossRef]
23. Shimada, M.; Honma, T.; Komatsu, T. Laser patterning of oriented $LiNbO_3$ crystal particle arrays in NiO-doped lithium niobium silicate glasses. *Int. J. Appl. Glass Sci.* **2018**, *9*, 518–529. [CrossRef]
24. Desmarchelier, R.; Poumellec, B.; Brisset, F.; Mazerat, S.; Lancry, M. In the Heart of Femtosecond Laser Induced Nanogratings: From Porous Nanoplanes to Form Birefringence. *World J. Nano Sci. Eng.* **2015**, *5*, 115–125. [CrossRef]
25. Lancry, M.; Groothoff, N.; Poumellec, B.; Guizard, S.; Fedorov, N.; Canning, J. Time-resolved plasma measurements in Ge-doped silica exposed to infrared femtosecond laser. *Phys. Rev. B* **2011**, *84*, 1–8. [CrossRef]
26. Bansal, N.P.; Doremus, R. *Handbook of Glass Properties*; Academic Press: London, UK, 1986. [CrossRef]
27. Lotarev, S.V.; Lipatiev, A.S.; Lipateva, T.O.; Fedotov, S.S.; Naumov, A.S.; Moiseev, I.A.; Sigaev, V.N. Ultrafast-laser vitrification of laser-written crystalline tracks in oxide glasses. *J. Non-Cryst. Solids* **2019**, *516*, 1–8. [CrossRef]
28. Allix, M.; Cormier, L. Crystallization and Glass-Ceramics. In *Springer Handbook of Glass*; Springer: Cham, Switzerland, 2019; Chapter 4; pp. 113–167. [CrossRef]
29. Fokin, V.M.; Nascimento, M.L.; Zanotto, E.D. Correlation between maximum crystal growth rate and glass transition temperature of silicate glasses. *J. Non-Cryst. Solids* **2005**, *351*, 789–794. [CrossRef]
30. He, X.; Liu, Q.; Lancry, M.; Brisset, F.; Poumellec, B. Space-Selective Control of Functional Crystals by Femtosecond Laser: A Comparison between SrO-TiO_2-SiO_2 and Li_2O-Nb_2O_5-SiO_2 Glasses. *Crystals* **2020**, *10*, 979. [CrossRef]
31. Varshneya, A.K.; Mauro, J.C. Fundamentals of Inorganic Glasses. *Fundam. Inorg. Glasses* **2019**. [CrossRef]
32. Cabral, A.; Cardoso, A.; Zanotto, E. Glass-forming ability versus stability of silicate glasses. I. Experimental test. *J. Non-Cryst. Solids* **2003**, *320*, 1–8. [CrossRef]
33. Prapitpongwanich, P.; Penggpat, K.; Rüssel, C. Phase separation and crystallization in $LiNbO_3$/SiO_2 glasses. *Mater. Chem. Phys.* **2009**, *113*, 913–918. [CrossRef]
34. Neuville, D.R.; Cormier, L.; Caurant, D.; Montagne, L. *From Glass to Crystal*; EDP Sciences: Les Ulis, France, 2017; p. 645.

35. Richter, S.; Heinrich, M.; Döring, S.; Tünnermann, A.; Nolte, S.; Peschel, U. Nanogratings in fused silica: Formation, control, and applications. *J. Laser Appl.* **2012**, *24*, 042008. [CrossRef]
36. Poumellec, B.; Lancry, M.; Chahid-Erraji, A.; Kazansky, P.G. Modification thresholds in femtosecond laser processing of pure silica: Review of dependencies on laser parameters [Invited]. *Opt. Mater. Express* **2011**, *1*, 766–782. [CrossRef]
37. Zhang, H.; Eaton, S.M.; Li, J.; Herman, P.R. Heat accumulation during high repetition rate ultrafast laser interaction: Waveguide writing in borosilicate glass. *J. Phys. Conf. Ser.* **2007**, *59*, 682–686. [CrossRef]
38. Shimizu, M.; Sakakura, M.; Ohnishi, M.; Yamaji, M.; Shimotsuma, Y.; Hirao, K.; Miura, K. Three-dimensional temperature distribution and modification mechanism in glass during ultrafast laser irradiation at high repetition rates. *Opt. Express* **2012**, *20*, 934–940. [CrossRef]